

**MULTIPLE SCATTERING CORRELATION
MEASUREMENTS IN FLUID/PARTICLE
SUSPENSIONS: APPLICATION TO
PARTICLE CHARACTERIZATION**

By

FARHAD DORRI-NOWKOORANI

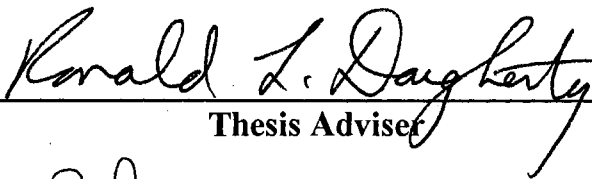
**Bachelor of Science
Oklahoma State University
Stillwater, Oklahoma
1984**

**Master of Science
Oklahoma State University
Stillwater, Oklahoma
1989**


**Submitted to the Faculty of the
Graduate College of
Oklahoma State University
in partial fulfillment of
the requirements for
the Degree of
DOCTOR OF PHILOSOPHY
May, 1995**

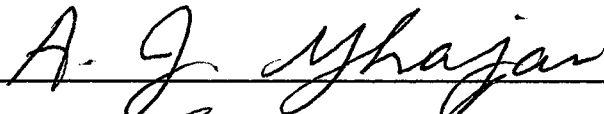
**MULTIPLE SCATTERING CORRELATION
MEASUREMENTS IN FLUID/PARTICLE
SUSPENSIONS: APPLICATION TO
PARTICLE CHARACTERIZATION**

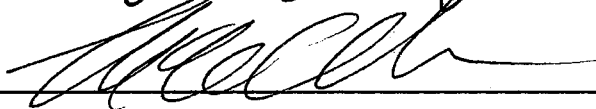
Thesis Approved:

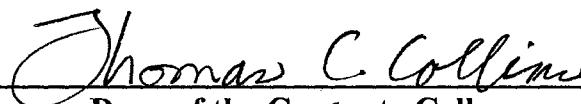


Thesis Adviser









Dean of the Graduate College

ACKNOWLEDGMENTS

"Thank God for all his blessings, protection, guidance, and forgiveness. There is nothing beyond him and there is no existence before and after him."

Then I would like to dedicate this thesis to my wife, Fatemeh, for her love, understanding, encouragement, and support during all these years of my study. She bore with me through all the hard times that we went through during all these years, and without her help, I could not have finished my Masters and Doctoral degrees. I also gratefully appreciate my parents for their help and support of me all my life, and they went through lots of difficulties and problems just for me to live better and more comfortably. I also extend my appreciation to my mother-in-law for her help which made life easier for me. I love all of them so much and God bless them.

I wish to express my sincere and deep appreciation to my adviser, Dr. Ronald L. Dougherty, for his intelligent supervision, constructive guidance, encouragement, and support. I still remember the first time that I talked to him and chose him as my adviser, and his long distance call to me concerning financial support. I admire him not only for this constructive supervision but his respectable personality and his caring for students. I learned a lot from him. Also I appreciate his wife, Kathe, for her time and help to correct my grammatical problems in my proposal for my preliminary examination. I have best wishes for both of them.

My sincere appreciation extends to Dr. Bruce J. Ackerson for his suggestions and assistance for this study. And I would like to thank my other committee members, Dr. Afshin J. Ghajar and Dr. Frank W. Chambers for their gracious help, time, and concern. Again I deeply appreciate all of my committee members for Their flexibility in scheduling the time for my defense which was not convenient for any of them.

Moreover, special thanks go to my colleagues, Nafaa M. Reguigui, Ulf Nobbmann, Cho-Chun Liu, and Y. Tian for their contributions, assistance, and kindness.

Also, I would like to mention my two sons, Mohammad Ali and Mohammad Ameen, who brought happiness to my life. I will give this thesis to them one time as my memory, and they should know that I always love them and ask God to protect and guide them to the right path.

Finally, I invoke God's blessing for those people who sacrifice their lives for the sake of God to light up the darkness and open my eyes so I can find the right path.

TABLE OF CONTENTS

Chapter	Page
I. INTRODUCTION.....	1
Applications	2
Review of Techniques	4
Image Analysis.....	5
Electrical Zone Sensing.....	6
Gravitational Sedimentation	7
Light Scattering Techniques	8
Summary	10
Objective	11
II. LITERATURE REVIEW	13
III. METHODOLOGY	18
Theoretical Background.....	18
Single Scattering	19
Multiple Scattering.....	20
Numerical Development	25
Exact Solution.....	25
Approximate Solution (Improved P_N Approximation)	26
Classical P_N Approximation.....	26
Improvement of P_N Approximation.....	32
Boundary Conditions	33
Experimental Setup and Procedure	35
IV. RESULTS AND DISCUSSION.....	41
Sample Container Factors	42
Effect of Glass Cell Back Reflection	42
One Dimensionality.....	43
Effect of Different Cells.....	44
Optical Thickness Effects	45
Single to Multiple Scattering.....	46
Comparison of Experiment to CT Theory	48
Off Angle Measurements	54
Polarization Effects	56
A Proposal for Characterizing Particle Size	59

Chapter	Page
Improved P_N Approximation.....	64
V. CONCLUSION AND RECOMMENDATIONS	165
Summary and Conclusions.....	165
Recommendations	168
REFERENCES.....	170
APPENDIXES	175
APPENDIX A--Error Analysis	176
Temperature Sensitivity.....	176
Detector Position.....	177
Comparison of Experiment to Theory for Single Scattering	177
Repeatability of the Data	178
Comparison of the Experimental Data to DWS.....	178
Homodyning Versus Heterodyning.....	179
Laser Stability	180
APPENDIX B--1 Term g^1 Expansion Exact Program for Correlation Transfer (CT) Theory.....	191
APPENDIX C--Finite Difference Method with Variable Grid Sizes	198
APPENDIX D--Modified P_N Approximation Program.....	100

LIST OF TABLES

Table	Page
1. Mie scattering cross-sections and asymmetry factors (refraction index of 1.59) of spherical particles suspended in distilled water (refractive index of 1.33).....	39
2. Summary of the results for particle characterization at 10° (outside sample) from direct back-scattering measurements (for a room temperature of 22 °C).....	63
3. Summary of the results for particle characterization at 30° (outside sample) from direct back-scattering measurements (for a room temperature of 22 °C).....	64

LIST OF FIGURES

Figure	Page
1. Example of an electrical zone sensing diagram.....	69
2. Schematic of laser diffraction particle sizing system.....	69
3. Example of intensity fluctuation with time.	70
4. Typical plot of normalized single scattering intensity correlation function.	70
5. The geometry for reflection at both boundaries.	71
6. Experimental setup.....	71
7. Expanded laser beam incident on test cell.	72
8. Effect of laser beam diameter on one-dimensionality of measurements, unkown optical thickness, particle diameter of 0.3 μm , and laser wavelength of 514.5 nm.....	72
9. Back-scattering: Effect of glass back reflection on correlation measurement for optical thickness of 10, particle diameter of 0.3 μm , and wavelength of 514.5 nm.	73
10. Back-scattering: Effect of glass back reflection on correlation measurement for optical thickness of 100, particle diameter of 0.3 μm , and laser wavelength of 514.5 nm.....	74
11. Back-scattering: Effect of the laser beam diameter on correlation measurements for optical thickness of 10, particle diameter of 0.3 μm , and laser wavelength of 514.5 nm.....	75
12. Back-scattering: Effect of the laser beam diameter on correlation measurements for optical thickness of 100, particle diameter of 0.3 μm , and laser wavelength of 514.5 nm.....	76

13. Back-scattering: Effect of cell size on correlation measurements for optical thickness of 100, particle diameter of 0.3 μm , and laser wavelength of 514.5 nm.....	77
14. Back-scattering: Effect of optical thickness on correlation measurements for particle diameter of 0.3 μm and laser wavelength of 514.5 nm.	78
15. Transmission: Effect of optical thickness on correlation measurements for particle diameter of 0.3 μm and laser wavelength of 514.5 nm.	79
16. Back-scattering: Effect of high optical thickness on correlation measurements for particle diameter of 0.3 μm and laser wavelength of 514.5 nm.	80
17. Transmission: Comparison of experimental data with theoretical single scattering g^1 for optical thicknesses of 0.05 to 0.25, particle diameter of 0.3 μm , laser wavelength of 514.5 nm, and 29° (inside sample) detection angle.	81
18. Transmission: Comparison of experimental data with theoretical single scattering g^1 for optical thicknesses of 0.1 to 0.5, particle diameter of 0.3 μm , laser wavelength of 514.5 nm, and 29° (inside sample) detection angle.	82
19. Transmission: Comparison of experimental data with theoretical single scattering g^1 for optical thicknesses of 0.05 to 0.50, particle diameter of 0.3 μm , laser wavelength of 514.5 nm, and 34° (inside sample) detection angle.	83
20. Transmission: Comparison of experimental data with theoretical single scattering g^1 for optical thicknesses of 0.05 to 0.50, particle diameter of 0.3 μm , laser wavelength of 514.5 nm, and 34° (inside sample) detection angle.	84
21. Transmission: Comparison of experimental data with theoretical single scattering g^1 for optical thicknesses of 0.05 to 0.50, particle diameter of 0.3 μm , laser wavelength of 514.5 nm, and 45° (inside sample) detection angle.	85

Figure	Page
22. Transmission: Comparison of experimental data with theoretical single scattering g^1 for optical thicknesses of 0.05 to 0.50, particle diameter of 0.3 μm , laser wavelength of 514.5 nm, and 45° (inside sample) detection angle.	86
23. Comparison of experimental data with theoretical single scattering g^1 for optical thicknesses of 0.10 to 0.50 using ALV5000 setup, particle diameter of 0.3 μm , laser wavelength of 514.5 nm, and 90° (outside sample) detection angle.	87
24. Comparison of experimental data with theoretical single scattering g^1 for optical thicknesses of 0.10 to 0.50 using ALV5000 setup, particle diameter of 0.3 μm , laser wavelength of 514.5 nm, and 90° (outside sample) detection angle.	88
25. Comparison of experimental data with theoretical single scattering for optical thicknesses of 0.50 to 1.40 using ALV5000 setup, particle diameter of 0.3 μm , laser wavelength of 514.5 nm, and 90° (outside sample) detection angle.	89
26. Transmission: Comparison of experimental data with isotropic preaveraged theory ($f=0$, $n=1.0$) for different optical thicknesses, particle diameter of 0.3 μm and laser wavelength of 514.5 nm.....	90
27. Transmission: Comparison of experimental data with anisotropic preaveraged theory ($f=0.727$, $n=1.0$) for different optical thicknesses, particle diameter of 0.3 μm and laser wavelength of 514.5 nm.....	91
28. Transmission: Comparison of experimental data with isotropic preaveraged theory ($f=0$, $n=1.331$) for different optical thicknesses, particle diameter of 0.3 μm and laser wavelength of 514.5 nm.....	92
29. Transmission: Comparison of experimental data with anisotropic preaveraged theory ($f=0.727$, $n=1.331$) for different optical thicknesses, particle diameter of 0.3 μm and laser wavelength of 514.5 nm.	93
30. Transmission: Comparison of experimental data with the anisotropic one term Legendre expansion of g^1 ($f=0.727$, $n=1.331$) for different optical thicknesses, particle diameter of 0.3 μm and laser wavelength of 514.5 nm.	94

31. Back-scattering: Comparison of experimental data with isotropic preaveraged theory ($f=0$, $n=1.0$) for different optical thicknesses, particle diameter of $0.3\ \mu\text{m}$ and laser wavelength of $514.5\ \text{nm}$	95
32. Back-scattering: Comparison of experimental data with anisotropic preaveraged theory ($f=0.727$, $n=1.0$) for different optical thicknesses, particle diameter of $0.3\ \mu\text{m}$ and laser wavelength of $514.5\ \text{nm}$	96
33. Back-scattering: Comparison of experimental data with anisotropic preaveraged theory ($f=0.727$, $n=1.331$) for different optical thicknesses, particle diameter of $0.3\ \mu\text{m}$ and laser wavelength of $514.5\ \text{nm}$	97
34. Back-scattering: Comparison of experimental data with anisotropic one term Legendre expansion of g^1 ($f=0.727$, $n=1.331$) for different optical thicknesses, particle diameter of $0.3\ \mu\text{m}$ and laser wavelength of $514.5\ \text{nm}$	98
35. Back-scattering: Comparison of experimental data with anisotropic one term Legendre expansion of g^1 theory ($f=0.089$, $n=1.331$) for different optical thicknesses, particle diameter of $0.091\ \mu\text{m}$ and laser wavelength of $532\ \text{nm}$	99
36. Transmission: Comparison of experimental data with anisotropic one term Legendre expansion of g^1 theory ($f=0.089$, $n=1.331$) for different optical thicknesses, particle diameter of $0.091\ \mu\text{m}$ and laser wavelength of $532\ \text{nm}$	100
37. Back-scattering: Comparison of experimental data with anisotropic one term Legendre expansion of g^1 theory ($f=0.132$, $n=1.331$) for different optical thicknesses, particle diameter of $0.107\ \mu\text{m}$ and laser wavelength of $514.5\ \text{nm}$	101
38. Transmission: Comparison of experimental data with anisotropic one term Legendre expansion of g^1 theory ($f=0.132$, $n=1.331$) for different optical thicknesses, particle diameter of $0.107\ \mu\text{m}$ and laser wavelength of $514.5\ \text{nm}$	102
39. Back-scattering: Comparison of experimental data with the anisotropic one term Legendre expansion of g^1 theory ($f=0.858$, $n=1.331$) for different optical thicknesses, particle diameter of $0.497\ \mu\text{m}$ and laser wavelength of $514.5\ \text{nm}$	103

40. Transmission: Comparison of experimental data with the anisotropic one term Legendre expansion of g^1 theory ($f=0.858$, $n=1.331$) for different optical thicknesses, particle diameter of $0.497\ \mu\text{m}$ and laser wavelength of $514.5\ \text{nm}$	104
41. Back-scattering: Comparison of experimental data with preaveraged and 3 term Legendre expansion of g^1 for a semi-infinite medium, particle diameter of $0.3\ \mu\text{m}$ and laser wavelength of $514.5\ \text{nm}$	105
42. Transmission: Comparison of experimental data with the single scattering and Legendre expansion of g^1 in CT theory for 29° (inside sample) detection angle for a very dilute sample (single scattering medium), particle diameter of $0.3\ \mu\text{m}$, and laser wavelength of $514.5\ \text{nm}$	106
43. Transmission: Comparison of experimental data with the single scattering and 3 term Legendre expansion of g^1 in CT theory for 45° (inside sample) detection angle for very dilute sample (single scattering medium), particle diameter of $0.3\ \mu\text{m}$, and laser wavelength of $514.5\ \text{nm}$	107
44. Back-scattering: Effect of detection angle ($\mu=\cos\theta$) on experimental data for optical thickness of 10, particle diameter of $0.3\ \mu\text{m}$, and laser wavelength of $514.5\ \text{nm}$	108
45. Back-scattering: Effect of detection angle ($\mu=\cos\theta$) on isotropic preaveraged theory ($f=0.0$, $n=1.0$) for optical thickness of 10.....	109
46. Back-scattering: Effect of detection angle ($\mu=\cos\theta$) on anisotropic preaveraged theory ($f=0.727$, $n=1.331$) for optical thickness of 10.....	110
47. Back-scattering: Effect of detection angle ($\mu=\cos\theta$) on experimental data for optical thickness of 100, particle diameter of $0.3\ \mu\text{m}$, and laser wavelength of $514.5\ \text{nm}$	111
48. Back-scattering: Effect of detection angle ($\mu=\cos\theta$) on experimental data for optical thickness of 2, particle diameter of $0.3\ \mu\text{m}$, and laser wavelength of $514.5\ \text{nm}$	112

49. Back-scattering: Effect of detection angle ($\mu=\cos\theta$) on experimental data for optical thickness of 3, particle diameter of 0.3 μm , and laser wavelength of 514.5 nm.....	113
50. Back-scattering: Effect of detection angle ($\mu=\cos\theta$) on experimental data for optical thickness of 4, particle diameter of 0.3 μm , and laser wavelength of 514.5 nm.....	114
51. Back-scattering: Effect of detection angle ($\mu=\cos\theta$) on experimental data for optical thickness of 5, particle diameter of 0.3 μm , and laser wavelength of 514.5 nm.....	115
52. Transmission: Comparison of experimental data with anisotropic preaveraged theory ($f=0.727$, $n=1.331$) for optical thickness of 10 and different detection angles, particle diameter of 0.3 μm , and laser wavelength of 514.5 nm.....	116
53. Transmission: Comparison of correlation measurements for different low optical thicknesses at 34° and 45° (inside sample) detection angles, particle diameter of 0.3 μm , and laser wavelength of 514.5 nm.	117
54. Transmission: Effect of detection angle ($\mu=\cos\theta$) on experimental data for optical thickness of 5, particle diameter of 0.3 μm , and laser wavelength of 514.5 nm.....	118
55. Transmission: Effect of detection angle ($\mu=\cos\theta$) on experimental data for optical thickness of 8, particle diameter of 0.3 μm , and laser wavelength of 514.5 nm.....	119
56. Transmission: Effect of detection angle ($\mu=\cos\theta$) on experimental data for optical thickness of 9, particle diameter of 0.3 μm , and laser wavelength of 514.5 nm.....	120
57. Transmission: Effect of detection angle ($\mu=\cos\theta$) on experimental data for optical thickness of 10, particle diameter of 0.3 μm , and laser wavelength of 514.5 nm.	121
58. Back-scattering: Effect of polarization on correlation measurements for different optical thicknesses, particle diameter of 0.3 μm , and laser wavelength of 514.5 nm.	122

Figure	Page
59. Back-scattering: Effect of polarization on correlation measurements for optical thickness of 100, particle diameter of 0.3 μm , and laser wavelength of 514.5 nm.....	123
60. Back-scattering: Comparison of the unpolarized correlation function measurements to the average of the two polarized measurements for different optical thicknesses, particle diameter of 0.3 μm , and laser wavelength of 514.5 nm.....	124
61. Transmission: Effect of polarization on correlation measurements for different optical thicknesses, particle diameter of 0.3 μm , and laser wavelength of 514.5 nm.....	125
62. Transmission: Effect of polarization on correlation measurements for different optical thicknesses, particle diameter of 0.3 μm , and laser wavelength of 514.5 nm.....	126
63. Transmission: Comparison of unpolarized correlation measurements to the average of the two polarized measurements for different optical thicknesses, particle diameter of 0.3 μm , and laser wavelength of 514.5 nm.....	127
64. Back-scattering: Effect of polarization on detection angle of correlation measurements for optical thickness of 3, particle diameter of 0.3 μm , and laser wavelength of 514.5 nm.....	128
65. Back-scattering: Effect of polarization on detection angle of correlation measurements for optical thickness of 4, particle diameter of 0.3 μm , and laser wavelength of 514.5 nm.....	129
66. Back-scattering: Effect of polarization on detection angle of correlation measurements for optical thickness of 5, particle diameter of 0.3 μm , and laser wavelength of 514.5 nm.....	130
67. Transmission: Effect of polarization on detection angle of correlation measurements for optical thickness of 5, particle diameter of 0.3 μm , and laser wavelength of 514.5 nm.....	131
68. Transmission: Effect of polarization on detection angle of correlation measurements for optical thickness of 8, particle diameter of 0.3 μm , and laser wavelength of 514.5 nm.....	132

Figure	Page
69. Transmission: Effect of polarization on detection angle of correlation measurements for optical thickness of 9, particle diameter of 0.3 μm , and laser wavelength of 514.5 nm.....	133
70. Transmission: Effect of polarization on detection angle of correlation measurements for optical thickness of 10, particle diameter of 0.3 μm , and laser wavelength of 514.5 nm.....	134
71. Back-scattering: Comparison of intensity measurements with the numerical results for index of refraction change at both boundaries ($n=1.331$) at 30° (inside sample) detection angle, particle diameter of 0.3 μm , and laser wavelength of 514.5 nm.....	135
72a. Back-scattering: Matching of the intensity measurements with the numerical results for index of refraction change at both boundaries ($n=1.331$) at 10° (outside sample) detection angle, for different particle diameters, and laser wavelength of 514.5 nm.	136
72b. Back-scattering: Matching of the intensity measurements with the numerical results for index of refraction change at both boundaries ($n=1.331$) at 30° (outside sample) detection angle, for different particle diameters, and laser wavelength of 514.5 nm.	137
73. Matching correlation measurements to numerical results by changing τ_0 for a particle diameter of 0.3 μm and a laser wavelength of 514.5 nm.	138
74. Matching correlation measurements for different optical thicknesses to numerical results by changing τ_0 for particle diameter of 0.3 μm , laser wavelength of 514.5 nm, and 10° (outside sample) from back-scattering.	139
75. Matching correlation measurements for different optical thicknesses to numerical results by changing τ_0 for particle diameter of 0.497 μm , laser wavelength of 514.5 nm, and 10° (outside sample) from back-scattering.	140
76. Matching correlation measurements for different optical thicknesses to numerical results by changing τ_0 for particle diameter of 0.107 μm , laser wavelength of 514.5 nm, and 10° (outside sample) from back-scattering.	141

Figure	Page
77. Matching correlation measurements for different optical thicknesses to numerical results by changing τ_0 for particle diameter of 0.3 μm , laser wavelength of 514.5 nm, and 30° (outside sample) from back-scattering.	142
78. Matching correlation measurements for different optical thicknesses to numerical results by changing τ_0 for particle diameter of 0.497 μm , laser wavelength of 514.5 nm, and 30° (outside sample) from back-scattering.	143
79. Matching correlation measurements for different optical thicknesses to numerical results by changing τ_0 for particle diameter of 0.107 μm , laser wavelength of 514.5 nm, and 30° (outside sample) from back-scattering.	144
80. Back-scattering: Comparison of improved P_N approximation with exact 3 term Legendre expansion of g^1 for $L_0=1.0$	145
81. Back-scattering: Comparison of improved P_N approximation with exact 3 term Legendre expansion of g^1 for $L_0=5.0$	146
82. Back-scattering: Comparison of improved P_N approximation with exact 3 term Legendre expansion of g^1 for $L_0=10.0$	147
83. Back-scattering: Comparison of improved P_N approximation with exact 3 term Legendre expansion of g^1 for $L_0=25.0$	148
84. Transmission: Comparison of improved P_N approximation with exact 3 term Legendre expansion of g^1 for $L_0=1.0$	149
85. Transmission: Comparison of improved P_N approximation with exact 3 term Legendre expansion of g^1 for $L_0=5.0$	150
86. Transmission: Comparison of improved P_N approximation with exact 3 term Legendre expansion of g^1 for $L_0=10.0$	151
87. Transmission: Comparison of improved P_N approximation with exact 3 term Legendre expansion of g^1 for $L_0=25.0$	152
88. Transmission: Comparison of improved P_N approximation with exact 3 term Legendre expansion of g^1 for $L_0=10.0$	153

Figure	Page
89. Transmission: Comparison of improved P_N approximation with exact 3 term Legendre expansion of g^1 for $L_0=25.0$	154
90a. Back-scattering: Effect of refractive index change at the boundaries for improved P_5 approximation for $L_e=1.0, 10$, and 25	155
90b. Back-scattering: Effect of refractive index change at the boundaries for improved P_5 approximation for $L_e=1.0$ and 10	156
90c. Back-scattering: Effect of refractive index change at the boundaries for improved P_5 approximation for $L_e=1.0$ and 25	157
91. Transmission: Effect of refractive index change at the boundaries for improved P_5 approximation for $L_e=1.0$ and 10	158
92. Transmission: Comparison of improved P_5 approximation with exact 3 term Legendre expansion of g^1 for $L_0=1.0$ with no and one index of refraction change at the boundaries.	159
93. Back-scattering: Comparison of improved P_5 approximation with exact 3 term Legendre expansion of g^1 for $L_0=1.0$ with no and one index of refraction change at the boundaries.	160
94. Transmission: Comparison of improved P_5 approximation with exact 1 term Legendre expansion of g^1 for different optical thicknesses (the same as Fig. 30) with one index of refraction change at the boundaries.	161
95. Back-scattering: Comparison of improved P_5 approximation with exact 1 term Legendre expansion of g^1 for different optical thicknesses (the same as Fig. 34) with one index of refraction change at the boundaries.	162
96. Transmission: Comparison of improved P_5 approximation (with two index of refraction changes at the boundaries) with experimental data for different optical thicknesses (the same as Fig. 30), $0.3 \mu\text{m}$ particle sizes, and laser wavelength of 514.5 nm	163
97. Back-scattering: Comparison of improved P_5 approximation (with two index of refraction changes at the boundaries) with experimental data for different optical thicknesses (the same as Fig. 30), $0.3 \mu\text{m}$ particle sizes, and laser wavelength of 514.5 nm	164

A-1. Back-scattering: Effect of τ_0 (which depends on temperature) on correlation measurements for optical thickness of 5, particle diameter of 0.3 μm , and wavelength of 514.5 nm.	182
A-2. Transmission: Effect of detection angle change on theoretical single scattering g^1	183
A-3. Transmission: Comparison of correlation measurements with theoretical single scattering g^1 for optical thickness of 0.05, particle diameter of 0.3 μm , and wavelength of 514.5 nm, at different detection angles.	184
A-4. Back-scattering: Repeatability of the data at different times for optical thickness of 10, particle diameter of 0.3 μm , and laser wavelength of 514.5 nm.	185
A-5. Transmission: Comparison of experimental correlation to the DWS ($z_0/l^* = 1.21$) theory without considering internal reflection and improved P_5 approximation with and without index of refraction effects at the boundaries, for effective optical thickness of 13.65, particle diameter of 0.3 μm , and laser wavelength of 514.5 nm.	186
A-6. Transmission: Effect of heterodyning on homodyne correlation function measurements for low optical thicknesses of 1 and 3, particle diameter of 0.107 μm , and laser wavelength of 514.5 nm.	187
A-7. Back-scattering: Transition of correlation function measurements from pure homodyne signals to the pure heterodyne signals for optical thickness of 5, particle diameter of 0.3 μm , and laser wavelength of 514.5 nm.	188
A-8. Back-scattering: Change of incident laser (Argon-Ion) intensity over the time due to misalignment of the experimental setup for optical thickness of 5, particle diameter of 0.3 μm , and laser wavelength of 514.5 nm.	189
A-9. Back-scattering: Repeatability of the correlation measurements at different times corresponding to Fig. A-8 for optical thickness of 5, particle diameter of 0.3 μm , and laser wavelength of 514.5 nm.	190

NOMENCLATURE

a_g	gravitational acceleration (m^2/s)
A_n	dependent part of intensity Legendre expansion
c	multiple scattering intensity correlation function ($W^2/m^4 \text{ rad}^2$)
c_0	speed of light (m/s)
C_{abs}	absorption cross-section (cm^2)
C_{ext}	extinction cross-section (cm^2)
C_{sca}	scattering cross-section (cm^2)
d	diameter of particle (cm)
D	diameter of an aperture (cm)
D_0	diffusion constant of particles in the medium (m^2/s)
E	magnitude of electric field (N/C)
E^*	complex conjugate of electric field (N/C)
f	fraction of forward scattering in an anisotropic "spike"
f_c	frictional coefficient
f_m	phase function Legendre expansion coefficient
g	normalized correlation function
g^1	normalized single scattering field correlation function
g^2	normalized homodyne intensity autocorrelation function
G	electric field correlation function
G^m	multiple scattering field correlation function
G_i^m	incident multiple scattering field correlation
I	intensity of radiation ($W/m^2 \text{ rad}$)
J_1	first-order Bessel function of the first kind
k	magnitude of the free medium's wave vector (cm^{-1})

k_0	magnitude of the incident wave vector (cm^{-1})
k_B	Boltzmann constant ($\text{N m}/^\circ\text{K}$)
K	shape factor
K_s	perfect sphere shape factor
l^*	effective mean free path in the DWS theory (μm)
L	optical coordinate
L_0	optical thickness
L_e	effective optical coordinate
m	complex refractive index
M	highest order of Legendre polynomials in an expansion
M_e	particle effective mass (gm)
n	refractive index
N	order of Legendre expansion
N	scattering particle number density (cm^{-3})
P_i	Legendre polynomial of order i
q	incident beam flux per unit area (W/m^2)
Q	cross-sectional efficiency
r	spatial position vector (m)
R	resistance (Ohm)
s	Fresnel's reflection parameter
s_c	sedimentation coefficient ($\text{m}^3/\text{N s}$)
S	source function (W/m^2)
S_p	sphericity
t	time (s)
T_e	total experimental time for one run (s)
T	absolute temperature ($^\circ\text{K}$)
v	velocity of particle (m/s)
v_{bs}	beam scanning velocity (cm/s)

V	particle volume (cm^3)
x	particle size parameter
x_i	i -th coefficient of Legendre polynomial expansion
z_0	deposition depth parameter of DWS (μm)
Z	physical thickness of medium (cm)

Greek

α	sine of scattering angle, $\sin(\Theta)$
β	constant, refractive index dependent
γ	experimental proportionality constant
δ	Dirac delta function
η	solvent viscosity (N s/m^2)
θ	polar angle
Θ	scattering angle
Φ	scattering phase function
κ	absorption coefficient (cm^{-1})
λ	wavelength (nm)
μ	cosine of the polar angle, $\cos\theta$
ρ	reflectivity
ρ_p	particle density (gm/cm^3)
ρ_0	medium density (gm/cm^3)
ρ_f	resistivity of the medium (Ohm/cm^3)
σ	scattering coefficient (cm^{-1})
τ	correlation delay time (s)
τ_0	characteristic delay time, $1/D_0 k_0^2$ (s)
ω	single scattering albedo
ω_e	effective albedo
$d\Omega$	differential solid angle around the direction Ω

Ω	unit vector in scattered direction
Ω'	unit vector in incident direction

Subscripts

1	incident beam (top) boundary condition
2	other side (bottom) boundary condition
1o	outside top boundary
2o	outside bottom boundary

Superscripts

+	transmission
-	back-scattering

CHAPTER I

INTRODUCTION

Knowledge of the size of component particles is often required for research projects and is fundamental to a wide variety of industrial dispersions. Such information is valuable in the production of particles of specific sizes to control process efficiency and product quality. It has become more important to measure particle size in in-situ circumstances. Consider the various situations in which particle size is measured [Scarlett (1992)].

In the off-line situation, particle size can be measured by taking the sample from the process and investigating it in the laboratory. In this situation, the inaccuracy is always with the sampling, and because of the different environments and the time lag between sampling and measuring, it is difficult to know if what is analyzed is what originally existed. The next level is on-line analysis which only involves the addition of automation and robotics, so sampling and analyzing can be closer in both time and space. Moving to the in-line measurement, a probe is inserted into the stream or the apparatus in order to make a localized measurement, so it minimizes the time between sampling and testing. Disturbing the process or stream in this situation can cause inaccuracy between what is measured and what is supposed to exist. The next level is in-situ measurement in which the properties of the particles in a local region can be found by using non-destructive devices and signal processing from that region.

In the past, most efforts were being made to move from the off-line to the on-line situation. Today, many plants operate with on-line monitoring, and several in-line instruments are commercially available. In the recent research literature,

most efforts are being made to move to the in-situ situation, by devices which cause negligible disturbance of the process or negligible environmental effects such as laser scattering. So the in-situ situation is going to become common place in the near future. The measuring techniques from the off-line to the in-line situations may not represent a significance difference, but the shorter time scale and localized environment in which the information is available between these techniques improves the accuracy of determining the properties which originally existed. The improvement of using in-situ measurement means, for example, that the average particle size and its variation from region to region in the vessel (and the change in its variation) can be measured over a period of milliseconds. The amount of information which can be generated can be used for process modeling and implementing control strategies to improve product quality to a level that was unthinkable twenty years ago.

Applications

Particle sizing is important in a large number of practical applications. Raw materials are mostly found in nature in a form unsuitable for end use, and they are often pulverized for convenience in handling. Here particle size affects mechanical properties such as packing and flowing. Typically, such raw materials are converted into finished products by chemical and physical processes. Such processes include grinding, dissolving, evaporating, heating, and chemically reacting the raw material. Also many processes either start out as a powder, end up as a powder, or go through at least one powder stage. Particle size is a property that significantly affects these processes. The following have been collected from different references as examples of the effect of the size of particles in different applications.

Aerosol size characterization is a highly specialized science and has significance for drug delivery, environmental concerns (including production of pharmaceutical and electronic products), and areas such as the biological activity of many proteins and bacterial cells.

All pharmaceutical dosage forms are required to meet standards of drug content uniformity and quality. This is to ensure that the product will consistently deliver the intended dose, thereby achieving the desired efficiency and avoiding the adverse effects of inaccurate dosages [Hartly et al. (1985) and Orr et al. (1980)]. It is necessary to reduce the active material to a very fine particle size so that a sufficiently well dispersed system can be achieved. This will help to assure bioavailability and hence efficiency of the medicinal product. For example, for ointment intended for ophthalmic use, it is important to achieve a very fine product texture to avoid irritation of the very delicate surfaces of the eye that would arise from the presence of large abrasive particles.

The performance of pigment dispersions in terms of covering capacity and color development (i.e. paints) is also critically controlled by the size of the primary pigment particles and the number of primary particles forming aggregates [Carr (1978)]. Essential properties, such as covering capacity, penetration, film-forming ability, brushability, and stability are all critically influenced by the size of particles.

The process of principal interest in practical systems, such as furnaces, boilers, combustion chambers, and gas turbine combustors, is the transfer of heat liberated during the combustion of fuel to the heat transfer surface. Although the heat is transferred in such enclosures by radiation, convection and conduction, radiation is normally the dominant mechanism owing to the high temperatures involved [Sarofim (1986) and Viskanta and Menguc (1987)]. The field of radiative energy transfer in the above systems is getting ever increasing attention,

because accurate predictions of the performance of these devices and the thermal efficiency of these systems can be improved only if details of radiation heat transfer and its effects on combustion are fully understood. One important aspect of radiation in combustion is the size of particulates such as soot, flyash, etc. which are produced during the processes [Viskanta and Menguc (1987)].

In addition to a few specific applications which are mentioned above, the size of particles is important among applications which involve the processing of fine particle dispersions in either gaseous or liquid media, such as: bulk solid storage, handling and transportation units, and particle collection and separation units such as cyclones, filters, and electrostatic precipitators. Many other process units are engaged in the production or the use of solid particles such as spray dryers, mixers, blenders, fluidized bed reactors, crystallization and polymerization equipment. In most process fields which employ fine particles, in-situ measurement is important to characterize the specific particle sizes in order to control process efficiency and product quality.

Review of Techniques

There are a large number of techniques available for particle size analysis [Scarlett (1981)] with respect to industrial demands. However, no single technique may cover all sizes of interest. If the size range is restricted to below a few microns, which is the main interest of this research, the number of techniques reduces to a few: sedimentation/centrifugation, electric and light-zone blockage, hydrodynamic chromatography, sedimentation flow field fractionation, microscopy, and light scattering. However, each technique branches to many different variations. A few specific methods such as gravitational sedimentation, electrical zone sensing, image analysis, static and dynamic light scattering will be

presented to show the wide variety of methods which are available to measure particle size for different applications. Dynamic light scattering (DLS) will be covered separately since the research herein is based on DLS. It should be mentioned that the review of this technique will be in general and based on fundamental principles, and the reader is referred to other articles and books for detailed information.

Image Analysis

This technique consists of a microscope linked to a television screen and a computerized scanning and monitoring unit [Tuzun and Farhadpour (1985)]. Representative sections from each specially prepared sample slide are examined under the microscope to determine the size of particles. The sizes of the particles are calculated as the diameters of spheres with the same equivalent projected area as that of the particles:

$$d = \sqrt{\frac{4}{\pi}(\text{area})} \quad (1-1)$$

The sphericity, S_p , is defined by a shape factor

$$K = \frac{\text{projected area}}{(\text{perimeter})^2} \quad (1-2)$$

where

$$S_p = \frac{K}{K_s} \times 100(\%) = \frac{400}{\pi} K \quad (1-3)$$

and K_s is the shape factor for a perfect sphere (i.e. $\pi/4$).

Here, another technique should be mentioned, that of using electron microscopy [Allen (1981)] which is used in either the transmission or the

scanning mode, and is becoming more widely available. The slides from a sample photographed by this instrument can be directly visualized to measure the particle size. To my knowledge, image analysis is mostly used in off-line or on-line situations where particle size does not change due to the methods used in preparing to analyze the photographic slides of a sample.

Electrical Zone Sensing

The electrical zone sensing technique (Fig. 1), known as the Coulter technique, is a method based on the principal of monitoring the number and size of the particles suspended in an electrolyte solution by causing them to pass through a small orifice on either side of which is immersed an electrode [Bunville (1984)] (refer to Fig. 1). The resistance increases across the orifice when the particles are passing through as compared to that of the medium alone. The magnitude of this increase in electrical resistance, ΔR , for a spherical particle of diameter d suspended in an aperture of diameter D , is

$$\Delta R = \frac{8\rho_f d}{3\pi D^4} \left[1 + \frac{4}{5} \left(\frac{d}{D} \right)^2 + \frac{24}{35} \left(\frac{d}{D} \right)^4 + \dots \right] \quad (1-4)$$

where ρ_f is the resistivity of the conducting medium. With suitable external circuitry, this resistance pulse ΔR results in a voltage pulse $i\Delta R$ for a sphere of diameter d , where i is the current across the aperture. The resulting voltage pulses are counted and scaled using a multichannel analyzer. The success of this method depends very much on the feasibility of passing the suspension through the orifice, uninterrupted for a long period of time. So, this technique is applicable to very dilute samples. Also this technique is limited to the process fields which are not affected by electric fields.

Gravitational Sedimentation

This technique is simply based on the settling velocity of the particles in the medium [Bunville (1984)]. The steady state velocity of a particle suspended in a viscous medium, settling in a gravitational field, is given by

$$v = \frac{M_e a_g}{f_c} \quad (1-5)$$

where M_e is the particle effective mass, f_c is the frictional coefficient, v is the particle velocity, and a_g is the acceleration caused by gravity. Steady state velocities are usually expressed as the sedimentation coefficient, s_c , the particle velocity per sedimentation acceleration. So for the above equation

$$s_c = \frac{v}{a_g} = \frac{M_e}{f_c} \quad (1-6)$$

and the sedimentation coefficient is simply the ratio of the particle's effective mass to the frictional coefficient. If the densities of the particle, ρ_p , and of the medium, ρ_o , are known, s_c can be expressed as:

$$s_c = \frac{V(\rho_p - \rho_o)}{f_c} \quad (1-7)$$

where V is the particle volume. Finally, if the particles are spherical, with the frictional coefficient given by Stoke's law as $f_c = 3\pi\eta_o d$, for a particle of diameter d suspended in a medium with viscosity η , the sedimentation coefficient becomes

$$s_c = \frac{(\rho_p - \rho_o)d^2}{18\eta} \quad (1-8)$$

from which the particle diameter d may be calculated. In this method, the measurement depends on the particle shape and density, and on the density and viscosity of the medium. This technique is used for particle sizes greater than $5\mu\text{m}$ and Stoke's flow provides the upper limit of particle diameter.

Light Scattering Techniques

Light scattering phenomena can be classified into two areas according to the mode of application to particle size analysis. The first category is time-averaged or static light scattering, where either the scattered intensity or its spatial distribution is measured. The second is time-fluctuation or dynamic light scattering, which includes the analysis of the spectral distribution of the scattered radiation and photon correlation spectroscopy (PCS). As mentioned earlier, dynamic light scattering will be covered in a different section because of the main use of it in this research. Here, static light scattering is briefly reviewed.

When a beam of incident light interacts with a particle, it can be absorbed, scattered, or transmitted. Conservation of energy demands that the summation of the energy absorbed, scattered, and transmitted equal the incident energy. Defining the amount of energy scattered or absorbed as extinction of the beam, it follows that:

$$C_{\text{ext}} = C_{\text{sca}} + C_{\text{abs}} \quad (1-9)$$

where C_{ext} , C_{sca} , and C_{abs} are the total cross-sections for extinction, scattering (includes reflection, refraction, diffraction), and absorption, respectively. The units of C are length squared. The cross-sections represent effective cross-sectional areas of the particle.

It is convenient to define the dimensionless ratio of these effective cross-sections to the cross-sectional area of the particles. For a sphere of diameter d ,

$$Q = \frac{4C}{\pi d^2} \quad (1-10)$$

where Q is the cross-sectional efficiency.

The theory for calculating cross-section from first principles is called Lorenz-Mie theory [van de Hulst (1957)]. It starts from Maxwell's electromagnetic

equations and proceeds to exact answers for the cross-sectional efficiencies in terms of a size parameter, x , the index of refraction of the particle relative to the medium in which it is suspended, m , and the angle of detection, θ . The index of refraction can be a complex number, the imaginary part of which gives rise to absorption.

Through the size parameter, measurements of the scattered light intensity yield information on particle size. The size parameter for a sphere of diameter d is

$$x = \frac{\pi d}{\lambda} \quad (1-11)$$

where λ is the wavelength of the light in the suspending medium.

Although the Lorenz-Mie theory is exact for microscopic spherical particles, it does not, in general, lead to simple analytical solutions relating particle size to optical measurements. However for limiting cases, Rayleigh scattering and diffraction are much simpler. The criteria for the applicability of these limiting cases are stated simply in terms of diameter and wavelength as

$$d/\lambda < 0.2 \quad \text{Rayleigh scattering}$$

$$d/\lambda > 4.0 \quad \text{diffraction theory}$$

In the diffraction technique, the scattered light from the particles in the path of the light results in a set of light rings at various radii to the incident beam which are brought outside the geometric limits of the original beam with the use of a lens of a specified focal length (refer to Fig. 2). The proportion of the scattered light energy falling on each of the concentric rings can be measured, and the particle size is obtained by the iterative use of a numerical algorithm

which minimizes the difference between the measured light energies and the value calculated according to light scattering theory. Theoretical light intensities corresponding to the different particle sizes are calculated using either Fraunhofer diffraction or Mie theory. The Fraunhofer diffraction pattern which is produced by a layer of particles is given by the Airy equation [Plantz (1984)]:

$$I(\alpha) = qk^2 x^4 \left[\frac{J_1(kx\alpha)}{kx\alpha} \right]^2 \quad (1-12)$$

where q is the flux per unit area of the incident beam, $k=2\pi n/\lambda$, $\alpha=\sin(\Theta)$, and J_1 is the first-order Bessel function of the first kind. The dimensionless parameter, x , is defined by Eq. (1-11).

Summary

The techniques that have been presented in this section of the report show the wide variety of methods available in particle size measurement. Each technique has some advantages and disadvantages, and its application depends on the process fields. Since for most process fields which employ fine particles, in-situ measurement is important to characterize the specific particle sizes, the use of non-destructive light-based techniques has received much attention recently. However, it is frequently difficult to achieve the condition of light single scattering in a medium (allowing one to ignore the double or higher order scattering events in the medium), and only multiple scattering characteristics can be measured. Thus, Ackerson et al. (1992) proposed the Correlation Transfer (CT) equation based on dynamic light scattering, and it is similar to the Radiative Transfer (RT) equation. Since the CT equation looks very similar to the RT

equation, the theoretical solution techniques applied in radiative transfer can be applied directly to the CT equation.

Objective

The focus of this research is to apply dynamic light scattering (DLS) experimental techniques in different concentrations of fluid/particle suspensions to investigate the accuracy of CT theory as compared to experimental data, and to develop a rapid experimental procedure (based on CT theory) to determine particle diameters. The combination of CT theory and experimental data can lead us to determine the size of particles in the multiple scattering regime.

Implementing the first major objective, the one-dimensional experimental setup is described; and the effects of different parameters, such as glass cell back reflection, beam size, and polarization, are experimentally investigated. Different optical thicknesses from the very dilute (single scattering limit) to the very thick media are experimentally studied for transmission, back-scattering, and off angle detection; and their results are compared to the one-dimensional CT theory. The effects of index of refraction and anisotropic phase function on the correlation function are also investigated. It should be mentioned that the purpose of this research was not to exhaustively study the particular parameters mentioned above. Instead, the purpose was a broad investigation of each of these parameters thoroughly enough to have a good idea of its individual impact on Correlation Transfer, thus providing direction for future research on a specific parameter or parameters. These results have been partially presented at different conferences and published as conference papers [Reguigui et al. (1993), Dorri-Nowkooorani et al. (1993), and Dorri-Nowkooorani et al. (1994)].

Then, for the second major objective, a method is proposed to determine the diameters of spherical particles which only scatter and do not absorb. An approximate fast numerical technique is suggested and developed to reduce the time involved from that required to execute the exact numerical program, and the results are compared to the exact solution. Possible sources of errors are discussed and repeatability of the experimental data is examined (see Appendix A).

CHAPTER II

LITERATURE REVIEW

Single scattering measurements for particle size characteristics have been used for a long period of time and a great number of techniques and methods have been developed. Multiple scattering measurement has not been used for particle sizing until recently because of the complexity involved in theoretical development. Here, the review of a few articles will be presented.

Harrison (1988) presented a new experimental setup, and he claimed to measure the particle diameter from 0.5 μm to 1000 μm and for a wide range of process concentrations from 0.1% to 30% and higher (by volume). This instrument was based on back-scattering measurements using a static light scattering technique. He used a laser beam which was focused on a very small spot of about 10 μm diameter, a couple of photodiodes for light detection at backward angles, and a container with suspended particles which were stirred to maintain suspension. Particle size was statistically determined by a time measurement (for a pulse length), and not by the intensity of the light signal, using a LAB-TECTM 1000 counter coupled with a computer program for data analysis. The lens which focused the laser light was vibrated at a higher frequency than that represented by the velocity of the flowing particles. By reducing the data only for this high frequency, the measurements were independent of the effects of particle flow velocity. The particle size was determined from

$$d = \beta v_{bs} t \quad (2-1)$$

where v_{bs} is the beam scanning velocity, t_t is a transition time, and β depends on the ratio of the refractive index of the particles to that of the fluid solution. No results were presented.

Gougeon et al. (1987) presented a new optical technique which they called VIDE (visible infrared double extinction) for simultaneously measuring the particle diameters from 20 μm to 80 μm at different concentrations corresponding to a weakly multiple scattering medium. They assumed isotropic, homogenous spherical particles with no index of refraction change at the boundaries in their model, and they used the N-flux method for the theory behind their experimental analysis. [The 4-flux model development for particle sizing has been published by Meheu et al. (1984) and Meheu and Gousbet (1986).] They used two different wavelengths for their experimental measurements: 0.6328 μm from a He-Ne laser as visible light and 337 μm from a HCN laser for infrared light. Sieved coal particles with different diameters were suspended in a specially made container which could be rotated and vibrated. A photo-multiplier tube and a two-channel recorder were used for transmission detection and data print out, respectively. Their particle diameter measurements did not compare well to their expectations, and they suggested that the uncertainties were due to the non-sphericity of the coal particles. They discussed the applicability of using this technique for diagnostics in a weakly multiple scattering particle laden flow.

In other research, Gouesbet et al. (1988) used the same experimental setup and illustrated the results for spherical glass particles. They sieved the particles to provide different diameters in the ranges from 20/32 to 80/100 μm . Their results show large discrepancies between their experimental particle size measurements and the original particle diameters. They said the measurement was done up to an optical thickness (physical thickness multiplied by the

scattering cross-section and number density of the particles) of about 9 in general, but they did not mention what optical thickness they used for the each specific measurement. They modified their VIDE theory, and improved their results. They showed that the difference between the sieving diameter and their experimental data ranged from 17% to 44%, for large to small particles, respectively. They suggested that these errors were due to unsatisfactory preparation of the samples.

Cao et al. (1991) investigated the laser diffraction particle sizing in a multiple scattering medium. They corrected the diffraction theory for multiple scattering measurement. They used glass spheres as particles and changed the sample concentration based on percent of light obscuration. They changed this parameter from about 18% to about 99%, and they suggested that the method of single scattering measurements can be used for up to 50% light obscuration. They compared the glass size distribution for different light obscuration levels all together. The agreement was good when they used corrected theory for multiple scattering. They also measured the size distribution of glycol-water mixture droplets from industrial-scale atomizer sprays for low to high light obscuration. Their results compared well up to about 96% light obscuration, but they showed about 10% lower size distribution for 99% light obscuration when they used multiple scattering to correct the theory. They suggested that the inhomogeneity of the particle field may have caused errors for very high concentrations.

Maret and Wolf (1987) presented some experimental results for the back-scattered correlation function using dynamic light scattering in a multiple scattering medium. They used four different particle sizes ranging from $0.109\text{ }\mu\text{m}$ to $0.796\text{ }\mu\text{m}$ in two different concentrations of 0.1% and 10%. They performed back-scattering measurements at a 15° angle. They tried to eliminate the heterodyne signal by using an index matched cell, but they observed some

residual heterodyne mixing for long correlation time when they were doing some single scattering measurements. They observed almost a single scattering decay rate at long times from their multiple scattering correlation measurements for different particle sizes, while they observed faster decay than for single scattering at short delay times. They discussed the effect of static structure factor on the anisotropic phase function and the relaxation time. The calculated value of this factor turned out to be about 1, and their measurements verify this to be true for all particles except the small particles of 0.109 μm diameter.

Pine et al. (1988) developed the Diffusive Wave Spectroscopy (DWS) theory for the direct back-scattering and transmission correlation functions for multiple scattering media. Their development was based on the application of dynamic light scattering in diffusing media. They used one variable parameter of l^* in their transmission model and two variable parameters of l^* (effective transport mean free path) and γ in their back-scattering model. These parameters were determined by fitting their transmission and back-scattering models to the experimental data. They compared the experimental correlation data of thick media using 0.497 μm particle sizes and a laser wavelength of 488 nm to their transmission model, and they achieved very good agreement by using $l^*=143 \mu\text{m}$. They used the same l^* in the back-scattering and showed very good agreement between theory and experimental data when they set $\gamma=2.0$. Using different particle sizes, γ was varied by $\pm 15\%$. They also presented the correlation measurements for a mixture of two different interacting and non-interacting particle sizes in thick media. The correlation measurements for the non-interacting mixture of particles decayed faster than that of the interacting particles for both transmission and back-scattering.

Pine et al. (1990a) used the photon correlation (or dynamic light scattering) technique in multiple scattering media. They introduced a closed form solution

for for DWS theory anisotropic back-scattering and transmission and compared their theory to the measurements from very dense media. They expanded the beam of an Argon-ion laser to 1 cm and used latex particles in the range of 0.091 μm to 0.605 μm for the water/particle suspensions under investigation. They studied the correlation function for very thick media (optical thicknesses of more than 70). Their transmission results showed that the anisotropic factor l^* which they used in their theory was 10% lower than that calculated from Mie theory. But they suggested that this discrepancy was due to the diffusion assumption breaking down near the boundaries, and thus they had to construct unrealistic boundary conditions.

The back-scattering experimental data for an infinite medium showed a linear dependence on the square root of time and compared well to the theoretical results. They also presented the effect of polarization on correlation measurements for different particle sizes. They concluded that isotropic (uniformly scattering) particles (with size parameters smaller than one) had a greater effect on polarization than do anisotropic (nonuniformly scattering) particles (with size parameters greater than one); but they compared two different particle sizes which had different optical thicknesses, and this was not a fair comparison.

They investigated polydispersity using a mixture of two different particle sizes, and they demonstrated good agreement between experimental data and theoretical results using an effective diffusion constant from the two particle diameters. They discussed the applicability of this technique to particle sizing, and they also investigated the factors of absorption and interacting particles. They reported some of these results in a different publication [Pine et al. (1990b)]

CHAPTER III

METHODOLOGY

Theoretical Background

The description of the time-dependency of the dynamic light scattering technique can be found in detail in the book by Berne and Pecora (1976). Here, we give a very brief review of a few basic concepts. In a quiescent fluid/particle suspension, the particles are experiencing Brownian motion, and their positions are continually changing. The scattered electric field, which is a function of particle position, is also continuously changing. Since the intensity is proportional to the square of the electric field [Siegel and Howell (1981)], intensity is also fluctuating in time. Figure (3) [intensity fluctuation] shows schematically the intensity of the scattered light versus time. It consists of a time-averaged part and a temporally fluctuating part. The dynamic information of interest is contained in the fluctuations, and the most efficient way to analyze the intensity fluctuations is to average the product of the signal from a detector and a [time] delayed version of the signal as a function of that delay time (τ). This is known as autocorrelation, and an intensity autocorrelation function is defined as follows [Berne and Pecora (1976)]:

$$\begin{aligned} c(\tau) &= \langle I(t)I(t+\tau) \rangle \\ &= \lim_{T_e \rightarrow \infty} \frac{1}{T_e} \int_0^{T_e} I(t)I(t+\tau) dt \\ &\propto \left\{ 1 + \gamma [G(\tau)]^2 \right\} \end{aligned} \tag{3-1}$$

where the intensity I has, in general, different values at time t and $t+\tau$. T_e represents the total experimental duration time, over which the product of the intensity with delayed versions of itself is averaged; and T_e is obviously much greater than τ . $G(\tau)$ is known as the normalized electric field correlation function:

$$G(\tau) = \langle E(t)E^*(t+\tau) \rangle \quad (3-2)$$

where E^* is the complex conjugate of the electric field. The intensity correlation function of Eq. (3-1) is measured experimentally by commercially available correlator hardware and/or software that multiplies the shifted intensity signals together and integrates the result [Weiner (1984)]. At long times, the autocorrelation function has decayed and is equal to the square of the average intensity. Figure 4 shows a typical intensity correlation function.

Single Scattering

For dilute and monodisperse samples, the field correlation function in Eq. (3-1) is found to be [Berne and Pecora (1976)]

$$\begin{aligned} g^1(k, \tau) &= \exp(-D_o \bar{k}^2 \tau) \\ &= \exp[-2D_o k_o^2 \tau (1 - \cos\Theta)] \end{aligned} \quad (3-3)$$

and is thus dependent on the scattering wave vector \bar{k} with magnitude $|\bar{k}| = 2\pi n / \lambda$ and the diffusion constant D_o . In Eq. (3-3), The relation $\bar{k}^2 = 2k_o^2(1 - \cos\Theta)$ has been used, where k_o is the magnitude of the incident wave vector, and Θ is the scattering angle measured from the forward direction. The diffusion constant D_o is given by the Stokes-Einstein relation for spherical particles [Weiner (1984)]

$$D_o = \frac{k_B T}{3\pi\eta d} \quad (3-4)$$

where k_B is the Boltzmann constant, T is the absolute temperature, η is the solvent viscosity, and d is the diameter of a particle suspended in the sample. If the scattering volume contains a large number of independent scatterers, there is a very simple relation between $g^1(\tau)$ and the normalized homodyne intensity autocorrelation function $g^2(\tau)$:

$$g^2(\tau) = 1 + \gamma [g^1(\tau)]^2 \quad (3-5)$$

where γ is an experimental signal to noise ratio. Experimental results are generally reported as the normalized homodyne autocorrelation function $g^2(\tau)$. Another useful parameter, which is used to nondimensionalize delay time in the experimental data, is the correlation delay time constant τ_o :

$$\tau_o = 1/D_o k_o^2 \quad (3-6)$$

τ_o will also be used to determine particle size as will be explained later.

Multiple Scattering

Equation (15) is only valid for dilute samples. In concentrated samples, the correlation function looks different from Eq. (3-3). In that case, an integro-differential equation [Ackerson et al. (1992)]

$$\begin{aligned} (1/c_o) \frac{\partial G^m(r, \Omega, t, \tau)}{\partial t} + \Omega \cdot \nabla G^m(r, \Omega, t, \tau) + \kappa G^m(r, \Omega, t, \tau) + \\ \sigma G^m(r, \Omega, t, \tau) = \frac{\sigma}{4\pi} \int_{4\pi} G^m(r, \Omega', t, \tau) g^1(k', \tau) \Phi(\Omega, \Omega') d\Omega' \end{aligned} \quad (3-7)$$

has to be solved for G^m , subject to the appropriate boundary conditions of the problem. The integration over all directions Ω' takes into account the correlation "scattered" from other directions into the direction of interest. The "weighting function" Φ is the form factor (phase function), and the transport of correlation happens via the single scattering function g^1 . The first two terms on the left side denote the temporal and spatial propagation. The next two terms are absorption and scattering of correlation. This CT equation looks almost the same as the RT equation of Siegel and Howell (1981)

$$(1/c_o) \frac{\partial I(r, \Omega, t)}{\partial t} + \Omega \cdot \nabla I(r, \Omega, t) + \kappa I(r, \Omega, t) + \sigma I(r, \Omega, t) = \frac{\sigma}{4\pi} \int_{4\pi} I(r, \Omega', t) \Phi(\Omega, \Omega') d\Omega' \quad (3-8)$$

except for $g^1(k', \tau)$ inside the integral of Eq. (3-7).

The one-dimensional form of Eq. (3-7) for a scattering and absorbing medium, assuming azimuthal symmetry, is

$$\mu \frac{dG^m(L, \mu, \tau)}{dL} + G^m(L, \mu, \tau) = \frac{\omega}{2} \int_{-1}^1 G^m(L, \mu', \tau) g^1(k', \tau) \Phi(\mu, \mu') d\mu' \quad (3-9)$$

where L is the optical coordinate, μ is the cosine of the polar angle, and ω is the single scattering albedo. The solution of Eq. (3-9) can be shown to be [Ackerson et al. (1992)]

$$G^m(L, \mu, \tau) = G_i^m(L, \mu, \tau) e^{-L/\mu} + \frac{\omega}{2\mu} \int_0^L \int_{-1}^1 G^m(L', \mu', \tau) g^1(k', \tau) \Phi(\mu, \mu') \exp(|L - L'|/\mu) d\mu' dL' \quad (3-10)$$

where G_i^m is the "incident" multiple scattering field correlation. Equation (3-10) can be solved by the same methods as used for a standard RT equation, with an extra term, the singly scattered correlation function (g^1), inside the integral. In the case of using the isotropic scattering assumption [$\Phi(\mu, \mu') = 1.0$], when applying RT solution techniques in finding G^m , one can use a preaveraging technique [Ackerson et al. (1992)] to approximate g^1 , or one can expand g^1 in a series of Legendre polynomials [Reguigui et al. (1993)]

$$g^1(k, \tau) = \omega_e \sum_{i=0}^M x_i P_i(\cos \Theta) \quad (3-11)$$

where ω_e is the effective albedo; and in the case of a pure scattering medium ($\omega=1.0$), ω is replaced by ω_e . This effective albedo may be defined differently depends on different solution approaches for correlation function. The x_i 's are the Legendre expansion coefficients and are given by Reguigui et al. (1993) for a second order expansion.

In the preaveraging technique [Ackerson et al. (1992)], the integral on the right side of Eq. (3-9) can be rewritten (by approximating the exponential function in Eq. (3-3)) as

$$\frac{\omega}{2} \int_{-1}^1 G^m(L, \mu', \tau) g^1(k', \tau) d\mu' \cong \frac{\omega}{2} \int_{-1}^1 G^m(L, \mu', \tau) d\mu' - \omega \frac{2\tau}{\tau_0} G^m(L, \mu, \tau) \quad (3-12)$$

Using the approximation of Eq. (3-12), the solution for Eq. (3-9) for an isotropically scattering and absorbing medium is

$$G^m(L_e, \mu, \tau) = G_i^m(L_e, \mu, \tau) e^{-L_e/\mu} + \frac{\omega_e}{2\mu} \int_0^{L_e} \int_{-1}^1 G^m(L_e', \mu', \tau) \exp(|L_e - L_e'|/\mu) d\mu' dL_e' \quad (3-13)$$

where ω_e [different from Eq. (3-11)] and L_e are defined as

$$\omega_e = \frac{\omega}{1 + (2\tau/\tau_o)} \quad (3-14)$$

$$L_e = \frac{L}{\omega_e} = \frac{L}{\omega} [1 + (2\tau/\tau_o)]$$

which is an equation whose solution is already available [Jiang (1990)].

Substitute Eq. (3-6) into Eq. (3-3), and the expression for g^1 becomes

$$g^1(k, \tau) = \exp(-2\tau/\tau_o) \exp[(2\tau/\tau_o)(\cos\Theta)] \quad (3-15)$$

If the g^1 in Eq. (3-15) is expanded in a Legendre series as in Eq. (3-11), the x_0 is 1.0 and

$$\omega_e = \left(\frac{2\tau}{\tau_o}\right)^{-1} \exp\left(\frac{-2\tau}{\tau_o}\right) \sinh\left(\frac{2\tau}{\tau_o}\right) \quad (3-16)$$

$$L_e = L_o$$

and for a one term expansion, g^1 simply becomes

$$g^1 = \left(\frac{2\tau}{\tau_o}\right)^{-1} \exp\left(\frac{-2\tau}{\tau_o}\right) \sinh\left(\frac{2\tau}{\tau_o}\right) \quad (3-16a)$$

In addition to approximating g^1 , the phase function, Φ , must also be handled adequately. Since the use of the exact form of phase function in Eq. (3-10)

makes that equation very difficult to solve, different approximate forms have been proposed [van de Hulst (1980)]. When the scattering particles are large compared to the wavelength of the incident light, the scattering is peaked in the forward direction. Among the proposed approximate forms, the Fraunhofer diffraction approximation is easier to apply to achieve reasonable results. In this form, the phase function is represented by a forward peak combined with an isotropic phase function [van de Hulst (1980)], i.e.,

$$\Phi(\cos\Theta) = 2f\delta(1-\cos\Theta) + (1-f) \quad (3-17)$$

where f is the fraction of the energy scattered in the forward direction. In this form of the phase function approximation, f is the same as the asymmetry factor calculated from Mie theory. It can be computed by using the Mie theory phase function calculation applied to the equation

$$f = \frac{1}{2} \int_{-1}^1 \Phi(\cos\Theta) \cos\Theta d(\cos\Theta) \quad (3-18)$$

Substituting Eq. (3-17) into Eq. (3-9) yields

$$\mu \frac{dG^m(L_e, \mu, \tau)}{dL_e} + G^m(L_e, \mu, \tau) = \frac{\omega_e}{2} \int_{-1}^1 G^m(L_e, \mu', \tau) g^1(k', \tau) d\mu' \quad (3-19)$$

This is an equation for correlation which is again similar to using Eq. (3-17) in an RT equation -- yielding an equivalent isotropic scattering equation. Just as with the equivalent isotropic scattering RT equation, the modified CT equation yields an effective scattering albedo and an effective optical thickness (different from previous definitions) which are redefined as:

$$\begin{aligned}
L_e &= (1 - \omega f)L \\
\omega_e &= \frac{1 - f}{1 - \omega f} \omega
\end{aligned}
\tag{3-20}$$

Equation (3-19) will be numerically solved using the preaveraged approximation, Eq. (3-14), or the g^1 expansion in one and three term Legendre series, Eq. (3-16). The results will be compared with experimental data and the improved classical P_N approximation.

Numerical Development

Exact Solution

The program which was developed by X. Y. Jiang [Jiang (1990)] is used to obtain the exact results for the CT equation (Eq. (3-19)). This program models an absorbing and isotropically scattering medium with a collimated incident beam at the top boundary which has an index of refraction change (Fig. 5). The index of refraction outside the lower boundary of the medium is the same as the index of refraction inside the medium. This program has been simplified, corrected (due to a few errors), and modified to be used for both the preaveraging technique and the one term g^1 expansion in terms of Legendre polynomials as shown in Eqs. (3-11)-(3-16). The program needs to be run several times according to the number of desired τ/τ_0 's for correlation numerical results. The optical thickness and scattering albedo must both be changed for different τ/τ_0 's in the case of preaveraging (Eq. (3-14)), while optical thickness remains constant in the case of the one term g^1 expansion. So the one term g^1 expansion is more convenient and faster, even though the execution time is long (more than one hour for an optical thickness of 5 on an IBM RISC6000 system) for both methods, especially for high optical thicknesses and refractive indices different

than 1.0. The program produces the results for back-scattering and transmission for different angles from 0° to 90° by 10° increments. A listing of the program is provided in Appendix B.

Approximate Solution (Improved P_N Approximation)

Since the program to obtain the exact solution results has a long execution time, especially for high optical thicknesses or index of refraction effects, it may not be very convenient (due to the required turn-around time) to use for solution of the CT equation, especially for rapid on-line particle size characterization. Among the various approximate methods in radiative transfer theory, the improved P_N approximation is a suitable method to be used [Modest (1993)]. This method is based on the expansion of both intensity and phase function in the form of Legendre polynomials. It will be a useful method for solving the CT equation, since the single scattering correlation function, $g^1(k, \tau)$, can also be expanded in the form of Legendre polynomials as mentioned in the section "Theoretical Background". Although this technique has been used in the form of a first order approximation (P_1) for calculating the flux in radiation transfer, it is very poor for calculating intensity [Modest (1993)]. Therefore, it will be better for an intensity type of calculation to use an N th order approximation (P_N). First the classical version will be reviewed.

Classical P_N Approximation The general transport equation for a one-dimensional absorbing and scattering medium is written as (Ozisik, 1973)

$$\mu \frac{\partial I(L, \mu)}{\partial L} + I(L, \mu) = S(L, \mu) = \frac{\omega}{2} \int_{-1}^1 I(L, \mu') \Phi(\mu, \mu') d\mu' \quad (3-21)$$

The scattering phase function $\Phi(\mu, \mu')$ can be represented as a series of Legendre polynomials (Ozisik, 1973)

$$\Phi(\cos\Theta) = \Phi(\mu, \mu') = \sum_{m=0}^N (2m+1) f_m P_m(\mu) P_m(\mu') \quad (3-22a)$$

where the coefficients f_m are specified depending on the anisotropic scattering phase function in a given medium

$$f_m = \frac{2m+1}{2} \int_{-1}^1 P_m(\cos\Theta) \Phi(\cos\Theta) d(\cos\Theta) \quad (3-22b)$$

For the P_N approximation, the intensity $I(L, \mu)$ is also assumed to be an expansion in a series of Legendre polynomials (Ozisik, 1973)

$$I(L, \mu) = \frac{1}{4\pi} \sum_{n=0}^N (2n+1) P_n(\mu) A_n(L) \quad (3-23)$$

Putting Eqs. (3-22) and (3-23) into Eq. (3-21), the result will be

$$\begin{aligned} \frac{\mu}{4\pi} \sum_{n=0}^N (2n+1) P_n(\mu) \frac{dA_n(L)}{dL} + \frac{1}{4\pi} \sum_{n=0}^N (2n+1) P_n(\mu) A_n(L) = \\ \frac{\omega}{2} \int_{-1}^1 \left[\frac{1}{4\pi} \sum_{n=0}^N (2n+1) P_n(\mu') A_n(L) \sum_{m=0}^N (2m+1) f_m P_m(\mu) P(\mu') \right] d\mu' \end{aligned} \quad (3-24)$$

The right hand side of Eq. (3-24) can be rearranged to become

$$\frac{\omega}{8\pi} \sum_{n=0}^N \sum_{m=0}^N (2n+1)(2m+1) A_n(L) f_m P_m(\mu) \int_{-1}^1 P_n(\mu') P_m(\mu') d\mu' \quad (3-25)$$

and using the integral relation for Legendre polynomials

$$\int_{-1}^1 P_n(\mu') P_m(\mu') d\mu' = \begin{cases} 0 & n \neq m \\ \frac{2}{2n+1} & n = m \end{cases} \quad (3-26)$$

the integral in Eq. (3-25) reduces to $\frac{2}{2n+1}$ but n must equal m . Equation (3-24) reduces to

$$\begin{aligned} \mu \sum_{n=0}^N (2n+1) P_n(\mu) \frac{dA_n(L)}{dL} + \sum_{n=0}^N (2n+1) P_n(\mu) A_n(L) = \\ \omega \sum_{n=0}^N (2n+1) A_n(L) f_n P_n(\mu) \end{aligned} \quad (3-27)$$

With the recurrence relation [Abramowitz and Stegun (1972)]

$$(2n+1)\mu P_n(\mu) = nP_{n-1}(\mu) + (n+1)P_{n+1}(\mu) \quad (3-28)$$

Eq. (3-27) will become

$$\begin{aligned} \sum_{n=0}^N [nP_{n-1}(\mu) + (n+1)P_{n+1}(\mu)] \frac{dA_n(L)}{dL} + \sum_{n=0}^N (2n+1) P_n(\mu) A_n(L) = \\ \omega \sum_{n=0}^N (2n+1) A_n(L) f_n P_n(\mu) \end{aligned} \quad (3-29)$$

Changing the index (n) in the first term of Eq. (3-29), it can be written as

$$\begin{aligned} \sum_{n=0}^N (n+1) P_n(\mu) \frac{dA_{n+1}(L)}{dL} + \sum_{n=0}^N n P_n(\mu) \frac{dA_{n-1}(L)}{dL} + \sum_{n=0}^N (2n+1) P_n(\mu) A_n(L) = \\ \omega \sum_{n=0}^N (2n+1) A_n(L) f_n P_n(\mu) \end{aligned} \quad (3-30)$$

Then combining all of the summations and taking $P_n(\mu)$ as a factor, the above equation becomes

$$\sum_{n=0}^N \left[(n+1) \frac{dA_{n+1}(L)}{dL} + n \frac{dA_{n-1}(L)}{dL} + (2n+1)A_n(L) - \omega(2n+1)A_n(L)f_n \right] P_n(\mu) = 0 \quad (3-31)$$

Since in general, $P_n(\mu) \neq 0$, each of the coefficients multiplying $P_n(\mu)$ must be zero, or the following relationship among the $A_n(L)$'s can be found:

$$(n+1) \frac{dA_{n+1}(L)}{dL} + n \frac{dA_{n-1}(L)}{dL} + (2n+1)(1 - \omega f_n)A_n(L) = 0 \quad (3-32)$$

This differential equation can be solved for the $A(L)$'s by using numerical techniques for two point boundary valued problems [Fox (1957)]. Applying this solution technique coupled with the finite difference method produces a matrix with the elements of $A_n(L)$'s and boundary values.

There are two kinds of boundary conditions that have been used for the P_N approximation: Mark's and Marshak's (Ozisik, 1973). Here Marshak's boundary conditions are used and they are

$$\int_0^1 I^+(0, \mu) \mu^{2i-1} d\mu = \int_0^1 I_1^+(\mu) \mu^{2i-1} d\mu = I_{1i} \quad i = 1, 2, 3, \dots, (N+1)/2 \quad (3-33a)$$

$$\int_0^1 I^-(L_0, \mu) \mu^{2i-1} d\mu = \int_0^1 I_2^-(\mu) \mu^{2i-1} d\mu = I_{2i} \quad i = 1, 2, 3, \dots, (N+1)/2 \quad (3-33b)$$

where $I_1^+(\mu)$ and $I_2^-(\mu)$ are the boundary conditions at the top and bottom, respectively (for both above equations, $0 \leq \mu \leq 1$). The intensities $I^+(0, \mu)$ and $I^-(L_0, \mu)$ can be calculated from Eq. (3-23); but to reduce the size of the matrix created when solving Eq. (3-32), the following development will be applied to Eq. (3-32).

The odd and even numbers of n will be separated in Eq. (3-23) such that the intensity $I(L, \mu)$ will be

$$I(L, \mu) = \frac{1}{4\pi} \sum_{\substack{n=0 \\ n=\text{even}}}^N (2n+1) P_n(\mu) A_n(L) + \frac{1}{4\pi} \sum_{\substack{n=1 \\ n=\text{odd}}}^N (2n+1) P_n(\mu) A_n(L) \quad (3-34)$$

Substituting $2k$ for n in the first summation and $2k+1$ for n in the second summation of the right side of the above equation, it becomes

$$I(L, \mu) = \frac{1}{4\pi} \sum_{k=0}^{N/2} (4k+1) P_{2k}(\mu) A_{2k}(L) + \frac{1}{4\pi} \sum_{k=0}^{(N-1)/2} (4k+3) P_{2k+1}(\mu) A_{2k+1}(L) \quad (3-35)$$

Considering only odd orders in solving the P_N formulation, the two summations in Eq. (3-35) can be combined and reduced to

$$I(L, \mu) = \frac{1}{4\pi} \sum_{k=0}^{(N-1)/2} [(4k+1) P_{2k}(\mu) A_{2k}(L) + (4k+3) P_{2k+1}(\mu) A_{2k+1}(L)] \quad (3-36)$$

$A_n(L)$ can be found as a function of $A'_{n+1}(L)$ and $A'_{n-1}(L)$ from Eq. (3-32) and it can be substituted for even values of $A_n(L)$ in the above equation. Then the intensity equation becomes

$$I(L, \mu) = \frac{1}{4\pi} \sum_{k=0}^{(N-1)/2} \left[- \frac{(2k+1) A'_{2k+1}(L) + 2k A'_{2k-1}(L)}{(1 - \omega f_{2k})} P_{2k}(\mu) + (4k+3) P_{2k+1}(\mu) A_{2k+1}(L) \right] \quad (3-37)$$

Applying the closed form representation of Legendre polynomials as [Abramowitz and Stegun (1972)]

$$P_k(x) = 1/2^k \sum_{r=0}^{k/2} (-1)^r \frac{(2k-2r)!}{(k-r)!r!(k-2r)!} x^{k-2r} \quad (3-38)$$

where r takes on positive integer values, Eq. (3-37) will become

$$I(L, \mu) = \frac{1}{4\pi} \sum_{k=0}^{(N-1)/2} \left[- \frac{(2k+1)A'_{2k+1}(L) + 2kA'_{2k-1}(L)}{2^{2k}(1-\omega f_{2k})} \sum_{r=0}^k (-1)^r \frac{(4k-2r)!}{(2k-r)!r!(2k-2r)!} \mu^{2k-2r} + \frac{(4k+3)}{2^{2k+1}} A_{2k+1}(L) \sum_{r=0}^k (-1)^r \frac{(4k-2r+2)!}{(2k-r+1)!r!(2k-2r+1)!} \mu^{2k-2r+1} \right] \quad (3-39)$$

Applying this intensity equation in the boundary condition of Eq. (3-33a) and integrating over μ yields

$$\int_0^1 I^+(0, \mu) \mu^{2i-1} d\mu = \frac{1}{4\pi} \sum_{k=0}^{(N-1)/2} \left[- \frac{(2k+1)A'_{2k+1}(0) + 2kA'_{2k-1}(0)}{2^{2k}(1-\omega f_{2k})} \sum_{r=0}^k (-1)^r \frac{(4k-2r)!}{(2k-r)!r!(2k-2r)!(2k-2r+2i)} + \frac{(4k+3)}{2^{2k+1}} A_{2k+1}(0) \sum_{r=0}^k (-1)^r \frac{(4k-2r+2)!}{(2k-r+1)!r!(2k-2r+1)!(2k-2r+2i+1)} \right] \quad (3-40)$$

Now defining

$$a_{k,i} = \sum_{r=0}^k (-1)^r \frac{(4k-2r)!}{(2k-r)!r!(2k-2r)!(2k-2r+2i)} \quad (3-41a)$$

$$b_{k,i} = \sum_{r=0}^k (-1)^r \frac{(4k-2r+2)!}{(2k-r+1)!r!(2k-2r+1)!(2k-2r+2i+1)} \quad (3-41b)$$

the equation for the top boundary condition is

$$\int_0^1 I^+(0, \mu) \mu^{2i-1} d\mu = \frac{1}{4\pi} \sum_{k=0}^{(N-1)/2} \left[-\frac{(2k+1)A'_{2k+1}(0) + 2kA'_{2k-1}(0)}{2^{2k}(1-\omega f_{2k})} a_{k,i} + \frac{(4k+3)}{2^{2k+1}} A_{2k+1}(0) b_{k,i} \right] = I_{1i} \quad (3-42a)$$

Proceeding the same way for the bottom boundary condition of Eq. (3-33b) as was done for the top boundary condition (for $0 \leq \mu \leq 1$) yields

$$\int_0^1 I^-(L_o, \mu) \mu^{2i-1} d\mu = \frac{1}{4\pi} \sum_{k=0}^{(N-1)/2} \left[-\frac{(2k+1)A'_{2k+1}(L_o) + 2kA'_{2k-1}(L_o)}{2^{2k}(1-\omega f_{2k})} a_{k,i} - \frac{(4k+3)}{2^{2k+1}} A_{2k+1}(L_o) b_{k,i} \right] = I_{2i} \quad (3-42b)$$

The recurrence relation between the odd orders of $A_n(L)$ can be found by considering Eq. (3-32), i.e.,

$$\frac{(n+1)(n+2)(1-\omega f_{n-1})}{2n+3} \frac{d^2 A_{n+2}(L)}{dL^2} + \left[\frac{(n+1)^2(1-\omega f_{n-1})}{2n+3} + \frac{n^2(1-\omega f_{n+1})}{2n-1} \right] \frac{d^2 A_n(L)}{dL^2} + \frac{n(n-1)(1-\omega f_{n+1})}{2n-1} \frac{d^2 A_{n-2}(L)}{dL^2} - (2n+1)(1-\omega f_{n-1})(1-\omega f_n)(1-\omega f_{n+1}) A_n(L) = 0 \quad (3-43)$$

where $n=1, 3, 5, \dots, N$. In this recurrence relation, when n is equal to N , the parameters with $(n+1)$ should be zero and f_{n+1} should also be zero.

The finite difference technique can be applied to Eqs. (3-42) and (3-43) to produce a matrix for calculating $A_n(L)$, and intensity is directly related to the $A_n(L)$ by Eq. (3-37) or (3-39). This is the derivation of the classical P_N approximation. Next, I will show how the approximation can be improved.

Improvement of P_N Approximation: The analytical solution of Eq. (3-21) is (Ozisik, 1973)

$$I^+(L, \mu) = I_1^+(\mu) \exp(-L/\mu) + \int_0^L S(L', \mu) \exp[-(L-L')/\mu] dL'/\mu \quad 0 \leq \mu \leq 1.0 \quad (3-44a)$$

$$I^-(L, \mu) = I_2^-(\mu) \exp[-(L_0 - L)/\mu] + \int_L^{L_0} S(L', \mu) \exp[-(L'-L)/\mu] dL'/\mu \quad 0 \leq \mu \leq 1.0 \quad (3-44b)$$

For the P_N approximation, the source function $S(L, \mu)$ which is defined in Eq. (3-21) can be directly related to the $A_n(L)$'s as

$$S(L, \mu) = \frac{\omega}{4\pi} \sum_{n=0}^N (2n+1) A_n(L) f_n P_n(\mu) \quad (3-45)$$

Thus, the P_N approximation can be improved by substituting Eq. (3-45) into Eq. (3-44), and solving for the intensities. Since the $A_n(L)$'s remain inside the integrals, and a closed form solution of $A_n(L)$ is not available for higher order P_N approximations ($N > 1$), these integrals have to be calculated numerically. The $A_n(L)$'s which can be calculated from the matrix provided by the finite difference method with equal step sizes (ΔL) are not suitable $A_n(L)$'s for numerical integration by Gaussian quadrature. So, one must solve the matrix every time for the required optical thickness at each quadrature point and calculate $A_n(L)$, which requires large execution time for the program. However, a suitable matrix with the elements of $A_n(L)$ at Gaussian quadrature points can be obtained by using the finite difference method with variable step sizes. The equations for the finite difference method with variable step sizes are presented in Appendix B.

Boundary Conditions: The boundary conditions $I_1^+(\mu)$ and $I_2^-(\mu)$ in Eq. (3-33) can be defined as collimated incident light with an index of refraction

change at both the top and bottom interfaces. In this case, they are formulated to be [Reguigui and Dougherty (1992)]

$$I_1^+(\mu) = \mu_{10} I_{10} \frac{[1 - \rho(\mu_{10}, 1/n_1)]}{[1 - (1 - \mu_{10}^2)/n_1^2]^{1/2}} \delta \left\{ \mu - [1 - (1 - \mu_{10}^2)/n_1^2]^{1/2} \right\} + \quad (3-46a)$$

$$I_1^-(0, \mu) \rho(\mu, n_1)$$

$$I_2^-(\mu) = \mu_{20} I_{20} \frac{[1 - \rho(\mu_{20}, 1/n_2)]}{[1 - (1 - \mu_{20}^2)/n_2^2]^{1/2}} \delta \left\{ \mu - [1 - (1 - \mu_{20}^2)/n_2^2]^{1/2} \right\} + \quad (3-46b)$$

$$I_2^+(L_o, \mu) \rho(\mu, n_2)$$

where subscripts "1" and "2" refer to the top and bottom boundaries, respectively, and subscript "o" denotes the outside of the medium. The reflectivity ρ is calculated from Fresnel's reflection equation as [Ozisik (1973)]

$$\rho(\mu, n) = 1/2 \left[\left(\frac{s - \mu}{s + \mu} \right)^2 + \left(\frac{s - n^2 \mu}{s + n^2 \mu} \right)^2 \right] \quad (3-47)$$

where $s = \sqrt{n^2 - (1 - \mu^2)}$

Substituting Eqs. (3-46) into Eqs. (3-33) yields

$$I_{1i} = \mu_{10} I_{10} [1 - \rho(\mu_{10}, 1/n_1)] [1 - (1 - \mu_{10}^2)/n_1^2]^{i-1} + \int_0^1 I_1^-(0, \mu) \rho(\mu, n_1) \mu^{2i-1} d\mu \quad (3-48a)$$

$$I_{2i} = \mu_{20} I_{20} [1 - \rho(\mu_{20}, 1/n_2)] [1 - (1 - \mu_{20}^2)/n_2^2]^{i-1} + \int_0^1 I_2^+(L_o, \mu) \rho(\mu, n_2) \mu^{2i-1} d\mu \quad (3-48b)$$

where $i = 1, 2, 3, \dots, (N+1)/2$

In general, the boundary conditions for the experimental setup (which will be presented later) of this research model the collimated normal incident beam at one interface with the same change of refractive index at both interfaces (there is no incoming beam from the other interface). Applying the boundary conditions of Eqs. (3-48) to the experimental setup, I_{20} is equal to zero and μ_{10} is equal to 1.0. So Eqs. (3-48) reduce to

$$I_{1i} = I_{10} [1 - \rho(1.0, 1/n)] + \int_0^1 I^-(0, \mu) \rho(\mu, n) \mu^{2i-1} d\mu \quad (3-49a)$$

$$I_{2i} = \int_0^1 I^+(L_0, \mu) \rho(\mu, n) \mu^{2i-1} d\mu \quad (3-49b)$$

The intensities, $I^-(0, \mu)$ and $I^+(L_0, \mu)$, are unknown. So by assuming some values at the beginning and using an iteration technique [Fox (1957)] with the program, the results will be obtained if a refractive index other than 1.0 is selected. A listing of the program source code is also provided in Appendix D.

Experimental Setup and Procedure

The general experimental setup is shown in Fig. 6. Two lasers operating in the green region of the spectrum are used for the setup: one being a 5 watt water cooled Argon-Ion laser operating at a wavelength of 514.5 nm, and the other being an 80 mW DPY (diode pump YAG) laser with a wavelength of 532 nm. The original beam diameter of the Argon-Ion laser is 1.3 mm and is 0.1 mm for the Diode laser; and both lasers are vertically polarized. Both laser beams are expanded to much larger diameters and collimated by the lenses represented in

Fig. 6. The final diameters are 3.5 cm for the Argon-Ion laser and approximately 2.0 cm for the Diode laser. The expanded beams can be reduced to smaller diameters by a variable sized aperture as required. The mirror and beam splitter redirect the laser beam to enter the experimental cell normal to the cell surface (the incident beam to the cell surface is horizontally and vertically polarized for the Argon-Ion and Diode laser respectively, due to the positioning of the lasers on the table and redirecting the beam to the experimental setup by the mirrors). The cell is rectangular with a 4 cm by 4 cm surface area and a thickness of 0.2 cm. Spherical latex particles (0.091 μm , 0.107 μm , 0.3 μm , and 0.497 μm diameter) are suspended in distilled water to produce the test samples. The particles are assumed to scatter but not absorb, and only uniform sized particles are used at various levels of concentration to yield different optical thickness test solutions. The particles have a density of 1.05 g/cm^3 , and their index of refraction is 1.59 at 590 nm.

The instrumentation setup is designed for one-dimensional measurements in a rectangular coordinate system. Figure 7 shows the typical optical dimensions which the expanded beam covers in the radial direction as compared to the optical thickness of the test cell. For a dense sample, the expanded beam can be reduced to a smaller physical diameter if desired and still maintain one-dimensionality. One-dimensionality of the measurement depends on the laser beam's radial optical thickness. This radial optical thickness should be large enough to simulate an infinite radial optical thickness (100 for instance). However, as the sample is diluted, the beam should be expanded as much as possible in order to reduce the effects of scattering outside the area covered by the beam. Detection of light that is scattered through long paths that include the region outside that covered by the beam diameter will result in two-dimensional considerations being required to model the process.

Figure 8 shows an example of the effect of beam size on the measurements. The data at the shorter time corresponds to the scattering of light by particles closer to the center of the beam, and for longer time, the data provides information on (and is due to scattering by) particles further away from the center of the beam. As Fig. 8 shows, both measurements demonstrate the same slope for short time. But for larger times, the smaller diameter beam's correlation deviates from that of the larger beam due to the effect of scattering outside the area covered by the original beams -- the result of not maintaining a one-dimensional experimental setup. Although the difference between the curves appears small, the equipment and the measurements are reliable enough to reproduce this trend in correlation decay rates as a function of beam diameter. More details on one-dimensionality of the experimental measurements will be presented later in Chapter IV.

A 32 cm hollow tube with two small openings (about 0.3 mm) in each end was used as a probe to limit detection of the light leaving the test cell to almost a single direction (about 0.5 degree polar angle). A goniometer was used to move the probe manually to different detection angles: for direct back-scattering, transmission and "off angle" measurements (Fig. 6). A photomultiplier tube (PMT) was attached to the probe and provided the actual detection of scattered light. The signal from the PMT was read, correlated, and stored by an ALV autocorrelation board which was housed in an IBM compatible personal computer.

The signals from the PMT were presented as "count rate" by the ALV autocorrelation software (ALV5000 version 2.9) which represents the number of photons per second that are detected by the PMT. A low count rate yielded poor statistical averaging, thus it would reduce the signal-to-noise ratio; moderate count rate had good Gaussian statistics; and a high count rate would overload the

PMT. From much experience, a count rate between 70 to 120 kHz is a moderate count rate. The count rate and the signal-to-noise ratio can be improved by changing the laser intensity, choosing a smaller detector opening, using a neutral density filter, or by using a polarizer prior to detection. Assuming Gaussian statistics, the relative error would be proportional to " $1/\sqrt{\text{count rate}}$ ". Thus a count rate of 100 kHz represented a single scattering error of about 0.3%.

During a given run, the initial delay time (also the minimum delay time) was 200 nanoseconds, and was increased automatically by the autocorrelation software to an optimum value for the run. Several test runs were performed for three, five, and ten minutes of total data acquisition time [T_e in Eq. (3-1)], and there was not observed any changes in the correlation function for these kind of measurements. Therefore, there was no need to go to the longer time of 10 minutes, and total run times for a typical experiment were chosen to be set between three and five minutes. Data was stored as an intensity correlation, $c(\tau)$ of Eq. (3-1), and was converted to an electric field correlation, $g(\tau)$, using the relationship between the two correlation functions given in Eq. (3-2). It should be mentioned that this ALV board was designed and built for single scattering measurements, and all of the parameters settings (except time) such as temperature, wavelength, viscosity, etc. were not precisely applicable for multiple scattering measurements.

The optical thickness of the water/particle medium was determined for the experiment as described by Look (1979). He multiplied the particle scattering cross-section by the physical thickness of the sample and by the number density of the particles to obtain the optical thickness L_0 :

$$L_0 = N C_{\text{sca}} Z \quad (3-50)$$

where N is particle number density, C_{sca} is the scattering cross-section, and Z is the physical thickness of the medium. For this work, Z was 0.2 cm, which was the thickness of the test cell. The scattering cross-section was calculated from Mie theory [van de Hulst (1957)]. Table 1 shows the calculated information for the three particle diameters as determined from Mie theory.

Table 1: Mie scattering cross-sections and asymmetry factors (refractive index of 1.59) of spherical particles suspended in distilled water (refractive index of 1.33)

Particle Diameter (μm)	Wavelength (nm)	Scattering Cross-Section (cm^2)	Asymmetry factor f
0.091	514.5	0.7217×10^{-12}	0.095
0.300	514.5	0.2784×10^{-9}	0.727
0.497	514.5	0.2253×10^{-8}	0.858
0.091	532.0	0.6371×10^{-12}	0.089
0.300	532.0	0.2553×10^{-9}	0.722
0.497	532.0	0.2113×10^{-8}	0.853

From the calculated value of C_{sca} and the known physical thickness Z , the number of particles needed to produce a particular optical thickness could be calculated. The range of optical thicknesses addressed in this work was from 0.05 to 375.

Back-scattering measurements were performed by setting the probe to 9° (outside sample) off the direct back-scattering direction in order to eliminate the effects of reflection from the glass sides of the cell, and also keep the detector be out of the area of coherent back-scattering [Wolf et al. (1988)] Non-scattered signals (heterodyning) from the glass cell and coherent back-scattering could significantly decrease the quality of the signal and of the correlation produced. For dilute samples, transmission measurements were performed by placing a cross-polarizer in front of the probe. This polarizer blocked the non-scattered intensity passing through the test cell, which could again severely decrease the

quality of the correlation obtained. However, it should be mentioned that the correlation from a very dilute sample is polarization dependent; so great care and experience are necessary in order to accurately measure transmitted correlation from a very dilute sample. Off angle measurements can also be used to eliminate the non-scattered portion of the incident beam exiting a dilute test solution.

After making a solution of known optical thickness and moving the probe to the desired position, the signal processing system correlated the scattered intensity fluctuations detected by the PMT. As represented by Eq. (3-1), the correlator multiplied and averaged the intensity over a specified delay time for a total run time selected by the operator. For a multiple scattering test sample, the steepness the slope of the correlation curve versus delay time is an indication of the optical thickness of the sample.

Intensity measurements can also be made by this experimental setup since the autocorrelation software calculates and stores the average count rate which is directly proportional to the intensity that is detected by the PMT. The usefulness of these intensity measurements will be demonstrated near the end of the Results and Discussion section.

CHAPTER IV

RESULTS AND DISCUSSION

For all of the experimental correlation data that is graphically presented, it was necessary to remove approximately the first two microseconds of data (the first ten channels out of 256) due to the noise produced by afterpulsing of the PMT (for example see Appendix A, Fig. A-4). Channel numbers higher than 10 were not selected as the start point of the correlation measurements because some information about the correlation would be lost, and it was felt that most channels below 10 consistently contained erroneous data. Since only the slope of the correlation is important, and not the intercept, all correlation plots are shifted to begin at 1.0 for correlation (or 0.0 for the natural logarithm of correlation) at experimental delay time, τ , of two microseconds. All delay times are divided by the characteristic time constant τ_0 (Eq. (3-6)) in order to provide a nondimensional time which can be easily compared with theory and which is independent of various effects such as temperature, solute viscosity, particle diameter, and laser wavelength in the medium. All of the data are plotted as the natural logarithm of the correlation function versus the square root of nondimensional delay time (unless otherwise stated) because there is a near linear dependency between these two parameters for infinite optical thickness or for large τ for back-scattering [Ackerson et al. (1992) and Pine et al. (1990a)].

Examining these types of plots allows one to more easily analyze the data, since the degree of fit/deviation from a straight line is clearly discernible. The theoretical correlation function (CT) has been normalized to 1.0 at $\tau/\tau_0 = 0.0002$. As shown later, the correlation function is fairly flat at very

short time (up to about $\tau/\tau_o = 0.002$), so the experimental correlation data has been shifted a little (when necessary) to give better examination of the comparison of the slope to that of the theory. Most plots are for 0.3 μm particle diameter and 514.5 nm laser wavelength. If conditions are different, their values will be given.

Sample Container Factors

Effect of Glass Cell Back Reflection

As mentioned earlier, the back-scattering measurements are performed by setting the probe to about 9° (outside sample) from the direct back-scattering direction in order to eliminate the effects of reflection from the glass sides of the cell. Such non-scattered signals (resulting in heterodyning) can significantly affect the correlation measurements. Figures 9 and 10 show this effect on back-scattering correlation measurements when the detector was set to different "outside sample" angles. Figure 9 shows the same correlation from off angle (detector) measurements of 5° to 9° at long delay times for an optical thickness of 10. But 3° results show a completely different slope.

Figure 10 shows the effect of glass reflection at a 4° measurement for an optical thickness of 100. Note that Fig. 10 is plotted for shorter overall time. Even though the amount of deviation of 4° results in Fig. 10 is much larger than the 3° results of Fig. 9 (they are not consistent, which may be due to coherent back-scattering), it is clear that the reflection of the glass cell significantly affects the correlation measurement at detection angles lower than 5° to the normal direction. Also it has been suggested that the low detector angle effects on correlation measurements may be caused by coherent back-scattering [Wolf et al. (1988)]. The experimental data which are presented in the following sections

were taken from 9° to 10° (outside sample) from the normal direction, unless otherwise stated, to reduce the undesirable effects on correlation measurements which produce more noise in the results. More detailed discussion of the effect of heterodyning on homodyne correlation measurements is presented in Appendix A.

One Dimensionality

Figure 8 was presented earlier as an example of the effect of beam size on correlation measurements. Figures 11 and 12 show experimental data for different beam sizes for optical thicknesses of 10 and 100, respectively. The correlation measurements decay at the same rate for beam diameters of 2.0 and 3.2 cm for an optical thickness of 10 (Fig. 11), thus maintaining one-dimensionality of the measurements. For beam diameter large enough to achieve one-dimensionality, it is expected that changing the beam diameter slightly would have no effect on correlation measurements. From these results, it is not clear specifically where the cross over from two-dimensionality to one-dimensionality occurs, but it is clear that since there is no change in the correlation function for 2.0 and 3.2 cm beam diameters, the system simulates the one-dimensional experimental setup. To be conservative, it appears that the 3.2 cm beam should be used where possible. The decay rate is much slower for the pinhole situation which is a two-dimensional condition for this optical thickness of the sample.

Figure 12 shows that there is not a significant deviation in the decay rate results when the beam size is more than 1.0 cm for an optical thickness of 100. So the size of the beam needed to maintain one-dimensionality of the experiment depends on the density of the solution. However, as the sample is diluted, the

beam should be expanded as much as possible to reduce two-dimensional effects on the correlation measurements.

It should be mentioned that the effect of the two-dimensional situation is due to long correlation paths which include scattering from the region outside of that covered by the laser beam. This effect will eventually show up in the long time results of the correlation function even if the beam diameter is reasonably large. Also as shown in Figs. 11 and 12, the two-dimensional correlation function decays slower (lower slope) than the one-dimensional correlation function as also observed by Pine et al. (1990a). The experimental data which will be presented from this point was obtained from 3.0 or 4.0 cm beam size measurements.

Effect of Different Cells

Since it is difficult to maintain a one-dimensional experimental setup for the 1.0 cm cells for low optical thicknesses, very high optical thickness was selected for these experimental comparisons. Figure 13 shows the back-scattering measurement for optical thickness of 100 using different experimental cells. The two cells which are commercially available are 1.0 cm in width and either 0.1 or 0.2 cm thick. The third cell with the dimensions of 4.0×4.0×0.2 cm was made specifically for this experimental research.

As shown in Fig. 13, the correlation functions for the commercially available cells are the same while correlation decays a little faster for the bigger cell. From previous results, this difference may be due to non one-dimensionality or to different optical thicknesses. Since the beam was expanded more than 1.0 cm for all of the cells and such an expanded beam models a one-dimensional experimental setup at these high optical thicknesses, the correlation function differences should be due to inaccuracy in sample making for the two small cells. The sample was made for the two small cells with a different syringe which was

not very accurate. But this figure shows that, if the same tools are used to make a sample, the correlation will be the same for different cell thicknesses. Thus, correlation directly depends on optical thickness not volume fraction if one-dimensionally is maintained.

Optical Thickness Effects

Figures 14 and 15 show the effect of optical thickness on experimental correlation measurements for back-scattering and transmission, respectively. The incident laser beam has been expanded to about 3.5 cm in diameter in order to cover most of the test cell's surface area [relatively] uniformly. As optical thickness increases, the correlation function's slope gets larger with an increasing decay rate for both transmission and back-scattering (at short delay time). The same trend was observed by Pine et al. (1990). Correlation tends toward a straight line as shown by both figures. The correlation decays faster for transmission as compared to back-scattering, and transmission goes to zero (or reaches the limits of the experimental system's capabilities, yielding only noise in the final measurements) as optical thickness approaches the semi-infinite limit.

As shown in Fig. 15, noise in the system starts to become appreciable at short non-dimensional delay times (about 0.13) for an optical thickness of 50. Figure 14 shows an almost straight line as optical thickness goes to the semi-infinite limit, and all back-scattering correlation slopes are very close to each other for high optical thicknesses (or dense media). But for very high optical thickness, such as 200, the back-scattering correlation function curves upward at long delay times; the reason is not clear yet and more study is required to be conducted. Figure 14 shows that the back-scattering correlation functions appear to decay at the same rate after a long time and the same trend was presented by Maret and

wolf (1987). Since for dense media, correlation measurements are close together for back-scattering but separate widely for transmission, it appears that it will be more convenient to use transmission measurements for sizing the particles. Figure 16 shows the back-scattering experimental data for very high optical thicknesses. As optical thickness increases from 100 to 375, the trend of the correlation function is to start curving up at shorter times.

Single to Multiple Scattering

Even though much research has been performed on single scattering and highly multiple scattering media individually, little has been done to study or understand the transition between the two regimes. So researchers examining multiple scattering typically study only very dense media in order to avoid lesser orders of scattering, and researchers examining single scattering use very dilute samples in order to avoid any chance of multiple scattering. Thus, the two extremes have been investigated to a great degree, but the intermediate regime has had little exploration. However, for an unknown sample, especially with regard to situations demanding in-situ measurement, it is generally understood that neither [extreme] theory will work or be applicable.

Figures 17 to 23 are the results of testing to study the transition from the single scattering limit to the multiple scattering limit -- by comparing these experimental data to single scattering theory (Eq. (3-3)). These experimental data correspond to 0.3 μm particles and a laser wavelength of 514.5 nm. Recall that, in a single scattering medium, all multiple scattering cannot be eliminated, but the effects of double/triple/etc. scattering events are so insignificant that single scattering is the dominant scattering event for that situation. Thus, the

transition from the single scattering extreme begins when double and triple scattering start to affect the detected signal.

Figures 17, 18, 19, and 21 show the deviation of correlation measurements from single scattering theory when optical thickness increases from 0.05 to 0.5 for three different detection angles of 29°, 34°, and 45° (inside sample) -- measured to the direct transmission line of sight. As mentioned before and as is again visible in the figures, when optical thickness increases, the correlation function decays faster. Figures 20 and 22 present the same data as Figs. 19 and 21, respectively, but Figs. 20 and 22 plot the results as a function of the nondimensional delay time (τ/τ_0) rather than the square root of nondimensional delay time. According to Eq. (3-3), the natural logarithm of the single scattering correlation function ($\ln(g^1)$) is linearly related to τ/τ_0 , so that deviation from the single scattering straight line theory on Figs. 20 and 22 is easier to see than deviation from the curved line theory on Figs. 19 and 21. These figures show that optical thicknesses larger than about 0.05 will behave as multiple scattering (non-single scattering) media. So an error appears if the theoretical single scattering formula is assumed for these low optical thicknesses. As an example, there is a 5.65% difference between the slope of the correlation function of optical thicknesses of 0.05 and 0.2, and this difference corresponds to about 3.67% error in particle diameter if the theoretical single scattering formula is applied for both of them. On the other hand, Figs. 21 and 22 appear to indicate that single scattering theory still can predict 45° off angle (inside sample) transmission for optical thicknesses of 0.1 and 0.2.

Figures 23 to 25 show the transition from single to multiple scattering at 90° using the ALV5000, another independent setup, which is commercially available for single scattering measurements using the DLS technique. Note that the beam is not expanded in this setup, since the single scattering measurement does not

depend on dimensionality (Eq. (3-3)). Figure 24 plots the same result as Fig. 23 but as a function of the nondimensional delay time (τ/τ_0) for better observation as earlier mentioned. Figure 23 shows the deviation from single scattering at optical thickness of 0.1 but with an opposite direction of decay rate (decaying slower) as compared to Figs. 17 to 22.

From the results which are presented and discussed on one-dimensionality of the experiment, it may be concluded that the slower decay rates in Figs. 23 to 25 are due to the two-dimensionality effect, since the beam was not expanded. Figure 25 shows more clearly that increasing optical thickness (more multiple scattering) results in a slower decay rate for the correlation function. As a final conclusion on this matter (at this point and for these particles) the data suggests that an optical thickness of about 0.05 (effective optical thickness of about 0.013) is the beginning of the transition from the single to multiple scattering regimes. In addition to these results, as will be presented later, the CT equation can provide this information with the expansion of the g^1 function in the Legendre series of polynomials.

Comparison of Experiment to CT Theory

The transmission results measured at 10° (outside sample) from the normal direction ($\mu=0.985$) for $0.3\ \mu\text{m}$ particles are shown in Figs. 26-30 for optical thicknesses (L_0) of 5, 10, and 25. The numerical results were computed by applying the preaveraging technique [Eq. (3-13)] for Figs. 26-29 and a 1 term Legendre series expansion of g^1 [Eq. (3-16a)] for Fig 30. The experimental data shown in these figures correspond to scattering the 514.5 nm wavelength laser beam. Figure 26 presents the comparison of the experimental data with the numerical results for isotropic assumption ($f=0.0$) and with a unit index of

refraction ($n=1.0$). For this special case, the results are in poor agreement. This is expected because the effects of anisotropy and of the index of refraction were neglected.

When the forward scattering approximation theory ($f=0.727$, computed from Mie theory) is employed in the numerical results, as shown in Fig. 27, the deviation of the numerical results from the experimental data are much less than that observed with the isotropic results of Fig. 26. However, Fig. 28 shows that keeping the isotropic assumption and using an index of refraction different than one ($n=1.331$) in the theory leads to a poorer agreement with the experimental data. Thus, it appears that the forward scattering approximation and the real modeling of the index of refraction have opposite effects on the decay rate of theoretical correlation function (G^m), which suggests combining the two effects.

Figure 29 shows a comparison between experimental and theoretical transmission results for the correlation function when an index of refraction of 1.331 and the forward scattering approximation of $f=0.727$ for the phase function are assumed in the theory. The results are in much better agreement with the data as compared to those results (Figs. 26-28) where both or one of these effects are neglected. It should be noted that the numerical model considers only one index of refraction change (from air to water) at the boundary where the incident laser beam enters the test cell. Thus, the glass interfaces and the second water-to-glass-to-air interface is not modeled. The discrepancy between the experimental and theoretical results for a low optical thickness of 5 for these particles (effective optical thickness is 1.365) is probably due to neglecting the index of refraction change at the other boundary in the numerical solution. The other interface index of refraction change affects the correlation function for low optical thicknesses. As optical thickness increases, Fig. 30 shows greater deviation between the same experimental data and the numerical results from

more realistic approximations of g^1 . The reason for this disagreement is probably due to the phase function approximation and this requires further investigation.

In Figs. 31 to 34, a comparison between theoretical results and experimental data for 10° (outside sample) from normal back-scattering is presented for finite media with optical thicknesses of 5, 10, and 25 for $0.3 \mu\text{m}$ particles. In Fig. 31, the scattering is assumed isotropic ($f=0$) and the index of refraction is set equal to one in the preaveraged theory. As expected, this leads to poor agreement between theory and experiment. However, it is worth noting that, for the case of an optical thickness of 25, the theory presents the least disagreement with the data. This could be explained by the large number of multiple scattering events that go on in this large optical thickness medium where scattering becomes almost equally likely in all directions, and hence approaches the isotropic limit.

When the forward scattering approximation ($f=0.727$) is included in the theory, as shown in Fig. 32, the agreement with experiment is almost the same as compared to the isotropic results of Fig. 31. When both effects of the index of refraction ($n=1.331$) and the forward scattering assumption are included in the theory, the agreement with experiment is greatly improved as shown in Fig. 33. Figure 34 shows better agreement when the 1 term Legendre series expansion of g^1 was used instead of the preaveraged technique to obtain numerical results.

There is better agreement between CT theory and experimental data for short [nondimensional] delay times when the theoretical model considers both index of refraction (n) and anisotropic effects (i.e., the f factor). Therefore, both the index of refraction and the anisotropic scattering factor are used in computing the other numerical results for different particle sizes.

Figures 35 and 36 show the comparison of experimental correlation data (back-scattering and transmission, respectively) to numerical predictions for

0.091 μm particles and a laser wavelength of 532 nm. This laser beam was expanded to a little less than 2.0 cm in diameter due to the initially smaller diameter (0.1 mm) of the Diode (DPY) laser. From the figure labels including the anisotropic factor f , it can be seen that the low value of f (0.089) indicates that these particles are nearly isotropic scatterers. Figure 35 shows that, even though there is good agreement in back-scattered correlation for an optical thickness of 1.0, the results for the larger optical thicknesses of 3.0 and 5.0 deviate from each other at shorter delay times as optical thickness increases. However, Fig. 35 does show that the experimental data and numerical results appear to become parallel after a short delay time; so the initial differences may be less significant than might be thought from a first glance.

Figure 36 depicts the reverse trend for transmission, in that agreement improves as optical thickness increases. Note that this good agreement between theory and transmission data is possible due to the use of a cross-polarizer in taking the data. Since some unscattered light (parallel polarization) passes through the medium (heterodyning) and interferes with the direct transmission signal from the scattered light (which will generally become unpolarized after several scattering events), the cross-polarizer was used to filter out that non-scattered light. The use of this cross-polarizer also filters out the parallel component of polarized scattered light which can affect the correlation measurements and can cause different decay rates from what Fig. 36 presents.

Figures 37 and 38 show 10° (outside sample) off angle detection from normal back-scattering and transmission for 0.107 μm particle sizes and 514.5 nm laser wavelength for optical thicknesses of 3, 5, and 7 (corresponding to effective optical thicknesses of 2.604, 4.34, and 6.076 respectively). The numerical results were obtained from the 1 term expansion of g^1 . As optical thickness increases,

the numerical results predict better the experimental data for transmission (Fig. 38) but there is no agreement for back-scattering (Fig. 37).

Figures 39 and 40 present the same conditions as Figs. 37 and 38 for highly anisotropic particles sizes of $0.497\text{ }\mu\text{m}$ ($f=0.858$) but for optical thicknesses of 10, 20, and 30. These optical thicknesses correspond to effective optical thicknesses of 1.42, 2.84, and 4.26 respectively. The agreement between the numerical results and experimental data improves for transmission (Fig. 40) as optical thickness increases, and it is good for optical thickness of 30. Figure 39 shows a slower decay rate for the back-scattering correlation function of experimental data for optical thickness of 10 and a faster decay for optical thickness of 30 as compared to numerical results. It shows good agreement for optical thickness of 20. The second refractive index can also affect the correlation function (this will be presented later), specifically it has more effect at lower optical thicknesses. This better agreement at an optical thickness of 20 than at 30 appears to be just a coincidence.

The above comparisons for different particle sizes show that the numerical results using the Fraunhofer diffraction approximation (Eq. 3-17) for the phase function can predict the experimental correlation function for transmission better than for back-scattering for small particle sizes (low f factor). The back-scattering numerical predictions become better than transmission for bigger sized particles (higher f factor). The above comparisons also present the good potential of the CT which can predict experimental data if more realistic approximations are maintained in the numerical results. The DWS theory (Pine et al., 19990) can predict experimental data with the help of one and two floating parameters in transmission and back-scattering, respectively while there is no floating parameters in the CT theory.

A comparison of experimental data with the preaveraged CT results and using the 3 term Legendre expansion of g^1 [Reguigui et al. (1993)] is shown in Fig. 41 for the case of back-scattering from an infinitely thick medium. The theoretical results were obtained using index of refraction of one and the isotropic condition ($f=0.0$), since the effects of index of refraction other than one and the anisotropic assumption have negligible impact in an infinitely thick medium. In this figure the preaveraged results follow the experimental data at very short delay time, and as expected, the preaveraged approximation fails to predict the exact rate of the correlation function decay at longer delay times. However, when the 3 term Legendre expansion of the g^1 function is employed, the results fit the data much better for longer delay times. It appears that by including more Legendre terms in the expansion of g^1 , better agreement with experimental data can be obtained for longer delay time.

Figures 42 and 43 show the comparison of CT results to experimental data and single scattering g^1 (Eq. (3-3)) for very dilute samples at 30° (experimental data were obtained at 29°) and 45° (inside sample) from direct transmission, respectively. Figure 42 plots the CT results for 1 term (including both indexes of refraction of 1.0 and 1.33) and 3 term Legendre expansion (index of refraction of 1.0) of the g^1 function for optical thickness of 0.01. Figure 43 shows just the 3 term g^1 expansion for CT results for optical thickness of 0.01. The experiments which are presented in Figs. 42 and 43 are for an optical thickness of 0.05 at 29° and 45° (inside sample) from direct transmission, respectively.

As was already discussed, the correlation function for optical thicknesses lower than 0.05 can be predicted by the single scattering g^1 equation, and it can be assumed to be a single scattering medium. Figure 42 shows that index of refraction does not affect the correlation function for a very dilute sample (single scattering medium), but increasing the number of terms in the g^1 expansion will

improve the CT results and can predict the single scattering medium correlation function. Both Figs. 42 and 43 show good comparison between theory and experiment for very dilute samples. It appears that the CT theory has good promise in bridging the gap between single and multiple scattering correlation theories.

Off Angle Measurements

The effects of off-angle measurements on the correlation function are presented in Figs. 44 to 51 for back-scattering ($\mu < 0$) and in Figs. 52 to 57 for transmission ($\mu > 0$). All the measurements for different angles which will be presented are correspond to outside sample detection angles, otherwise stated. The back-scattering experimental measurements for an optical thickness of 10 are presented in Fig. 44 for detection angles (θ) ranging from 10 to 50 degrees from the normal back-scattering direction which is defined as $\theta = 0$ ($\mu = -\cos\theta$). It appears that off-angle measurements do not significantly affect the decay rate of the correlation at this optical thickness. Assuming isotropic scattering ($f = 0.0$) and no index of refraction change across the boundary ($n = 1.0$), the preaveraged theory predicts different decay rates for different angles (outside sample) of observation as shown in Fig. 45. However, when the anisotropic effects (i.e. the f factor) and index of refraction change across the incident beam boundary of the medium are included in the analysis, all of the curves lie on top of each other as shown in Fig. 46, and correlation decay rate is the same regardless of the angle of observation. The CT theory treats different angles exactly by having results for each angle, and it can accurately calculate the angle change between inside and outside of the sample due to the refractive index, while the other available theories cannot accurately do this.

Figure 47 shows the back-scattering off angle measurements for an optical thickness of 100 from 10° to 30° from the normal direction. The same conclusion can be drawn here as for Fig. 44. It appears that off angle detection does not affect the correlation function for large optical thicknesses where multiple scattering redistributes the radiation into all angles almost isotropically. But as optical thickness decreases, the back-scattering correlation function becomes angle dependent. Figure 48 shows these different decay rates from 10° to 50° off angle back-scattering measurements for a low optical thickness of 2.

Figures 49 to 51 present back-scattering off angle measurements from 10° to 50° from the normal back-scattering direction for optical thicknesses of 3 to 5. These figures show that the effect of off angle detection is less important as optical thickness increases. The off angle measurement does not significantly affect results at an optical thickness of about 5 (Fig. 51) while its effect is obvious as already shown for a low optical thickness of 2 (Fig. 48).

Comparison of transmitted experimental data and results from the anisotropic preaveraged theory with $n=1.331$ for an optical thickness of 10 is shown in Fig. 52. The off angle detection effect is insignificant. Figure 53 shows the significant change in decay rates in off angle transmission measurements for the three very small optical thicknesses of 0.05, 0.30 and 0.50. (This was obvious from the different effects of optical thickness on detection at inside sample angles of 29° , 34° and 45° in Figs. 17-22.) Also this effect is obvious for an optical thickness of 5 as shown in Fig. 54. As optical thickness increases from 8 to 10 (Figs. 55 to 57), the off angle transmission measurements have less effect on the correlation function, and detection angle can be ignored for optical thicknesses higher than about 10.

The experimental data for these figures also correspond to $0.3\ \mu\text{m}$ particles and a laser wavelength of 514.5 nm. These figures demonstrate that it is

important for theoretical models to predict off angle trends if they are to be used to study/predict dilute sample characteristics (i.e. particle size characterization), since it is more suitable to do the measurement (for dilute samples) at off angles from back-scattering or transmission in order to eliminate the effects of back reflection or the unscattered transmitted beam on the correlation measurements. As previously mentioned, CT's derivation without dense media restrictions/assumptions and its prediction of the single scattering correlation function for thin media (Figs. 42 and 43) provide the motivation for additional future investigation of CT's application in the intermediate scattering regimes at angles other than direct back-scattering and transmission.

Polarization Effects

An unscattered beam passing through a sample can affect direct transmission measurements similar to the way that glass back reflection can affect back-scattering measurements. The size of the effect depends on the magnitude of the signals received from the unscattered light (heterodyning) as compared to scattered light (homodyning). In order to reduce this effect for dilute samples, a cross polarizing filter (with polarization perpendicular to that of the laser beam) must be used for direct transmission measurements. Also, the cell glass back reflection affects the direct back scattering (heterodyning) and a cross polarizer must be used in this case. Since the correlation function is different for the two polarizations, horizontal and vertical, data was taken to investigate this effect.

Figure 58 shows the 10° (outside sample) off angle back-scattering data for optical thicknesses of 5, 10, and 40 for two different polarizations. Since there is no significant effect of glass back reflection at a 10° detector angle, the

difference in decay rates should be due to the effect of the two different polarizations. The parallel polarization always decays slower, and the cross polarization always decays faster than the unpolarized correlation function. Even though optical thickness was increased to 100 (Fig. 59), the correlation measurement shows different decay rates for the two polarizations. Pine et al. (1990a) also observed the slower decay rate for parallel polarization than for cross polarization when they were measuring back-scattering polarization for very high optical thicknesses using two different particle sizes. These figures show that the effect of polarization is significant in back-scattering, and the correlation function decays differently for the two polarizations regardless of optical thickness. Since there is always a chance for the light to scatter once in back-scattering, these different decay rates are probably due to the effect of single scattering on the back-scattering correlation function at any optical thickness.

Figure 60 shows the comparison of the unpolarized measurements to the average of the two polarization measurements for optical thickness of 5, 25, and 100. It shows that the unpolarized correlation function appears to be the average of the horizontal and vertical intensity correlation functions in back-scattering. This very interesting result requires further investigation for different diameter particles. Figures 61 to 63 present polarization effects for transmitted correlation measurements. Figure 61 shows significant polarization effects at low optical thicknesses while the two polarization correlation measurements have the same decay rates at an optical thickness of 25. Also it shows that the polarization correlation functions become closer together as optical thickness increases.

Experimental investigation has been performed to find the approximate optical thickness where the two polarization transmission correlation functions merge together. Figure 62 presents the results for optical thicknesses of 15, 17,

and 18. At an optical thickness of 18 (Fig. 62) which corresponds to an effective optical thickness of about 4.91 ($f=0.727$), the two polarized measurements and the unpolarized correlation measurement decay at the same rate. It should be recalled that the experimental data for these figures also corresponds to $0.3\ \mu\text{m}$ particles, and these trends may not be true for the other particle sizes. Figure 63 shows the same comparisons as presented for back-scattering in Fig. 60 for optical thicknesses of 5, 10, and 15. The unpolarized correlation function is not always the same as the average of the two polarized correlation functions like back-scattering. But as shown in this figure, this average becomes closer to the unpolarized correlation measurements as optical thickness increases, and they are the same for an optical thickness of 15, where the two polarization correlation functions come close each other (Fig. 62).

Figures 64 to 66 present off angle back-scattering for polarized correlation functions for optical thicknesses of 3, 4, and 5. Figure 64 shows that different detection angles do not affect cross polarization correlation measurements while there is a difference in decay rates for parallel polarization measurements. It also shows that there are larger differences in decay rates between 10° to 20° than between the other off angle measurements for parallel polarization (the same polarization as the laser beam). This may be due to heterodyning (glass back reflection) which combines with the homodyne signals from particles [Berne and Pecora (1976)] and affects the correlation function measurements at this low optical thickness ($L_0=3$). The laser had to be set to high power for low optical thickness back-scattering measurements to increase the count rate (i.e., intensity) for the measurements. This glass back reflection does not affect cross polarization measurements since the polarizer blocks this unscattered intensity. As optical thickness increases (Figs. 64 to 66), the off angle parallel polarization

measurement also becomes less affected, and it is not significant at an optical thickness of 5 (Fig. 66).

As presented earlier (Fig. 51), the off angle effect on back-scattering measurements also becomes insignificant for unpolarized detected light at an optical thickness of 5. Figures 67 to 70 show the polarization effect for transmission for optical thicknesses of 5, 8, 9, and 10 at different detection angles. The different detection angle measurements for parallel polarization show different slopes in correlation measurements for an optical thickness of 5 (Fig. 67) while the slopes are the same for cross polarization measurements regardless of the angle of detection. It appears from Figs. 67 to 70 that the effect of detection angle in parallel polarization transmission measurements reduces as optical thickness increases (the same as back-scattering). Figure 70 shows that different angles of detection do not significantly affect the slope of the polarization transmission correlation measurements at an optical thickness of 10 for short delay time $[(\tau/\tau_o)^{0.5} \leq 0.3]$, the same conclusion which was derived from unpolarized measurements (Fig. 57).

A Proposal For Characterizing Particle Size

Combining the information provided by the results of this experimental research indicates the strong possibility that CT theory may be robust enough to predict dynamic light scattering measurements from any multiple scattering solution. Verification of this proposal requires that a very wide variety of cases be studied both theoretically and experimentally. One way to ascertain the range of applicability of CT theory would be to use it to determine the sizes of particles in suspensions whose concentrations run from very thin to very thick. Since one of the major uses of dynamic light scattering is the determination of particle size,

this is an appropriate test of CT theory. Here I introduce the outline of a potential methodology for determining the size of particles in a solution of unknown concentration by comparing correlation measurements with CT predictions. This methodology has been published as a conference paper [Dorri-Nowkoorani et al. (1993)].

The first step in matching the results from experimental data to CT theory requires the determination of [effective] optical thickness of the unknown sample. Then, once optical thickness is known, CT theory can be run for that thickness, and the best characteristic delay time, τ_0 , must be found for the experimental data to yield an optimal match with the theory. Optical thickness measurements can be performed by matching the static light scattering (intensity) measurements with RT numerical results. Since absolute intensity measurements are difficult to perform accurately, the ratio of the intensity from an unknown sample to that of a standard sample with a known [effective] optical thickness can be obtained and used in the procedure.

Figure 71 shows an example of such a procedure, plotting back-scattered intensity at 30° off angle as a function of optical thickness, and normalizing all intensity values to that for an optical thickness of 3.0. The model which was used to obtain the numerical results of Figs. 71 and 72 considers a one-dimensional rectangular scattering medium with a refractive index of 1.331 relative to the material bounding the medium at the top and bottom interfaces. This model is a close approximation to our experimental cell. The numerical results are provided from the model of Reguigui and Dougherty (1992).

To check the reliability of comparing measurements to numerical data, a few measurements at 30° to direct back-scattering were made for the intensity from samples of known effective optical thicknesses. 0.3 μm particles and a 514.5 nm laser wavelength were used to obtain the data for Fig. 71. These

results were already normalized by the intensity measured from an effective optical thickness (considering f factor) of 3.0 (using 0.3 μm particle diameter) and then plotted on Fig. 71. All of the effective optical thicknesses were computed using the anisotropic scattering factor (f) as explained in the Theoretical Background and in the Experimental Setup and Procedure section. The intensity measurements were obtained from the autocorrelation software which provides the average PMT count rate over the run time of a given test.

Examining Fig. 71 shows that there is good agreement between the numerical predictions and the experimental data. Thus, it appears that by comparing intensity measurements from an unknown sample to a standard sample, effective optical thickness can be determined. However, from Fig. 71, it is obvious that there may be a maximum effective optical thickness (greater than about 12), above which resolution is not sufficient to use this procedure. However, as an example, an effective optical thickness of 12 corresponds to an optical thickness of about 44 for 0.3 μm particles suspended in the water and illuminated by a 514.5 nm wavelength laser beam.

After the effective optical thickness is determined, CT theory can be run for that corresponding optical thickness and the results plotted or digitized as a function of nondimensional delay time (τ/τ_0). The data which is obtained from the autocorrelator is available as a function of delay time (τ). Then, normalizing the correlation data by several potential characteristic delay times (τ_0), a suitable τ_0 can be found, and the experimental data can be matched to the numerical results. Knowing τ_0 and using Eqs. (3-4) and (3-6), the diameter of the scattering particles can be determined.

Figures 72 to 79 are some data used to check the accuracy of this procedure and the measurements required to find particle size. The three different known particle sizes of 0.3 μm , 0.497 μm , and 0.107 μm were used to

make different unknown concentrations of more disperse solutions. The back-scattered intensities from each sample solution were measured at 10° and 30° off angle. These intensities were normalized by the intensity measured from a known effective optical thickness of 3 which was made with $0.3\ \mu\text{m}$ particle sizes. These intensity ratios were graphically located on the plot of the numerical results for intensity (Figs. 72a and 72b) to find the corresponding optical thicknesses. Figures 72a and 72b present the numerical intensity results and the intensity measurements for different optical thicknesses at 10° and 30° off angle back-scattering for different particle sizes. After the effective optical thickness from each solution was determined (Tables 2 and 3), the corresponding theoretical correlation function was calculated (using CT theory with a one term Legendre expansion of g^1).

Figure 73 shows an example of matching the experimental correlation function to numerical results graphically by changing characteristic delay time τ_0 in the experimental data. This value of τ_0 is used to determine the particle size as explained earlier. Figures 74 to 79 show the results of this graphical matching technique for several solutions which were made with known particle sizes. The numerical results in these figures are from the 1 term Legendre g^1 expansion and using the Fraunhofer diffraction approximation for the phase function approximation (Eq. 3-17) and only an index of refraction change at the laser beam incident interface. A summary of these results is reported in Tables 2 and 3 on the next page. In these tables, L_e was determined from Figs. 72, and the matching of τ_0 was from Figs. 74 to 79. The particle sizes were calculated from matching τ_0 and are reported as "cal" in the tables. The percentage error was calculated with respect to the "actual" particle sizes (represented by the manufacturer of the particles).

These tables show that percentage errors are larger for smaller particle sizes (0.107 μm), and this is consistent with what was presented earlier in the "Comparison of Experiment to CT Theory" where the numerical results were compared to experimental data for back-scattering.

Table 2: Summary of the results for particle characterization at 10° (outside sample) from direct back-scattering measurements (for a room temperature of 22 °C).

intensity ratio	L_e	matching τ_o (ms)	particle dia. in μm (cal.)	particle dia. in μm (actual)	% error
1.182	4.75	2.70	0.323	0.300	6.2
0.882	2.22	2.30	0.275	0.300	9.5
0.566	1.0	2.15	0.257	0.300	15.4
1.067	3.55	1.45	0.173	0.107	62.0
0.703	1.42	1.10	0.132	0.107	22.9
0.330	0.45	0.85	0.102	0.107	5.0
0.781	1.75	3.90	0.466	0.497	6.2
1.038	3.30	4.50	0.538	0.497	8.3
1.282	6.45	5.00	0.598	0.497	20.3

For this range of effective optical thicknesses (from about 1.0 to 7.0), the largest error is about 20% for larger particle sizes of 0.3 μm and 0.497 μm . As optical thickness increases, the error becomes larger for 0.497 μm particle sizes, while the situation is reversed for 0.3 μm particle sizes. This may be due to having used the reference sample solution with effective optical thickness of 3 that was made of 0.3 μm particle sizes for normalizing back-scattered intensity. Also part of the error in particle sizing was due to the instability of the laser

intensity which was "walking around" with time and produced inaccuracies in intensity measurement. This problem, which is discussed in Appendix A, did not significantly affect the dynamic correlation over the period of the single test measurement (about 5 minutes), but had a greater effect on static scattering. Another possible source of error is in the approximations which were made in the numerical results.

Table 3: Summary of the results for particle characterization at 30° (outside sample) from direct back-scattering measurements (for a room temperature of 22 °C).

intensity ratio	L_e	matching τ_0 (ms)	particle dia. in μm (cal.)	particle dia. in μm (actual)	% error
1.0137	4.20	2.45	0.293	0.300	3.63
0.727	1.55	2.15	0.257	0.300	15.4
0.919	2.45	2.25	0.269	0.300	11.5
0.711	1.45	0.95	0.114	0.107	6.2
1.015	3.10	1.25	0.149	0.107	39.7
1.229	5.45	1.45	0.173	0.107	62.0
0.615	1.20	3.80	0.454	0.497	8.6
0.991	2.90	4.30	0.514	0.497	3.4
1.176	4.65	4.80	0.574	0.497	15.5

This investigation does not show completely satisfactory results for all particle sizes due to my approximating the theoretical phase function [Eq. (3-17)] and laser instability; but this appears to be a promising methodology for determining particle size in different ranges of multiple scattering if a more realistic phase function is used in the numerical solutions.

Improved P_N Approximation

Obtaining exact results from the CT equation requires significant computational time, especially if index of refraction and a Legendre expansion for single scattering g^1 are included in the calculations [Liu (1993)]. As the required optical thickness increases, the execution time for the program for the exact solution increases, and this would not be suitable for particle sizing when obtaining fast results are preferred. Since the CT equation is similar to the RT equation and expansion of the single scattering g^1 into more terms in a Legendre series can improve the theoretical results, as compared to the experimental data, the improved P_N approximation technique can be used to solve the CT equation - if the P_N solution can be shown to compare well with the exact solution's decay rate (or slope).

Figures 80 to 89 present the comparison of the exact unit refractive index solution for the 3-term g^1 expansion in a Legendre series [Reguigui et al. (1993)] to the numerical results of the improved P_1 , P_3 , P_5 , and P_7 approximation for back-scattering and transmission at optical thicknesses of 1, 5, 10, and 25. Part of these results have already been published as a conference paper [Dorri-Nowkoorani et al. (1994)]. It should be noted that the plots were normalized by the correlation function at a delay time of $\tau/\tau_o = 0.0002$. The improved P_N approximation can not be calculated at zero delay time due to a singularity problem. Recall that the slopes (decay rates) of the curves are important and not the absolute values or levels.

Figures 80 to 83 show that the agreement between improved P_N approximation and 3 term g^1 expansion (exact results) is improved for higher orders of approximation for back-scattering. The approximate results deviate from exact results for longer time due to the Legendre expansion for intensity

(curving down), but they agree well until $(\tau / \tau_o)^{0.5}$ reaches about 0.5 (for P_7). The agreement improves as optical thickness increases as shown from Figs. 80 to 83 for optical thicknesses of 1, 5, 10, and 25, respectively. These figures also show that, as the order of approximation of improved P_N increases, their correlation functions switch up and down alternatively as compared to the exact solution due to the characteristics of the Legendre polynomials in this approximate development. It appears that these approximate correlation functions (improved P_N) converge to the exact results (3 term g^1 expansion) as the order of the improved P_N approximation increases.

Figures 84 to 89 present very good comparisons for the third and higher order approximations to the exact results for transmission at optical thicknesses greater than 5. Higher orders of approximation have to be used for low optical thicknesses. These figures also show that the improved P_N approximation agreed better for transmission than for back-scattering (Figs. 80 to 83) as compared to the 3 term g^1 expansion (exact results). Since an accurate correlation function cannot be obtained from the experimental setup further than about three orders of (decay) magnitude (due to signal-to-noise limitations), the accuracy of this approximation for only these decay orders of magnitude for optical thicknesses of 10 and 25 is presented in Figs. 88 and 89. The comparison is good for this order of magnitude decay range.

The effect of index of refraction is shown in Figs. 90 to 92. Figures 90 present the modified P_5 back-scattering results for optical thicknesses of 1, 10, and 25. They show the significant effect of the first index of refraction on correlation while the second boundary's index of refraction does not affect the results for high optical thicknesses (10 and 25). Figure 91 shows that considering index of refraction changes at both boundaries is important at both low and high optical thicknesses for transmission. The index of refraction change at the

boundaries causes the back reflection of the light into the medium and consequently more scattering events occur, resulting in a faster correlation function decay rate. Figures 92 and 93 show the transmission and back-scattering comparisons of the improved P_5 approximation to the 3 term g^1 expansion (exact results) for no refractive index change at the boundaries and one refractive index change at the incident beam interface [Liu (1993)] for an optical thickness of 1.0. There is very good agreement between exact and approximate results up to $(\tau/\tau_o)^{0.5}$ of about 0.3. However, the comparison is also fairly good for longer delay times for both transmission and back-scattering (Figs. 92 and 93). These figures also show the significant effect of index of refraction on the correlation function.

Figures 94 and 95 present the comparisons of the same 1 term g^1 expansion (exact results) as shown in the Figs. 30 and 34 to the improved P_5 approximation with an index of refraction change at the incident beam interface. The effective optical thicknesses (L_e) which are presented in these figures, correspond to the experimental optical thicknesses of 5, 10, and 25 for particle sizes of 0.3 μm and laser wavelength of 514.5 nm. The transmission results (Fig. 94) have better agreement than the back-scattering results (Fig. 95). Since there is a good comparison between the 3 term g^1 expansion exact solution results to those of the improved P_5 approximation (Figs. 92 and 93), deviations between the 1 term g^1 expansion results and the improved P_5 approximation in Figs. 94 and 95 are probably due to the low order of the g^1 expansion results. As optical thickness increases, better agreement is achieved as shown in these two figures due to the greater accuracy of the 1 term g^1 expansion results for higher optical thicknesses.

Figures 96 and 97 present the comparisons of the same experimental data as shown in the Figs. 30 and 34 to the improved P_5 approximation with index of

refraction changes at both boundaries. These figures show the significant effect of the second refractive index change when they are compared to the results of Figs. 30 and 34. These two figures (Figs. 96 and 97) show that as optical thickness increases, better agreement between theory and experiment is achieved. The deviation of theoretical results from experimental data is mostly due to the phase function approximation [Eq. (3-17)] in the numerical results. The phase function has a greater effect on the theoretical results for lower optical thicknesses, and it has less effect as optical thickness increases, since the medium becomes more effectively isotropic as multiple scattering increases. These two figures show the same trend, that the error caused by the phase function approximation reduces as optical thickness increases.

The execution time for this approximation is much faster than for the exact solution. The exact solution takes more than one hour on an IBM RISC6000 for no index of refraction change at the boundary and 10 different delay times, while this approximation takes about 30 seconds for the same amount of delay time calculations. It is even faster by comparison when considering index of refraction changes at the boundaries as compared with the exact solution (more than about 200 times faster for one index of refraction change at the boundaries). The good comparisons between the exact solution and this approximation show that this technique can be used as a quick reliable method for application to particle size determination.

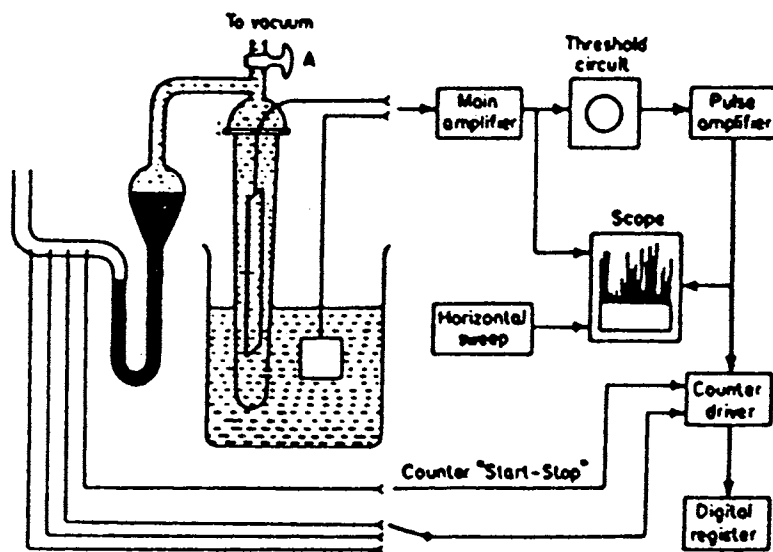


Fig. 1: Example of an electrical zone sensing diagram.

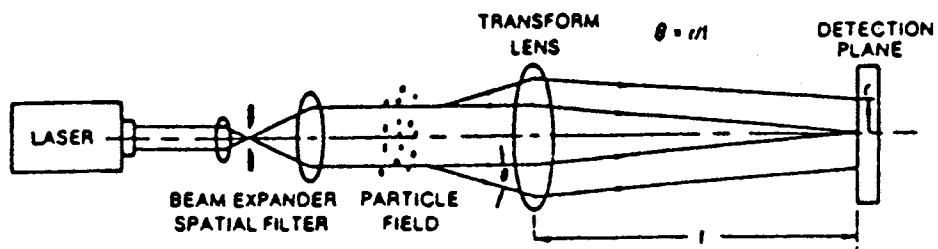
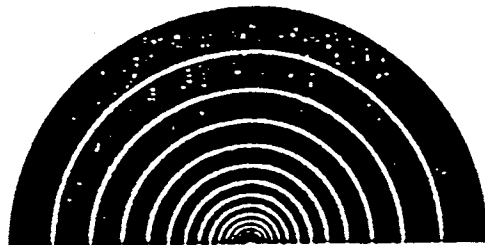


Fig. 2: Schematic of laser diffraction particle sizing system.

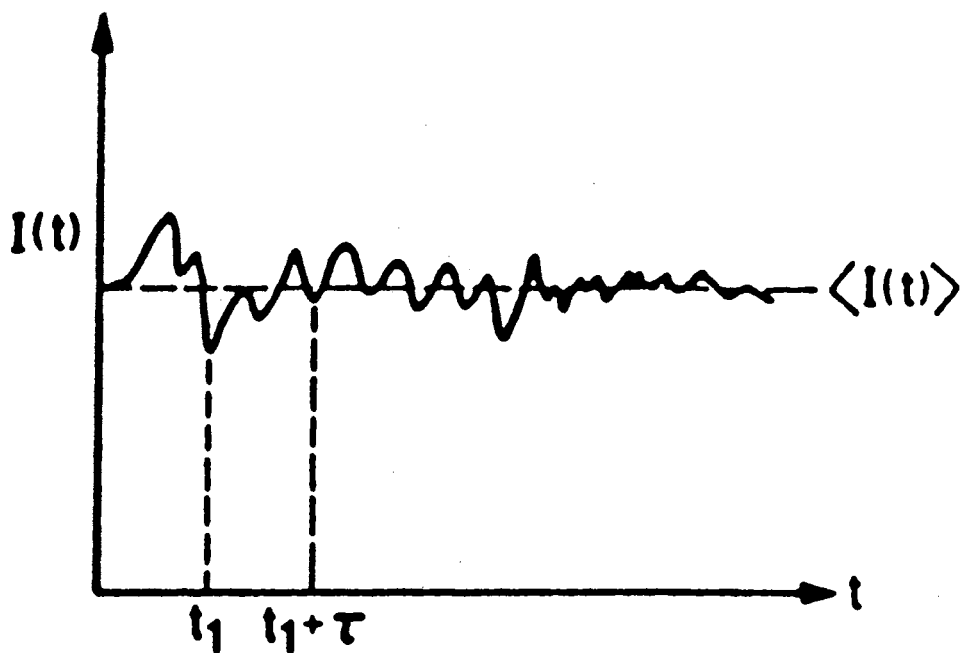


Fig. 3: Example of intensity fluctuation with time

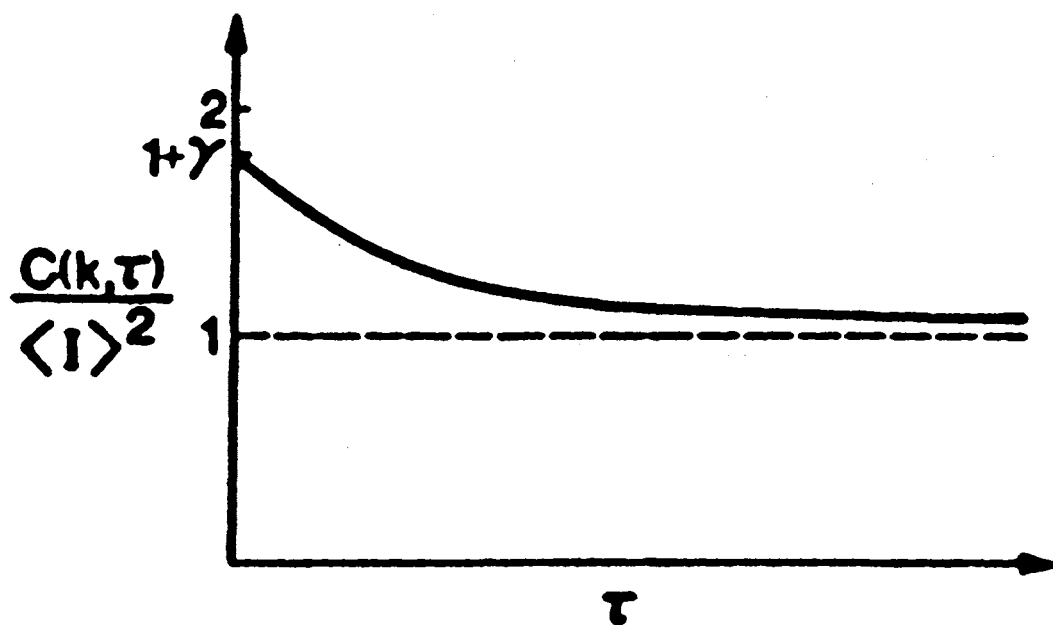


Fig. 4: Typical plot of normalized single scattering intensity correlation function

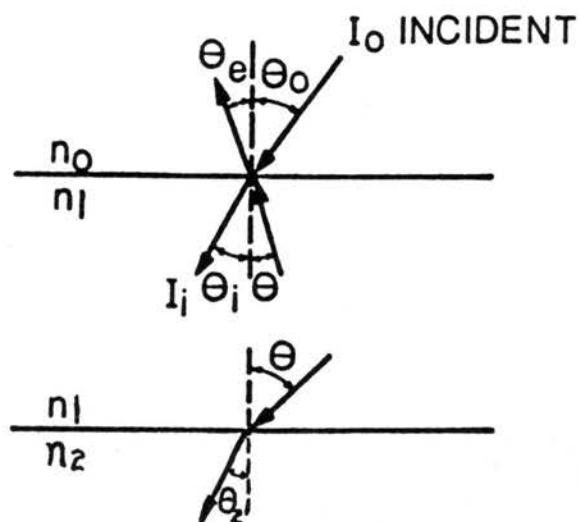


Fig. 5: The geometry for reflection at both boundaries

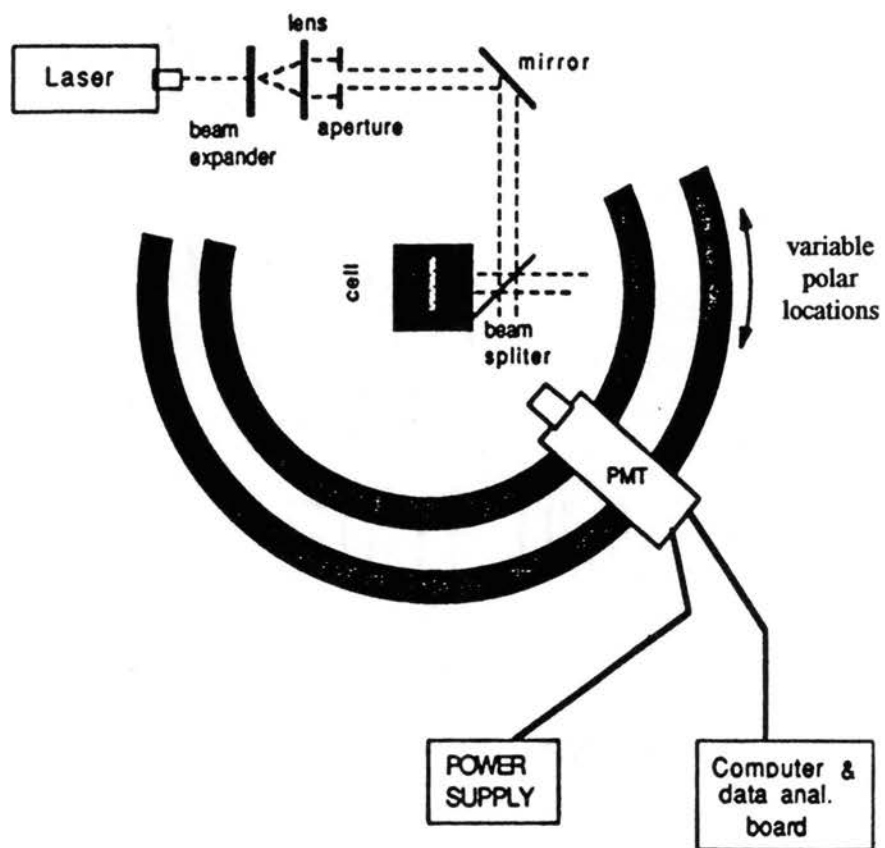


Fig. 6: Experimental setup

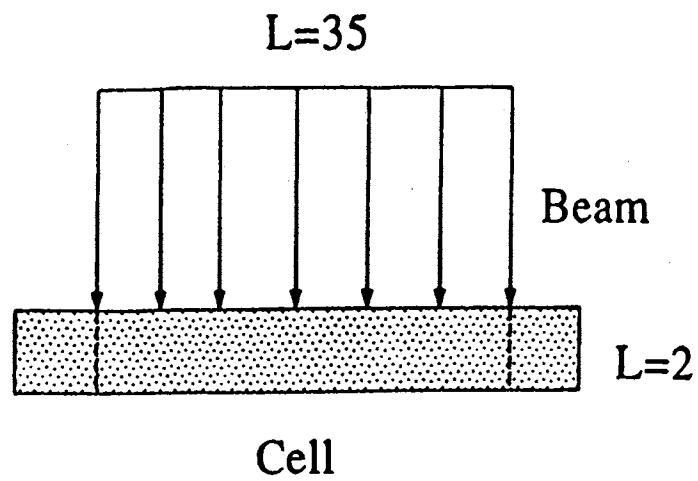


Fig. 7: Expanded laser beam incident on test cell

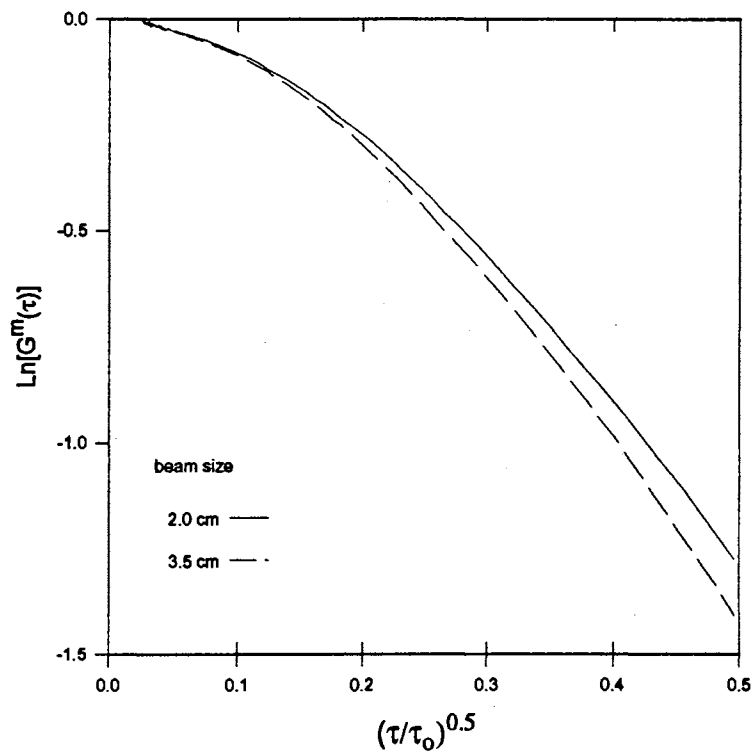


Fig. 8: Effect of laser beam diameter on one-dimensionality of measurements, unknown optical thickness, particle diameter of $0.3 \mu\text{m}$, and laser wavelength of 514.5 nm .

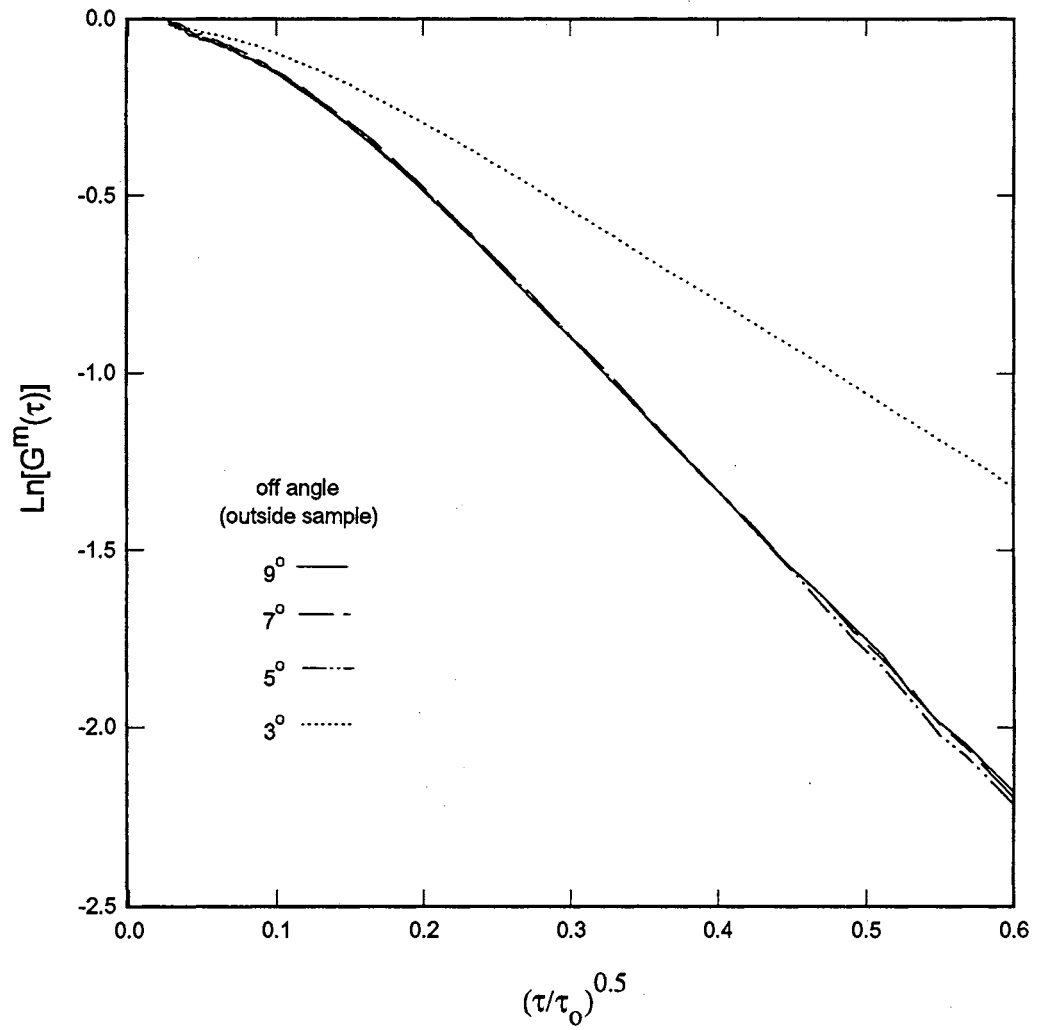


Fig. 9: Back-scattering: Effect of glass back reflection on correlation measurement for optical thickness of 10, particle diameter of 0.3 μm, and laser wavelength of 514.5 nm.

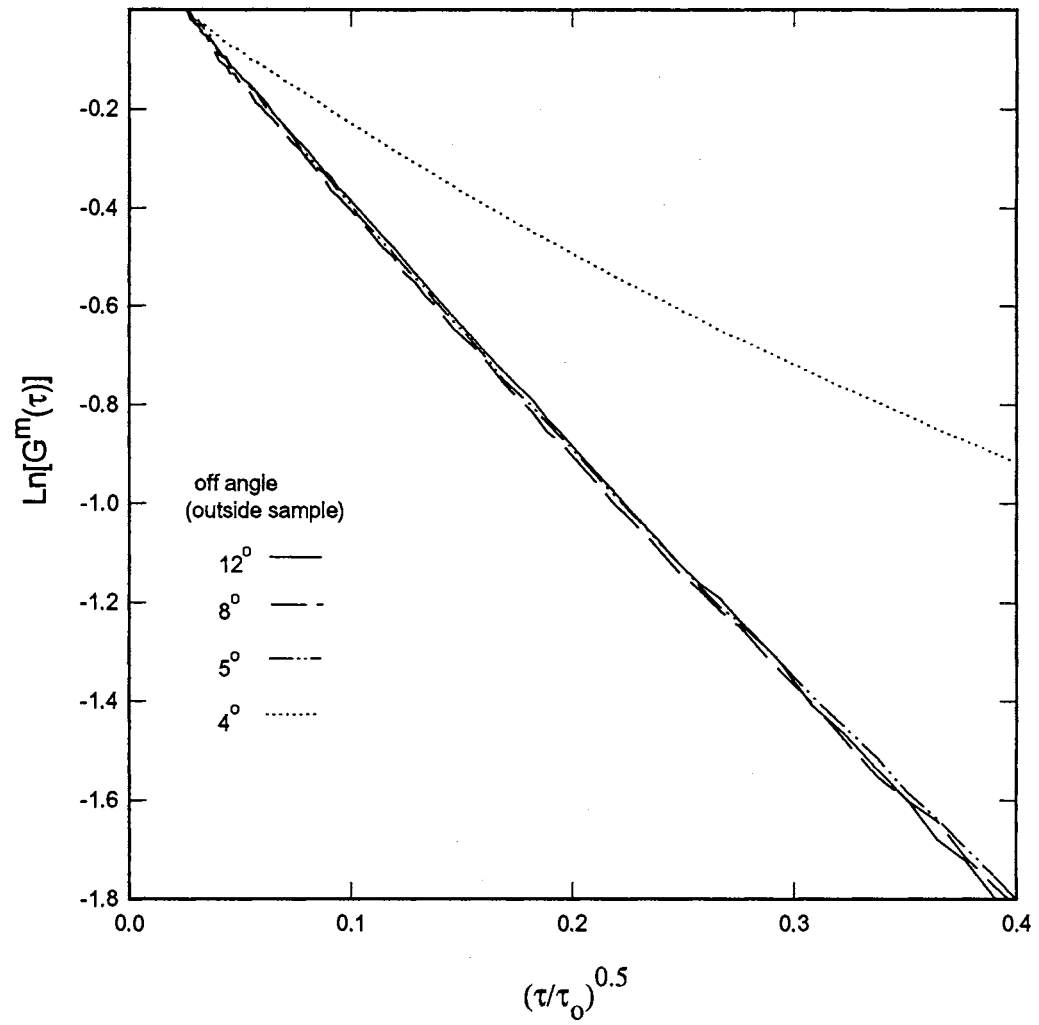


Fig. 10: Back-scattering: Effect of glass back reflection on correlation measurement for optical thickness of 100, particle diameter of 0.3 μm, and laser wavelength of 514.5 nm.

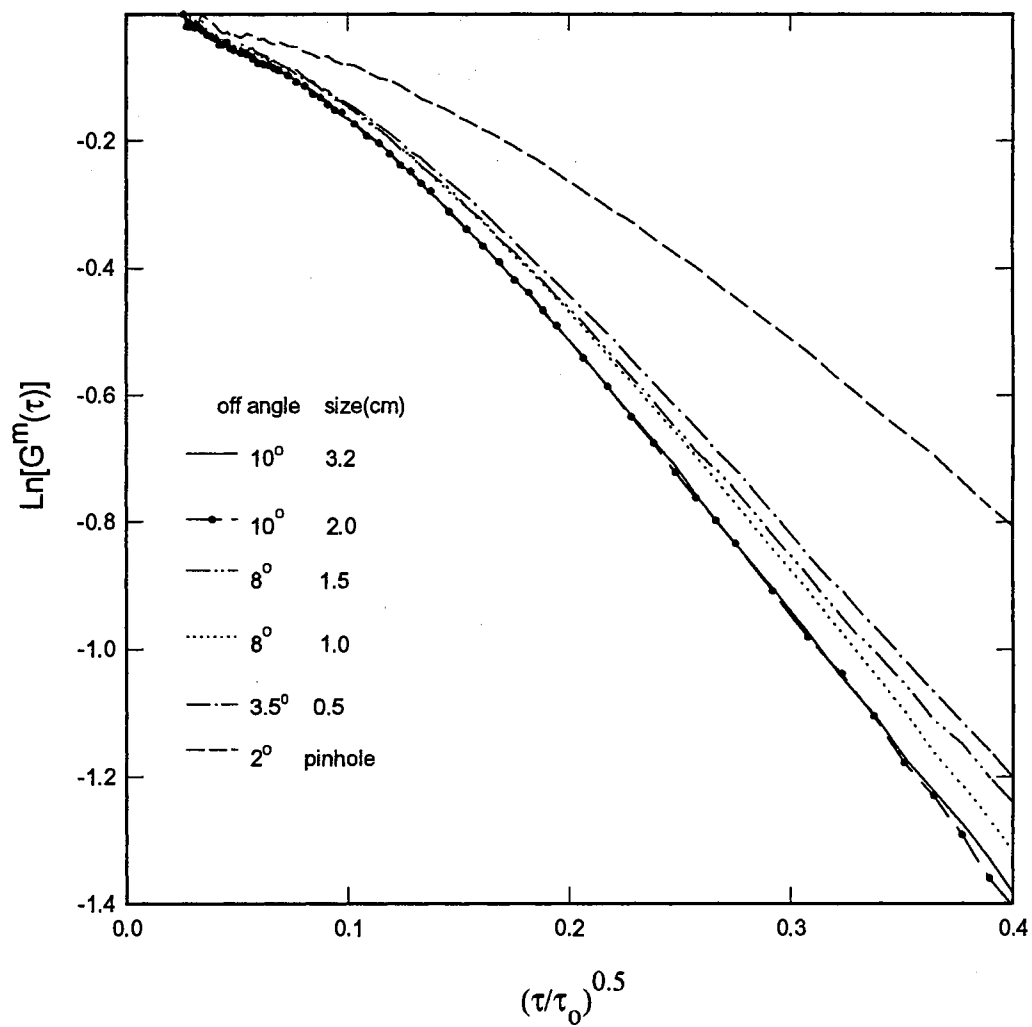


Fig. 11: Back-scattering: Effect of the laser beam diameter on correlation measurements for optical thickness of 10, particle diameter of 0.3 μm , and laser wavelength of 514.5 nm.

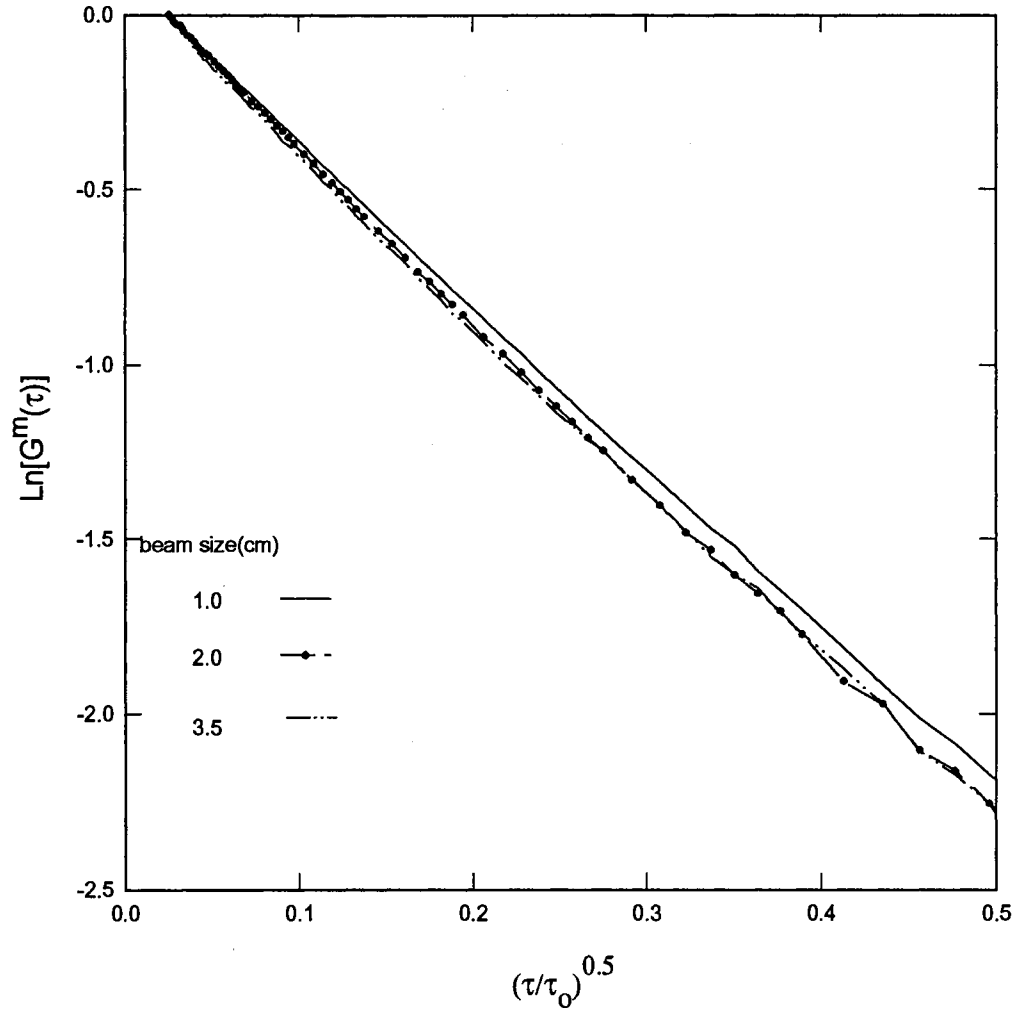


Fig. 12: Back-scattering: Effect of the laser beam diameter on correlation measurements for optical thickness of 100, particle diameter of $0.3 \mu\text{m}$, and laser wavelength of 514.5 nm .

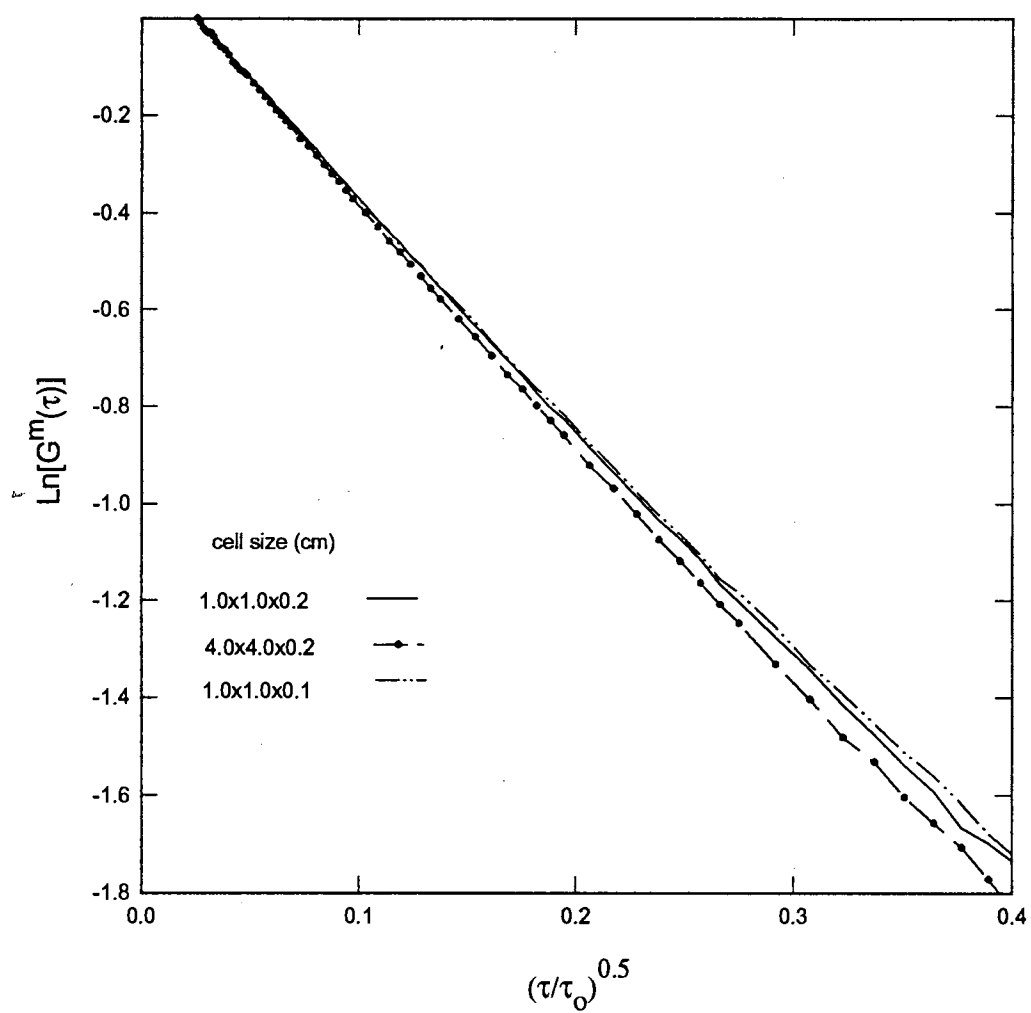


Fig. 13: Back-scattering: Effect of cell size on correlation measurements for optical thickness of 100, particle diameter of $0.3 \mu\text{m}$, and laser wavelength of 514.5 nm .

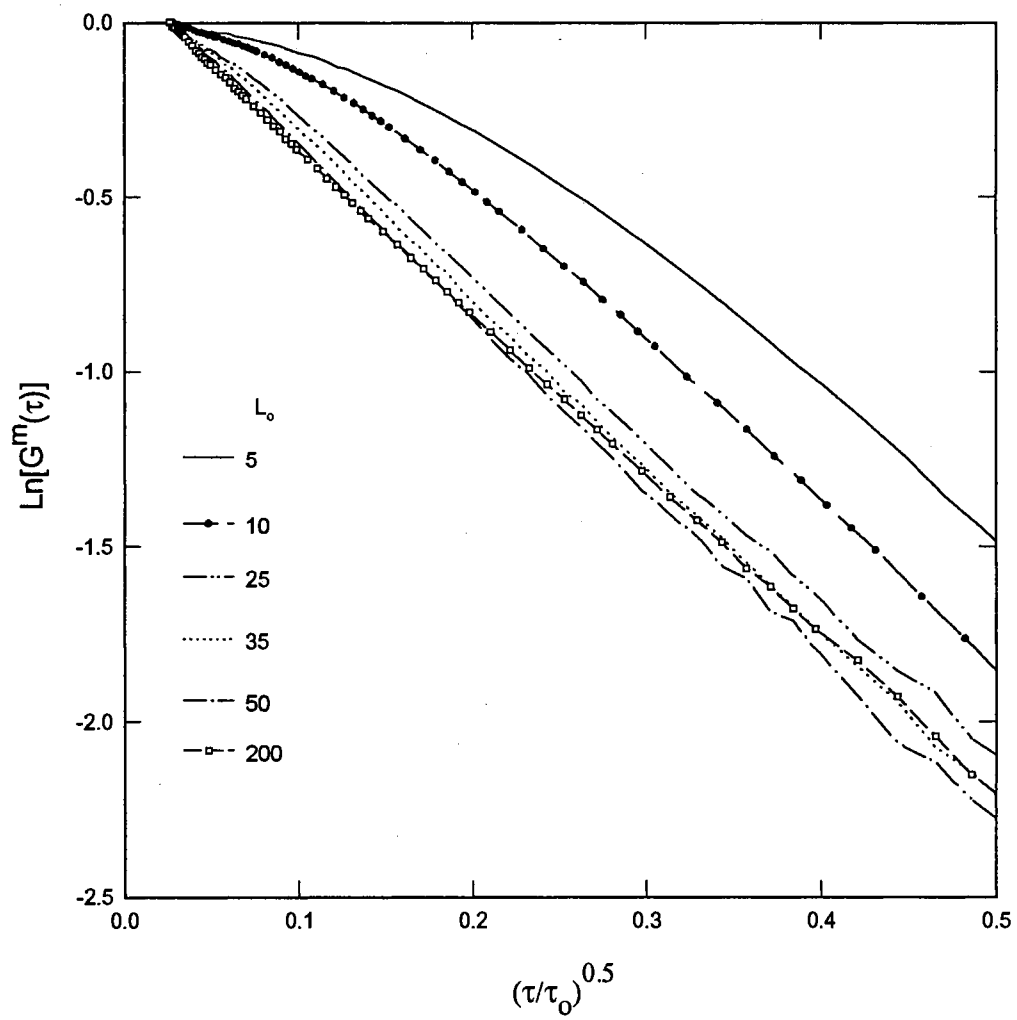


Fig. 14: Back-scattering: Effect of optical thickness on correlation measurements for particle diameter of 0.3 μm and laser wavelength of 514.5 nm.

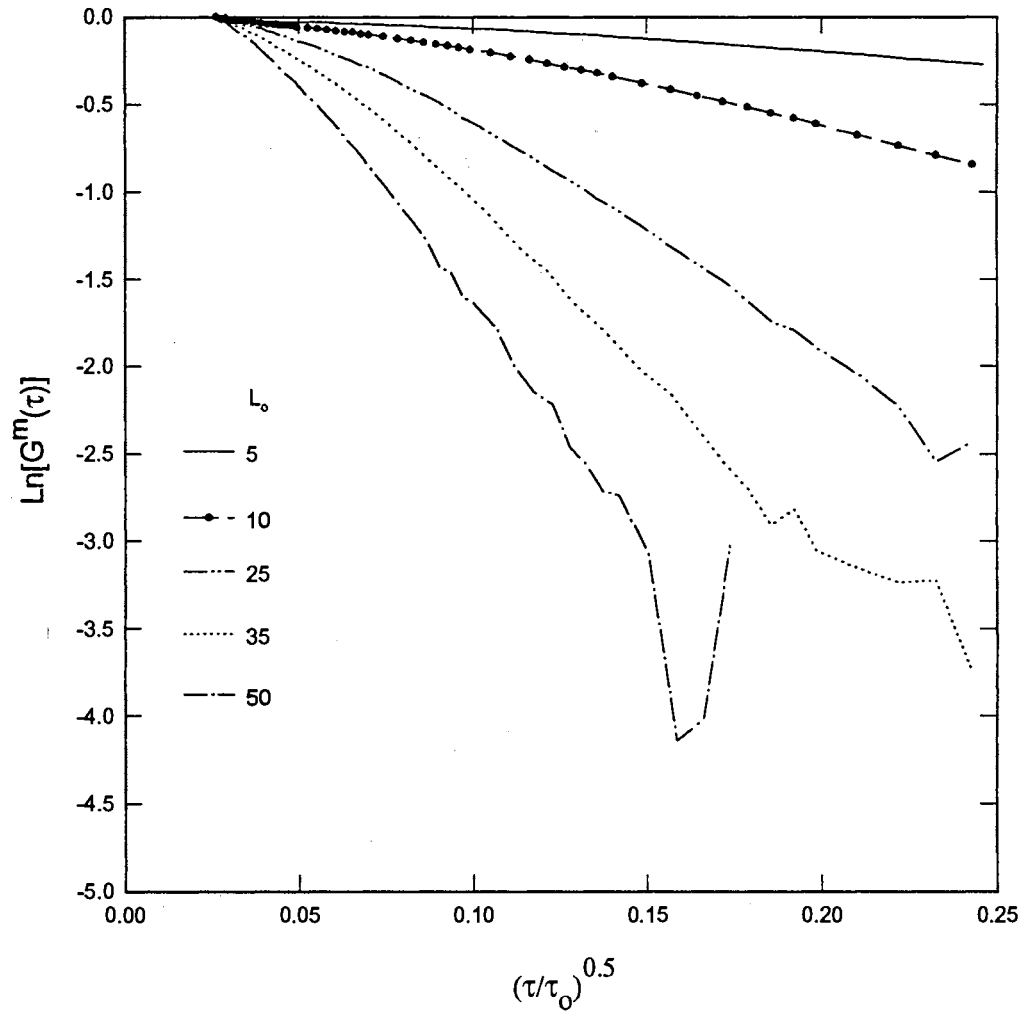


Fig. 15: Transmission: Effect of optical thickness on correlation measurements for particle diameter of 0.3 μm and laser wavelength of 514.5 nm.

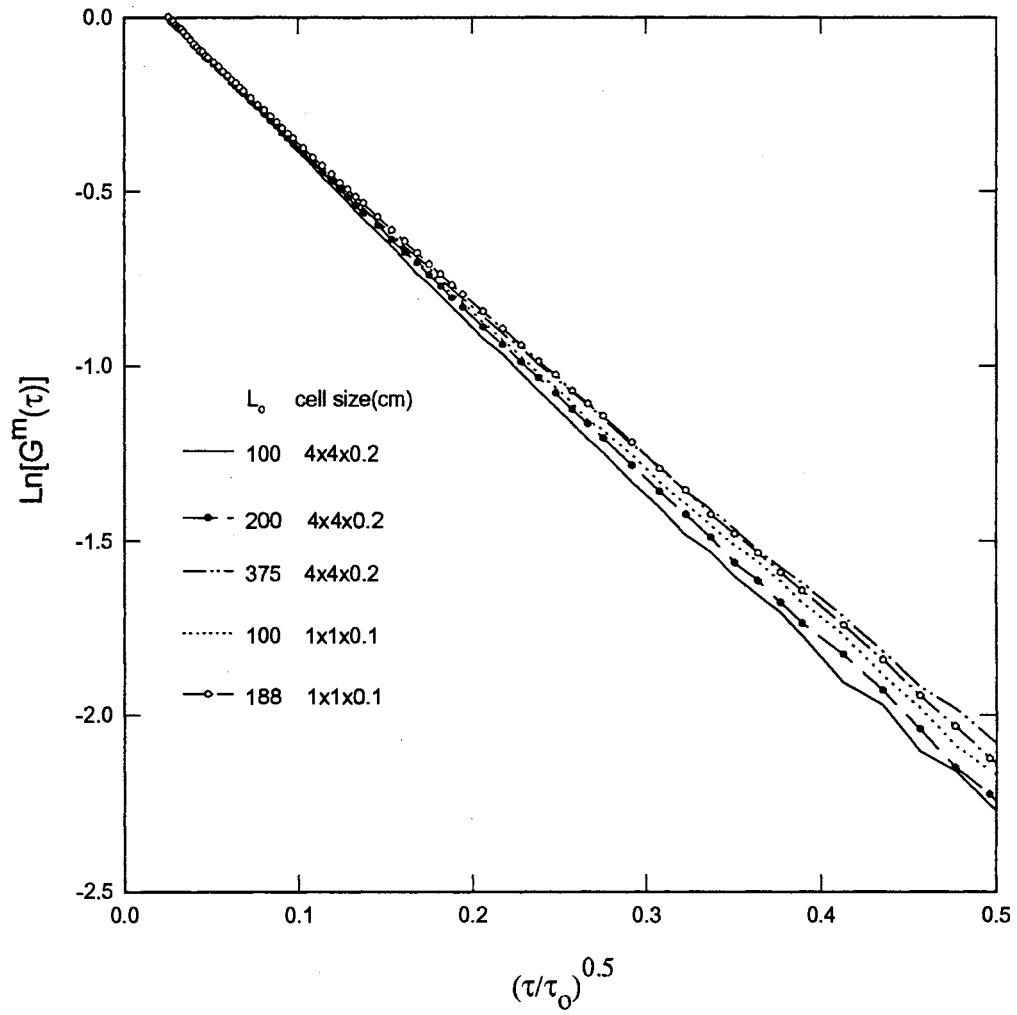


Fig. 16: Back-scattering: Effect of high optical thickness on correlation measurements for particle diameter of 0.3 μm and laser wavelength of 514.5 nm.

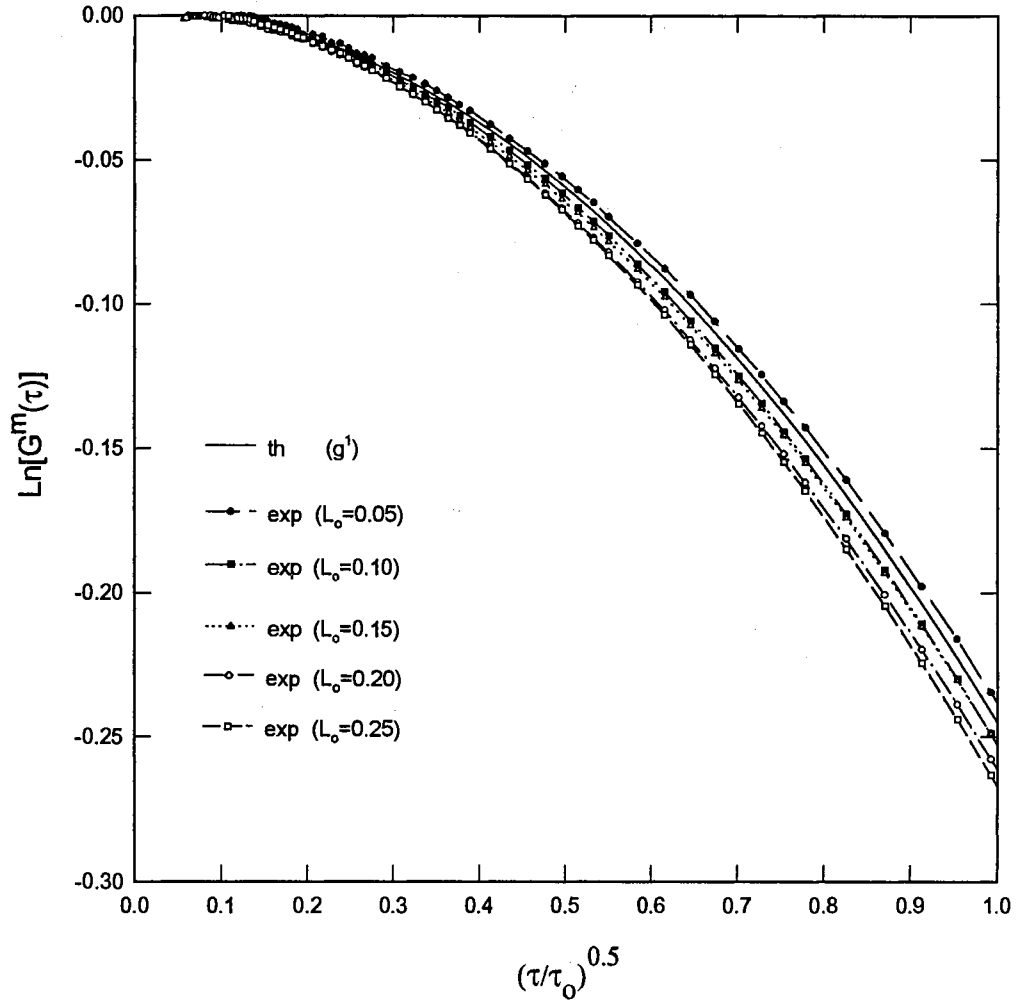


Fig. 17: Transmission: Comparison of experimental data with theoretical single scattering g^1 for optical thicknesses of 0.05 to 0.25, particle diameter of $0.3 \mu\text{m}$, laser wavelength of 514.5 nm , and 29° (inside sample) detection angle.

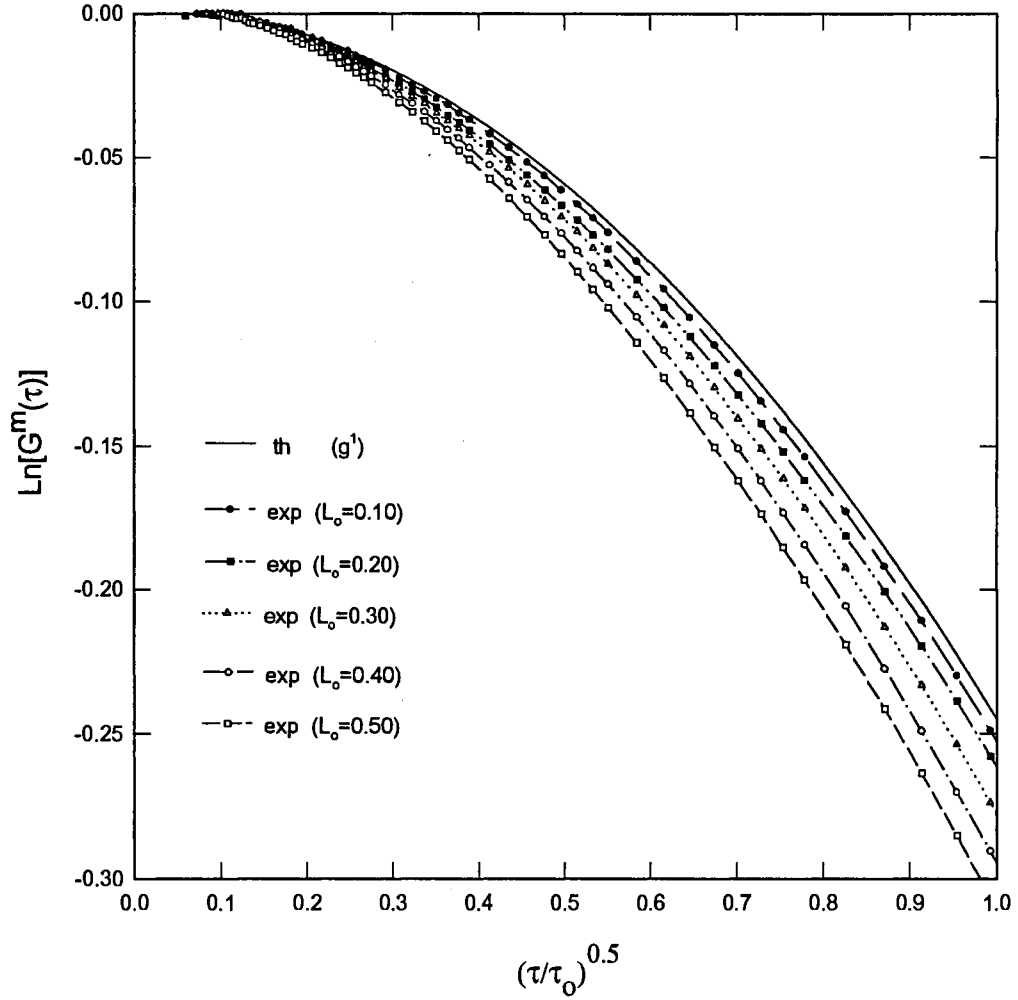


Fig. 18: Transmission: Comparison of experimental data with theoretical single scattering g^1 for optical thicknesses of 0.1 to 0.5, particle diameter of $0.3 \mu\text{m}$, laser wavelength of 514.5 nm , and 29° (inside sample) detection angle.

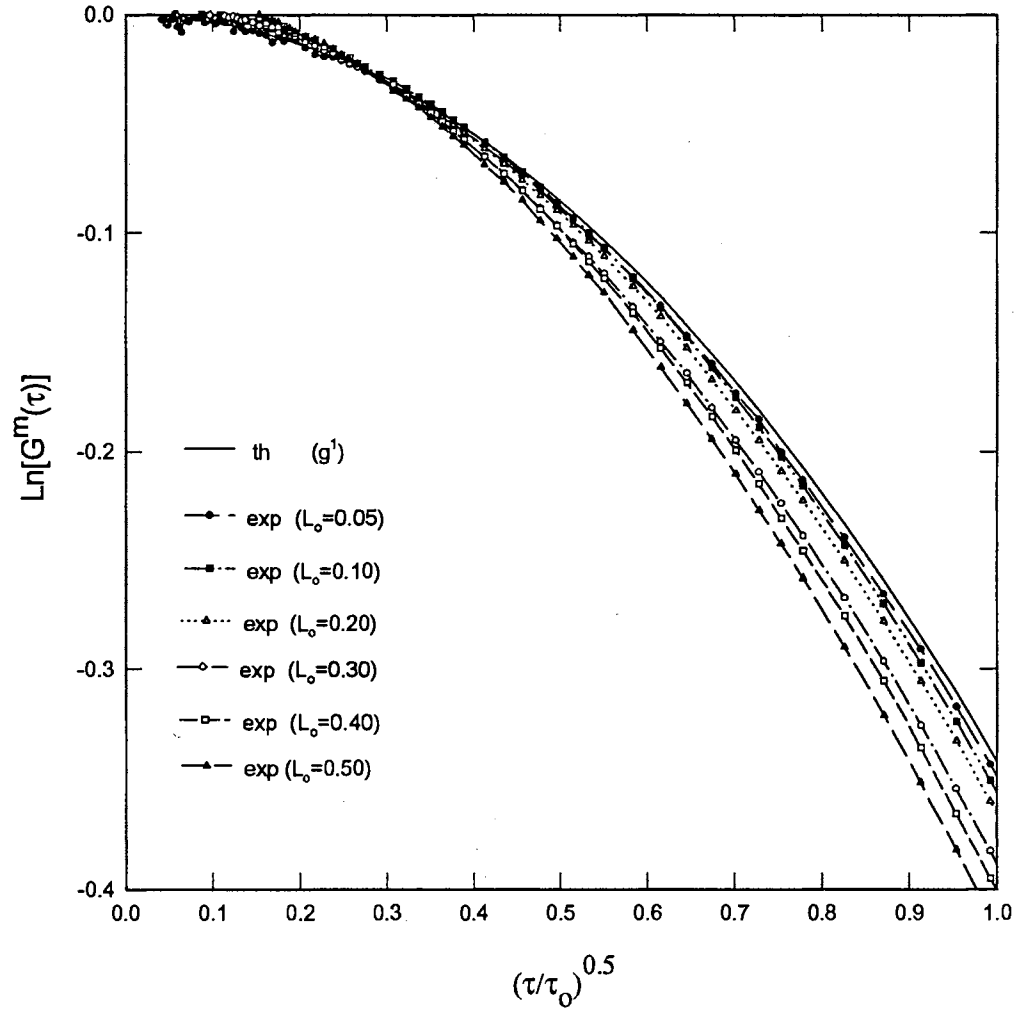


Fig. 19: Transmission: Comparison of experimental data with theoretical single scattering g^1 for optical thicknesses of 0.05 to 0.50, particle diameter of 0.3 μm , laser wavelength of 514.5 nm, and 34° (inside sample) detection angle.

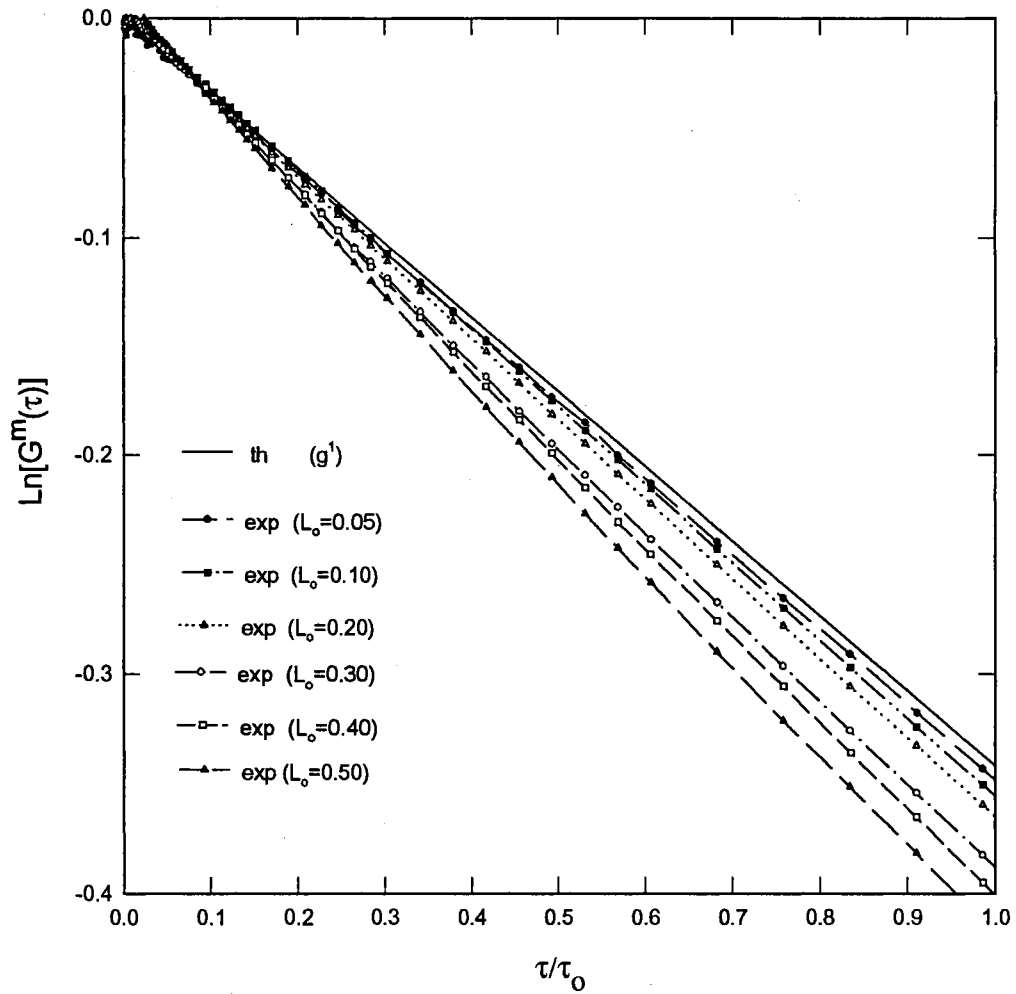


Fig. 20: Transmission: Comparison of experimental data with theoretical single scattering g^1 for optical thicknesses of 0.05 to 0.50, particle diameter of $0.3 \mu\text{m}$, laser wavelength of 514.5 nm , and 34° (inside sample) detection angle.

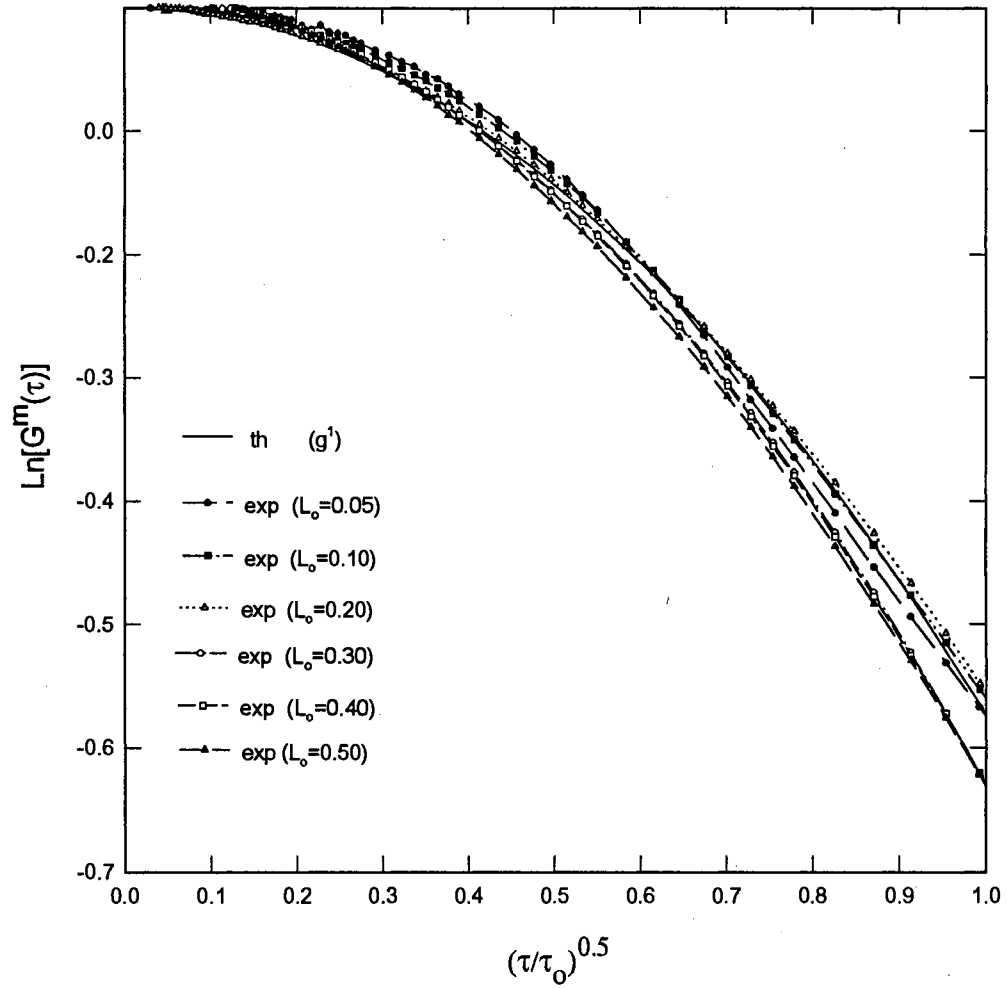


Fig. 21: Transmission: Comparison of experimental data with theoretical single scattering g^1 for optical thicknesses of 0.05 to 0.50, particle diameter of $0.3 \mu\text{m}$, laser wavelength of 514.5 nm , and 45° (inside sample) detection angle.

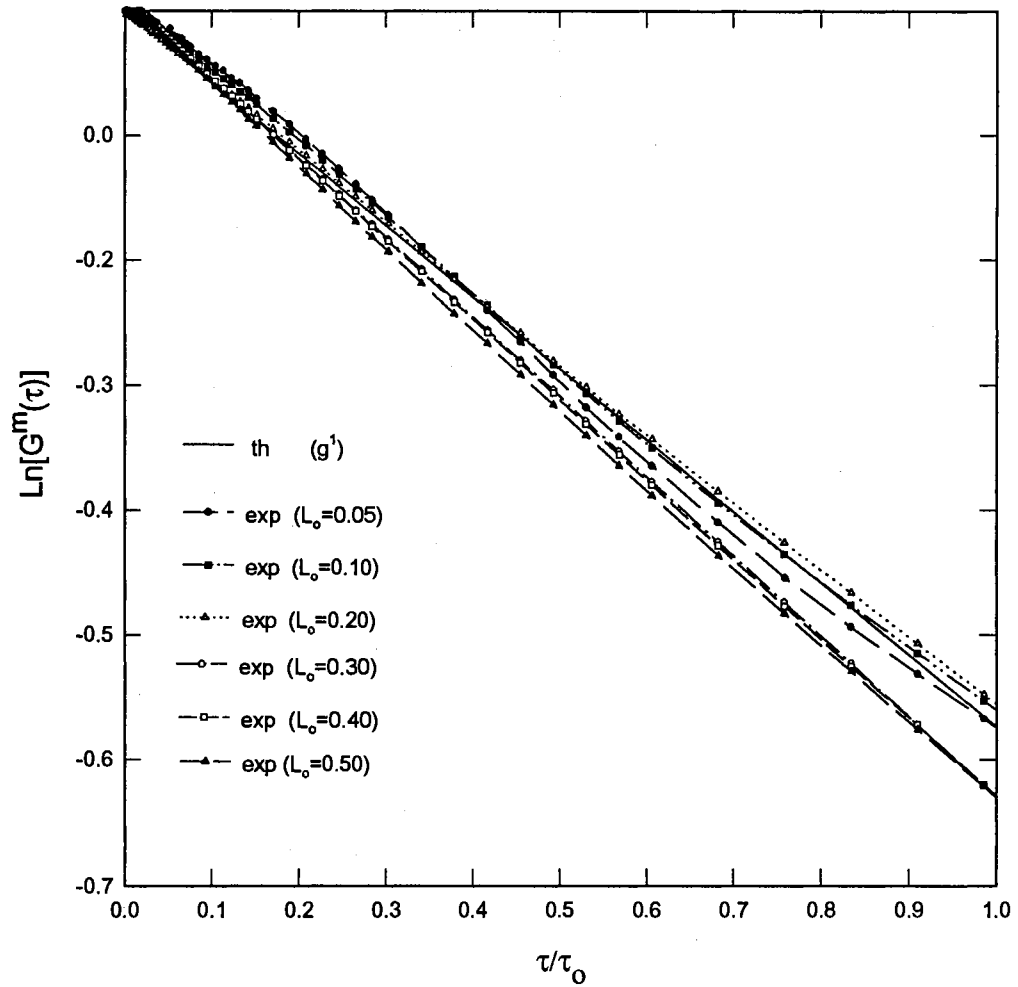


Fig. 22: Transmission: Comparison of experimental data with theoretical single scattering g^1 for optical thicknesses of 0.05 to 0.50, particle diameter of $0.3 \mu\text{m}$, laser wavelength of 514.5 nm , and 45° (inside sample) detection angle.

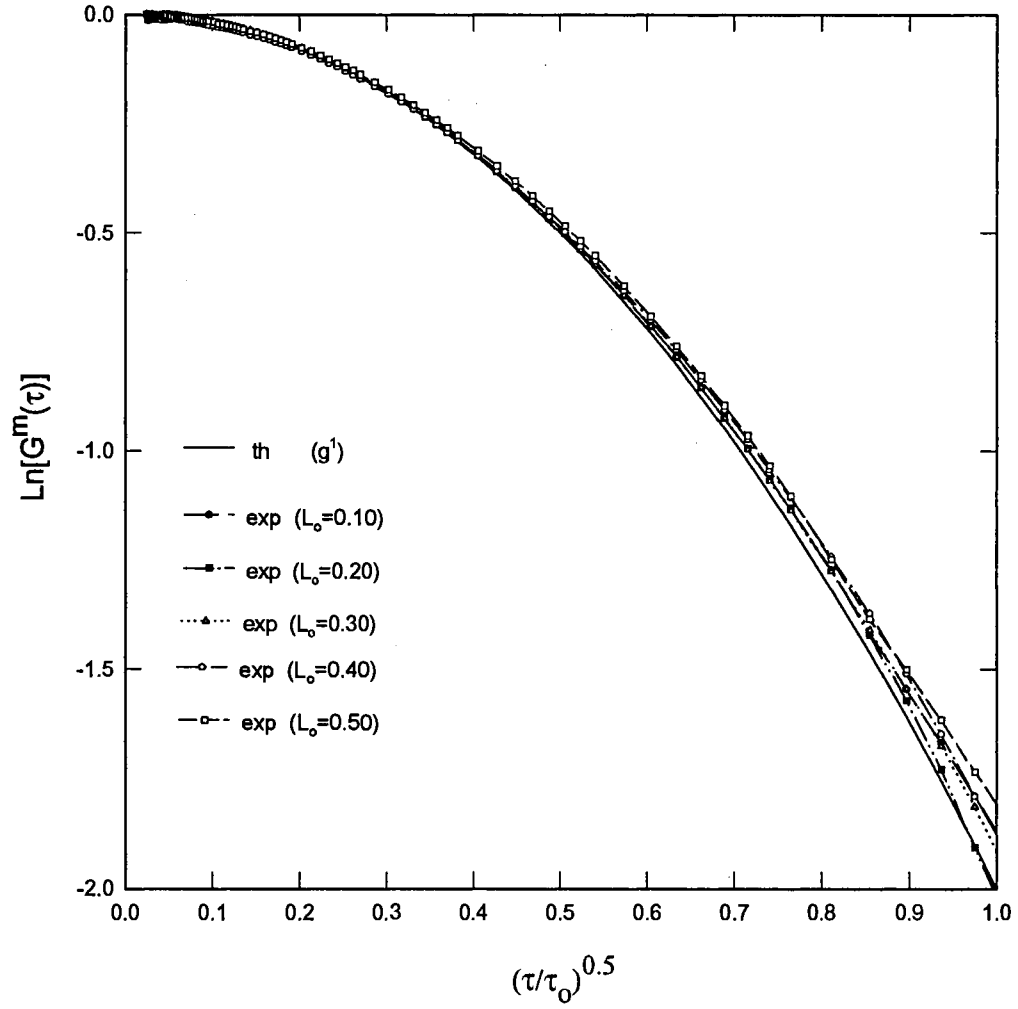


Fig. 23: Comparison of experimental data with theoretical single scattering g^1 for optical thicknesses of 0.10 to 0.50 using ALV5000 setup, particle diameter of $0.3 \mu\text{m}$, laser wavelength of 514.5 nm , and 90° (outside sample) detection angle.

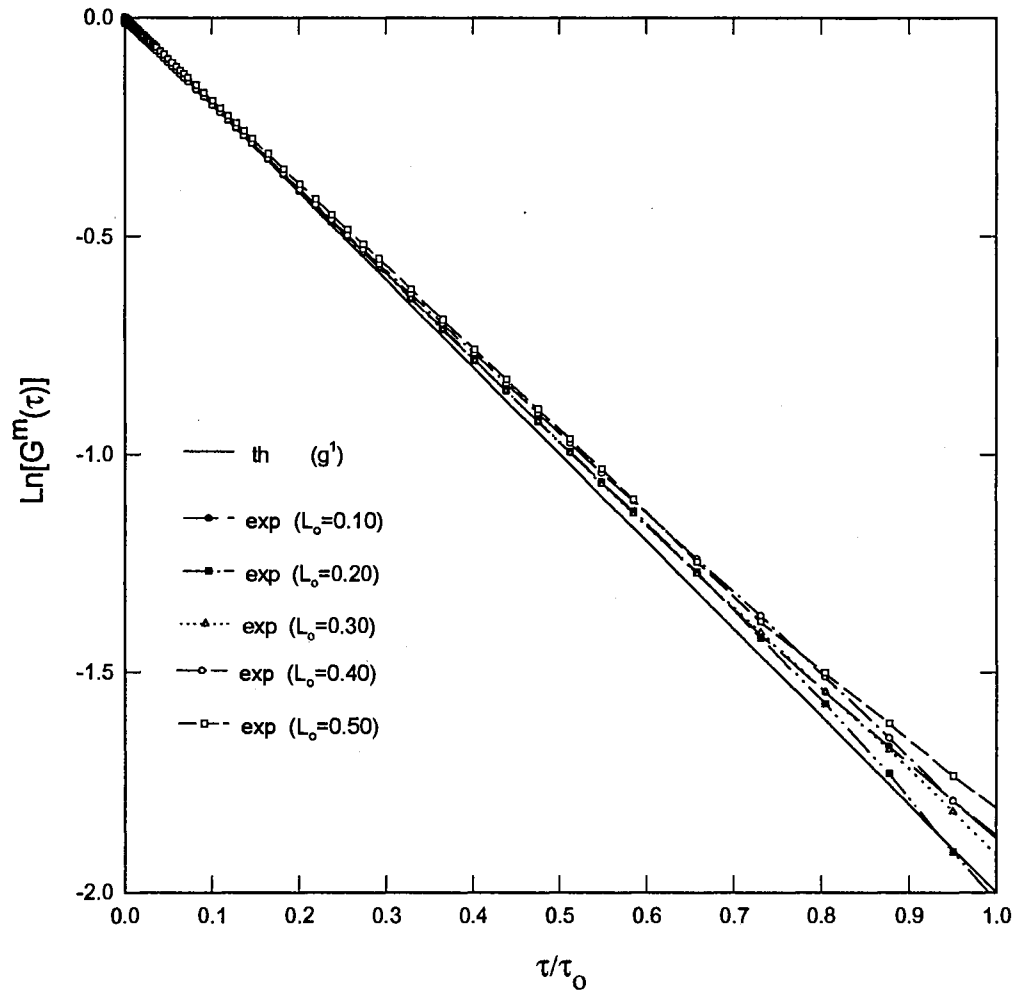


Fig. 24: Comparison of experimental data with theoretical single scattering g^1 for optical thicknesses of 0.10 to 0.50 using ALV5000 setup, particle diameter of $0.3 \mu\text{m}$, laser wavelength of 514.5 nm , and 90° (outside sample) detection angle.

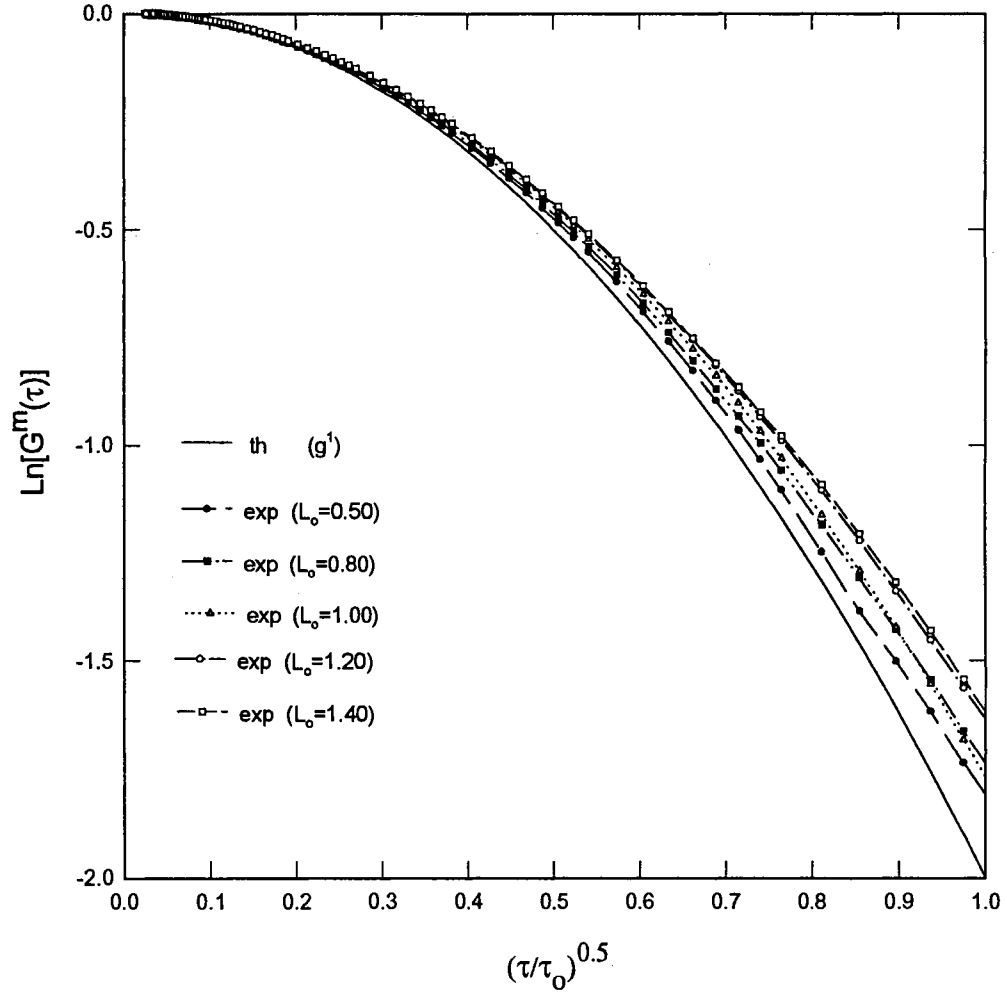


Fig. 25: Comparison of experimental data with theoretical single scattering for optical thicknesses of 0.50 to 1.40 using ALV5000 setup, particle diameter of 0.3 μm , laser wavelength of 514.5 nm, and 90° (outside sample) detection angle.

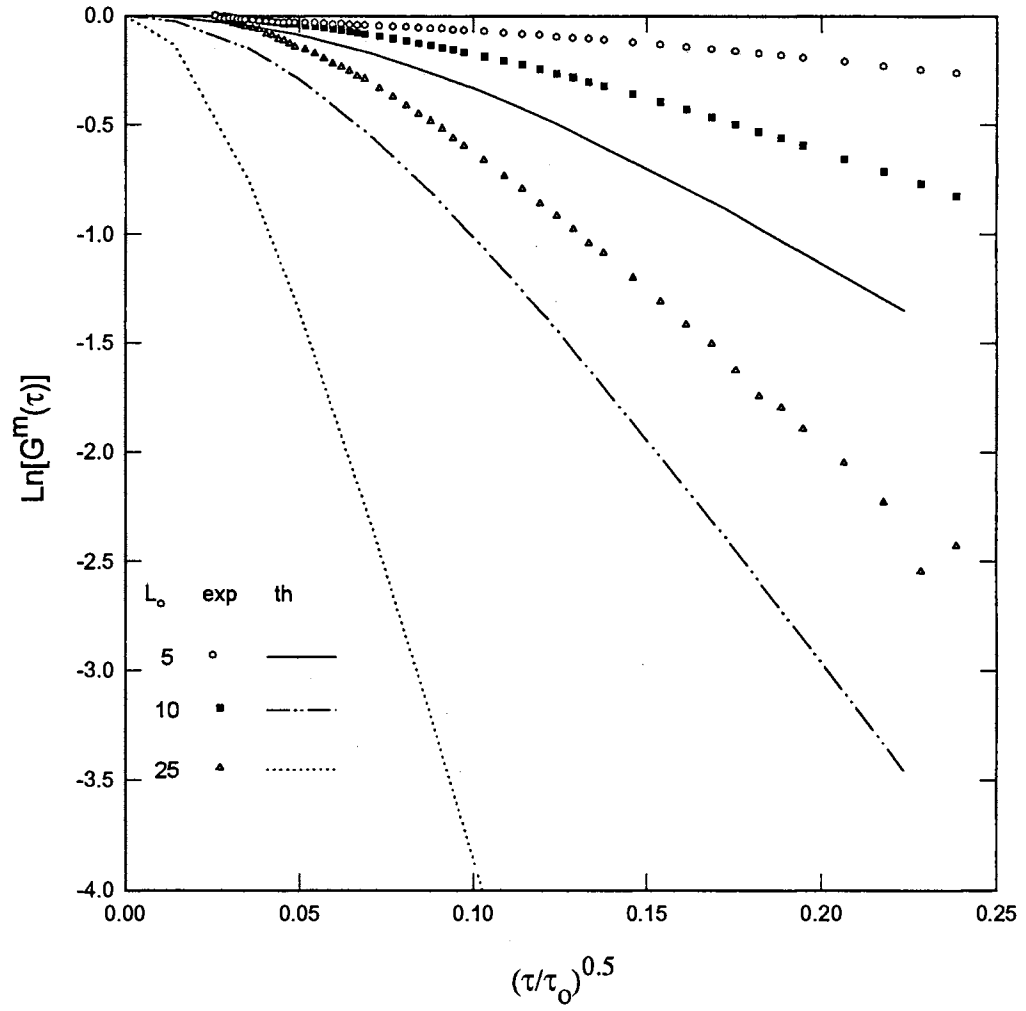


Fig. 26: Transmission: Comparison of experimental data with isotropic preaveraged theory ($f=0$, $n=1.0$) for different optical thicknesses, particle diameter of $0.3 \mu\text{m}$ and laser wavelength of 514.5 nm .

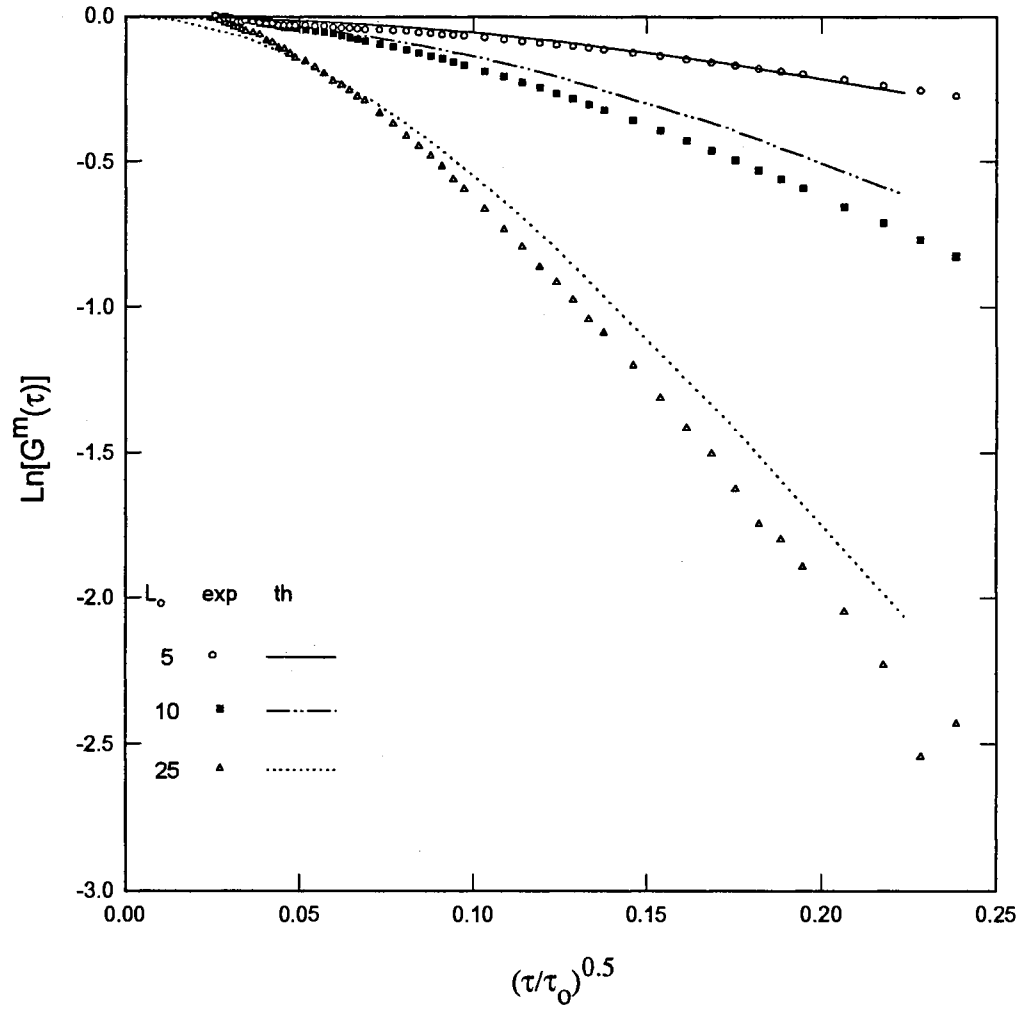


Fig. 27: Transmission: Comparison of experimental data with anisotropic preaveraged theory ($f=0.727$, $n=1.0$) for different optical thicknesses, particle diameter of $0.3 \mu\text{m}$ and laser wavelength of 514.5 nm .

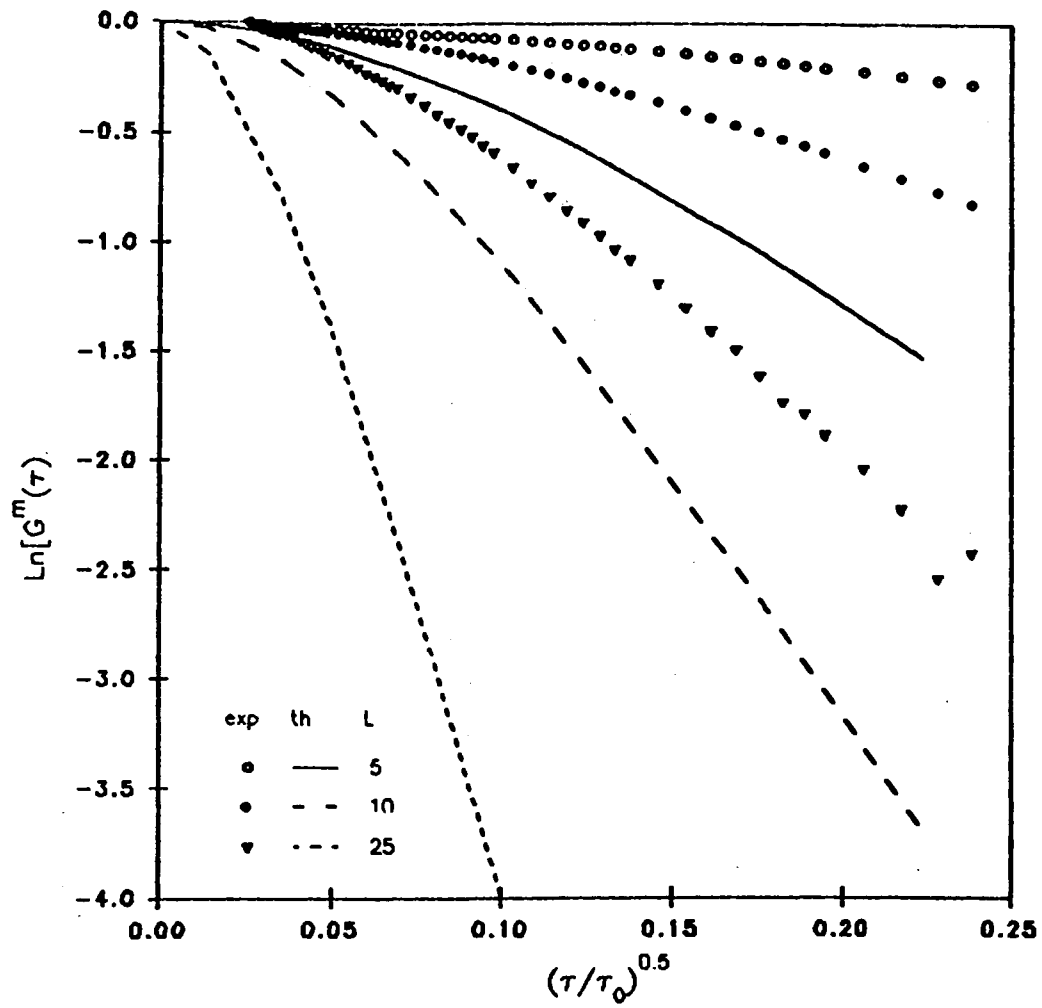


Fig. 28: Transmission: Comparison of experimental data with isotropic preaveraged theory ($f=0$, $n=1.331$) for different optical thicknesses, particle diameter of $0.3 \mu\text{m}$ and laser wavelength of 514.5 nm .

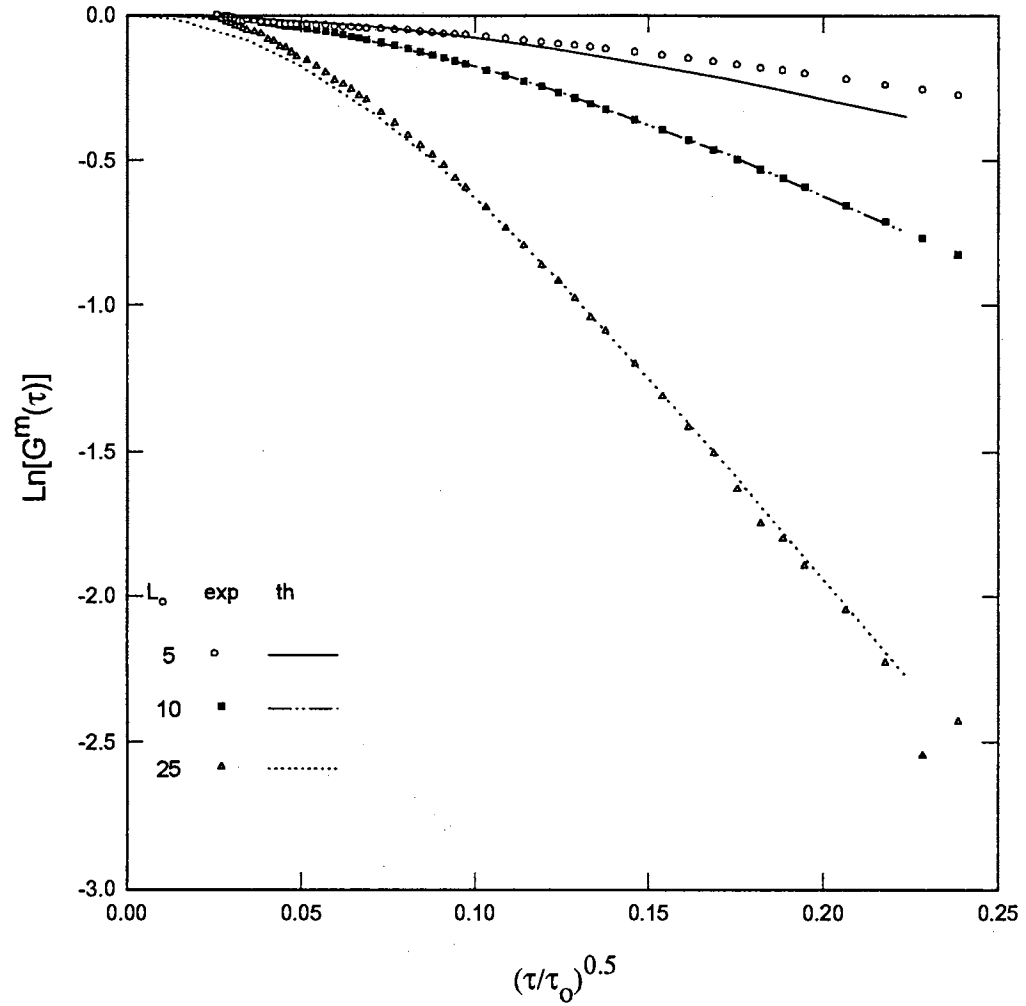


Fig. 29: Transmission: Comparison of experimental data with anisotropic preaveraged theory ($f=0.727$, $n=1.331$) for different optical thicknesses, particle diameter of $0.3 \mu\text{m}$ and laser wavelength of 514.5 nm .

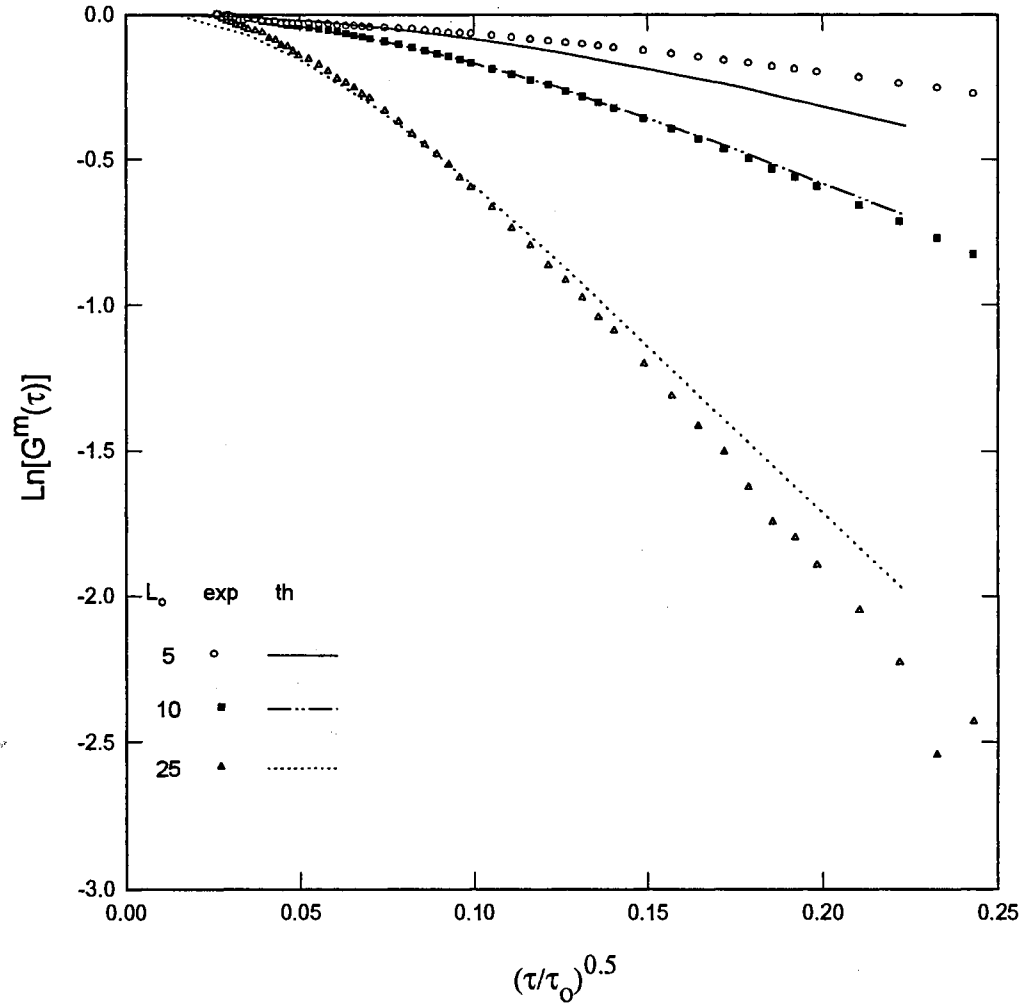


Fig. 30: Transmission: Comparison of experimental data with the anisotropic one term Legendre expansion of g^1 ($f=0.727$, $n=1.331$) for different optical thicknesses, particle diameter of $0.3 \mu\text{m}$ and laser wavelength of 514.5 nm .

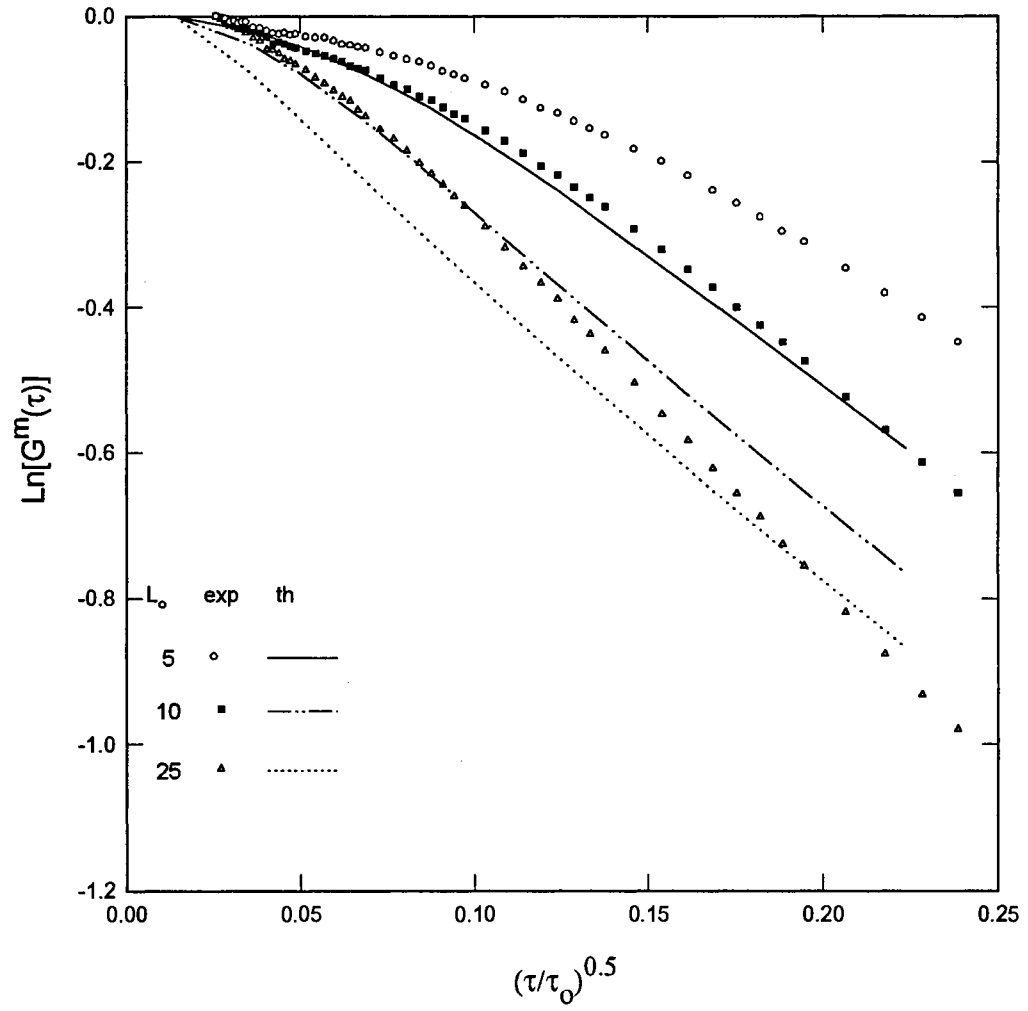


Fig. 31: Back-scattering: Comparison of experimental data with isotropic preaveraged theory ($f=0$, $n=1.0$) for different optical thicknesses, particle diameter of $0.3 \mu\text{m}$ and laser wavelength of 514.5 nm .

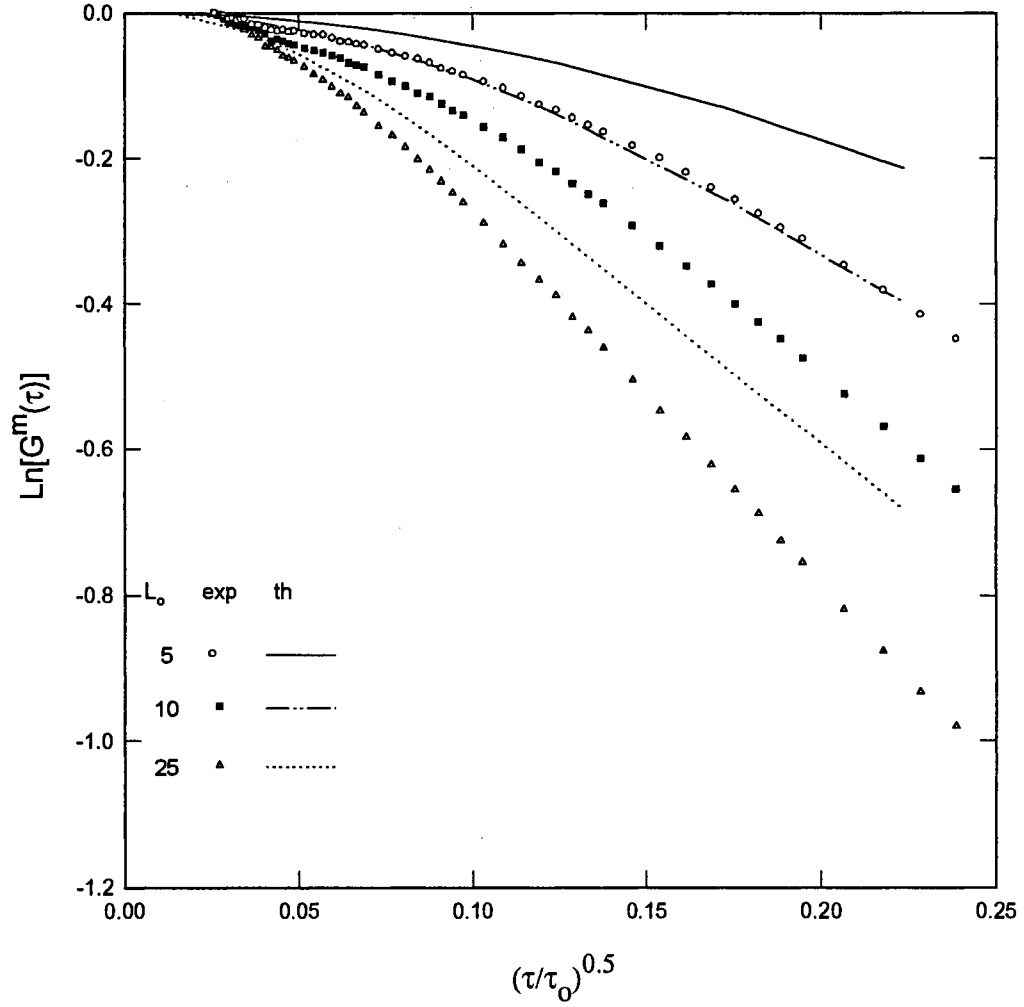


Fig. 32: Back-scattering: Comparison of experimental data with anisotropic preaveraged theory ($f=0.727$, $n=1.0$) for different optical thicknesses, particle diameter of $0.3 \mu\text{m}$ and laser wavelength of 514.5 nm .

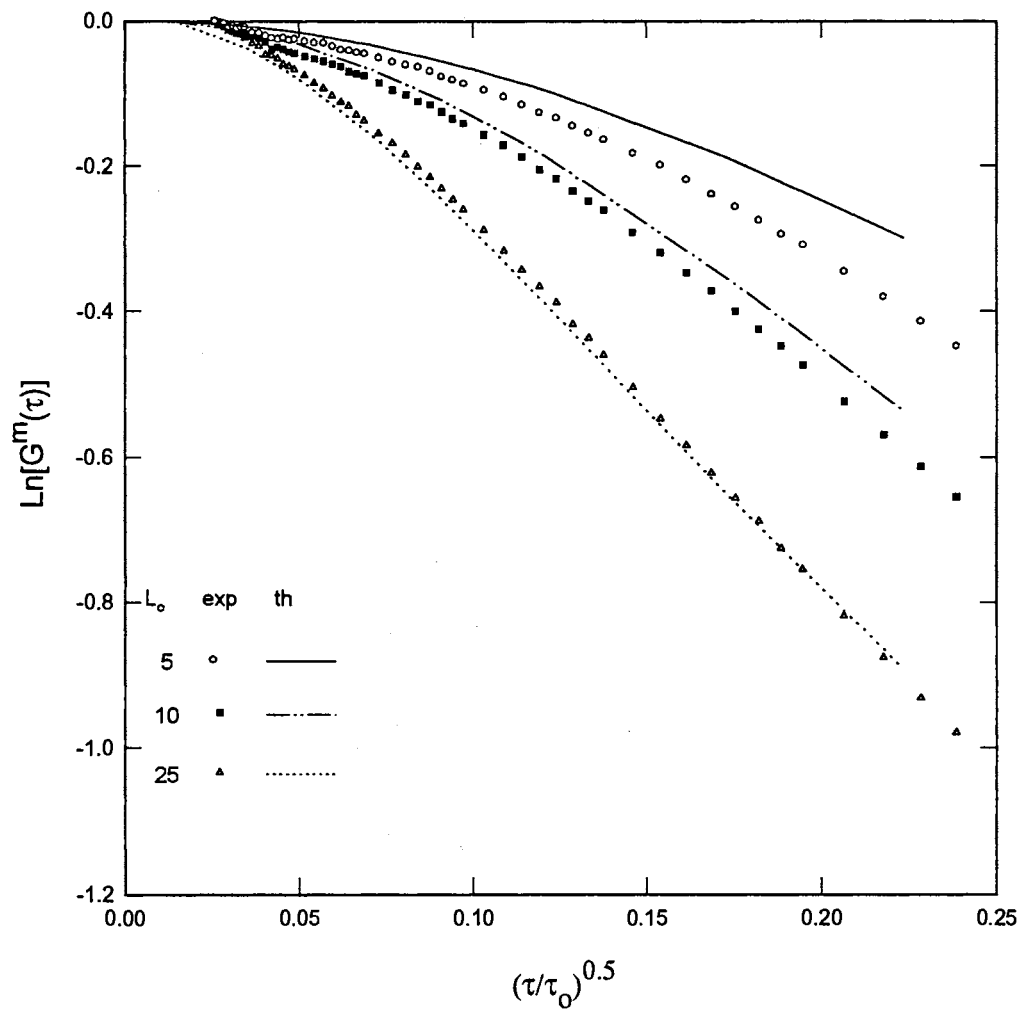


Fig. 33: Back-scattering: Comparison of experimental data with anisotropic preaveraged theory ($f=0.727$, $n=1.331$) for different optical thicknesses, particle diameter of $0.3 \mu\text{m}$ and laser wavelength of 514.5 nm .

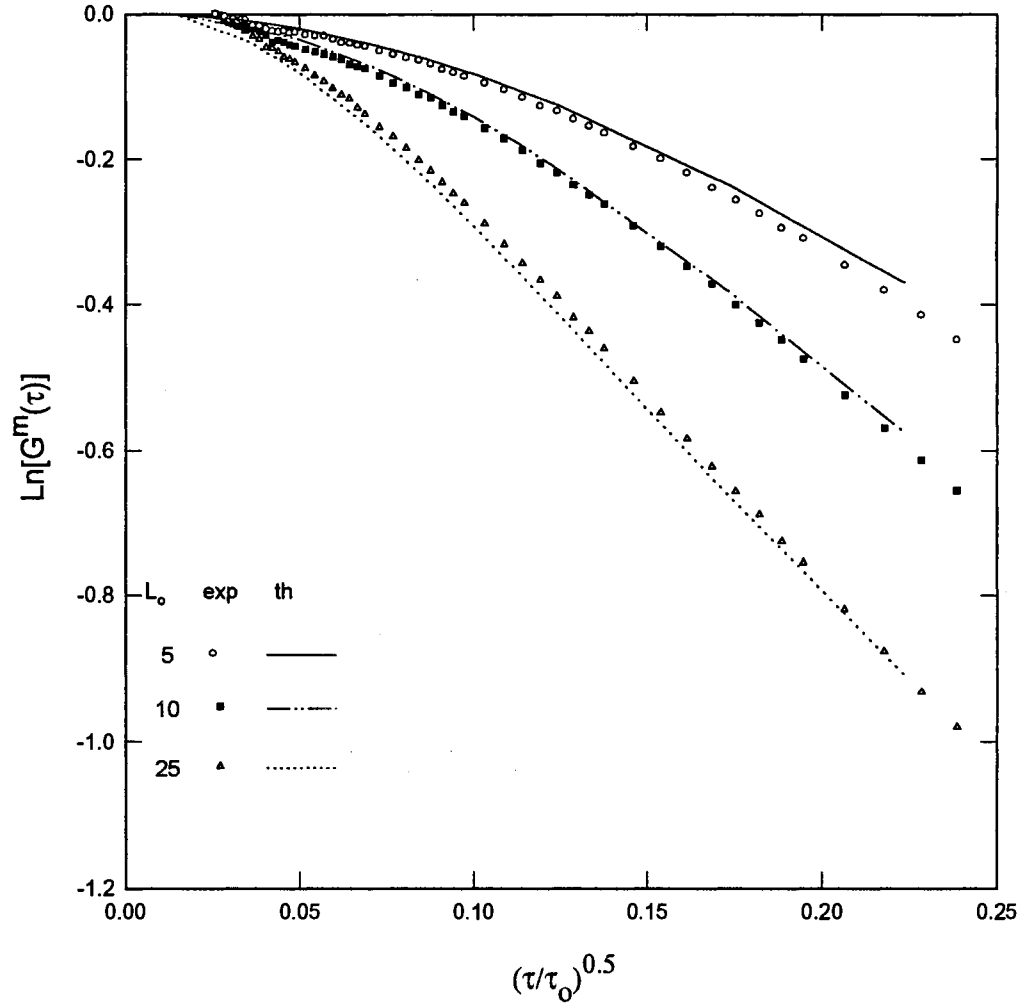


Fig. 34: Back-scattering: Comparison of experimental data with anisotropic one term Legendre expansion of g^1 ($f=0.727$, $n=1.331$) for different optical thicknesses, particle diameter of $0.3 \mu\text{m}$ and laser wavelength of 514.5 nm .

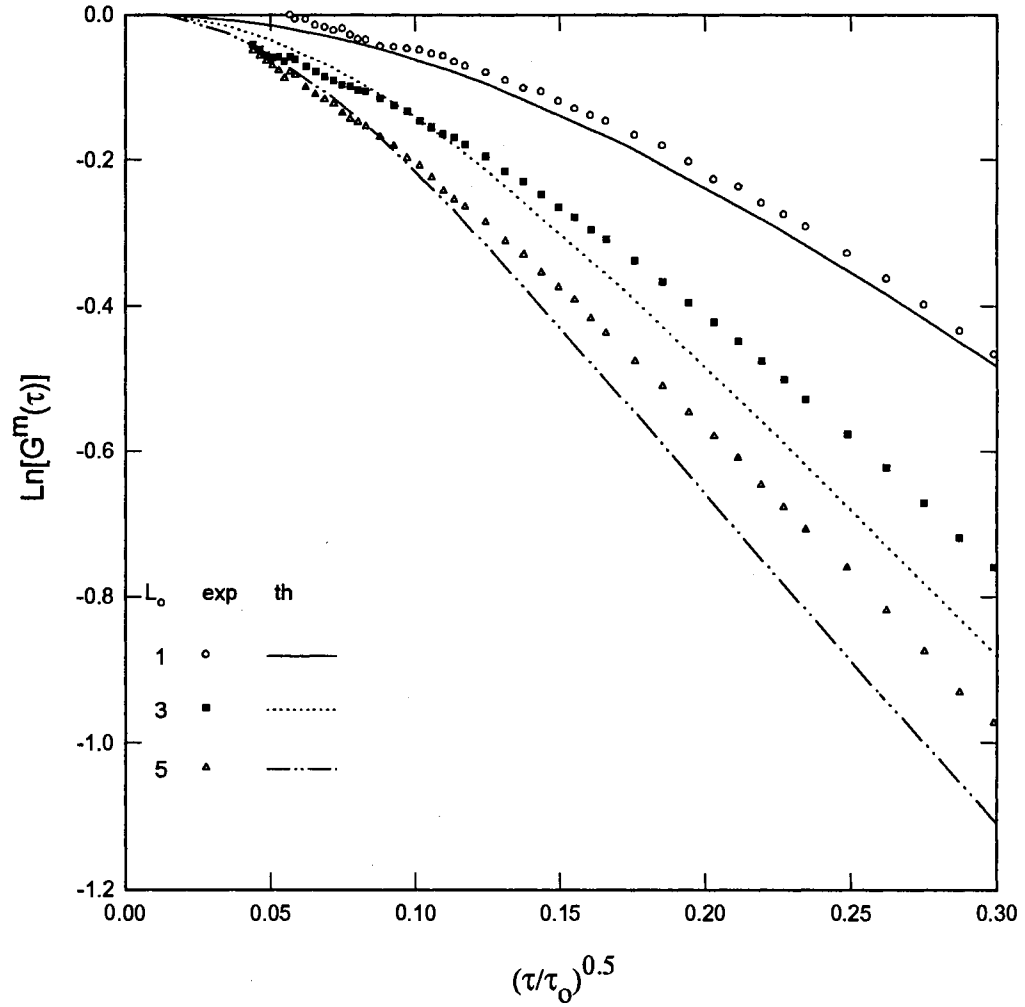


Fig. 35: Back-scattering: Comparison of experimental data with anisotropic one term Legendre expansion of g^1 theory ($f=0.089$, $n=1.331$) for different optical thicknesses, particle diameter of $0.091 \mu\text{m}$ and laser wavelength of 532 nm .

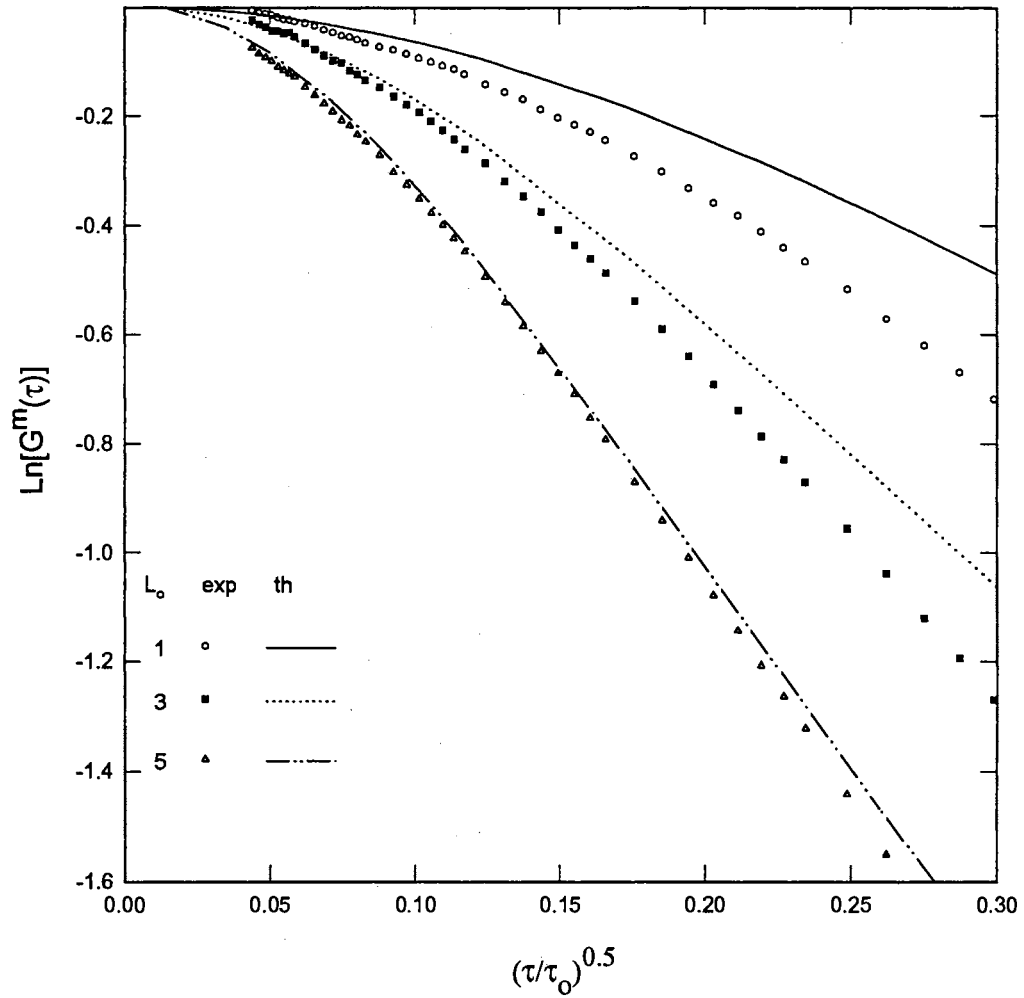


Fig. 36: Transmission: Comparison of experimental data with anisotropic one term Legendre expansion of g^1 theory ($f=0.089$, $n=1.331$) for different optical thicknesses, particle diameter of $0.091 \mu\text{m}$ and laser wavelength of 532 nm .

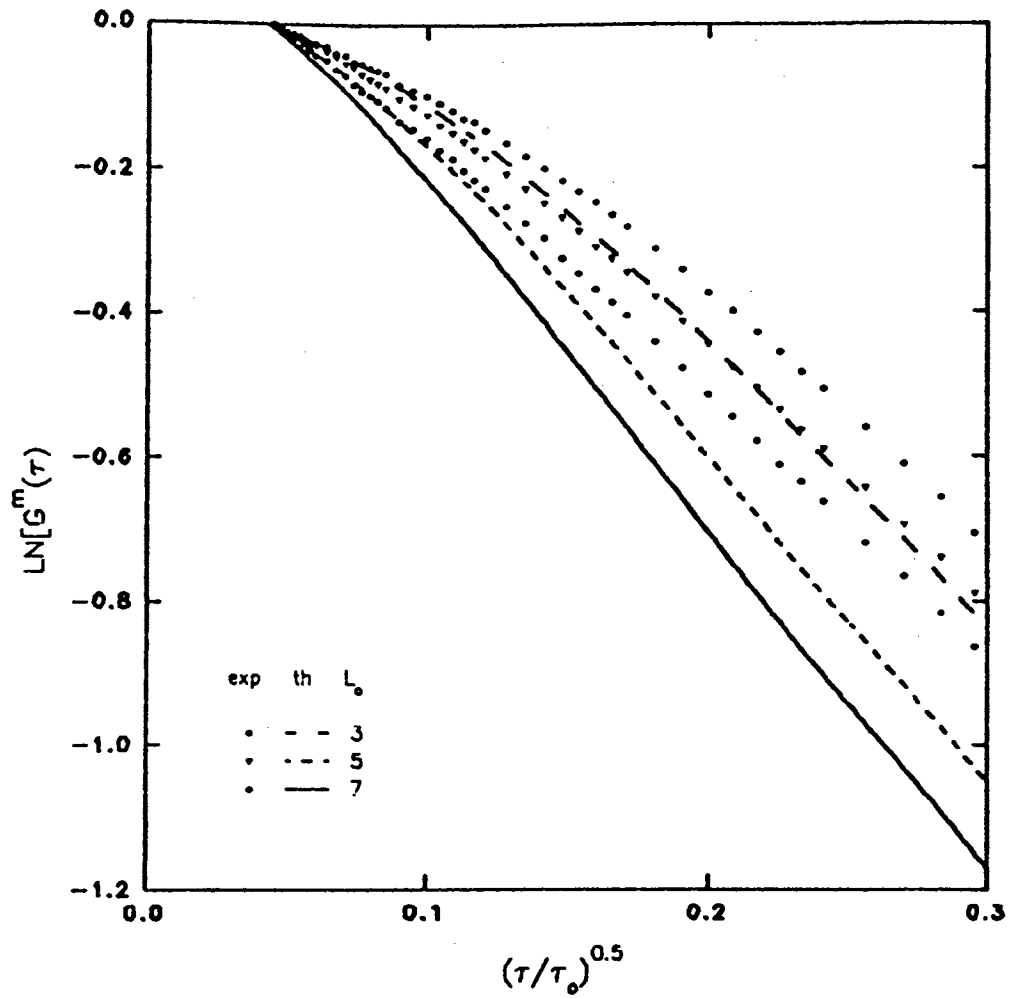


Fig. 37: Back-scattering: Comparison of experimental data with anisotropic one term Legendre expansion of g^1 theory ($f=0.132$, $n=1.331$) for different optical thicknesses, particle diameter of $0.107 \mu\text{m}$ and laser wavelength of 514.5 nm .

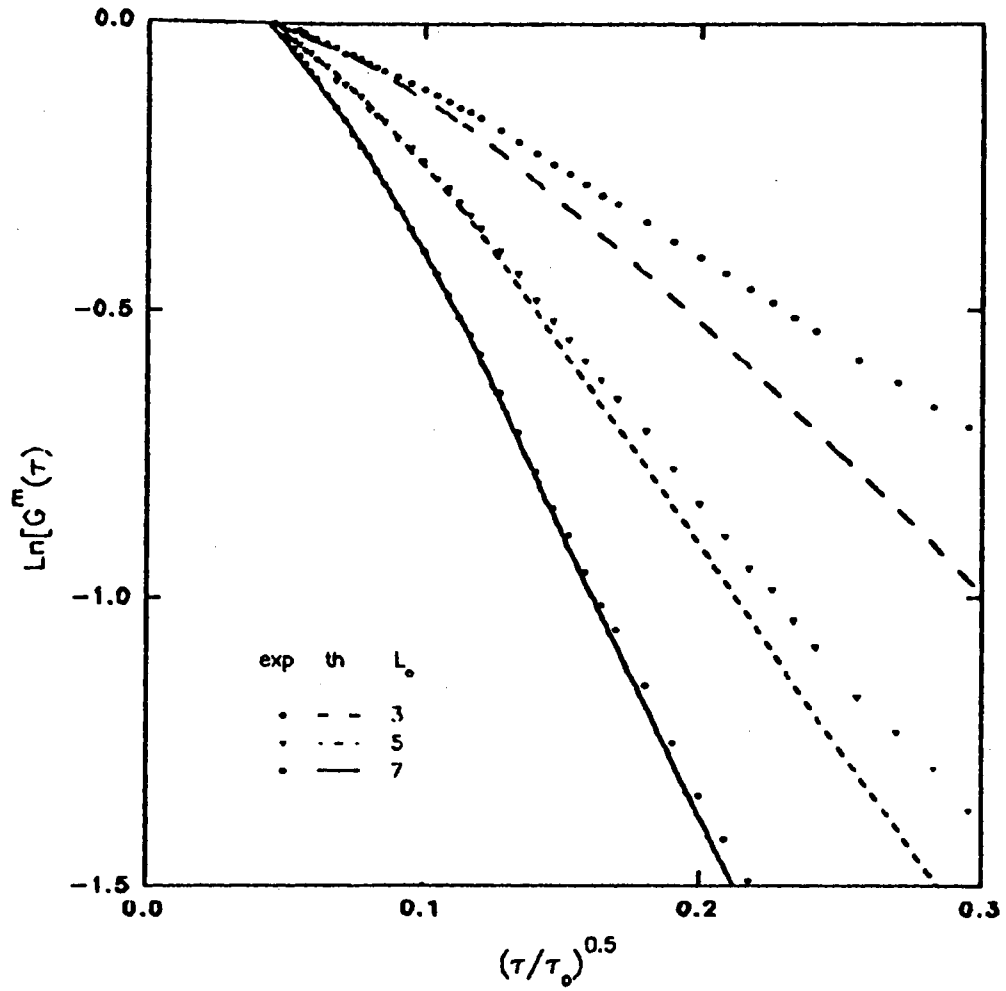


Fig. 38: Transmission: Comparison of experimental data with anisotropic one term Legendre expansion of g^1 theory ($f=0.132$, $n=1.331$) for different optical thicknesses, particle diameter of $0.107 \mu\text{m}$ and laser wavelength of 514.5 nm .

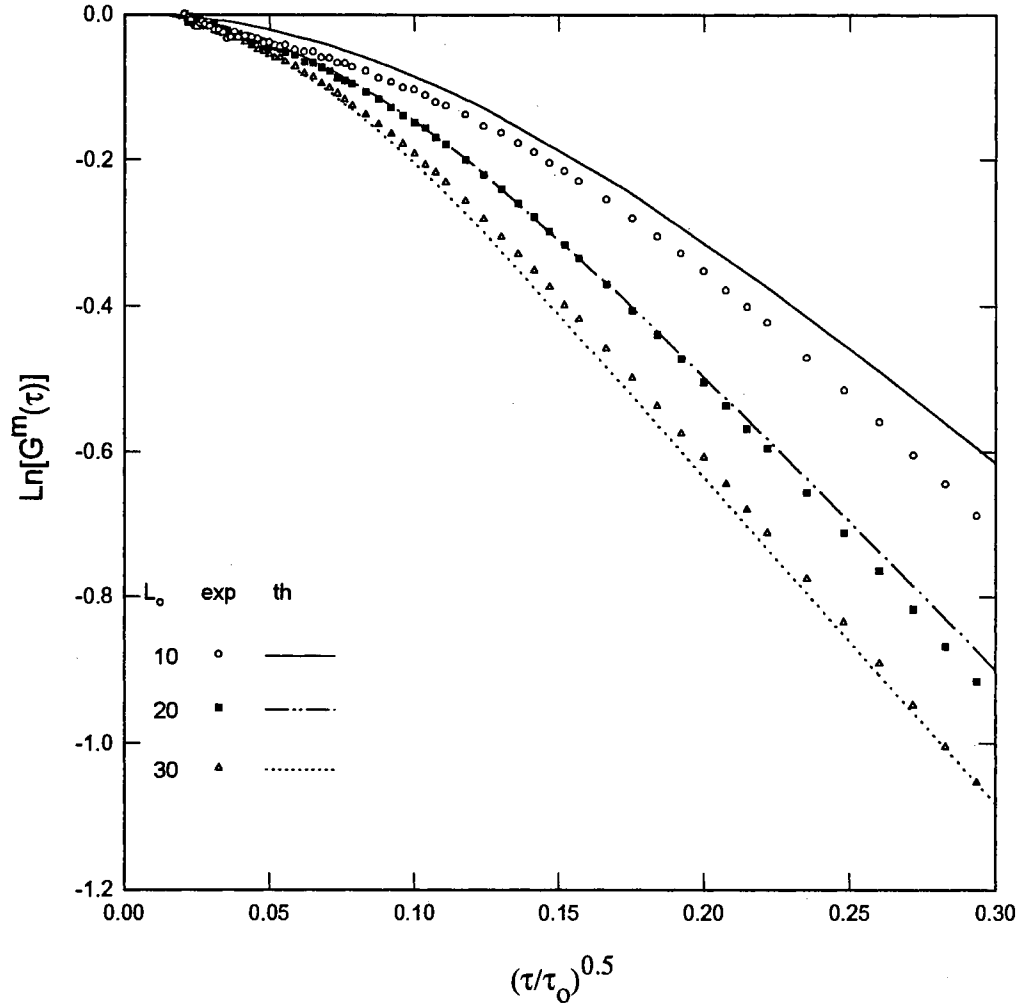


Fig. 39: Back-scattering: Comparison of experimental data with the anisotropic one term Legendre expansion of g^1 theory ($f=0.858$, $n=1.331$) for different optical thicknesses, particle diameter of $0.497 \mu\text{m}$ and laser wavelength of 514.5 nm .

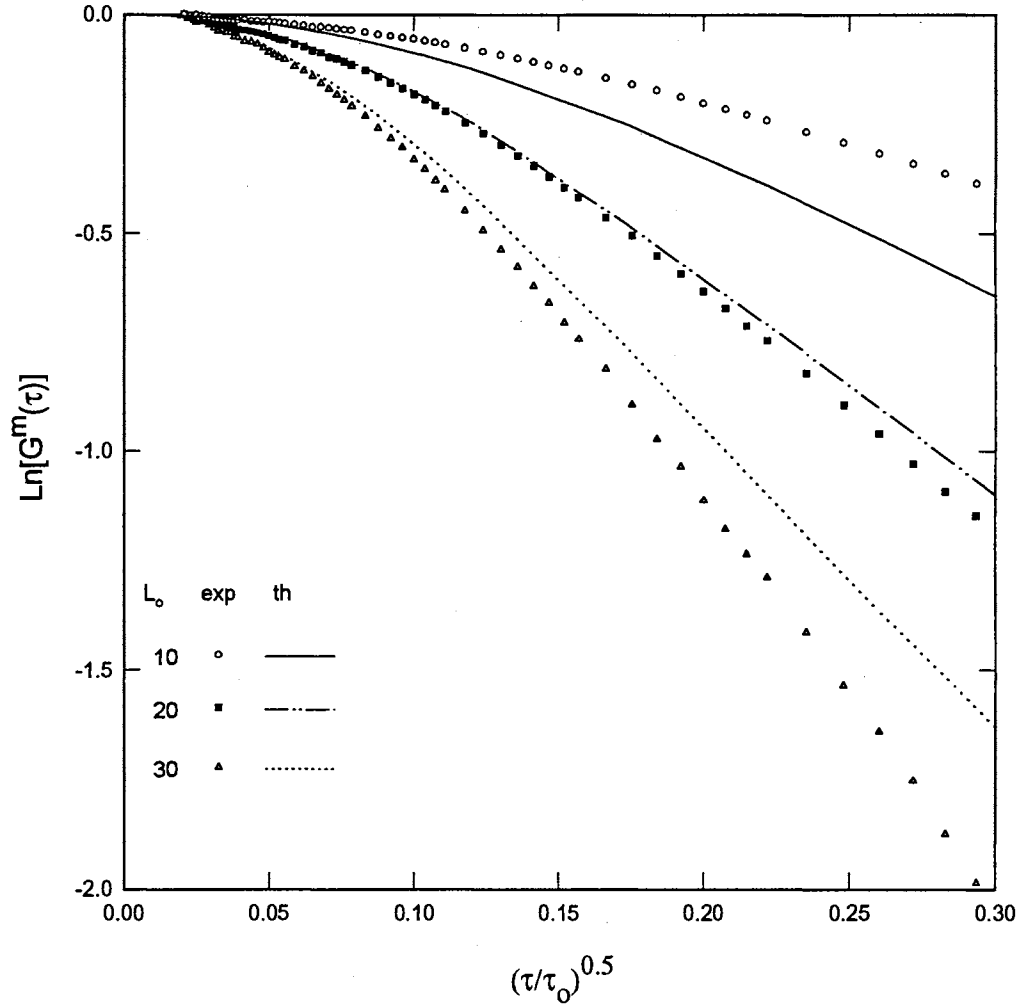


Fig. 40: Transmission: Comparison of experimental data with the anisotropic one term Legendre expansion of g^1 theory ($f=0.858$, $n=1.331$) for different optical thicknesses, particle diameter of $0.497 \mu\text{m}$ and laser wavelength of 514.5 nm .

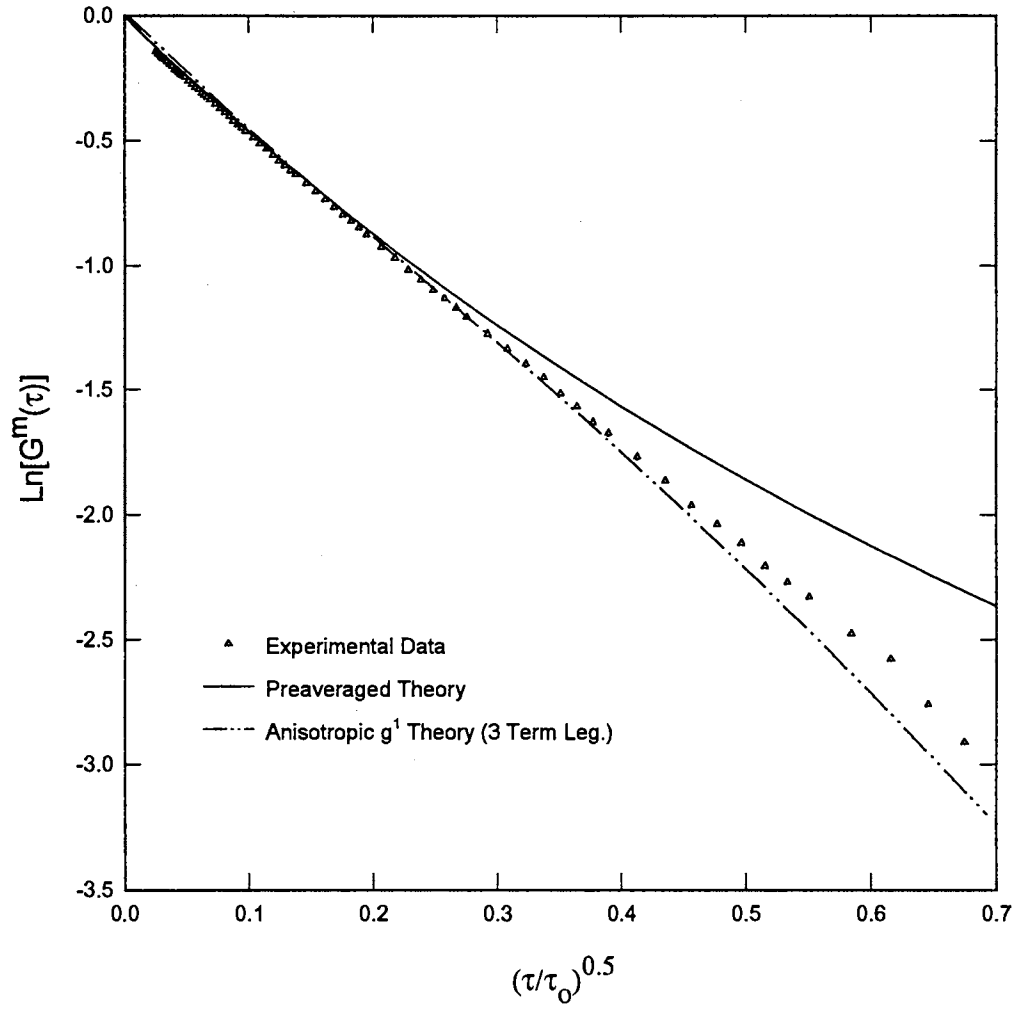


Fig. 41: Back-scattering: Comparison of experimental data with preaveraged and 3 term Legendre expansion of g^1 for a semi-infinite medium, particle diameter of 0.3 μm and laser wavelength of 514.5 nm.

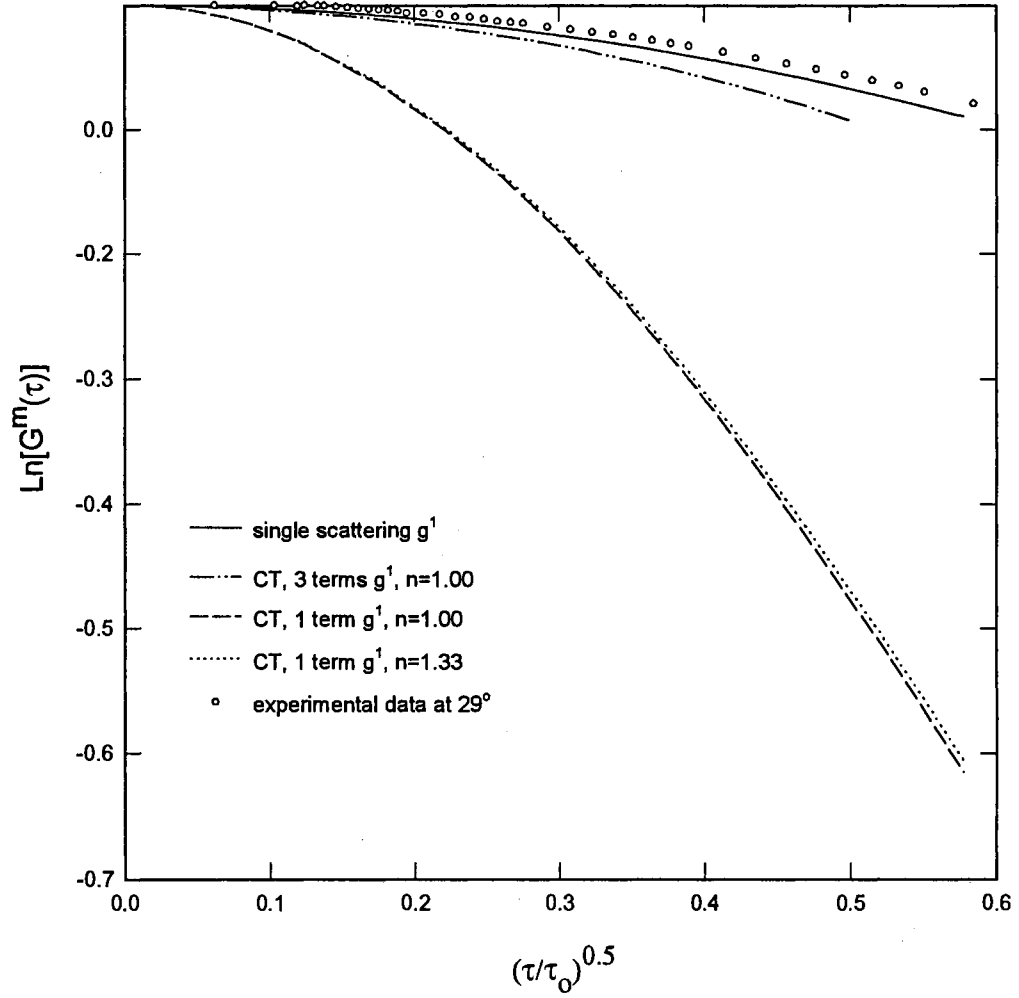


Fig. 42: Transmission: Comparison of experimental data with the single scattering and Legendre expansion of g^1 in CT theory for 29° (inside sample) detection angle for a very dilute sample (single scattering medium), particle diameter of $0.3 \mu\text{m}$, and laser wavelength of 514.5 nm .

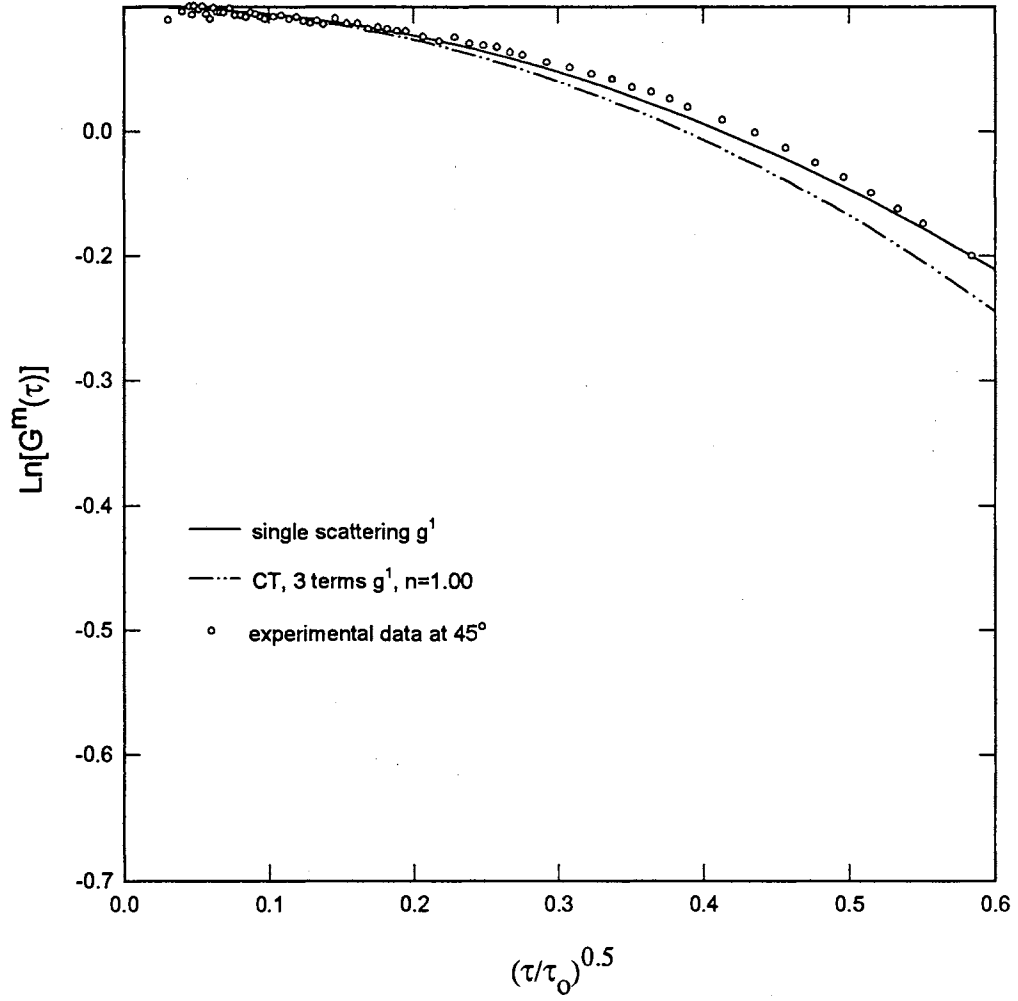


Fig. 43: Transmission: Comparison of experimental data with the single scattering and 3 term Legendre expansion of g^1 in CT theory for 45° (inside sample) detection angle for very dilute sample (single scattering medium), particle diameter of $0.3 \mu\text{m}$, and laser wavelength of 514.5 nm .

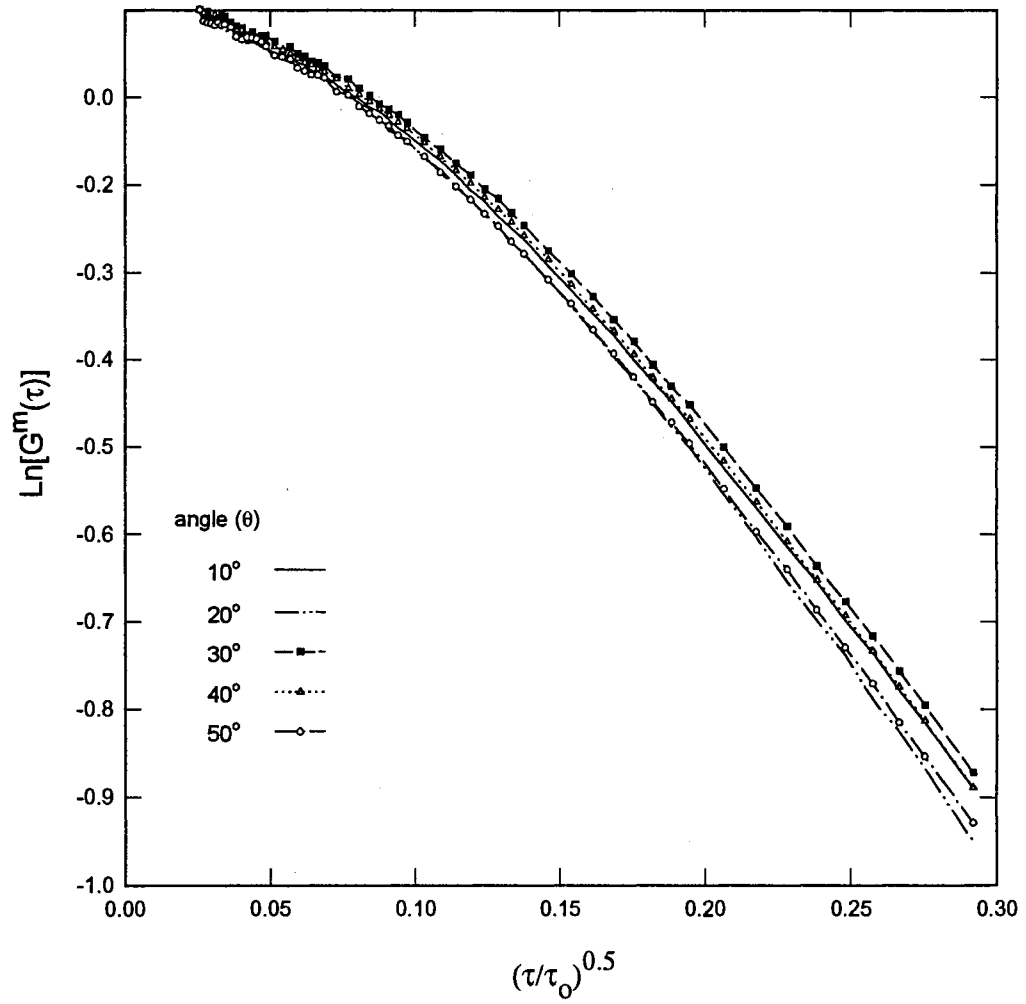


Fig. 44: Back-scattering: Effect of detection angle ($\mu=\cos\theta$) on experimental data for optical thickness of 10, particle diameter of $0.3\ \mu\text{m}$, and laser wavelength of $514.5\ \text{nm}$.

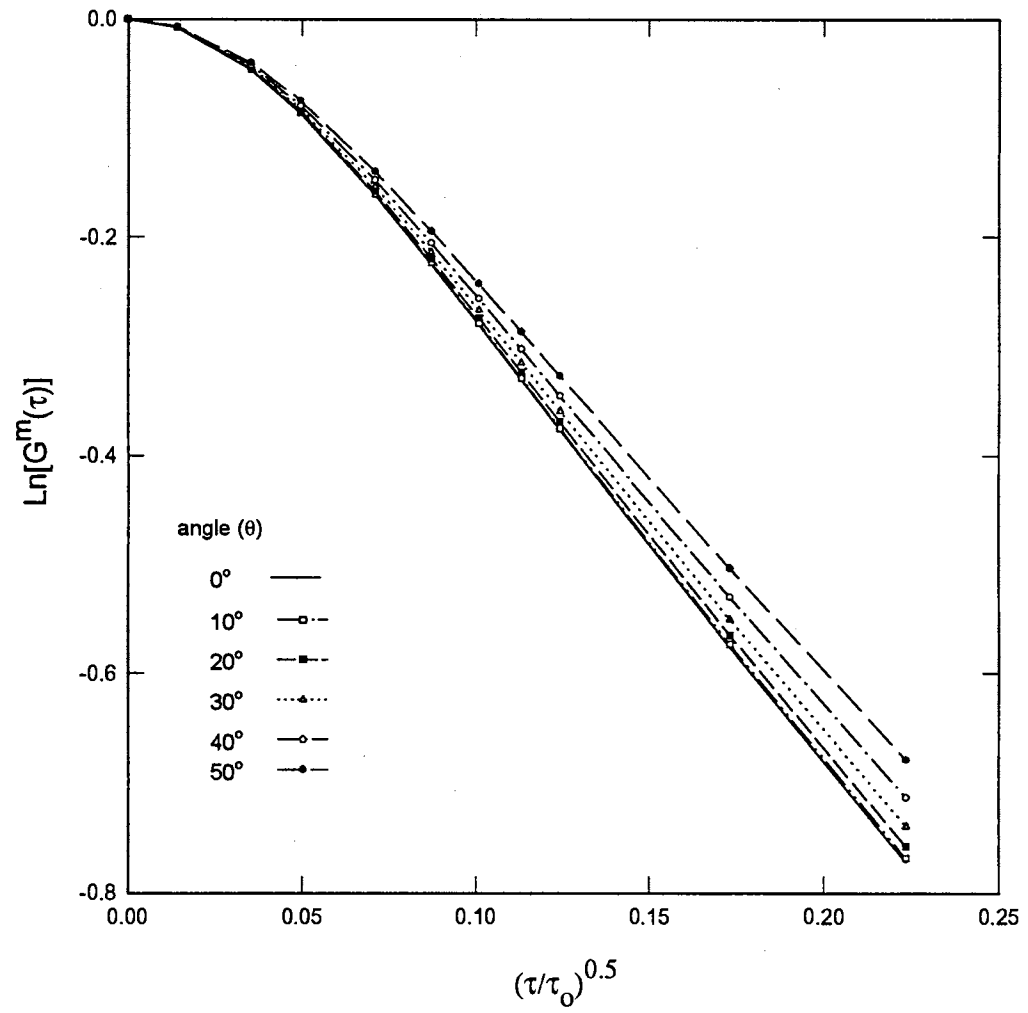


Fig. 45: Back-scattering: Effect of detection angle ($\mu=\cos\theta$) on isotropic preaveraged theory ($f=0.0$, $n=1.0$) for optical thickness of 10.

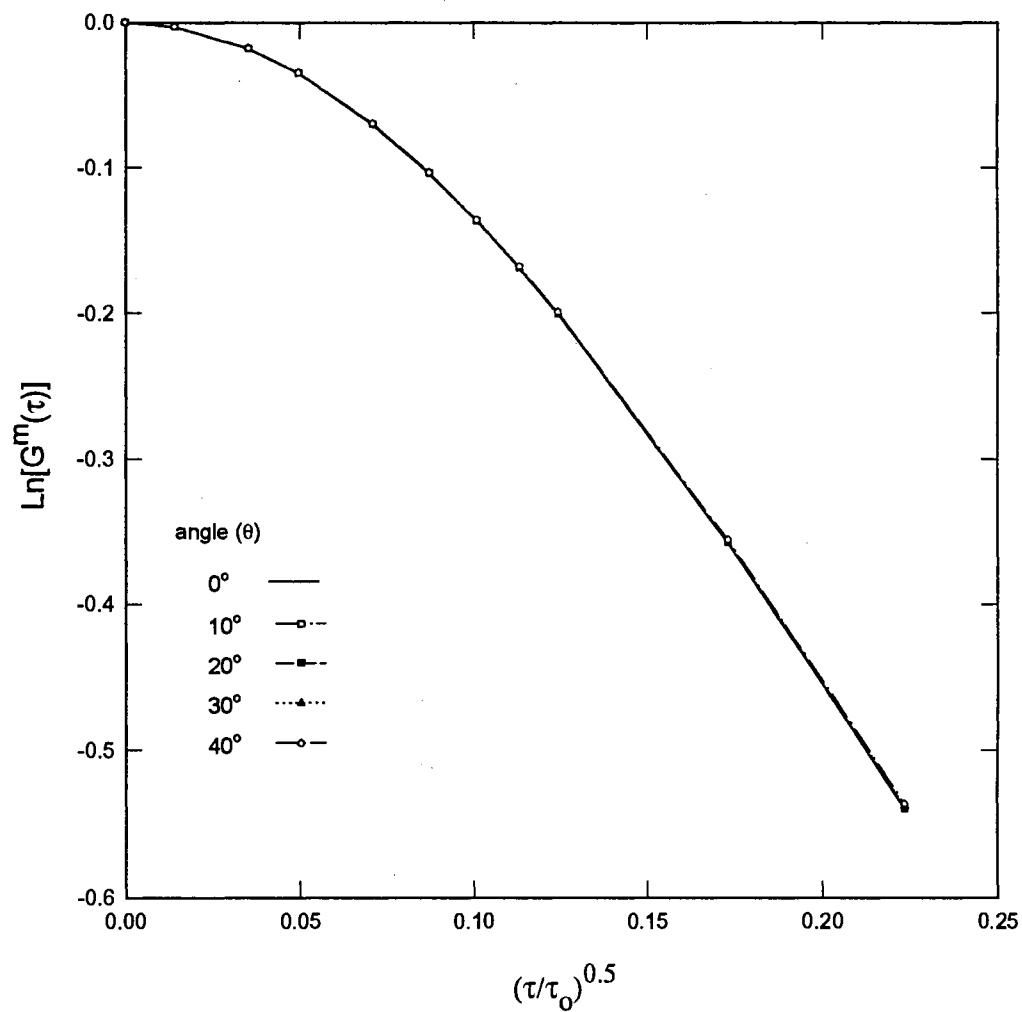


Fig. 46: Back-scattering: Effect of detection angle ($\mu=\cos\theta$) on anisotropic preaveraged theory ($f=0.727$, $n=1.331$) for optical thickness of 10.

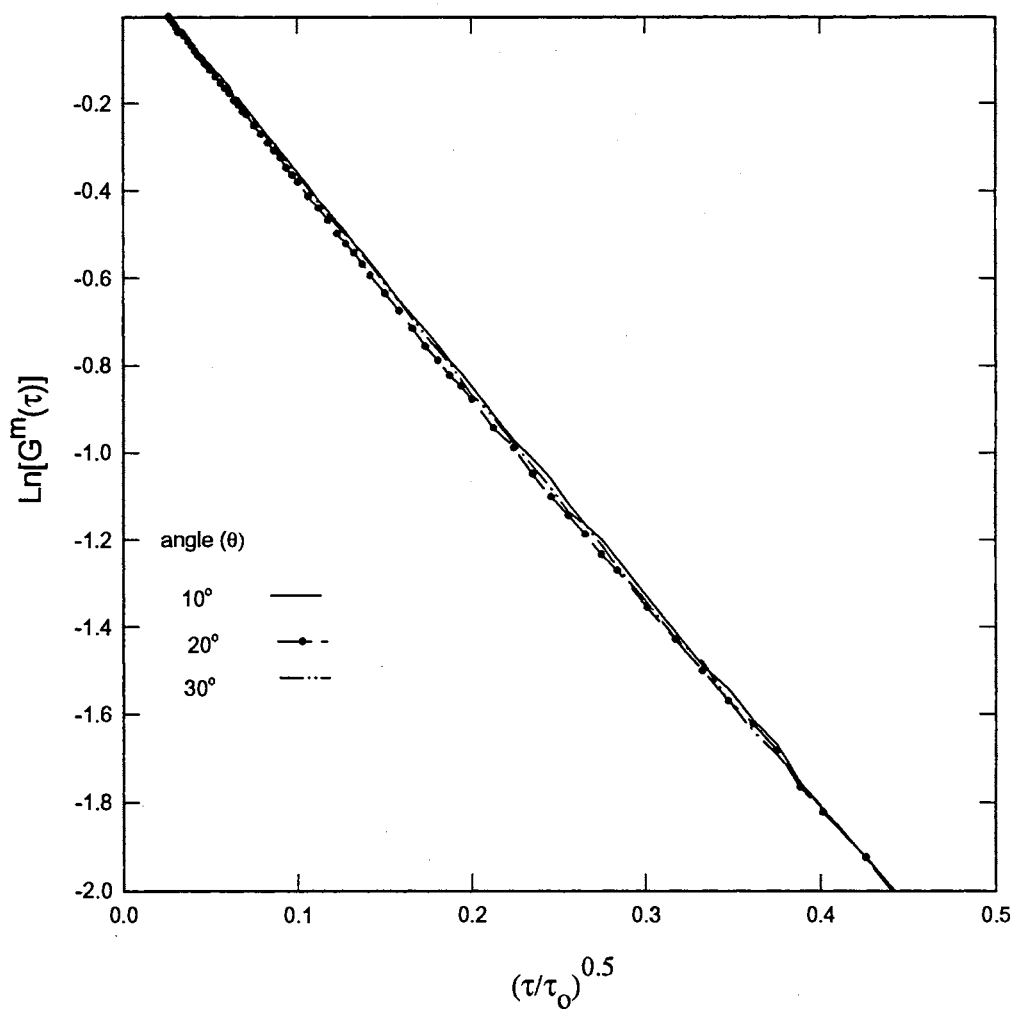


Fig. 47: Back-scattering: Effect of detection angle ($\mu=\cos\theta$) on experimental data for optical thickness of 100, particle diameter of $0.3\ \mu\text{m}$, and laser wavelength of $514.5\ \text{nm}$.

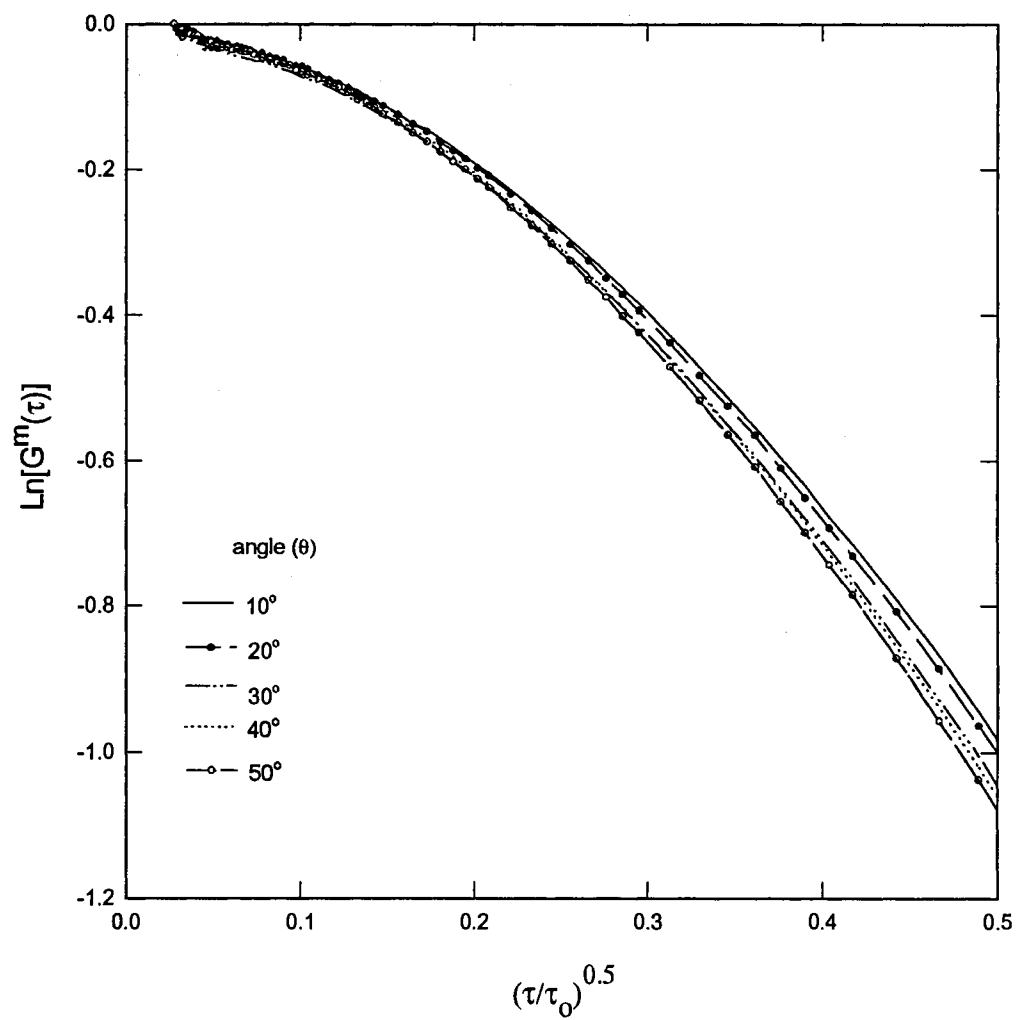


Fig. 48: Back-scattering: Effect of detection angle ($\mu=\cos\theta$) on experimental data for optical thickness of 2, particle diameter of $0.3\ \mu\text{m}$, and laser wavelength of $514.5\ \text{nm}$.

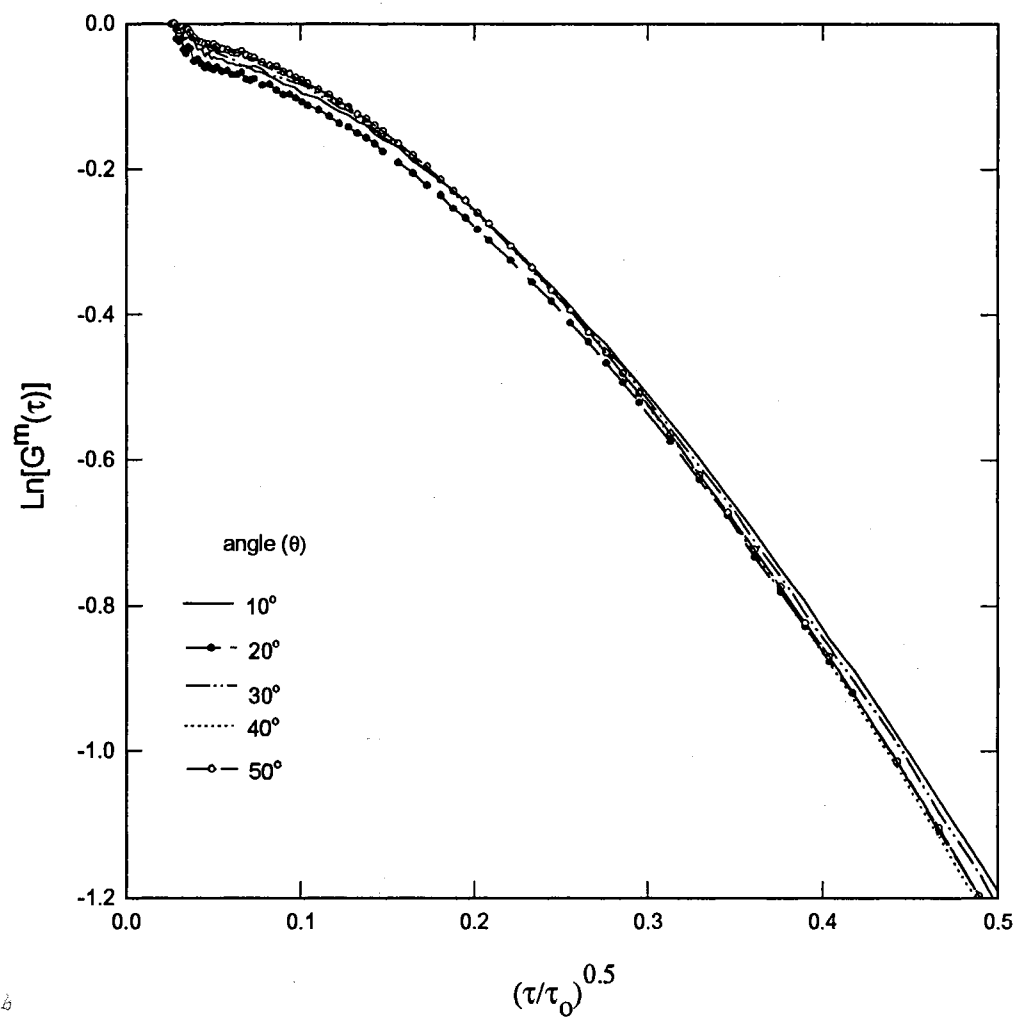


Fig. 49: Back-scattering: Effect of detection angle ($\mu=\cos\theta$) on experimental data for optical thickness of 3, particle diameter of 0.3 μm , and laser wavelength of 514.5 nm.

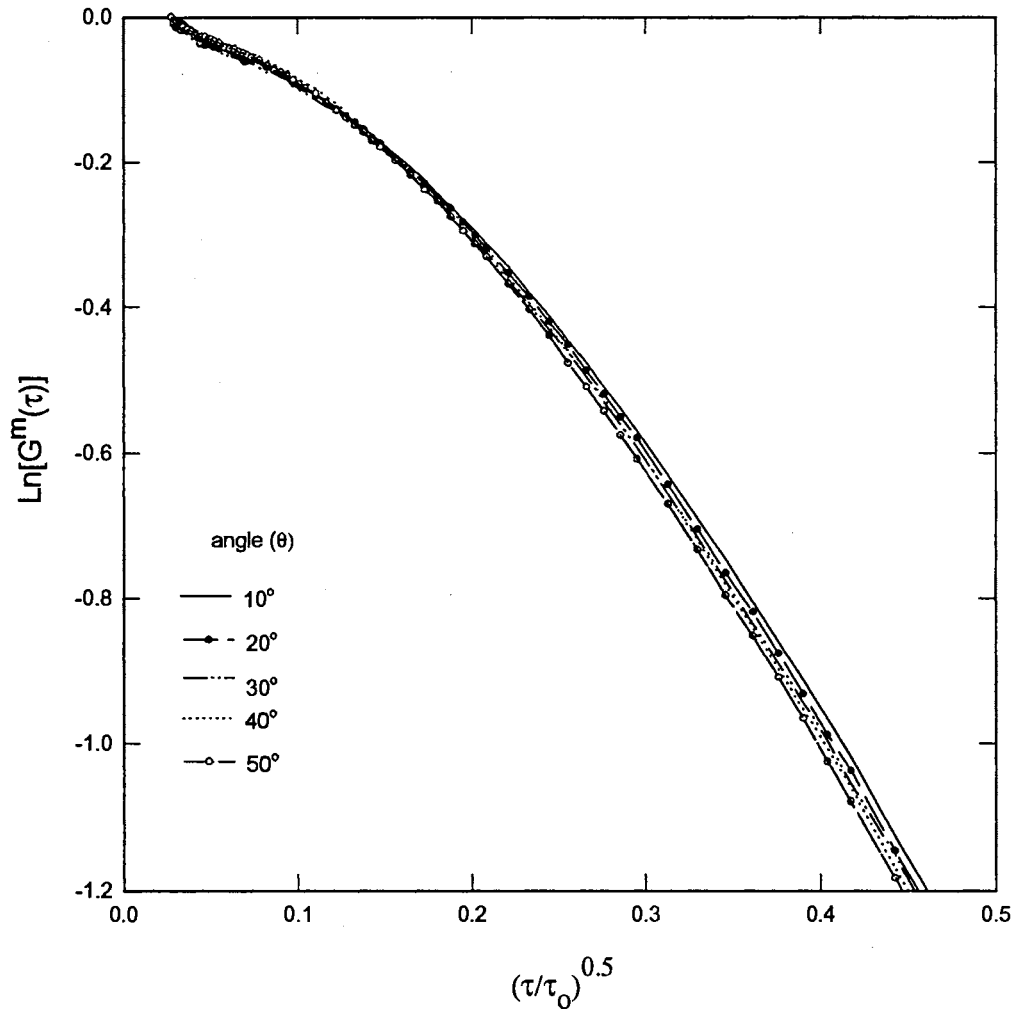


Fig. 50: Back-scattering: Effect of detection angle ($\mu=\cos\theta$) on experimental data for optical thickness of 4, particle diameter of $0.3\ \mu\text{m}$, and laser wavelength of $514.5\ \text{nm}$.

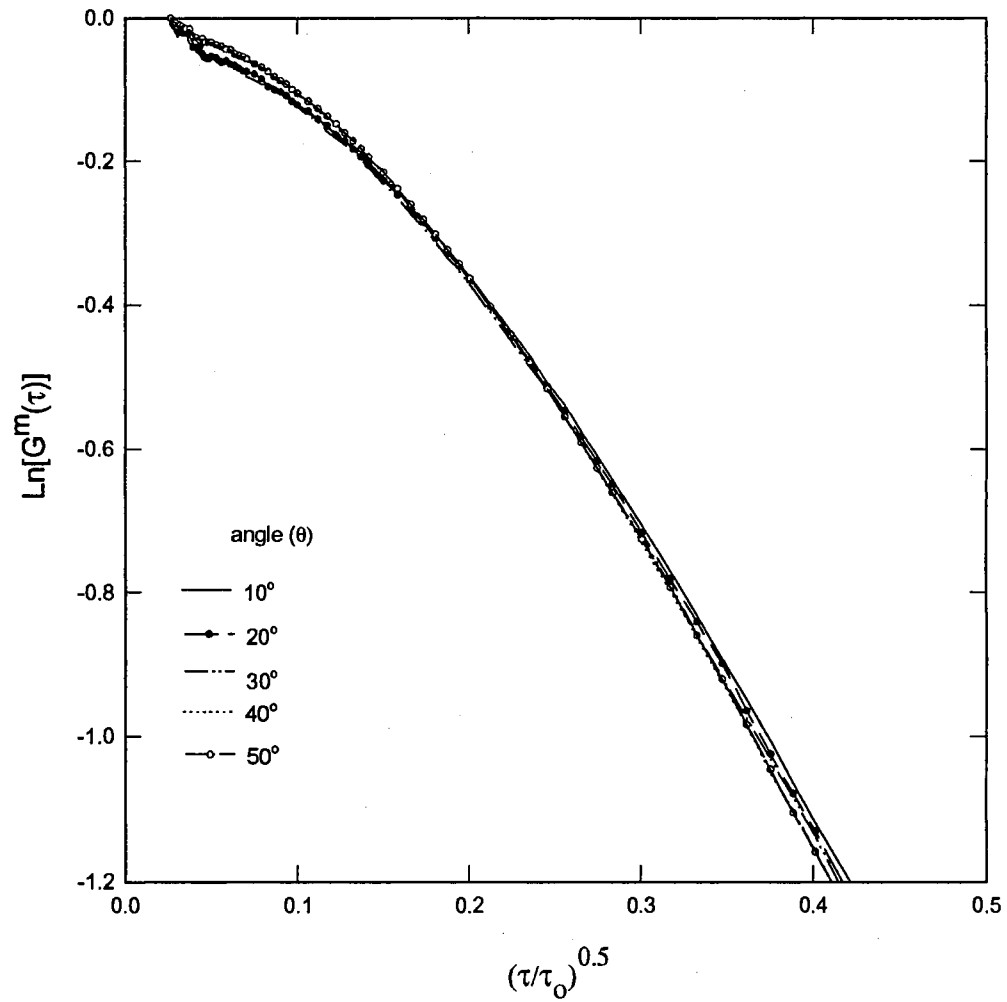


Fig. 51: Back-scattering: Effect of detection angle ($\mu=\cos\theta$) on experimental data for optical thickness of 5, particle diameter of $0.3\ \mu\text{m}$, and laser wavelength of $514.5\ \text{nm}$.

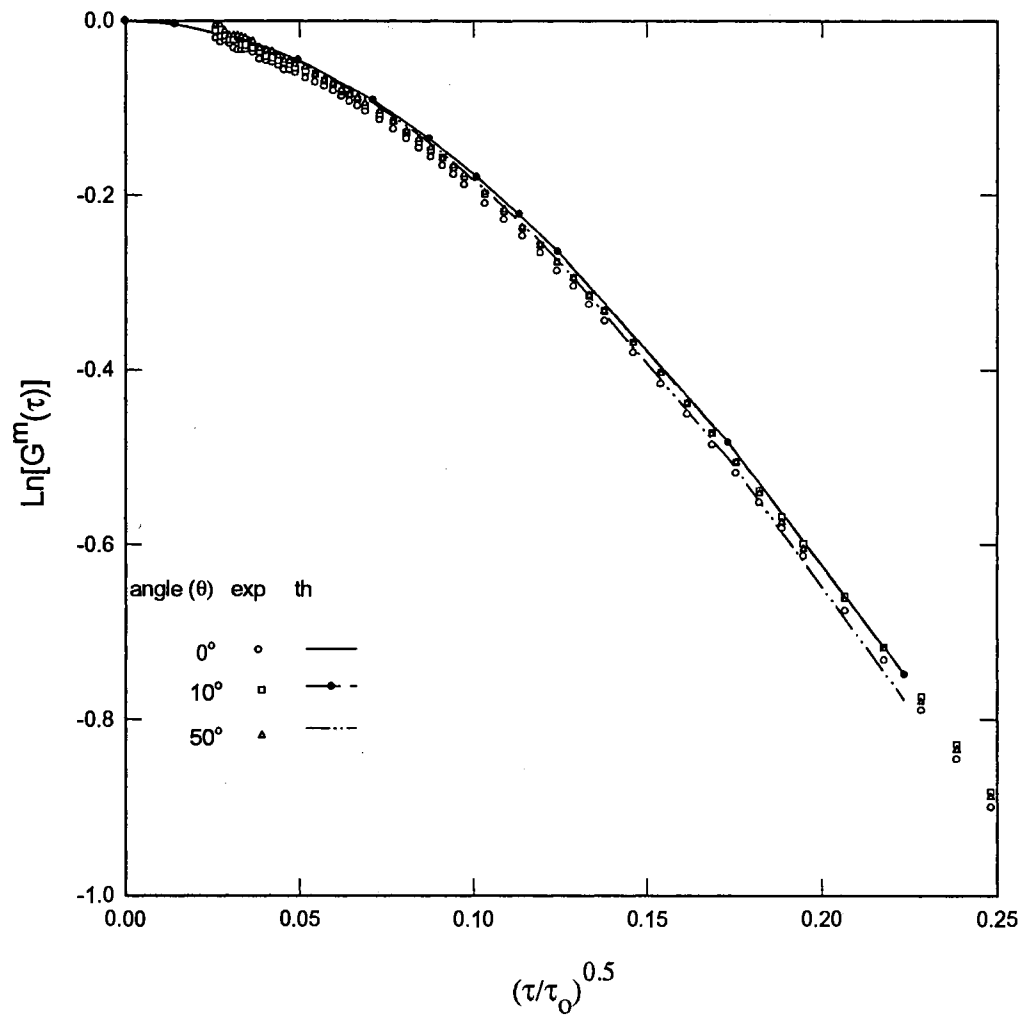


Fig. 52: Transmission: Comparison of experimental data with anisotropic preaveraged theory ($f=0.727$, $n=1.331$) for optical thickness of 10 and different detection angles, particle diameter of $0.3 \mu\text{m}$, and laser wavelength of 514.5 nm .

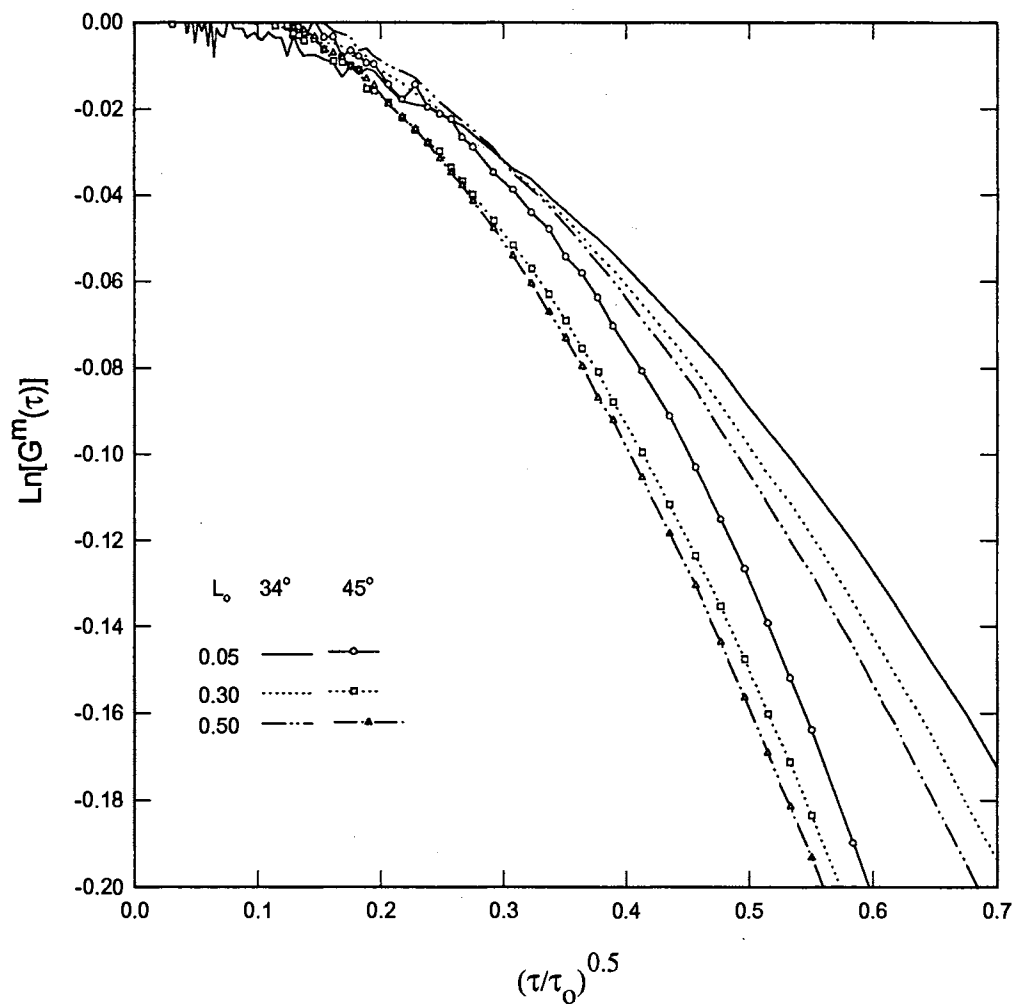


Fig. 53: Transmission: Comparison of correlation measurements for different low optical thicknesses at 34° and 45° (inside sample) detection angles, particle diameter of $0.3 \mu\text{m}$, and laser wavelength of 514.5 nm .

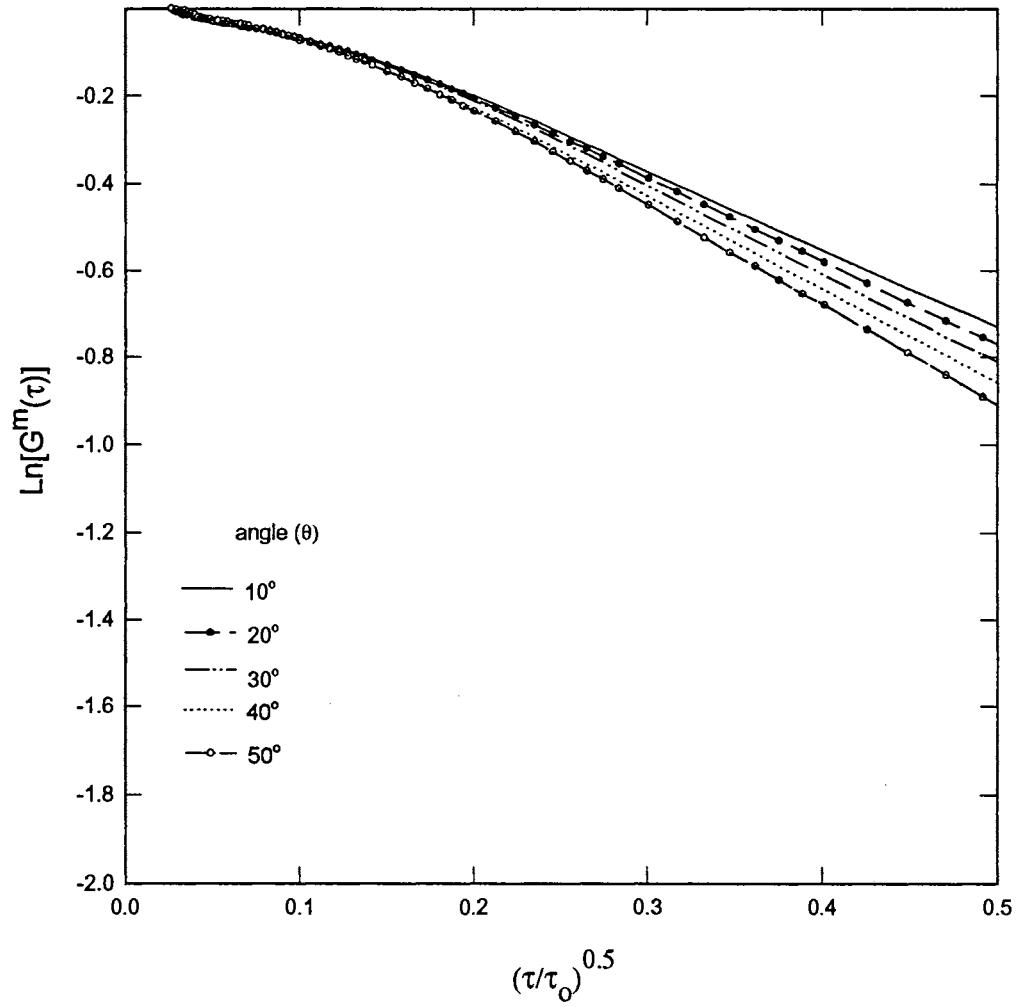


Fig. 54: Transmission: Effect of detection angle ($\mu=\cos\theta$) on experimental data for optical thickness of 5, particle diameter of $0.3\ \mu\text{m}$, and laser wavelength of $514.5\ \text{nm}$.

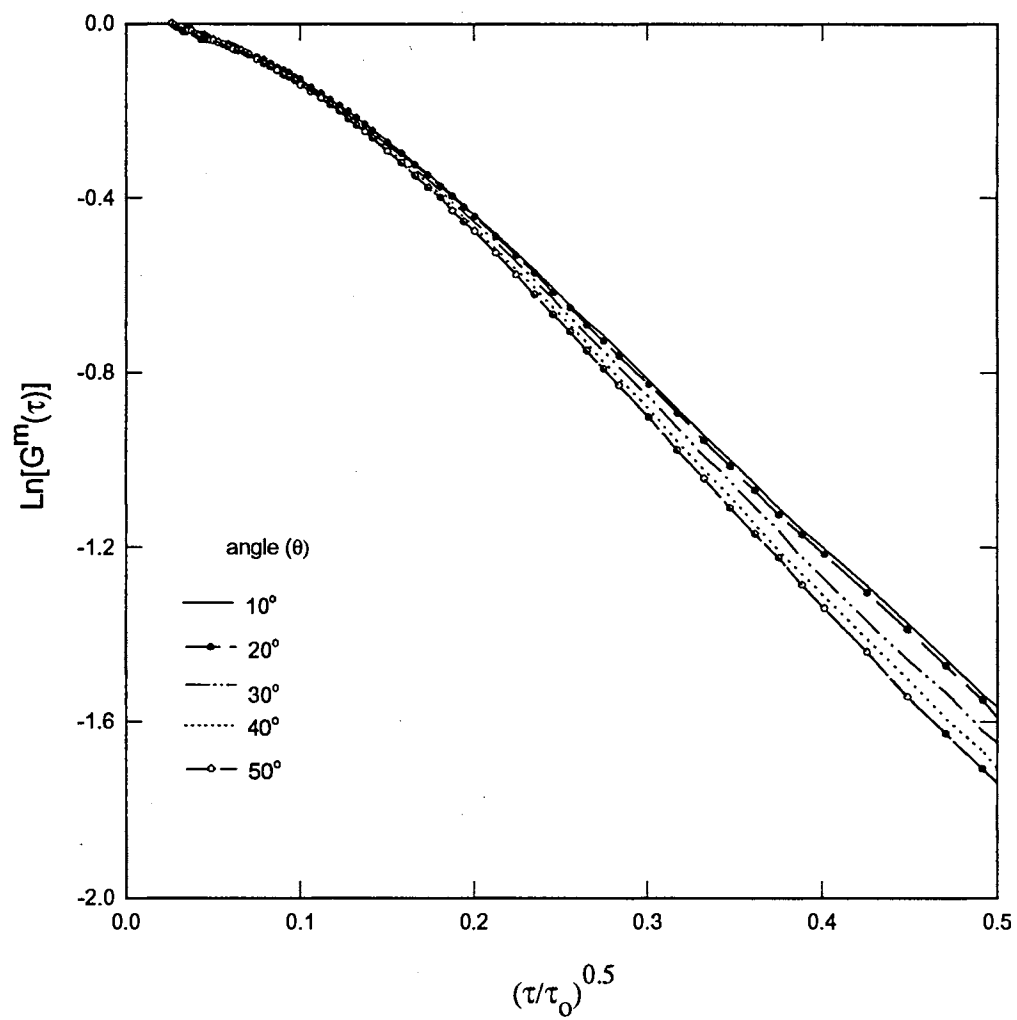


Fig. 55: Transmission: Effect of detection angle ($\mu=\cos\theta$) on experimental data for optical thickness of 8, particle diameter of 0.3 μm , and laser wavelength of 514.5 nm.

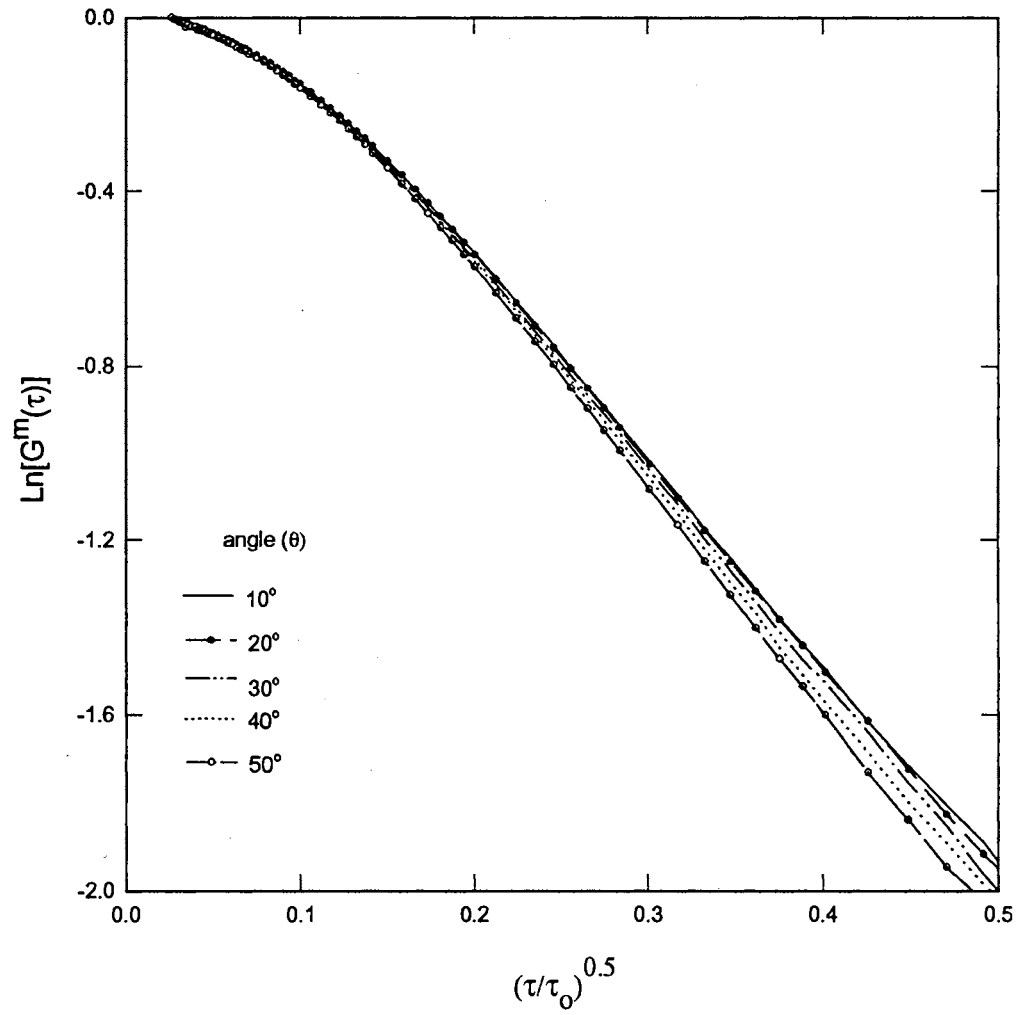


Fig. 56: Transmission: Effect of detection angle ($\mu=\cos\theta$) on experimental data for optical thickness of 9, particle diameter of $0.3\ \mu\text{m}$, and laser wavelength of $514.5\ \text{nm}$.

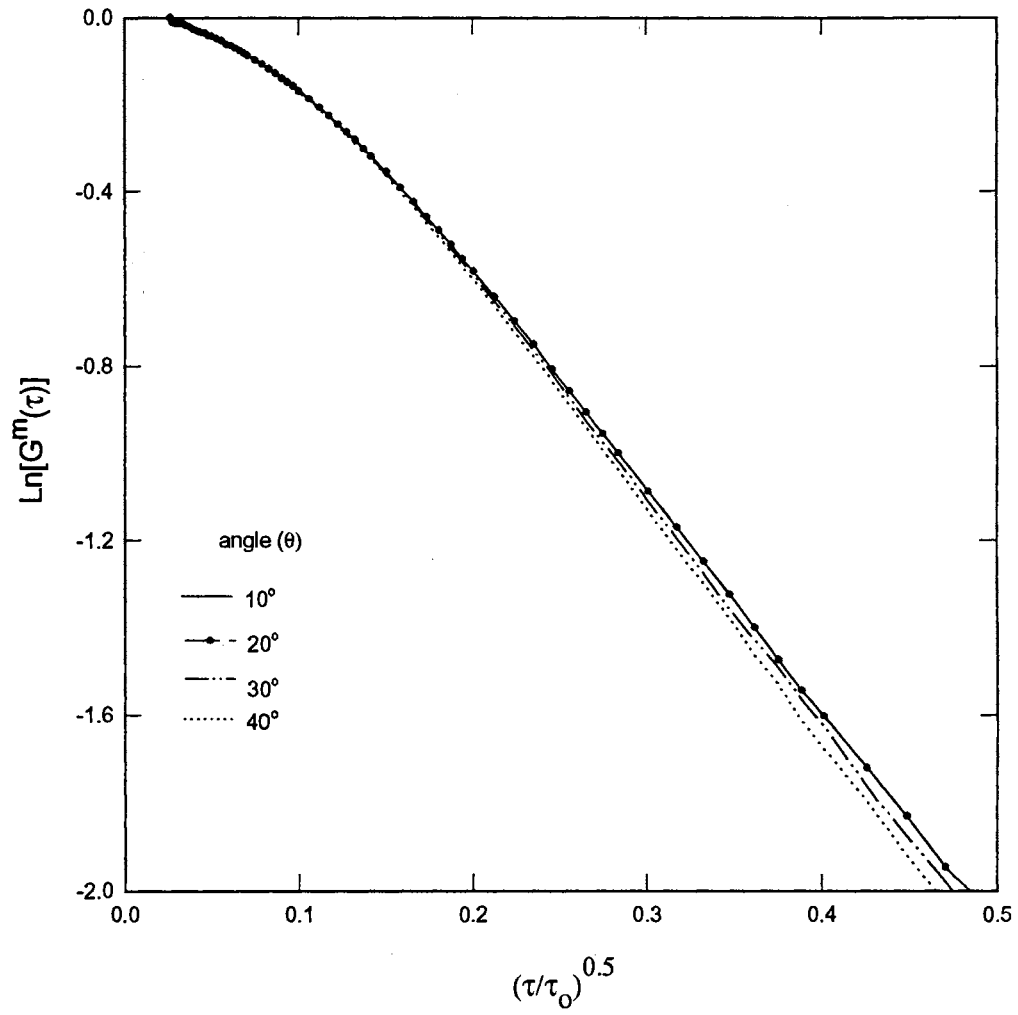


Fig. 57: Transmission: Effect of detection angle ($\mu=\cos\theta$) on experimental data for optical thickness of 10, particle diameter of $0.3\ \mu\text{m}$, and laser wavelength of $514.5\ \text{nm}$.

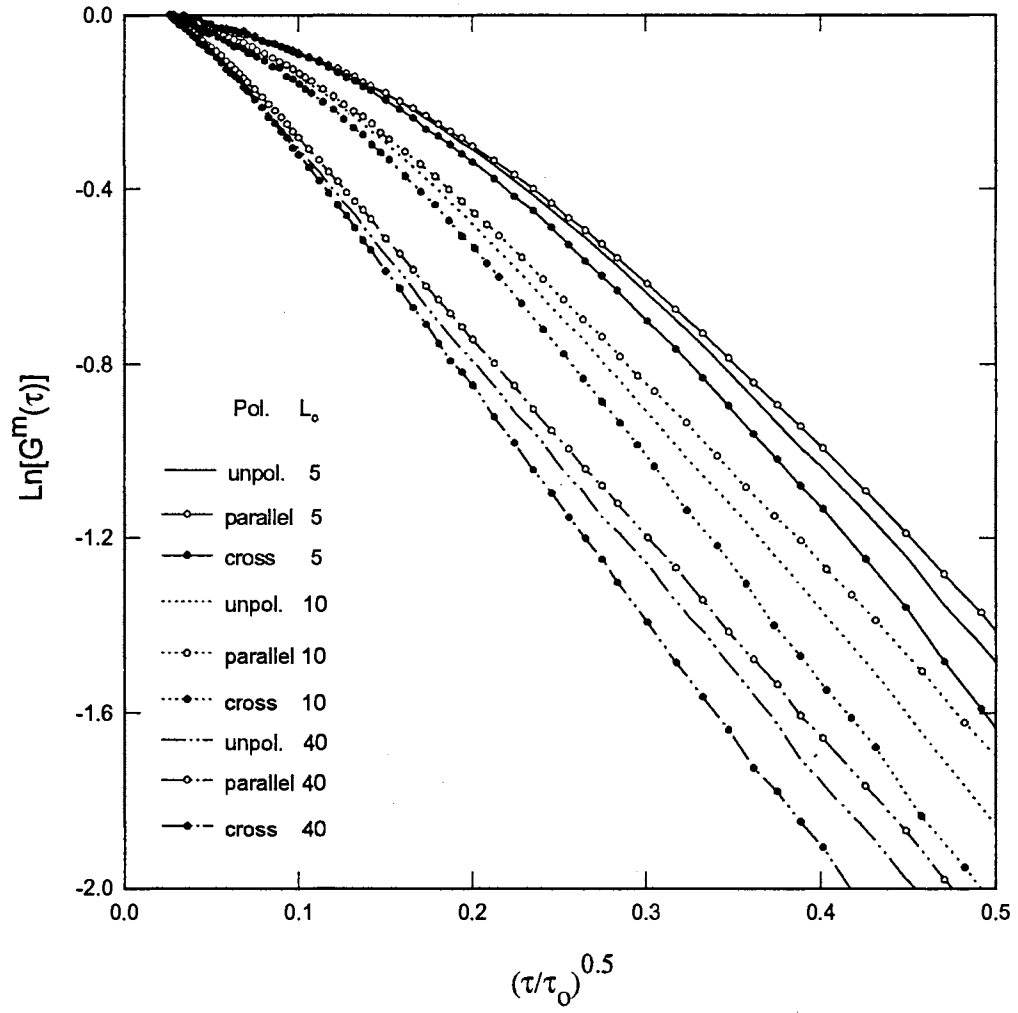


Fig. 58: Back-scattering: Effect of polarization on correlation measurements for different optical thicknesses, particle diameter of $0.3 \mu\text{m}$, and laser wavelength of 514.5 nm .

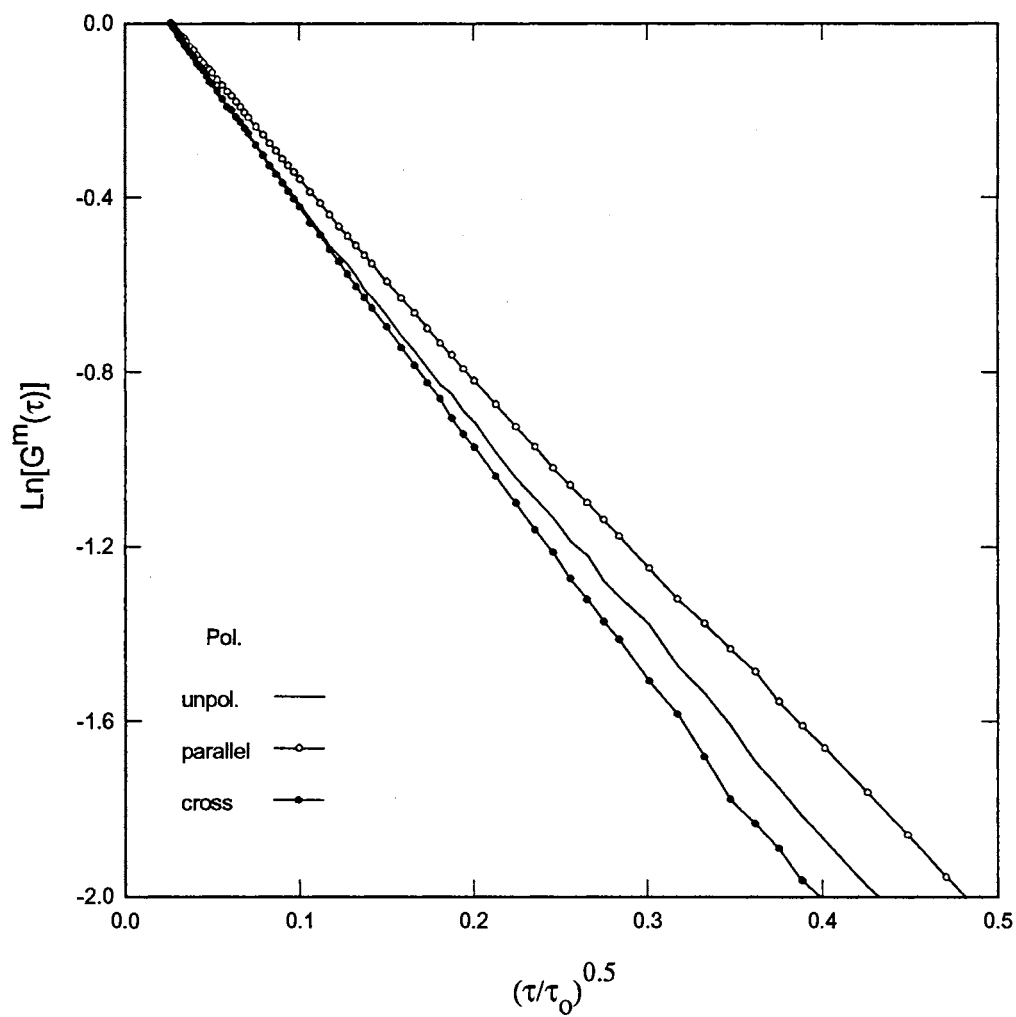


Fig. 59: Back-scattering: Effect of polarization on correlation measurements for optical thickness of 100, particle diameter of 0.3 μm , and laser wavelength of 514.5 nm.

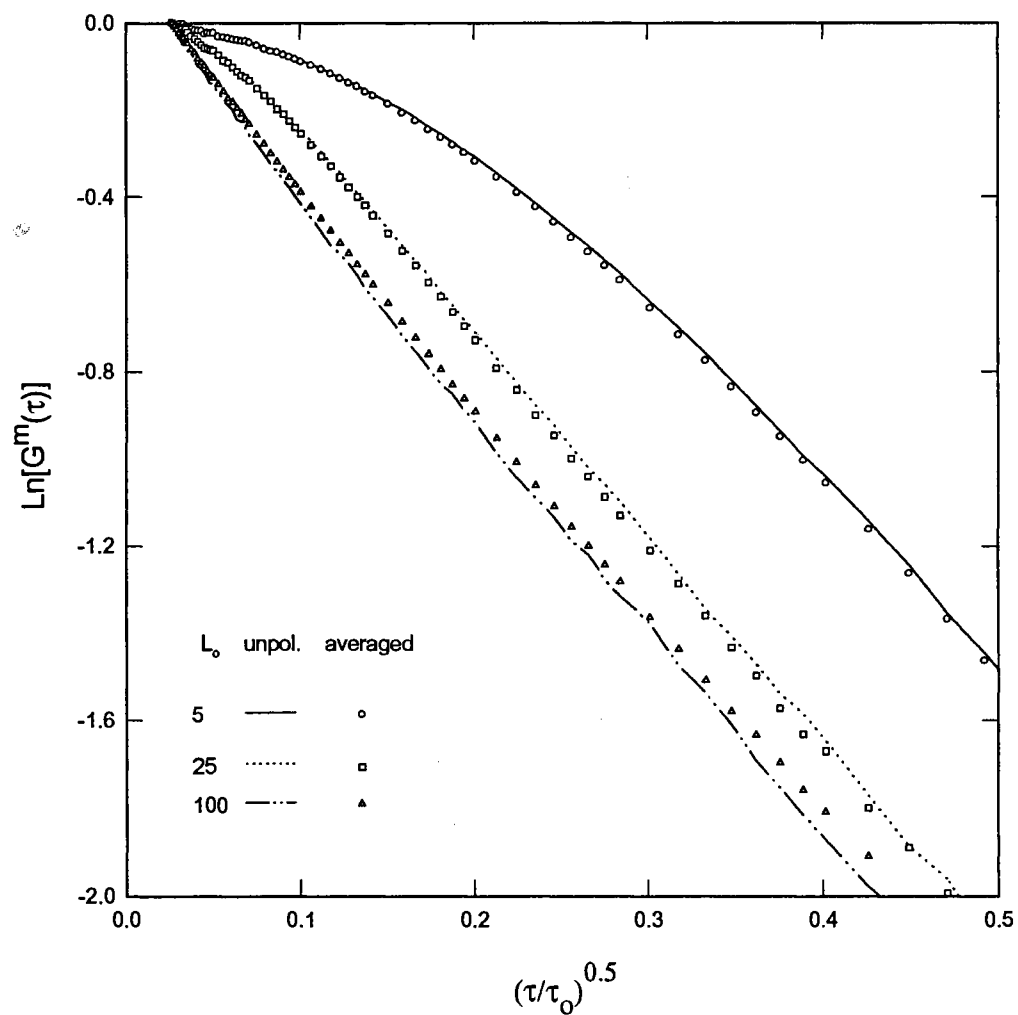


Fig. 60: Back-scattering: Comparison of the unpolarized correlation function measurements to the average of the two polarized measurements for different optical thicknesses, particle diameter of $0.3 \mu\text{m}$, and laser wavelength of 514.5 nm .

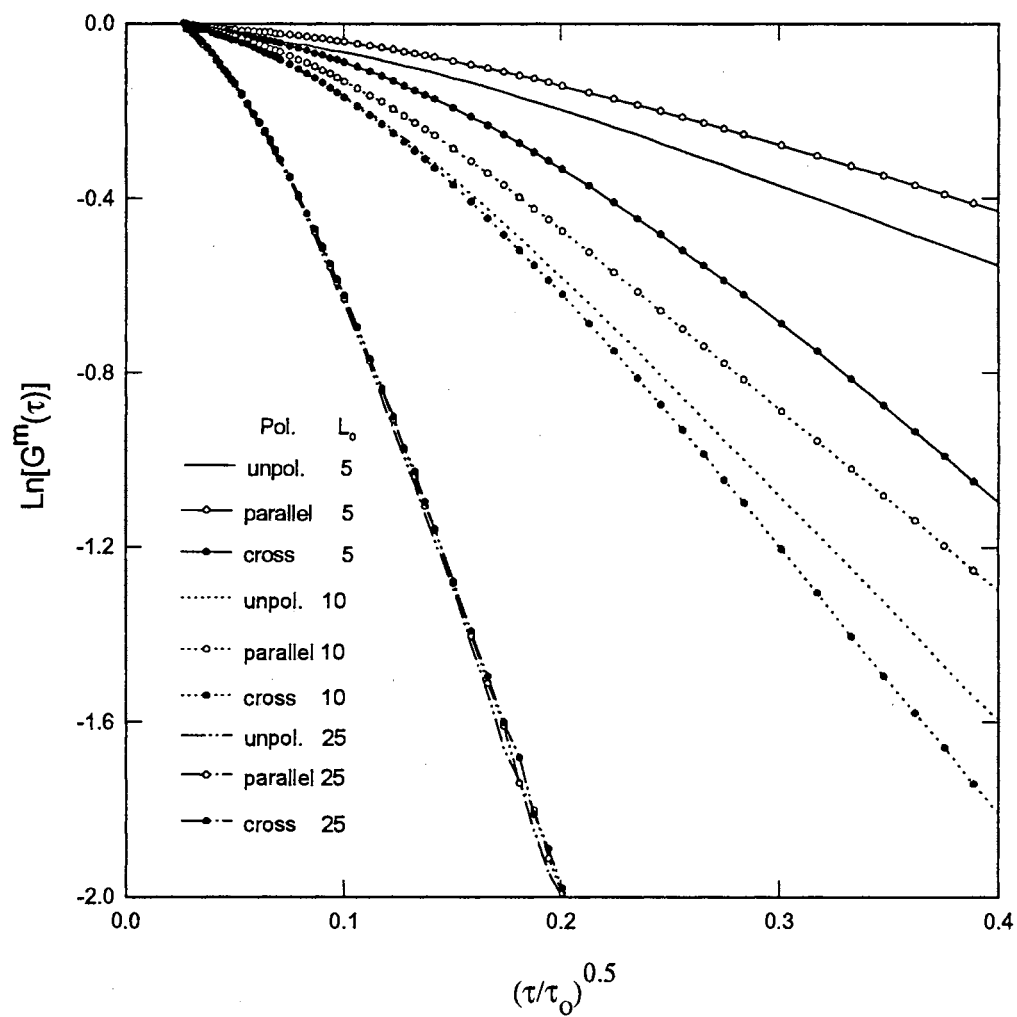


Fig. 61: Transmission: Effect of polarization on correlation measurements for different optical thicknesses, particle diameter of $0.3 \mu\text{m}$, and laser wavelength of 514.5 nm .

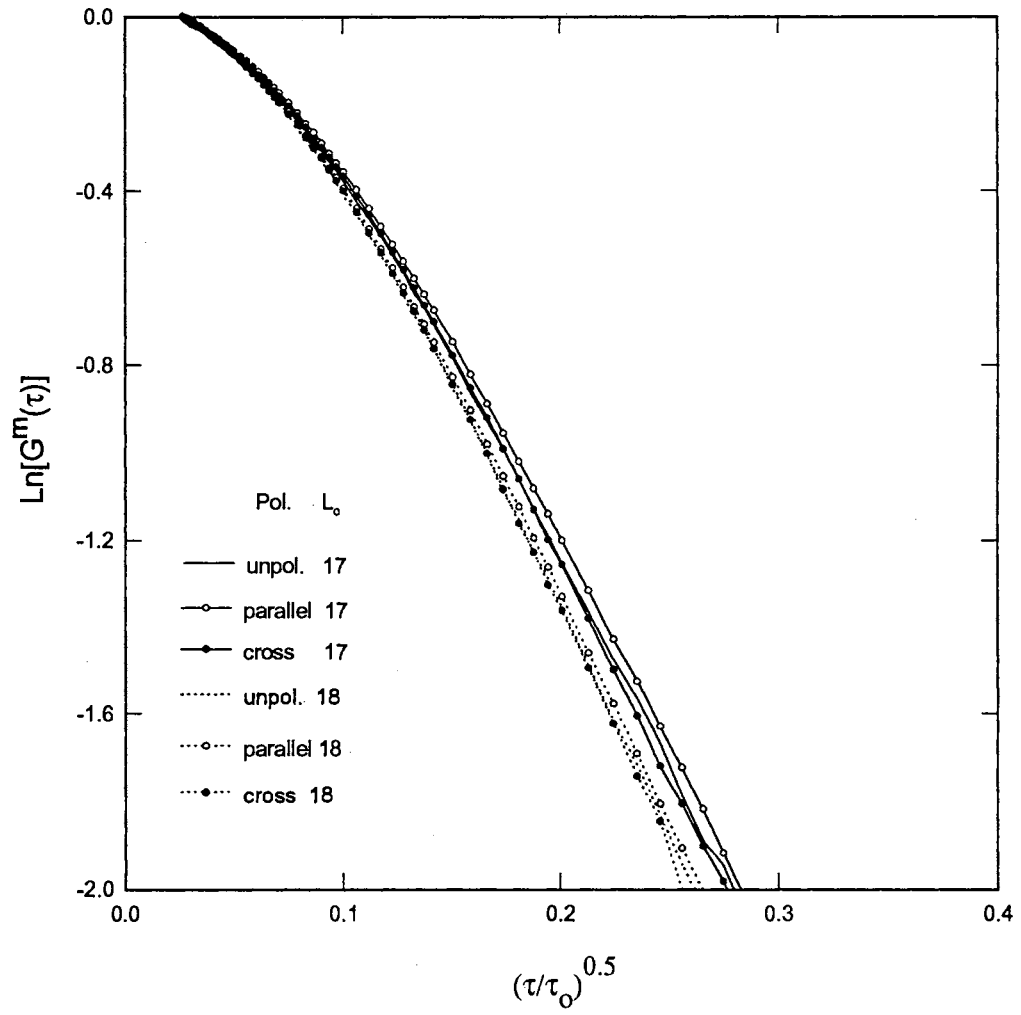


Fig. 62: Transmission: Effect of polarization on correlation measurements for different optical thicknesses, particle diameter of $0.3 \mu\text{m}$, and laser wavelength of 514.5 nm .

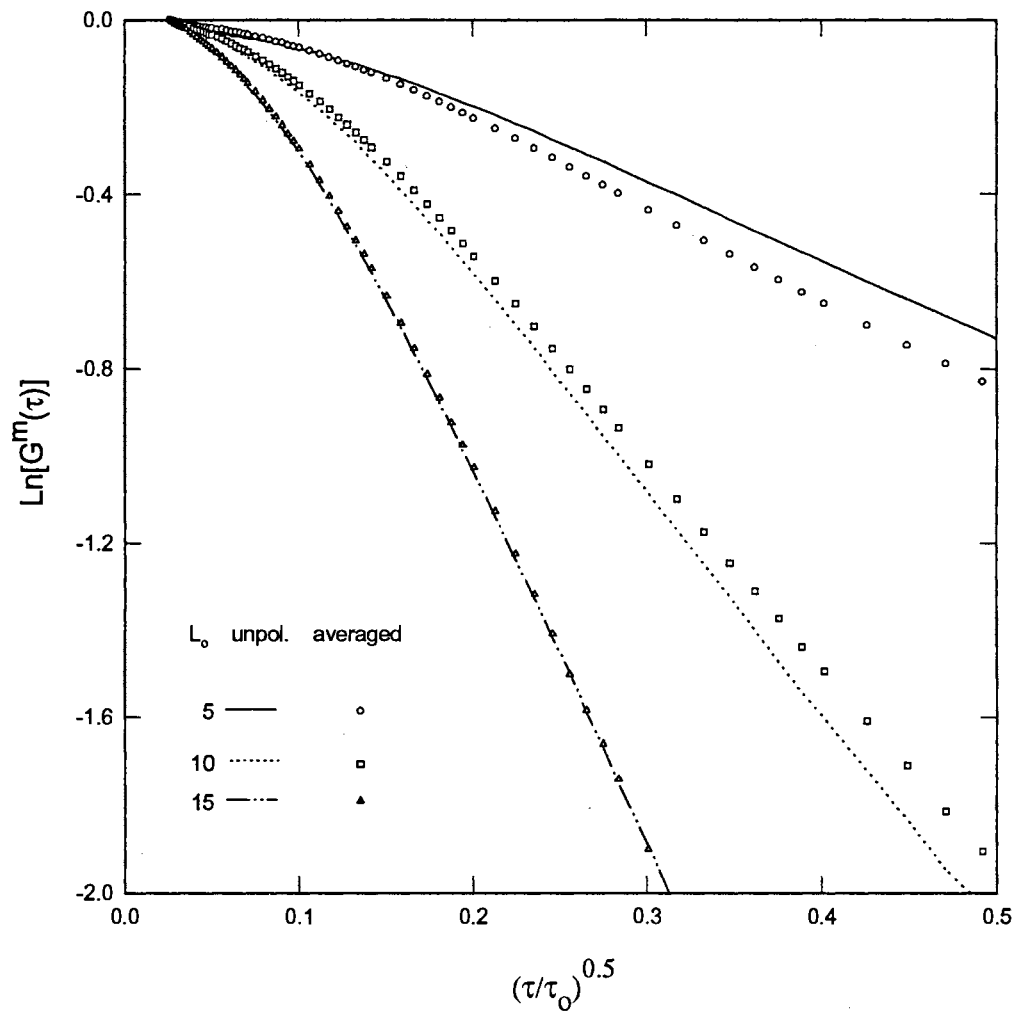


Fig. 63: Transmission: Comparison of unpolarized correlation measurements to the average of the two polarized measurements for different optical thicknesses, particle diameter of $0.3 \mu\text{m}$, and laser wavelength of 514.5 nm .

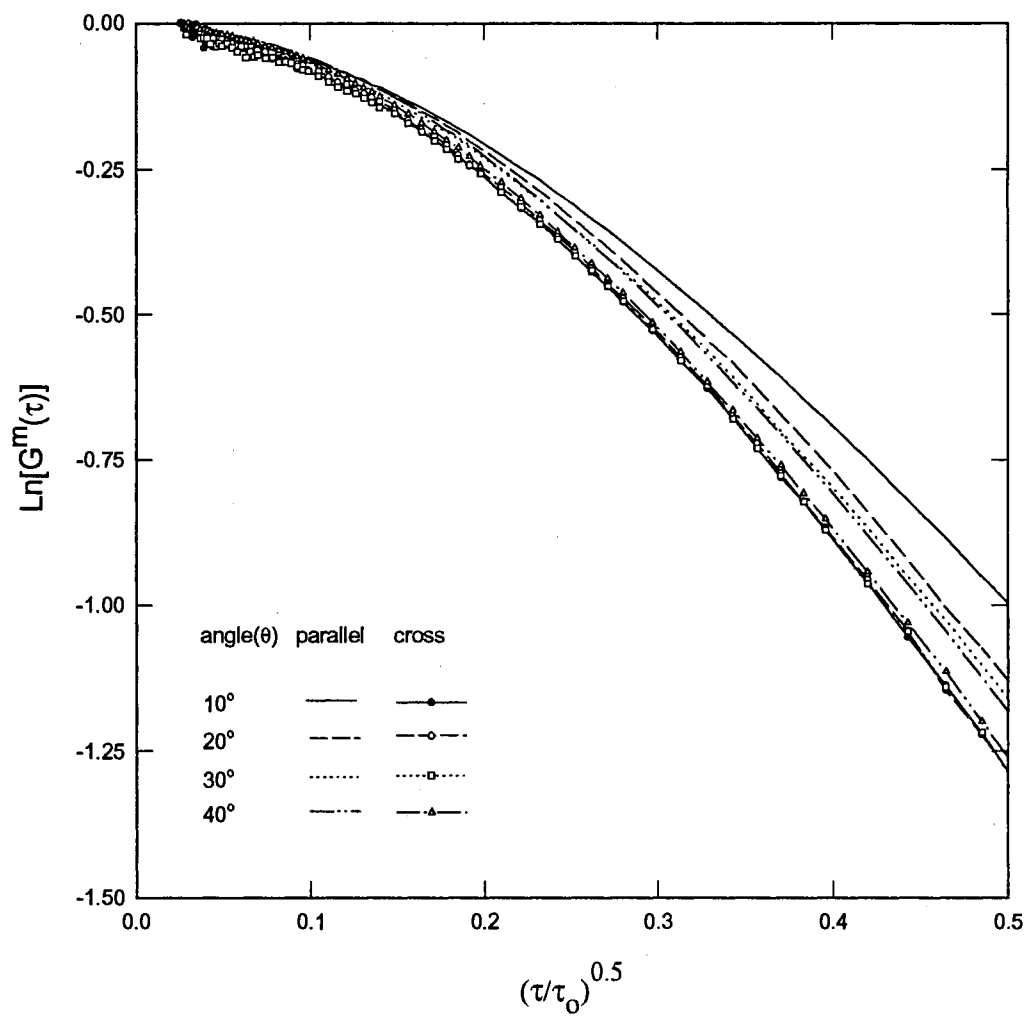


Fig. 64: Back-scattering: Effect of polarization on detection angle of correlation measurements for optical thickness of 3, particle diameter of 0.3 μm , and laser wavelength of 514.5 nm.

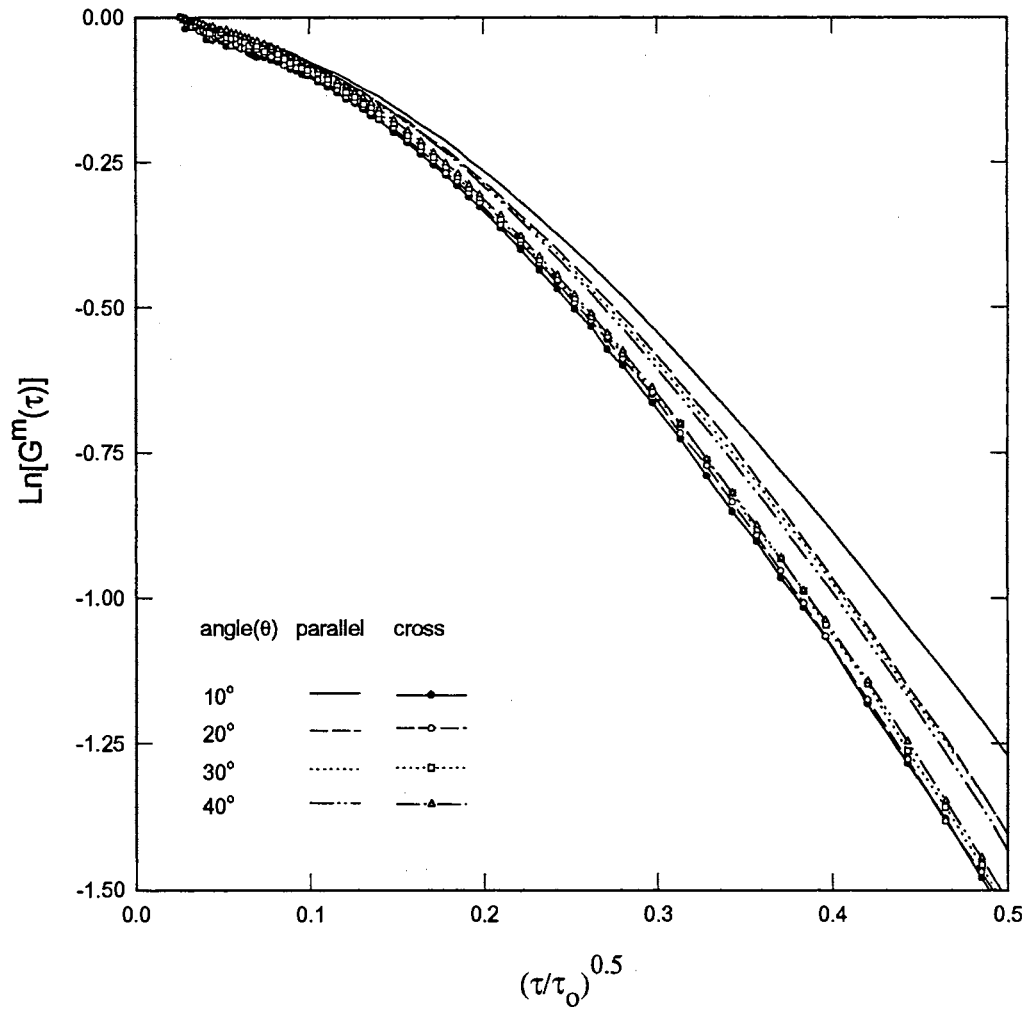


Fig. 65: Back-scattering: Effect of polarization on detection angle of correlation measurements for optical thickness of 4, particle diameter of $0.3 \mu\text{m}$, and laser wavelength of 514.5 nm .

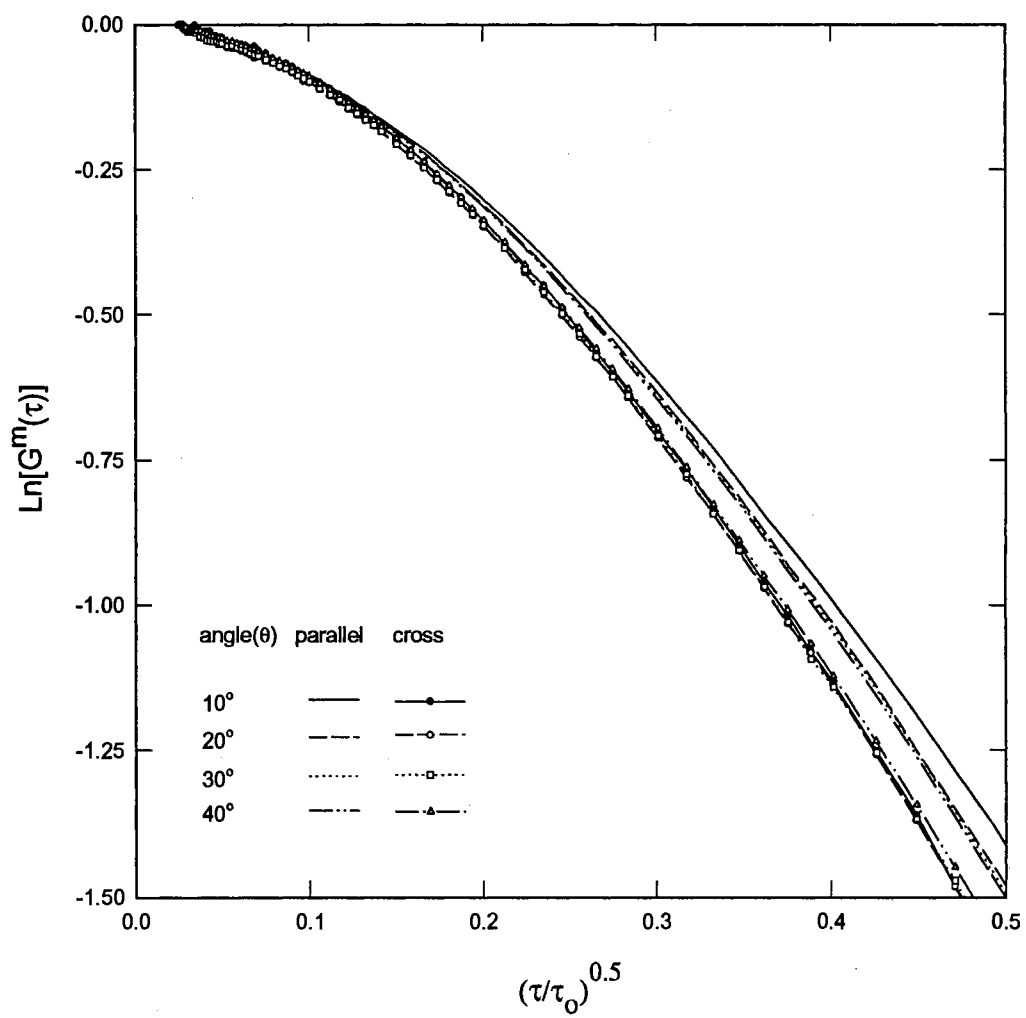


Fig. 66: Back-scattering: Effect of polarization on detection angle of correlation measurements for optical thickness of 5, particle diameter of 0.3 μm , and laser wavelength of 514.5 nm.

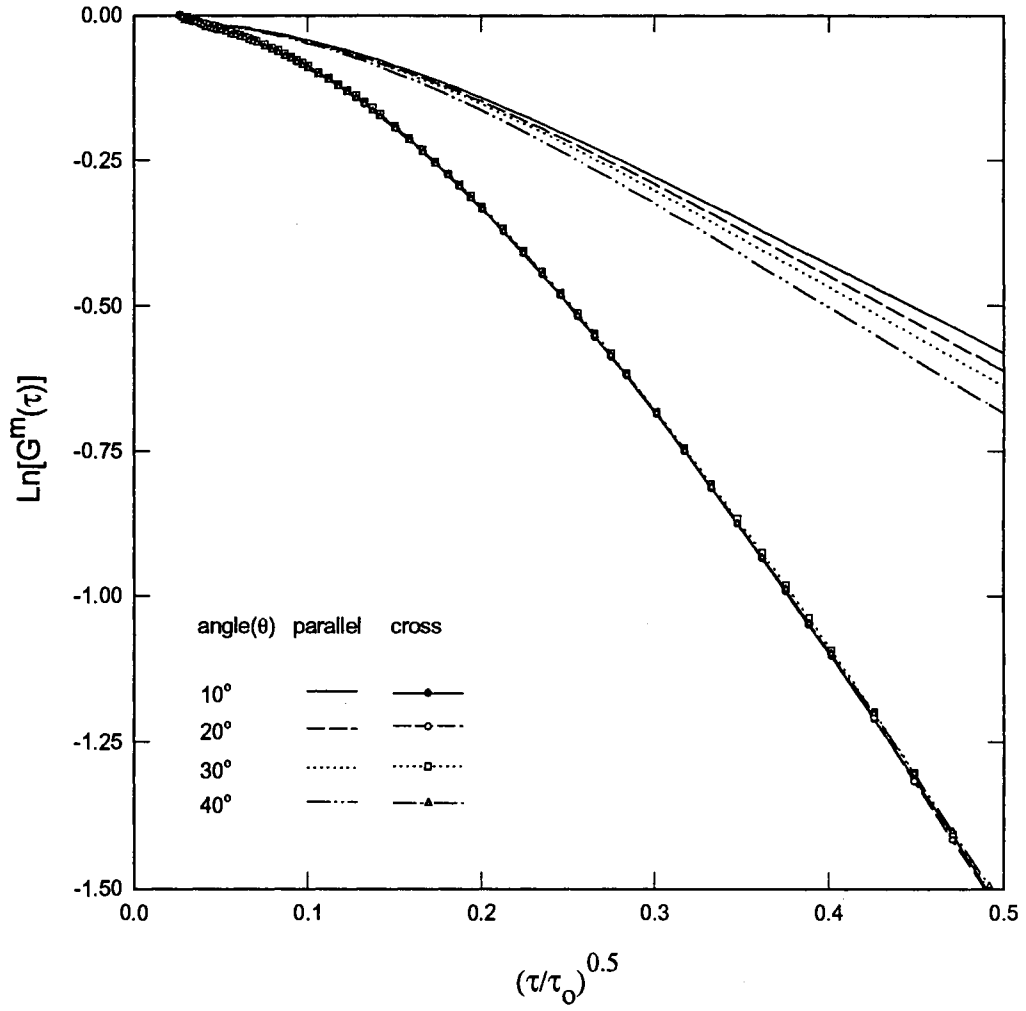


Fig. 67: Transmission: Effect of polarization on detection angle of correlation measurements for optical thickness of 5, particle diameter of 0.3 μm , and laser wavelength of 514.5 nm.

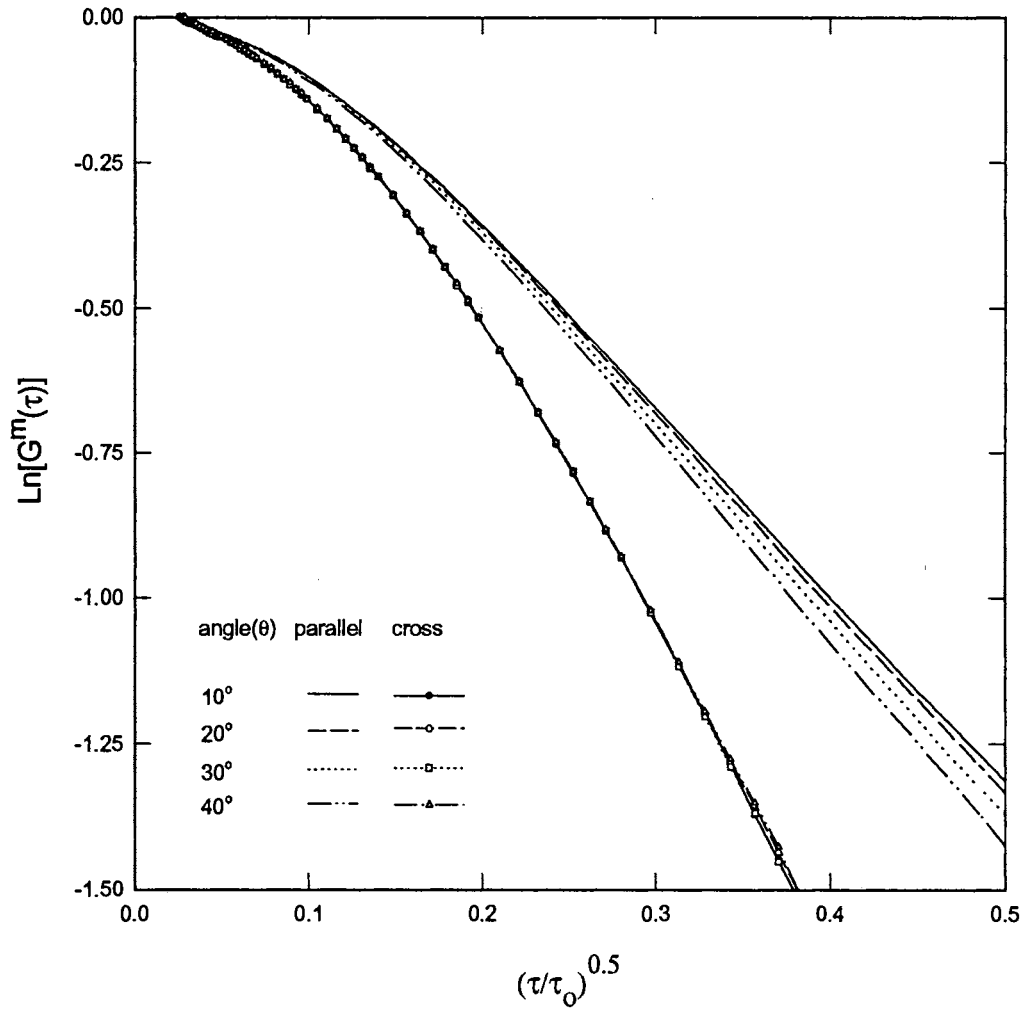


Fig. 68: Transmission: Effect of polarization on detection angle of correlation measurements for optical thickness of 8, particle diameter of 0.3 μm , and laser wavelength of 514.5 nm.

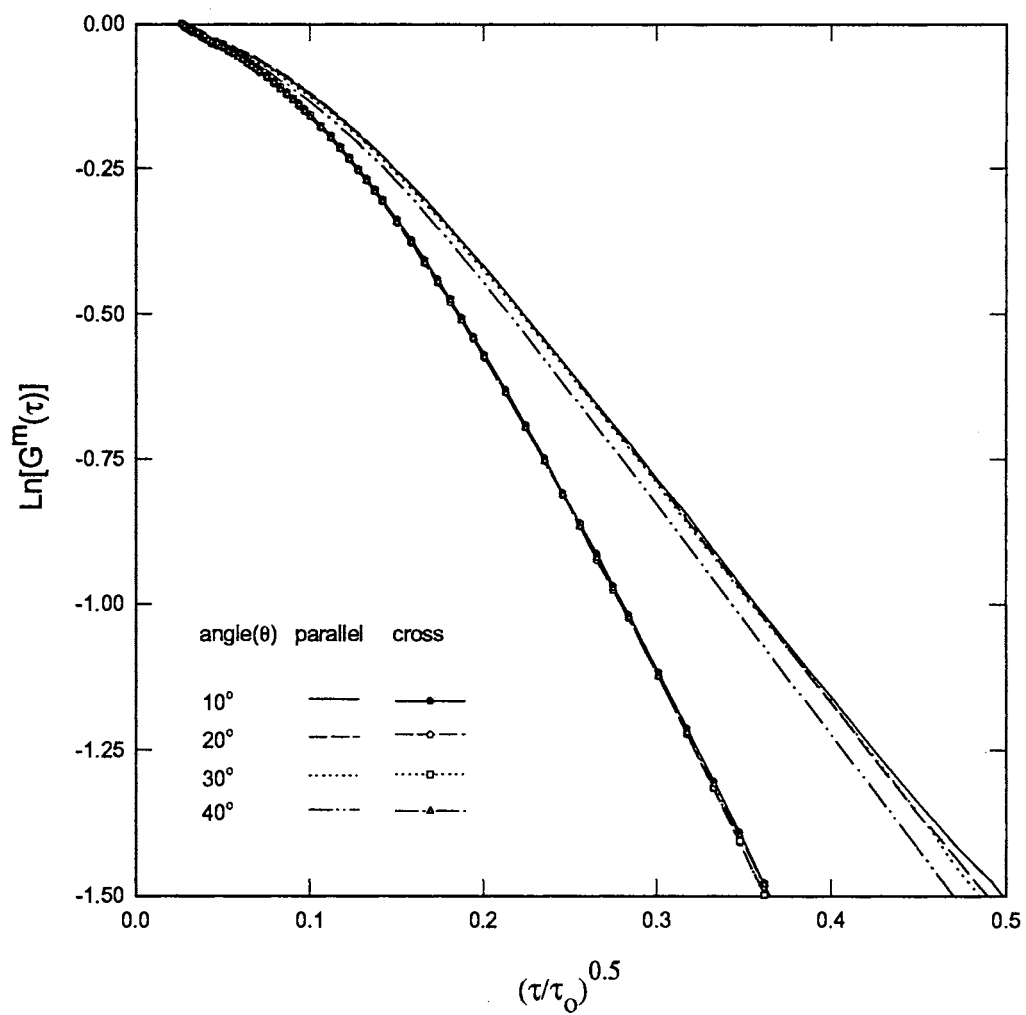


Fig. 69: Transmission: Effect of polarization on detection angle of correlation measurements for optical thickness of 9, particle diameter of 0.3 μm , and laser wavelength of 514.5 nm.

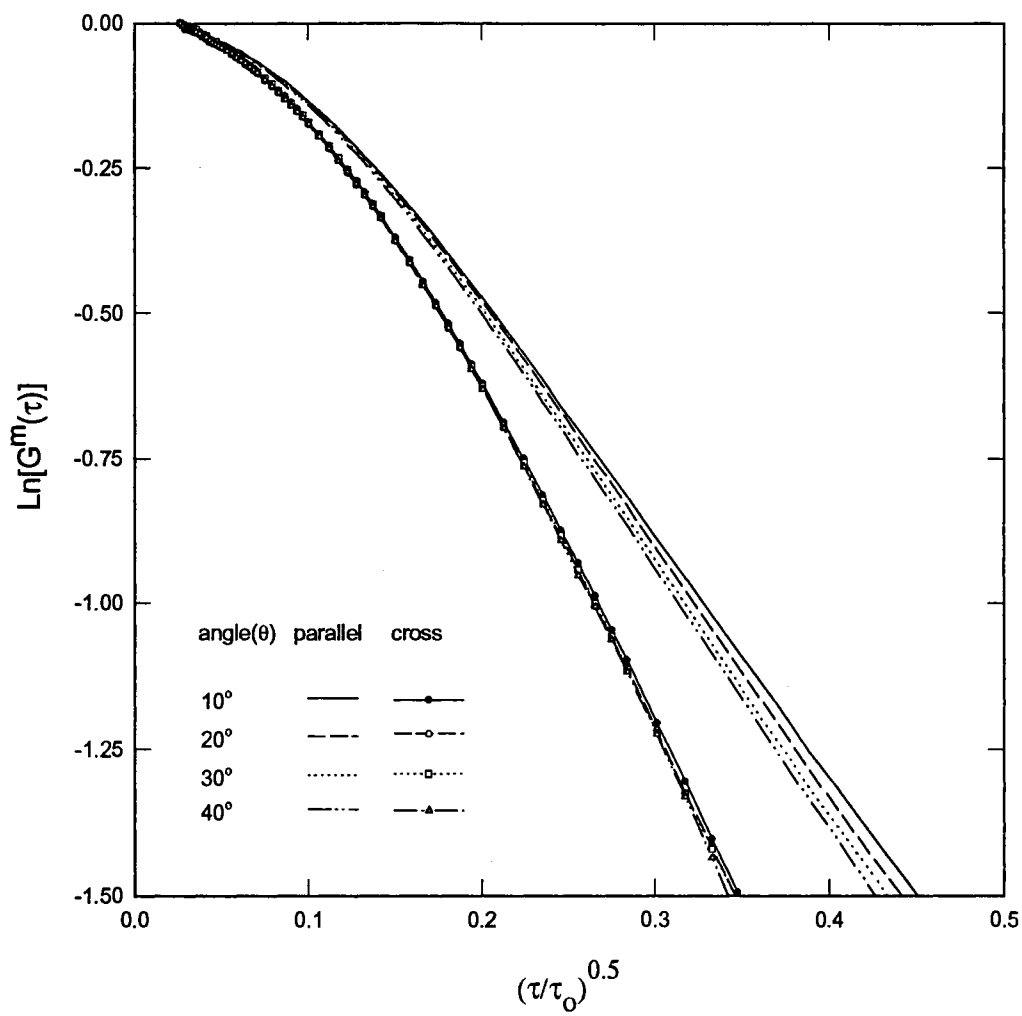


Fig. 70: Transmission: Effect of polarization on detection angle of correlation measurements for optical thickness of 10, particle diameter of 0.3 μm , and laser wavelength of 514.5 nm.

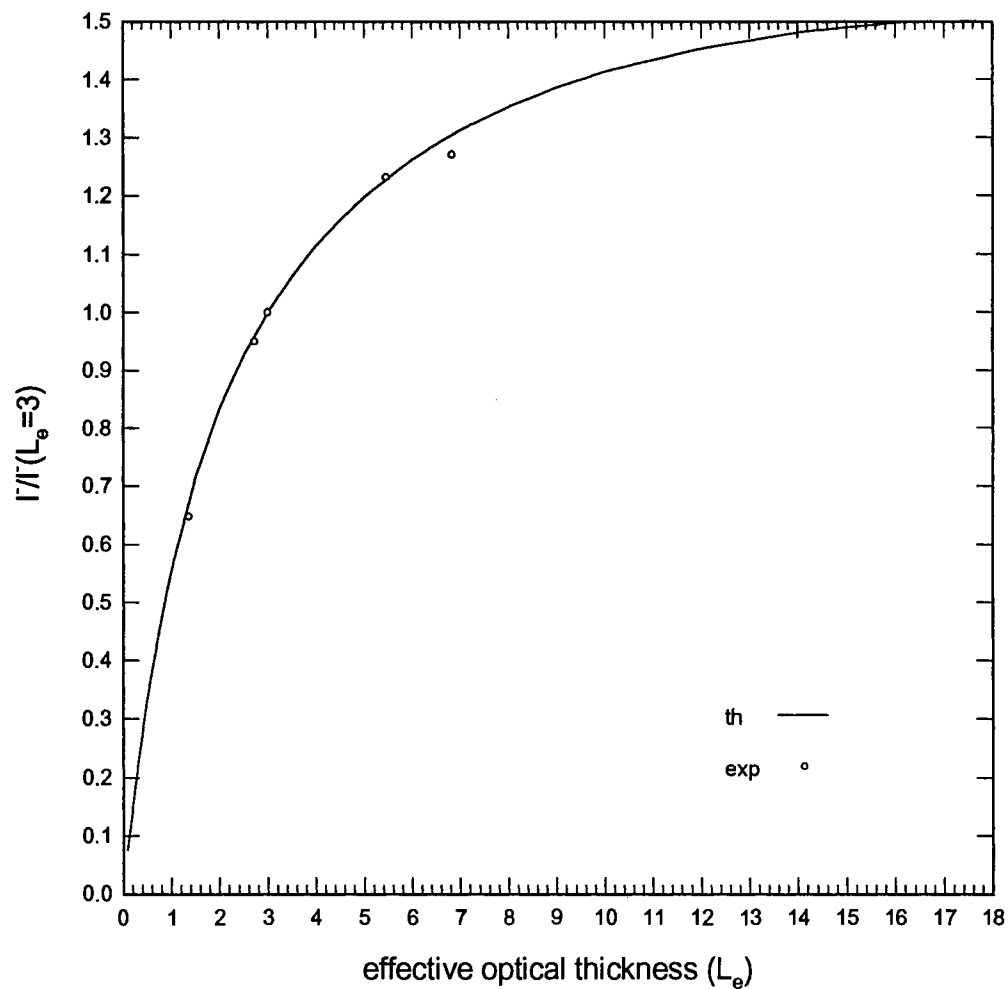


Fig. 71: Back-scattering: Comparison of intensity measurements with the numerical results for index of refraction change at both boundaries ($n=1.331$) at 30° (inside sample) detection angle, particle diameter of $0.3 \mu\text{m}$, and laser wavelength of 514.5 nm .

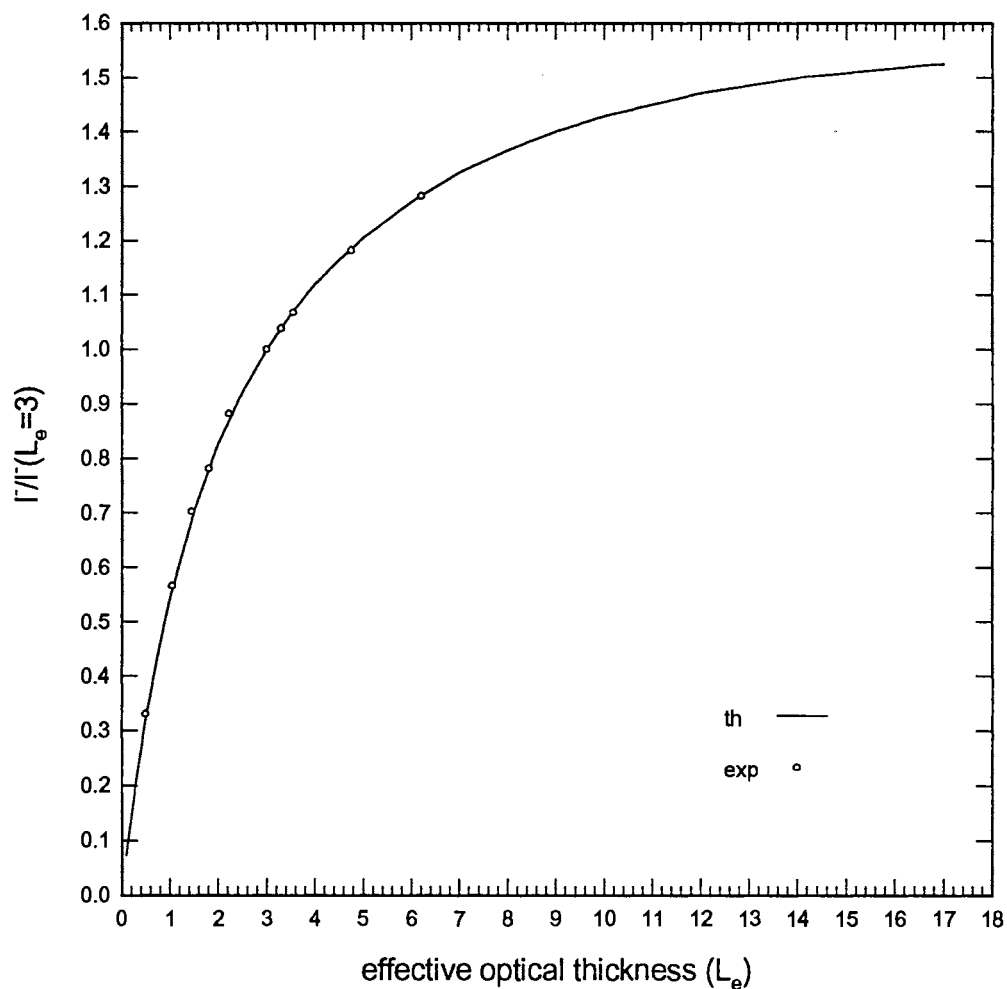


Fig. 72a: Back-scattering: Matching of the intensity measurements with the numerical results for index of refraction change at both boundaries ($n=1.331$) at 10° (outside sample) detection angle, for different particle diameters, and laser wavelength of 514.5 nm.

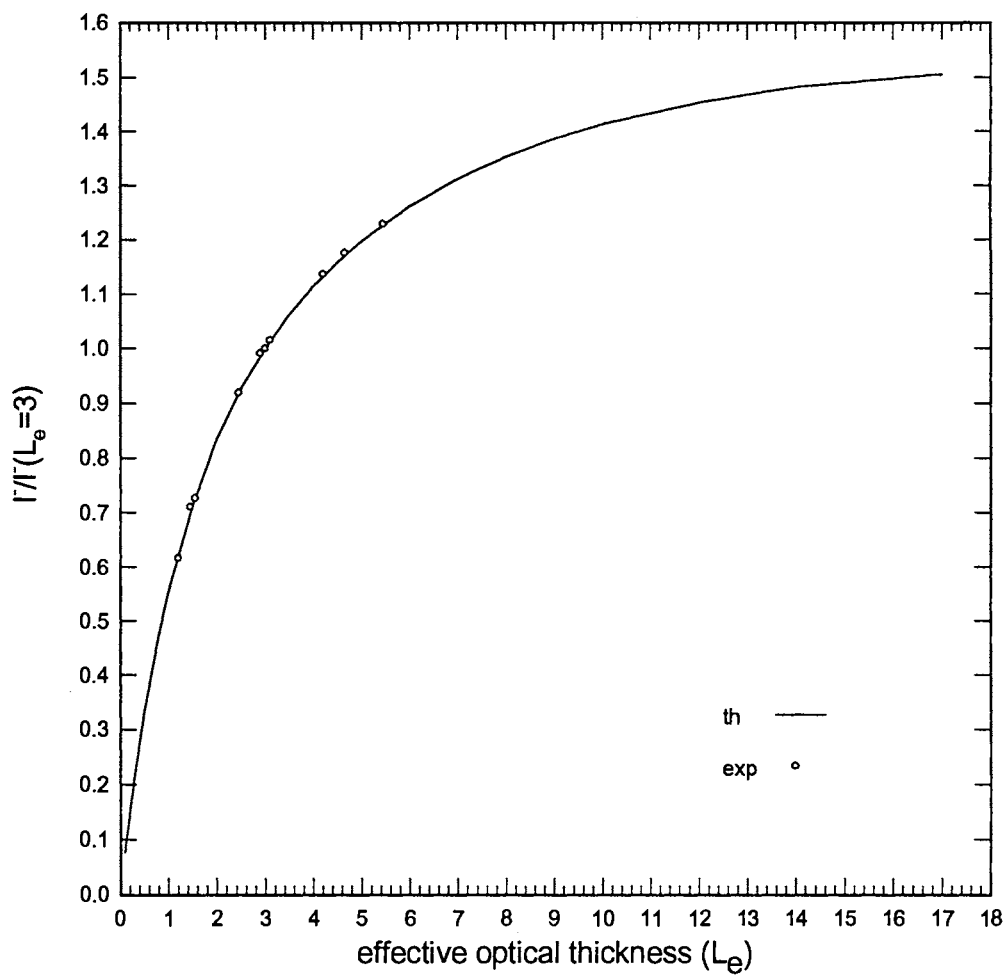


Fig. 72b: Back-scattering: Matching of the intensity measurements with the numerical results for index of refraction change at both boundaries ($n=1.331$) at 30° (outside sample) detection angle, for different particle diameters, and laser wavelength of 514.5 nm.

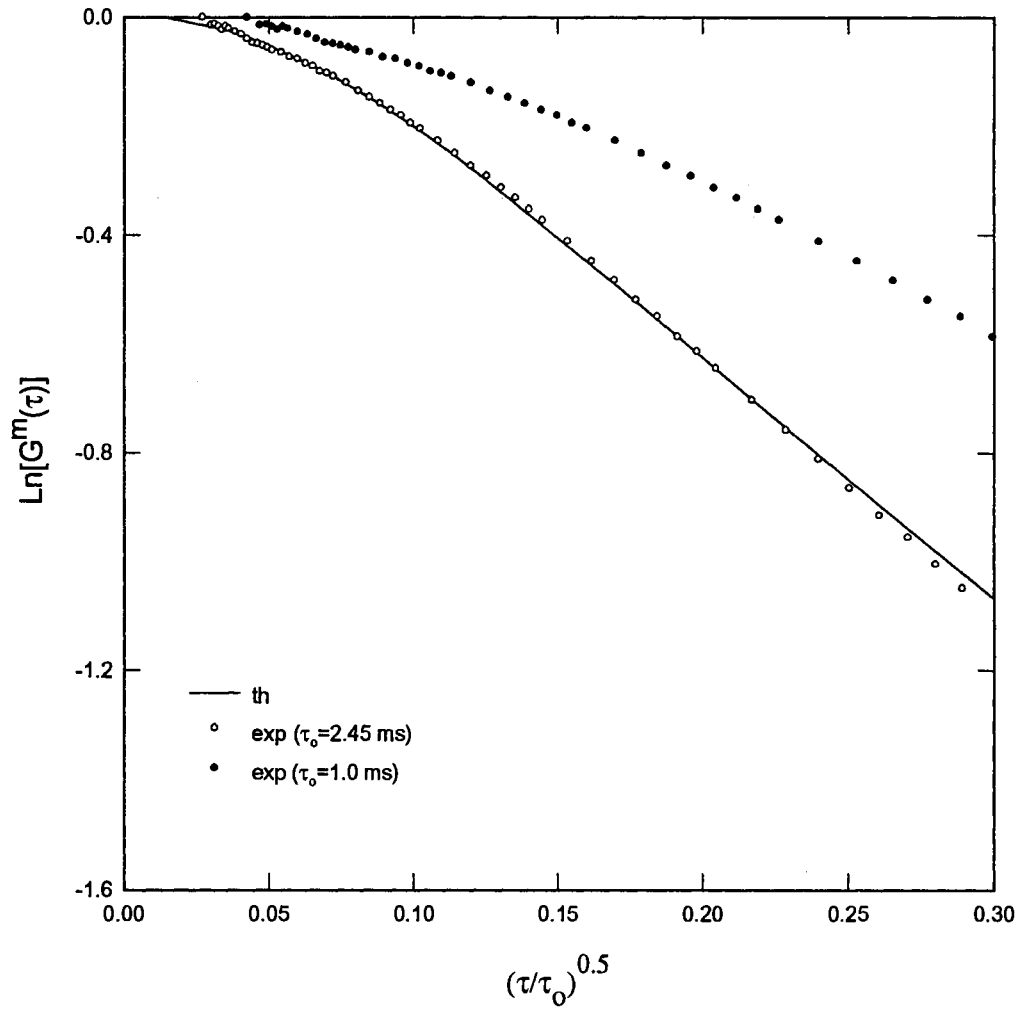


Fig. 73: Matching correlation measurements to numerical results by changing τ_0 for a particle diameter of $0.3 \mu\text{m}$ and a laser wavelength of 514.5 nm .

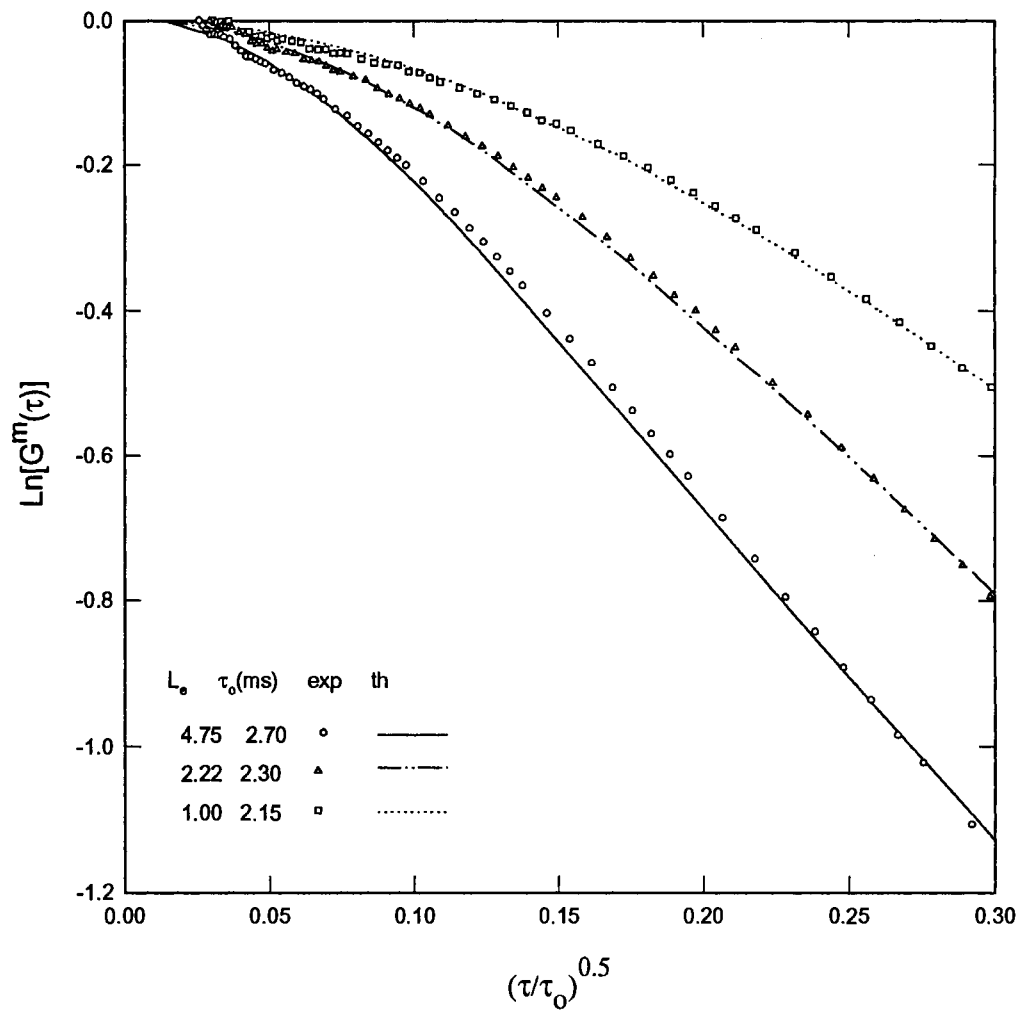


Fig. 74: Matching correlation measurements for different optical thicknesses to numerical results by changing τ_0 for particle diameter of $0.3 \mu\text{m}$, laser wavelength of 514.5 nm , and 10° (outside sample) from back-scattering.

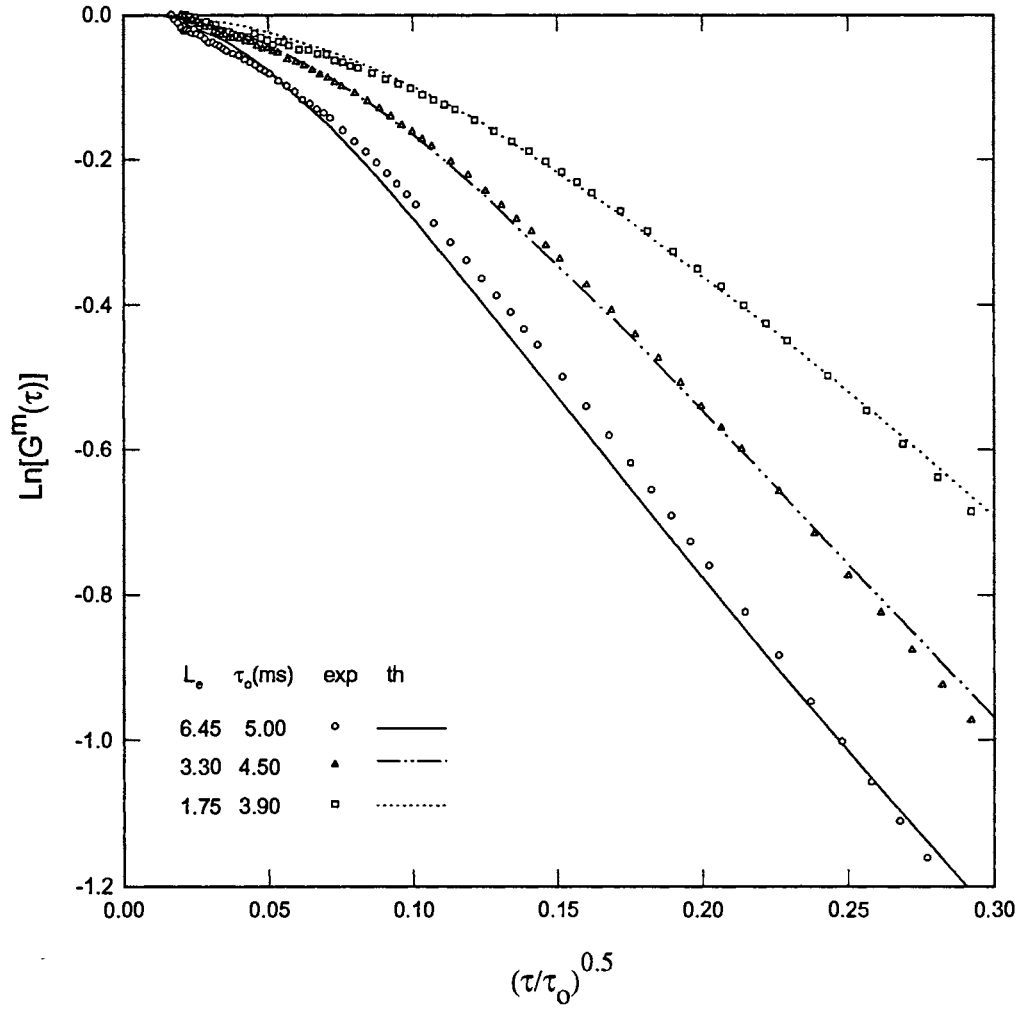


Fig. 75: Matching correlation measurements for different optical thicknesses to numerical results by changing τ_0 for particle diameter of 0.497 μm , laser wavelength of 514.5 nm, and 10° (outside sample) from back-scattering.

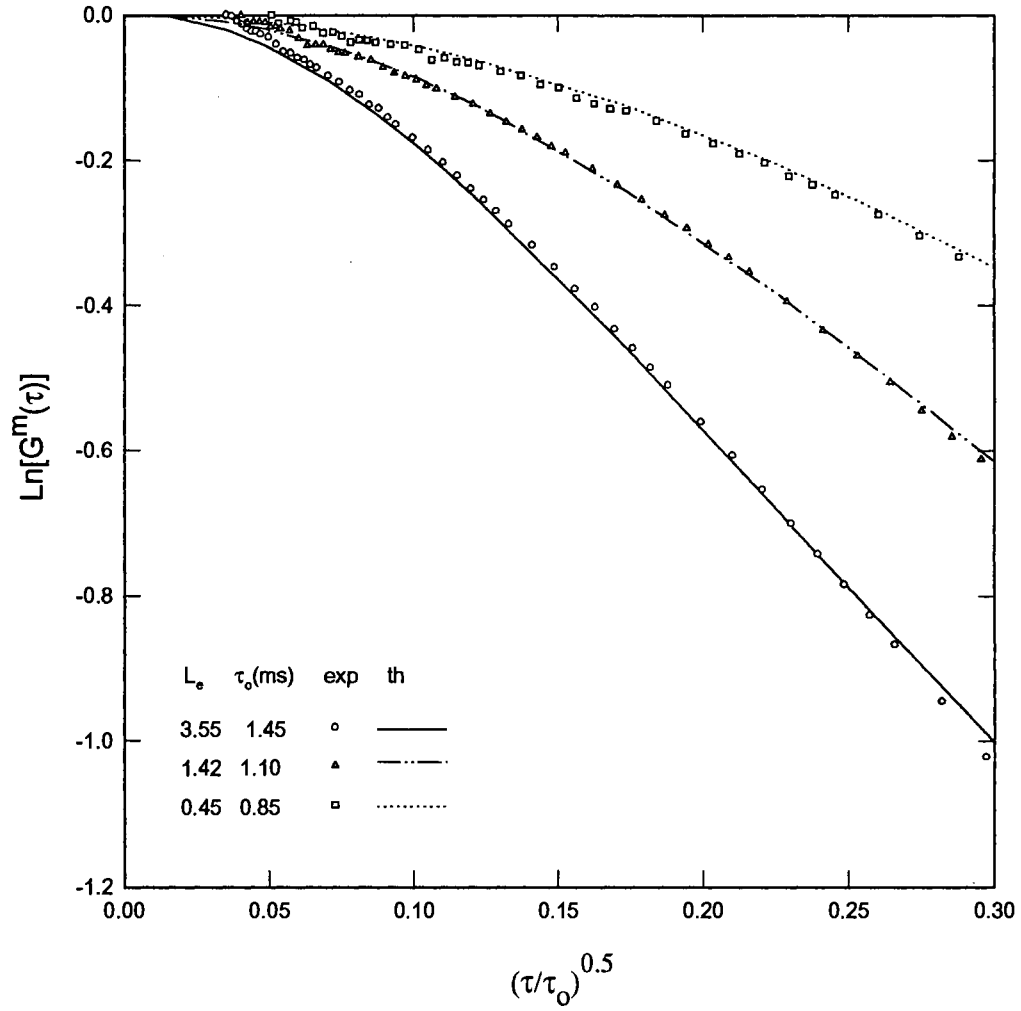


Fig. 76: Matching correlation measurements for different optical thicknesses to numerical results by changing τ_0 for particle diameter of 0.107 μm , laser wavelength of 514.5 nm, and 10° (outside sample) from back-scattering.

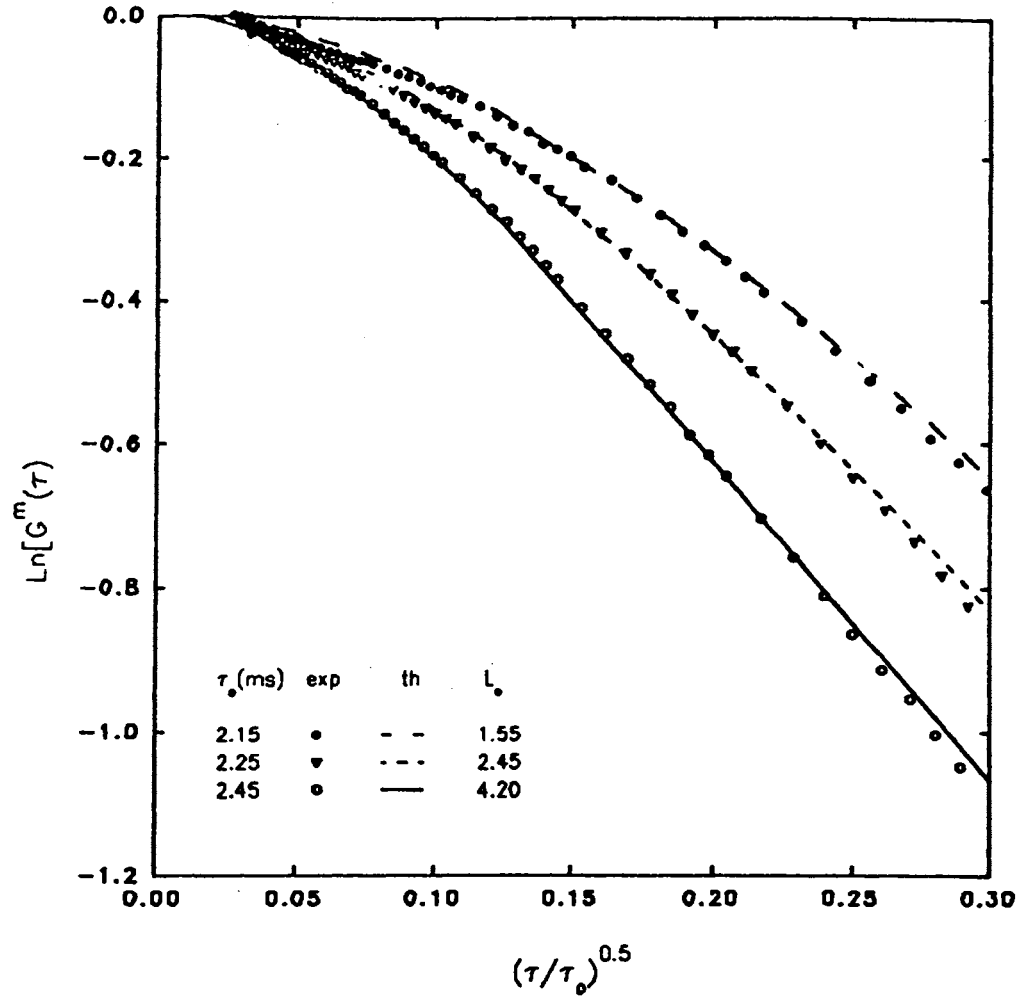


Fig. 77: Matching correlation measurements for different optical thicknesses to numerical results by changing τ_0 for particle diameter of $0.3 \mu\text{m}$, laser wavelength of 514.5 nm , and 30° (outside sample) from back-scattering.

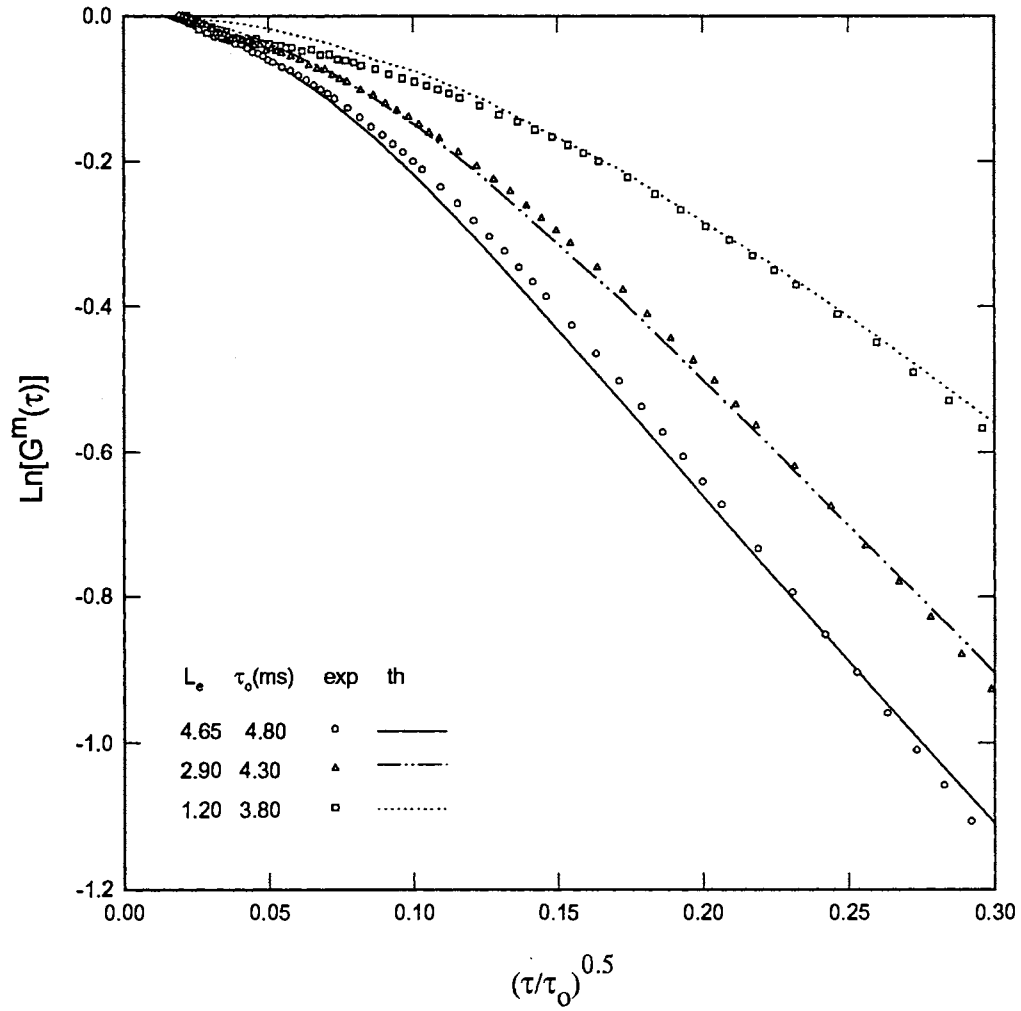


Fig. 78: Matching correlation measurements for different optical thicknesses to numerical results by changing τ_0 for particle diameter of 0.497 μm , laser wavelength of 514.5 nm, and 30° (outside sample) from back-scattering.

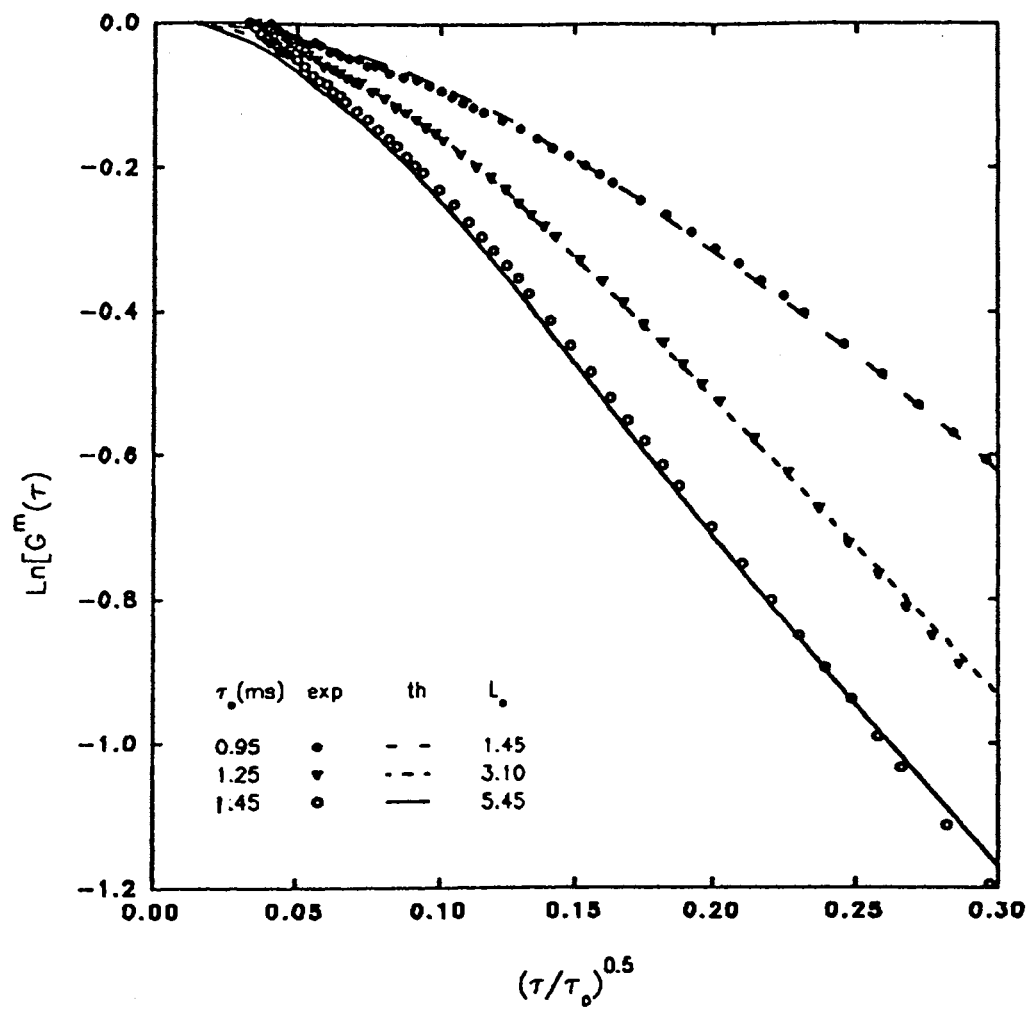


Fig. 79: Matching correlation measurements for different optical thicknesses to numerical results by changing τ_0 for particle diameter of 0.107 μm , laser wavelength of 514.5 nm, and 30° (outside sample) from back-scattering.

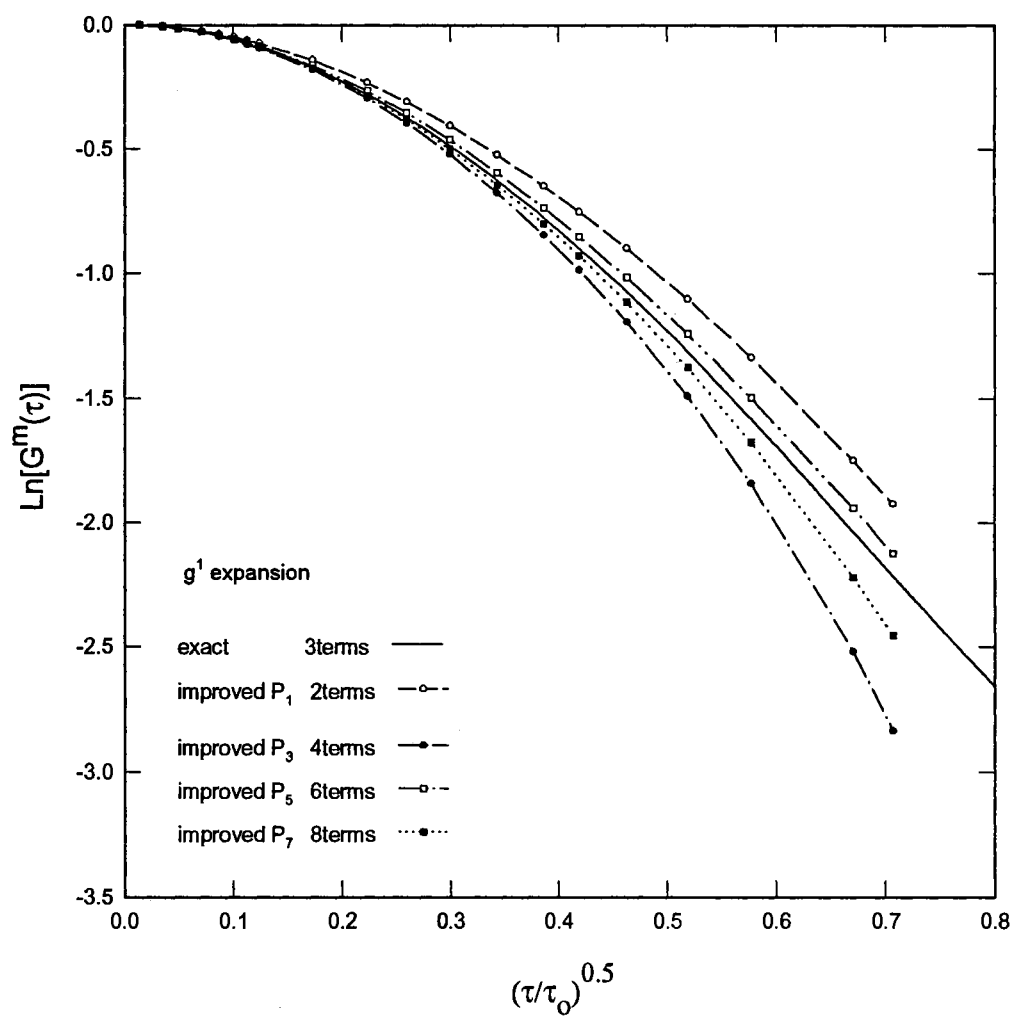


Fig. 80: Back-scattering: Comparison of improved P_N approximation with exact 3 term Legendre expansion of g^1 for $L_0=1.0$.

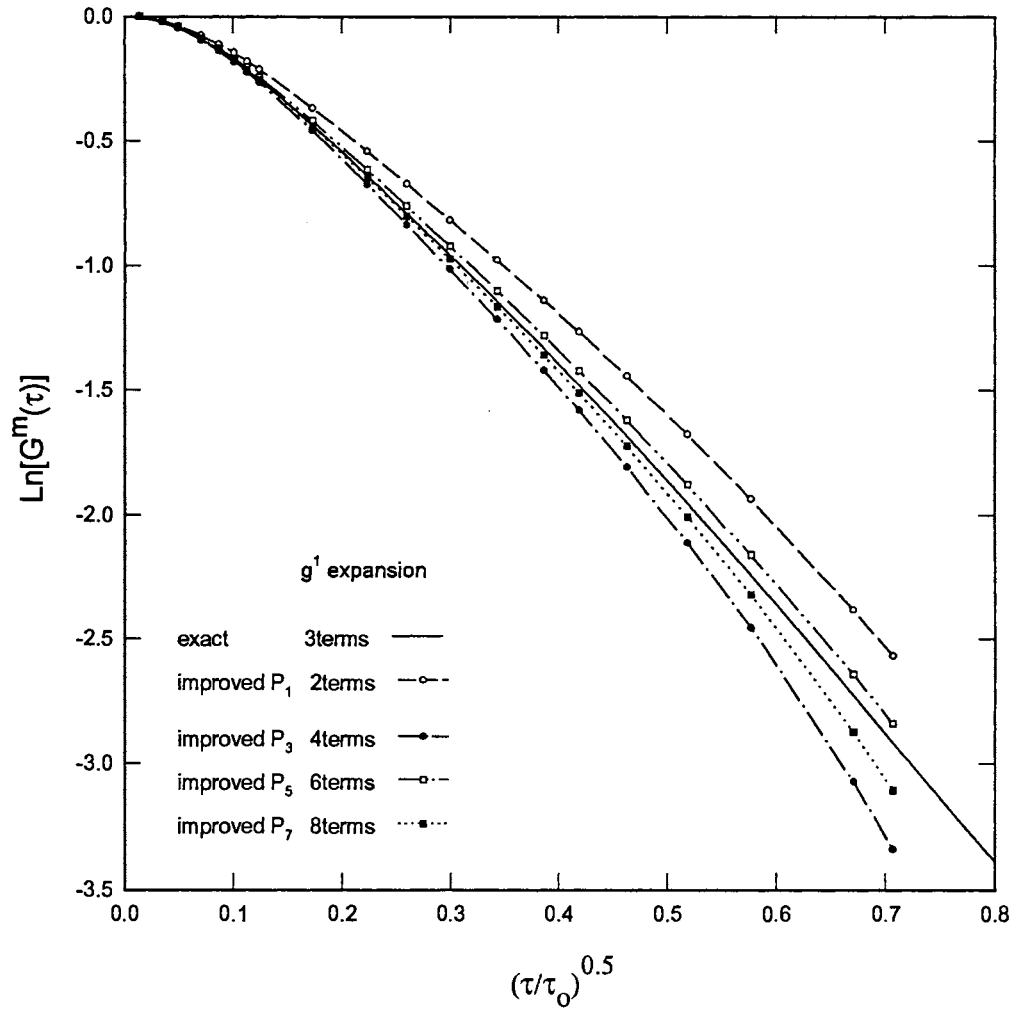


Fig. 81: Back-scattering: Comparison of improved P_N approximation with exact 3 term Legendre expansion of g^1 for $L_0=5.0$.

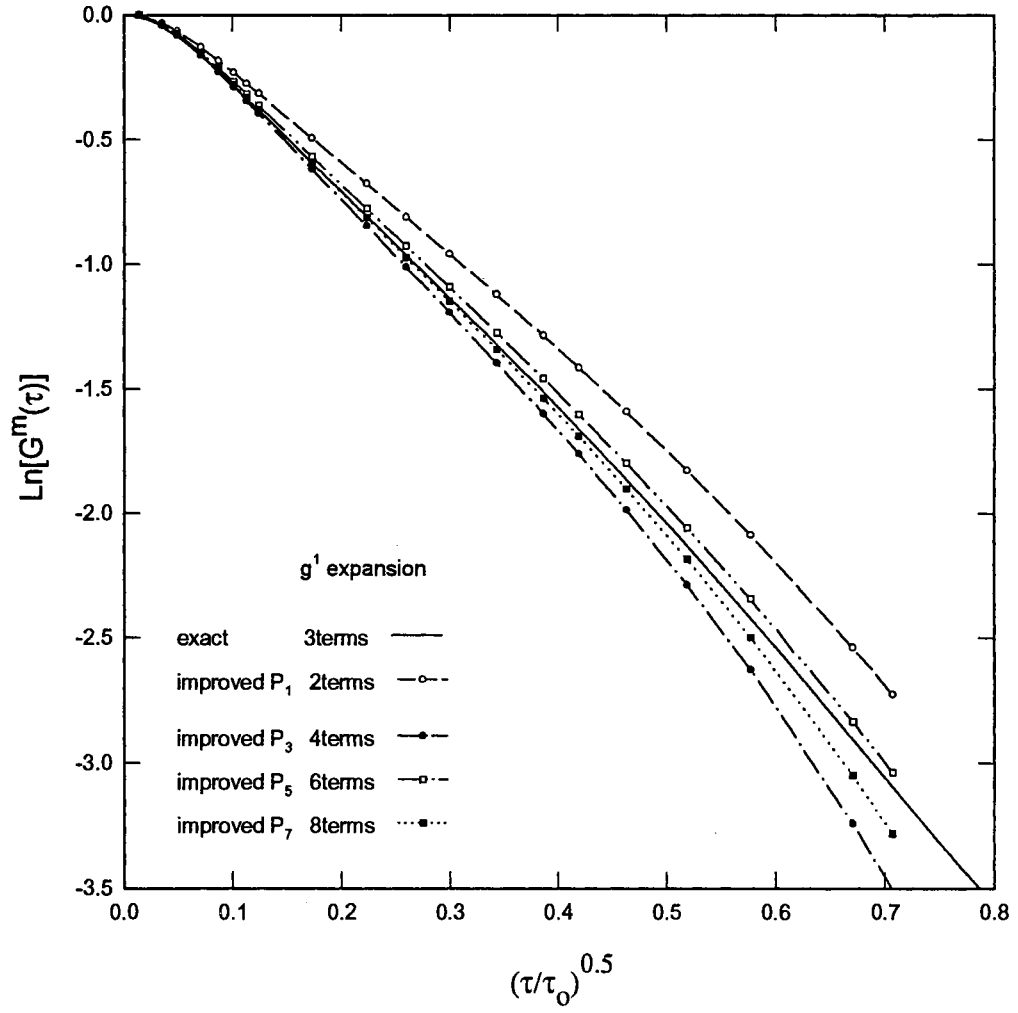


Fig. 82: Back-scattering: Comparison of improved P_N approximation with exact 3 term Legendre expansion of g^1 for $L_0=10.0$.

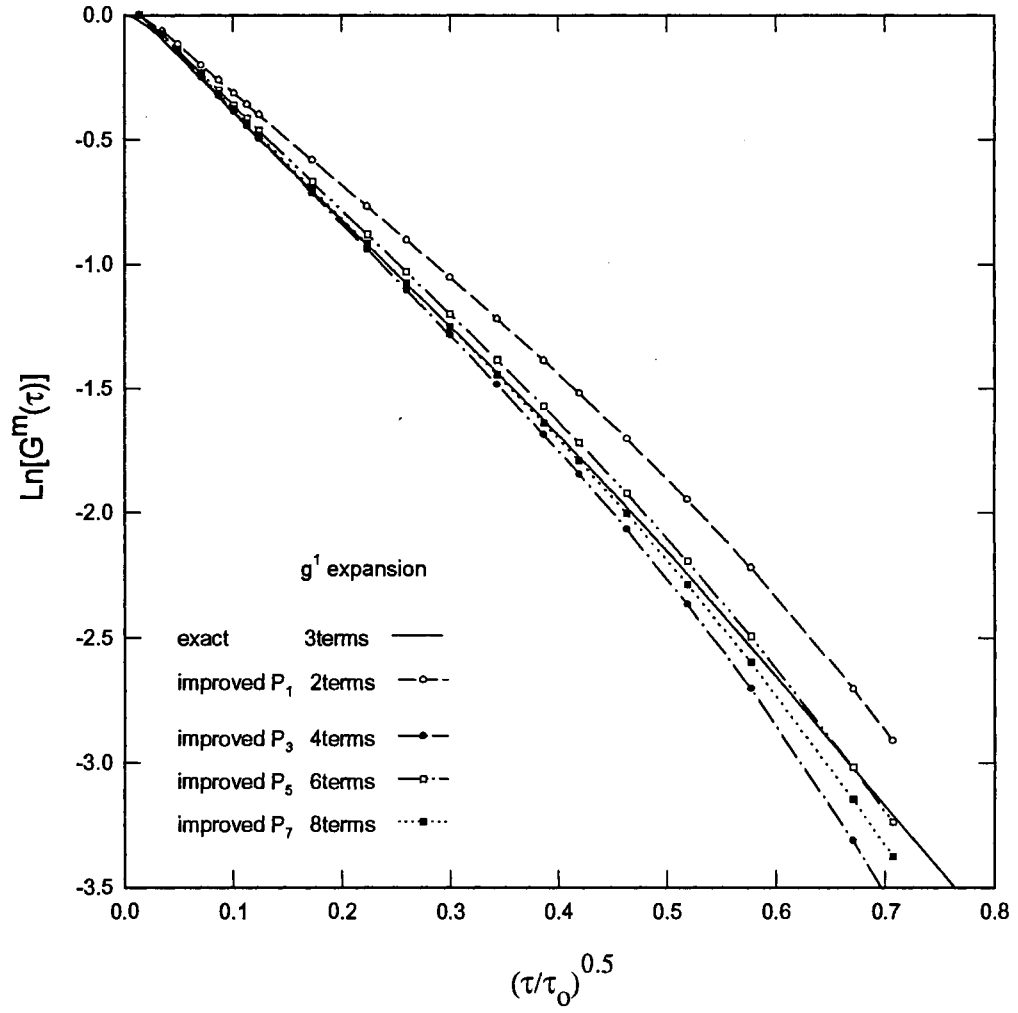


Fig. 83: Back-scattering: Comparison of improved P_N approximation with exact 3 term Legendre expansion of g¹ for L₀=25.0.

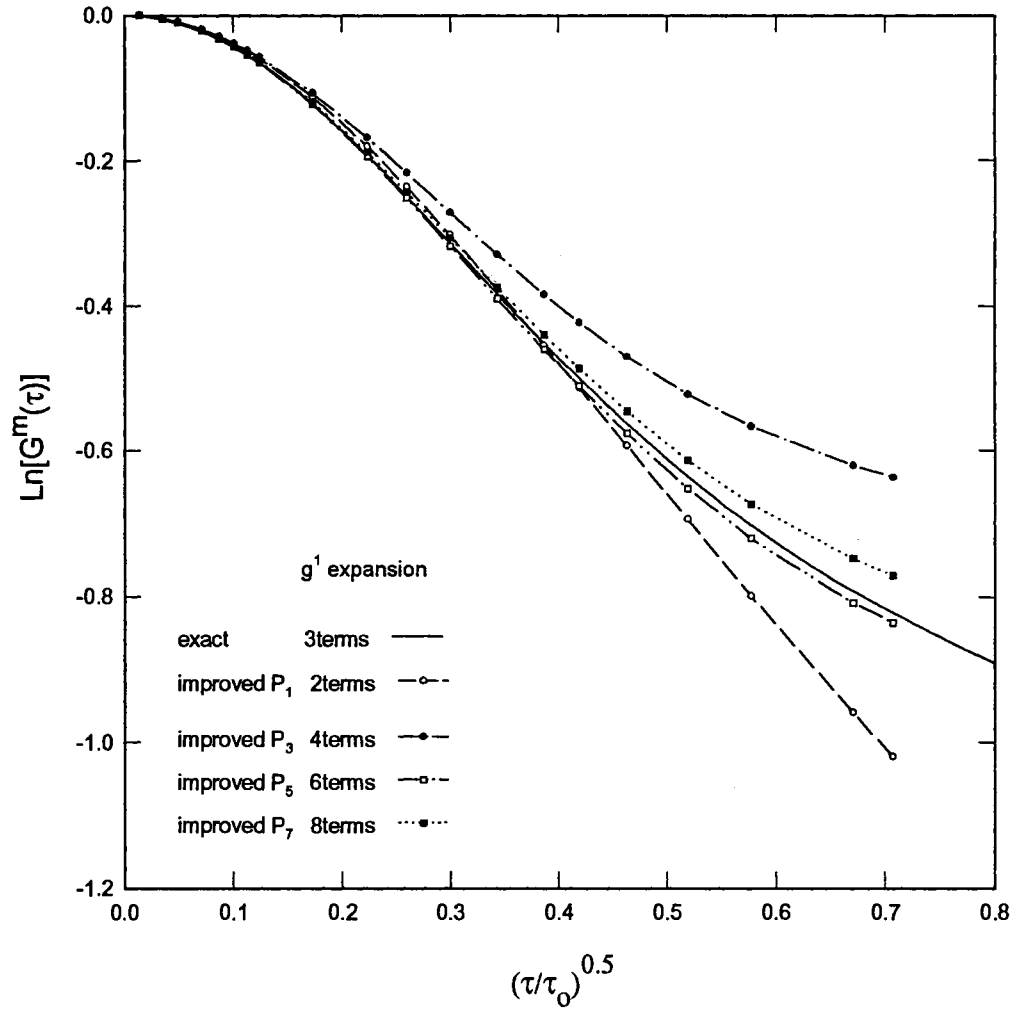


Fig. 84: Transmission: Comparison of improved P_N approximation with exact 3 term Legendre expansion of g¹ for L₀=1.0.

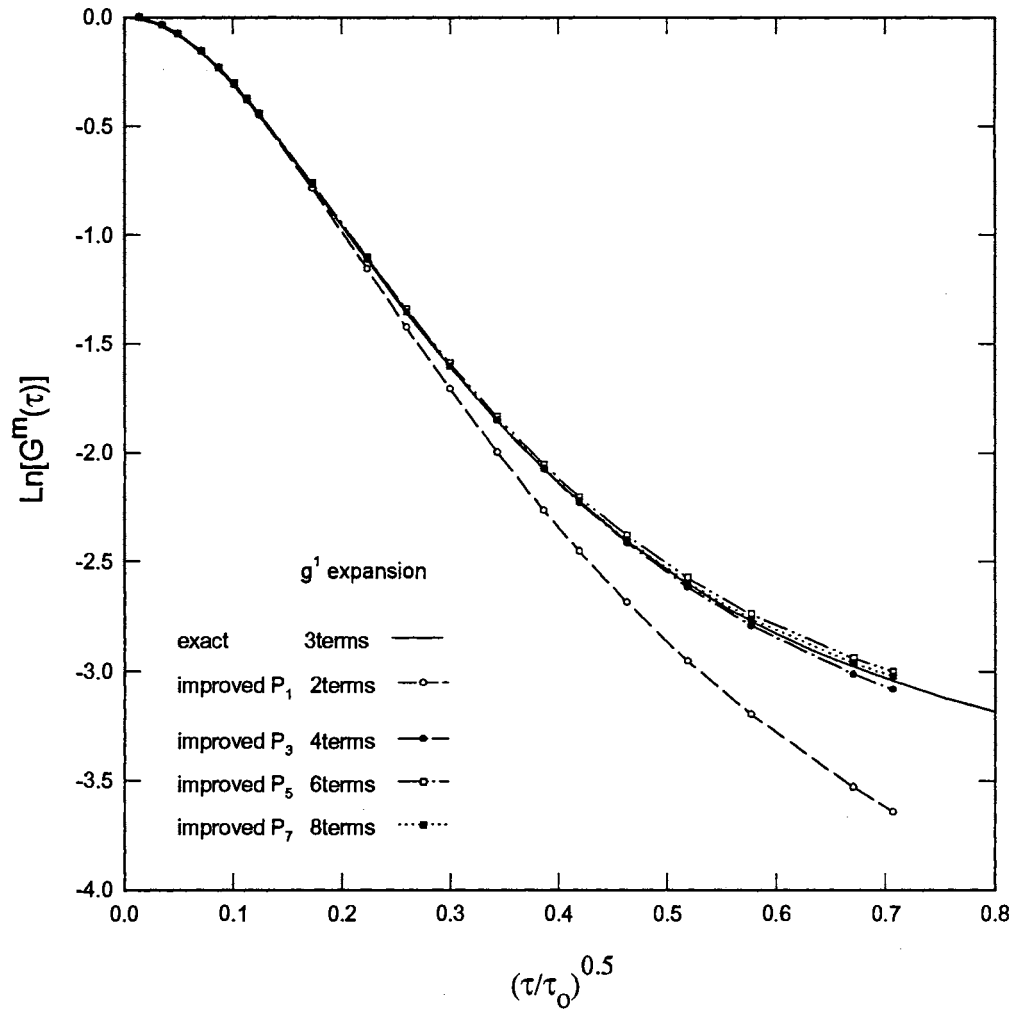


Fig. 85: Transmission: Comparison of improved P_N approximation with exact 3 term Legendre expansion of g^1 for $L_0=5.0$.

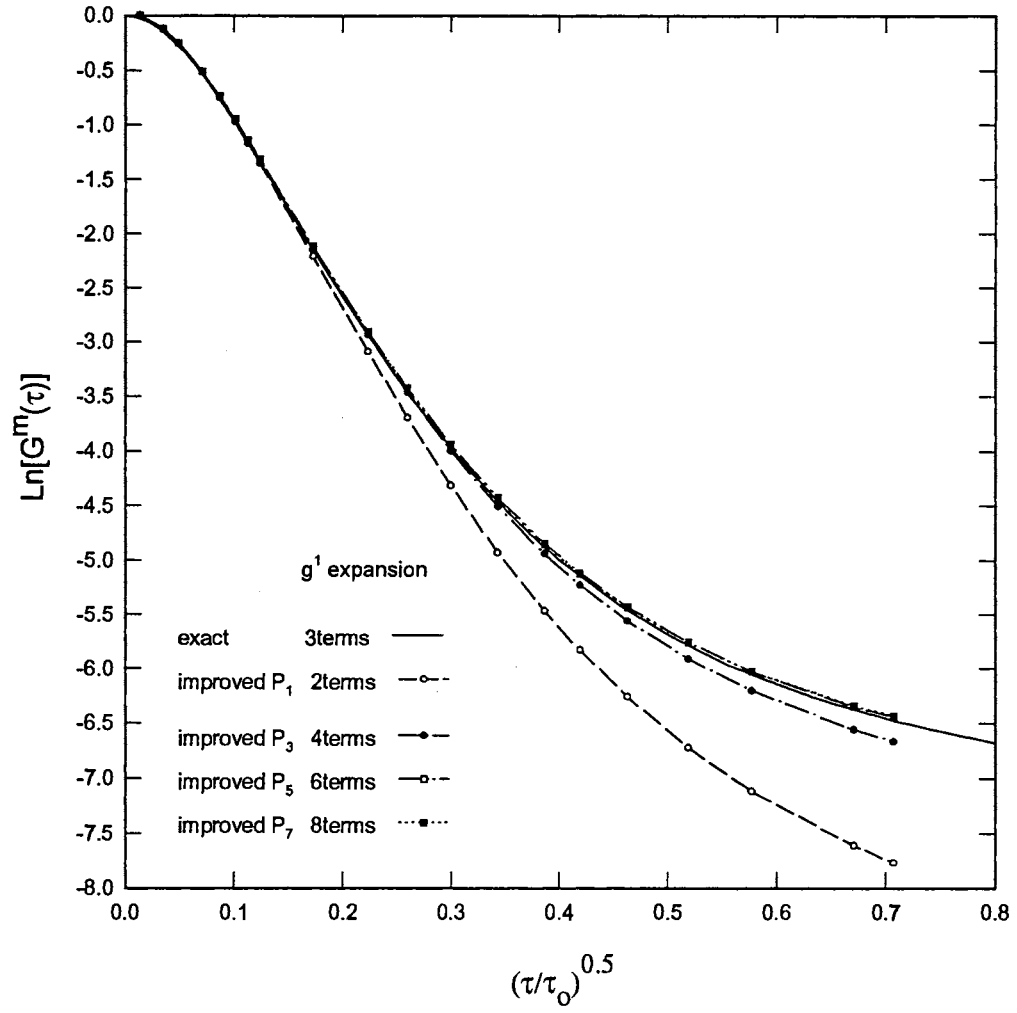


Fig. 86: Transmission: Comparison of improved P_N approximation with exact 3 term Legendre expansion of g^1 for $L_0=10.0$.

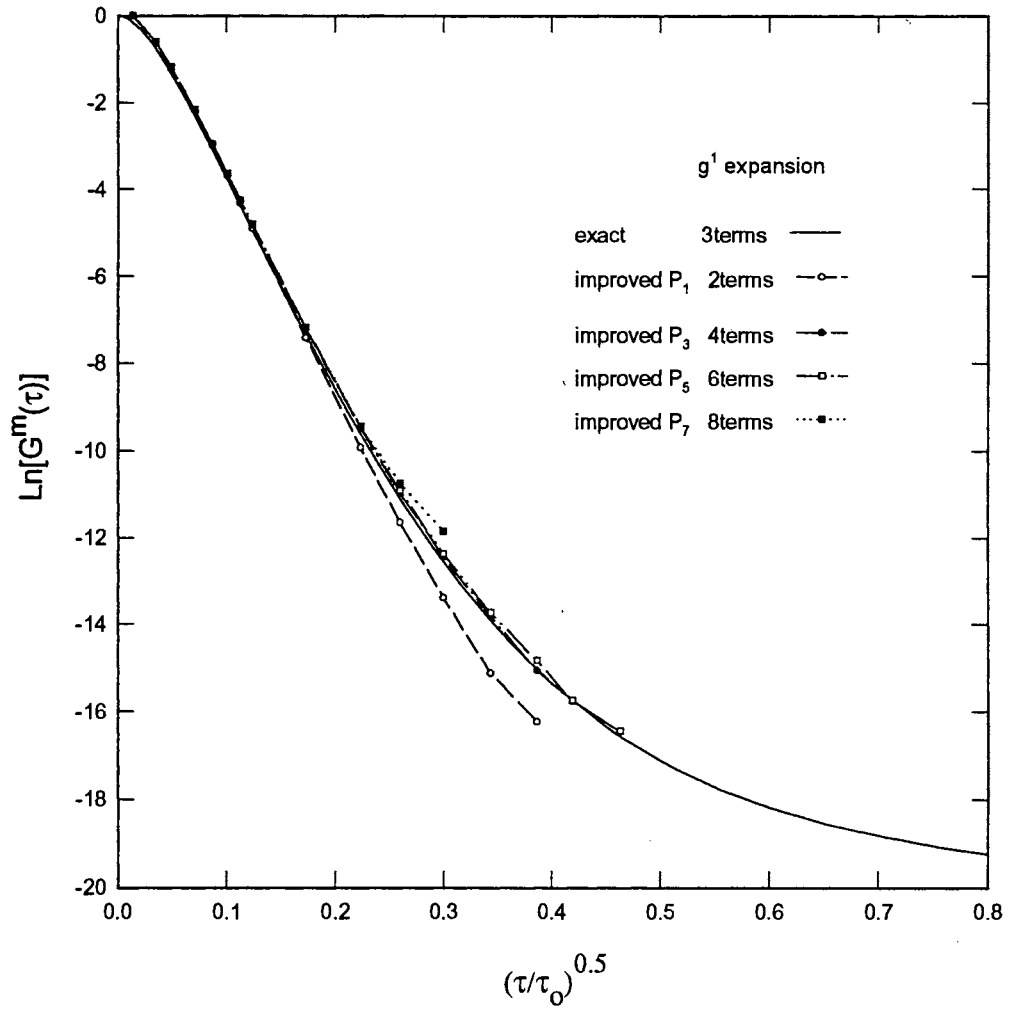


Fig. 87: Transmission: Comparison of improved P_N approximation with exact 3 term Legendre expansion of g^1 for $L_0=25.0$.

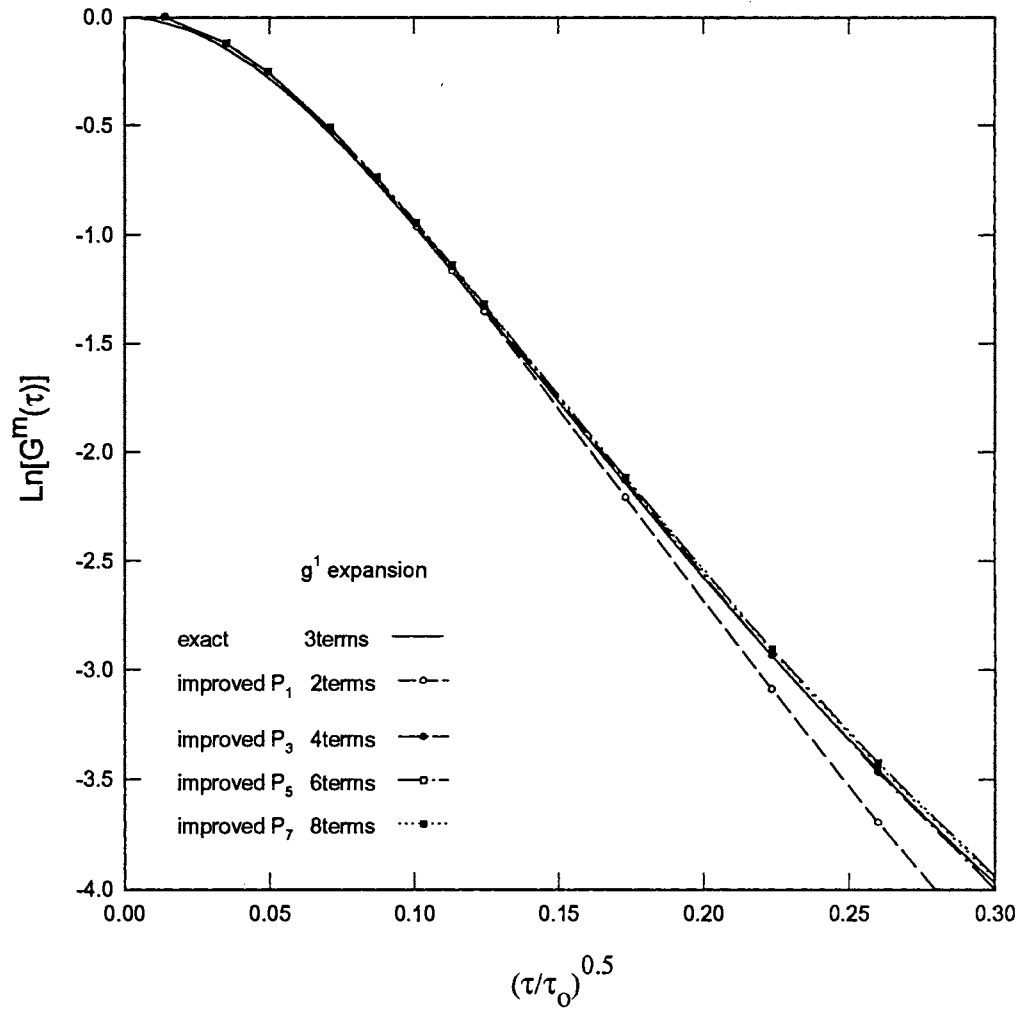


Fig. 88: Transmission: Comparison of improved P_N approximation with exact 3 term Legendre expansion of g^1 for $L_0=10.0$.

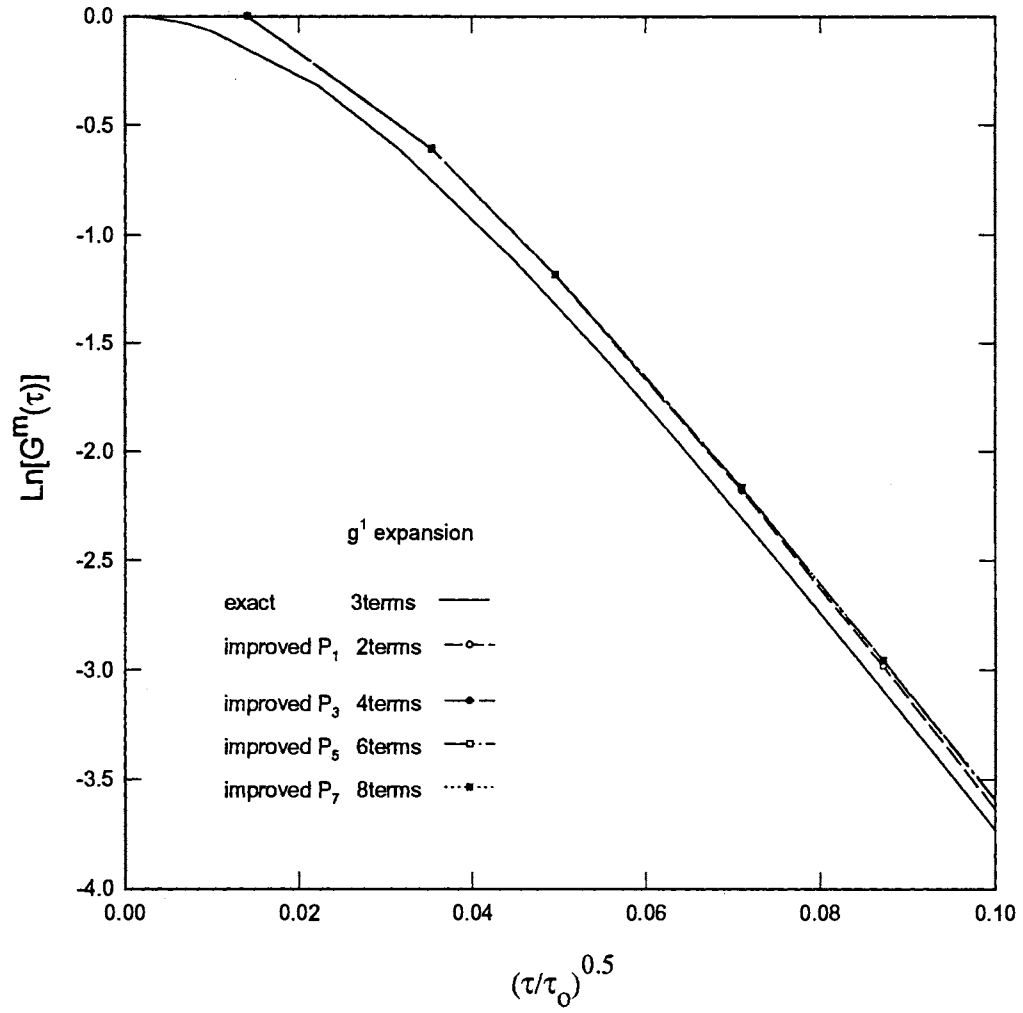


Fig. 89: Transmission: Comparison of improved P_N approximation with exact 3 term Legendre expansion of g^1 for $L_0=25.0$.

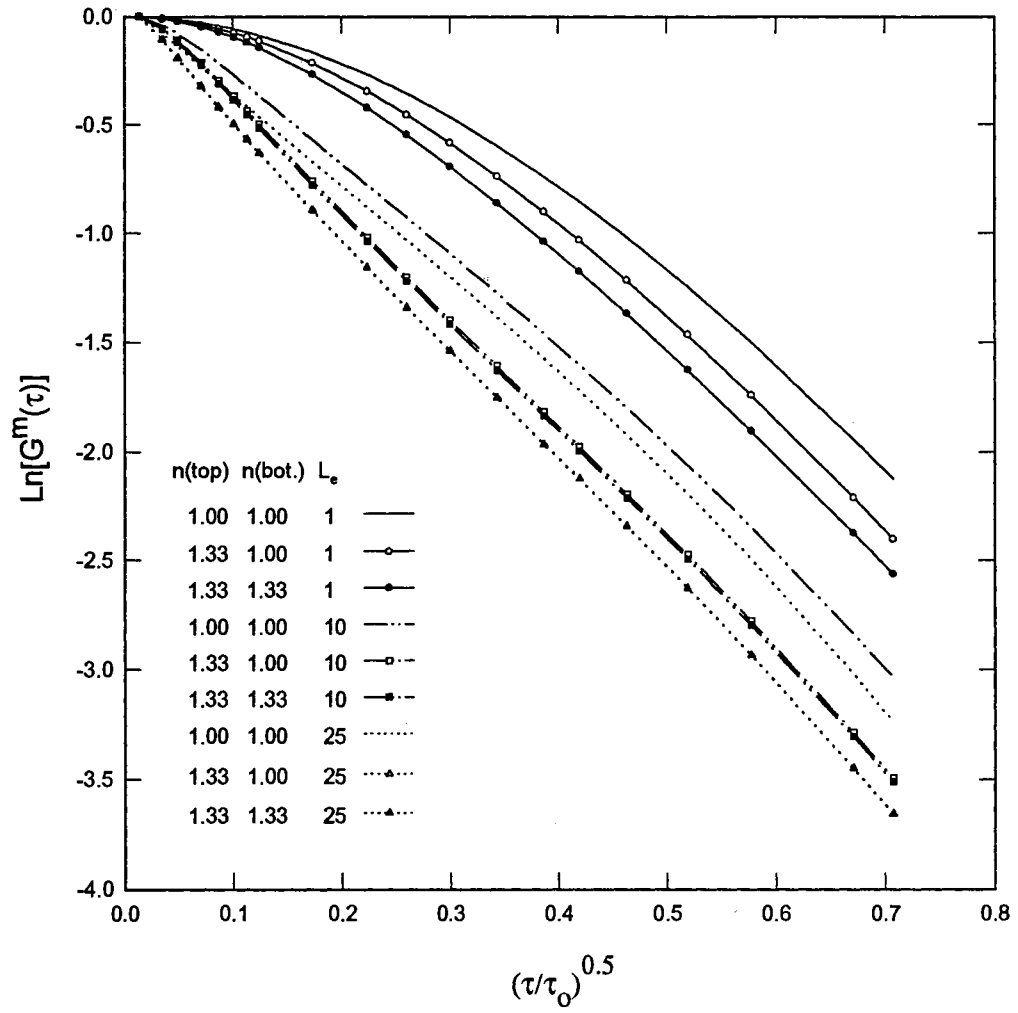


Fig. 90a: Back-scattering: Effect of refractive index change at the boundaries for improved P_5 approximation for $L_e=1.0$, 10, and 25.

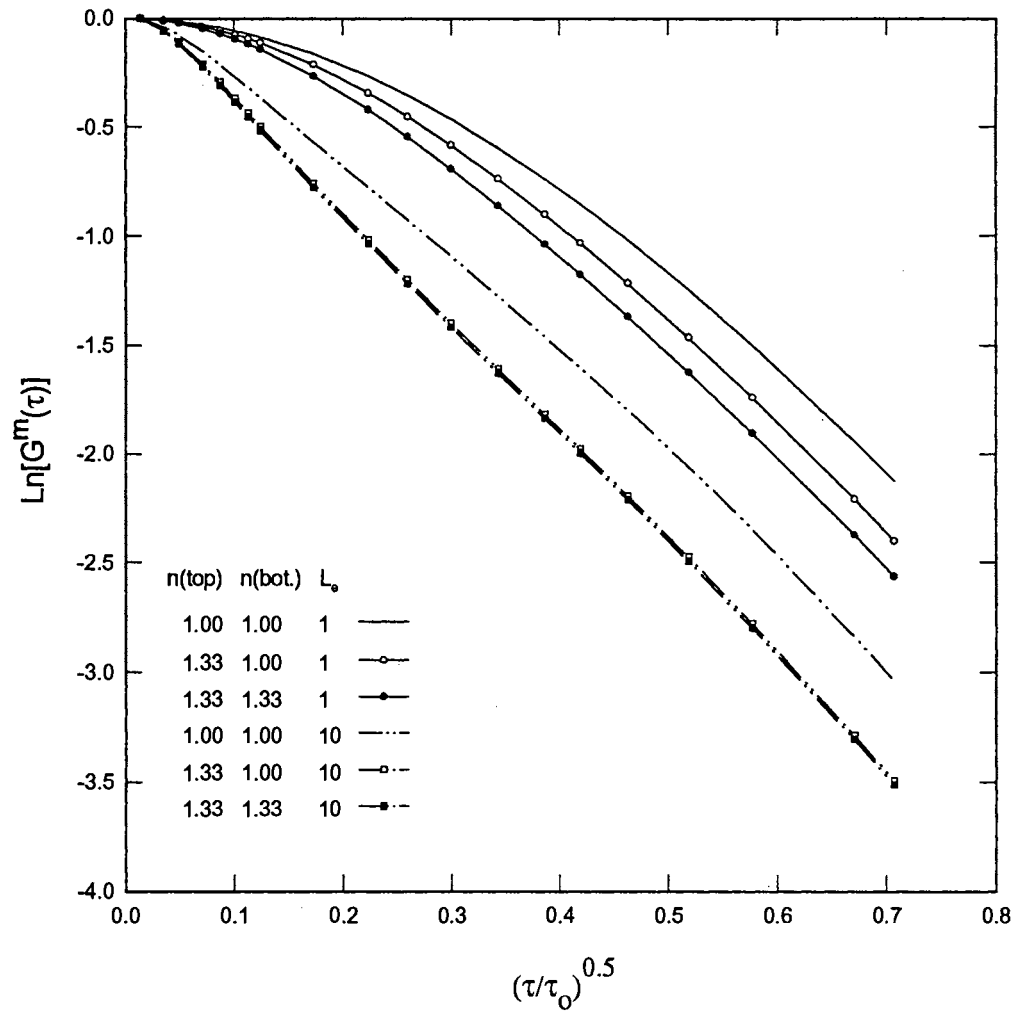


Fig. 90b: Back-scattering: Effect of refractive index change at the boundaries for improved P_5 approximation for $L_e=1.0$ and 10.

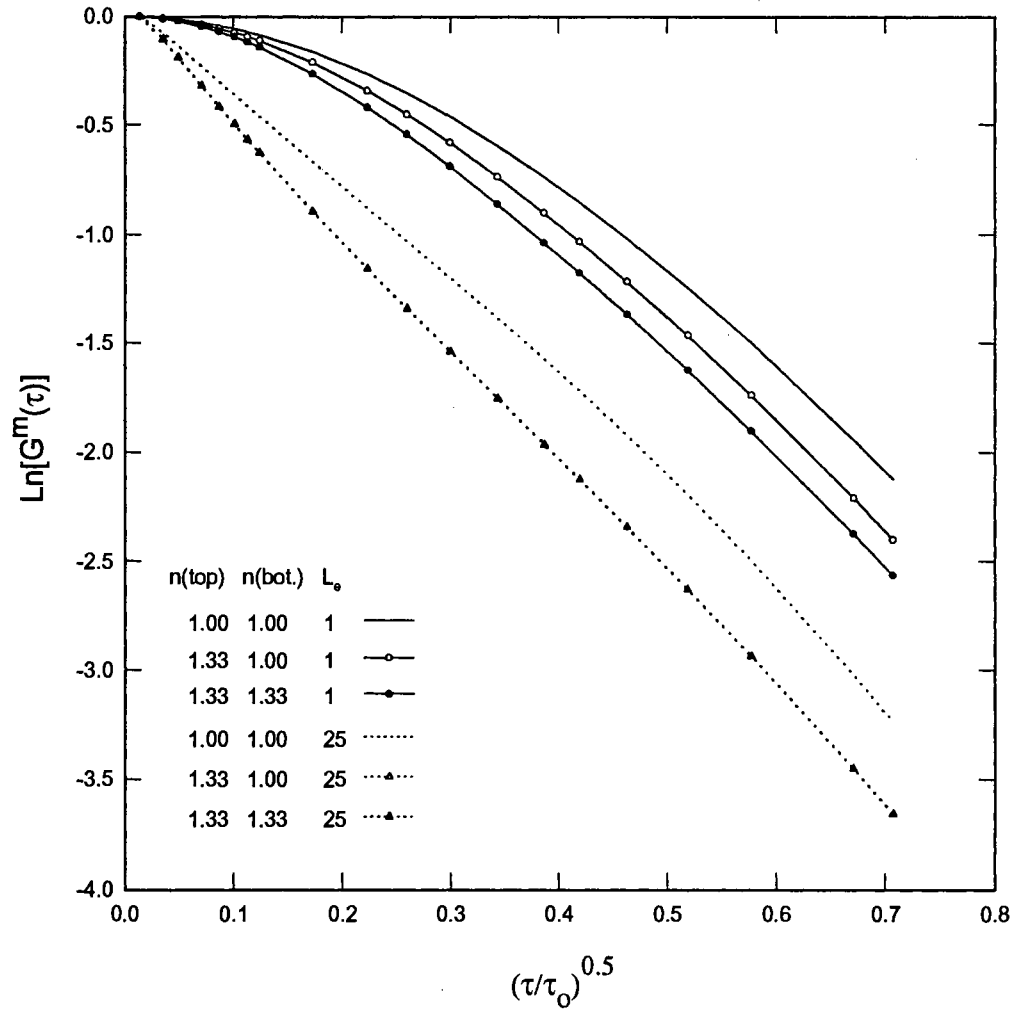


Fig. 90c: Back-scattering: Effect of refractive index change at the boundaries for improved P_5 approximation for $L_e=1.0$ and 25.

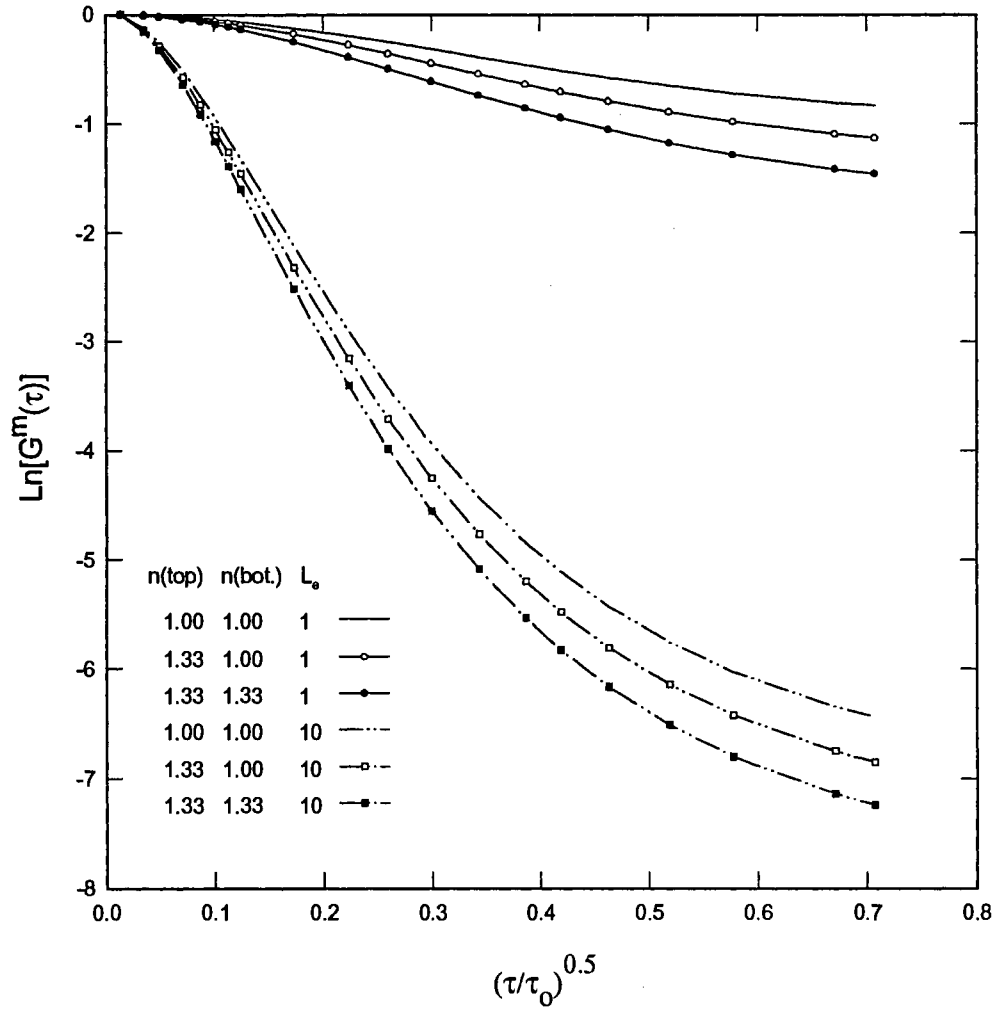


Fig. 91: Transmission: Effect of refractive index change at the boundaries for improved P_5 approximation for $L_e=1.0$ and 10 .

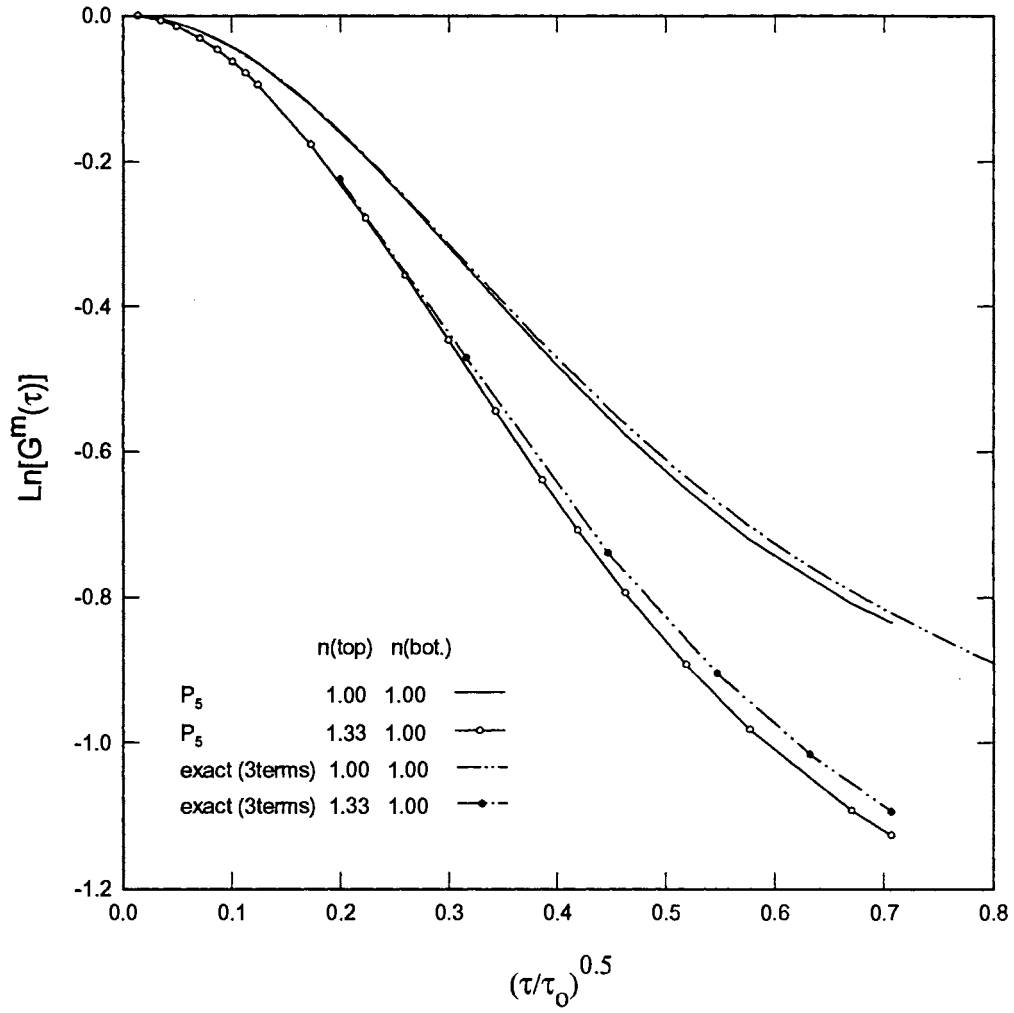


Fig. 92: Transmission: Comparison of improved P_5 approximation with exact 3 term Legendre expansion of g^1 for $L_0=1.0$ with no and one index of refraction change at the boundaries.

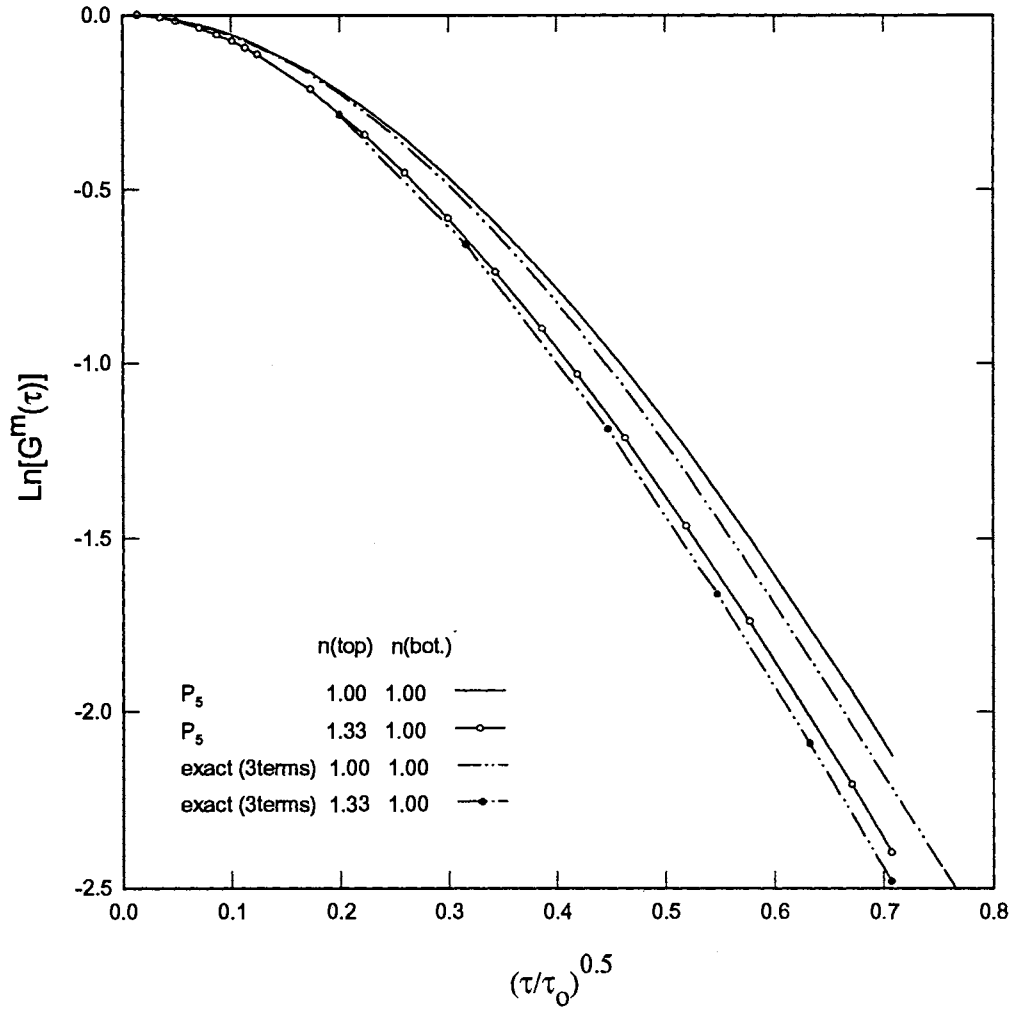


Fig. 93: Back-scattering: Comparison of improved P_5 approximation with exact 3 term Legendre expansion of g^1 for $L_0=1.0$ with no and one index of refraction change at the boundaries.

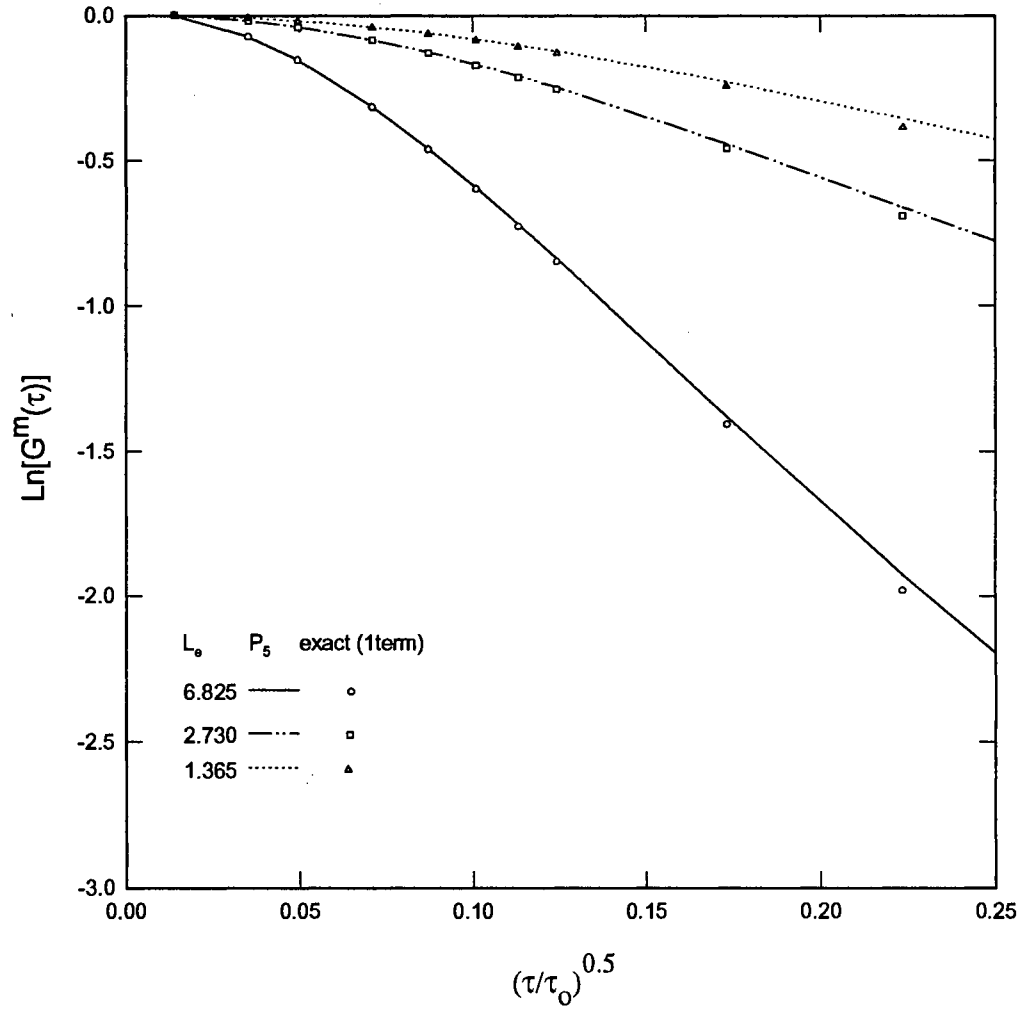


Fig. 94: Transmission: Comparison of improved P_5 approximation with exact 1 term Legendre expansion of g^1 for different optical thicknesses (the same as Fig. 30) with one index of refraction change at the boundaries.

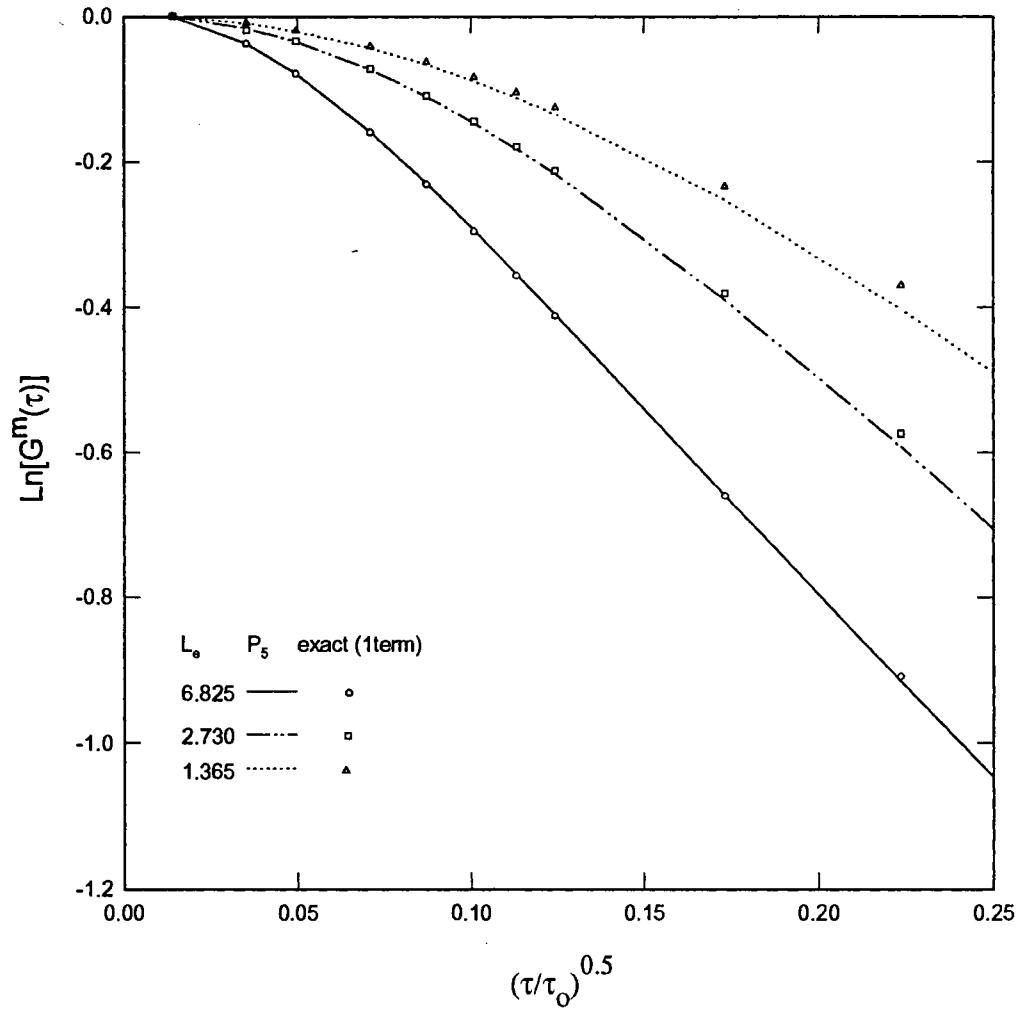


Fig. 95: Back-scattering: Comparison of improved P_5 approximation with exact 1 term Legendre expansion of g^1 for different optical thicknesses (the same as Fig. 34) with one index of refraction change at the boundaries.

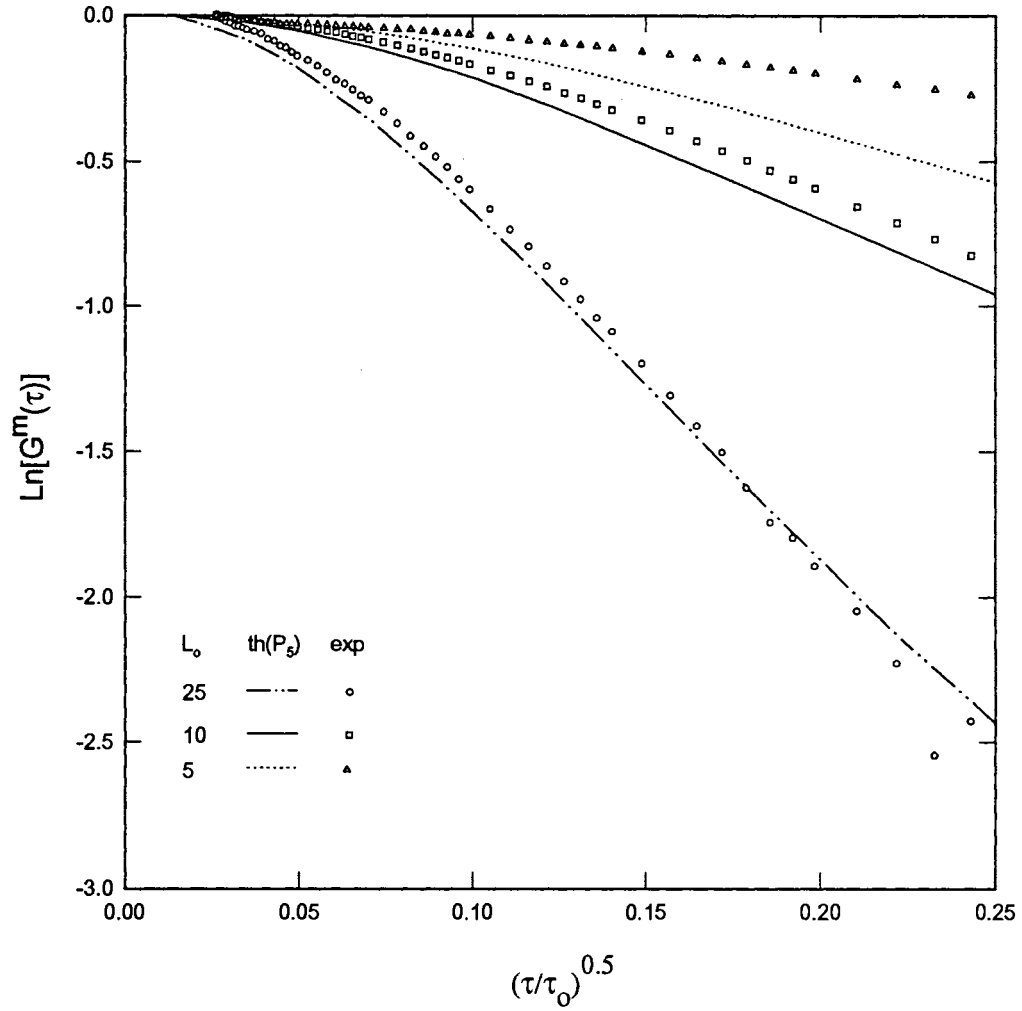


Fig. 96: Transmission: Comparison of improved P_5 approximation (with two index of refraction changes at the boundaries) with experimental data for different optical thicknesses (the same as Fig. 30), $0.3 \mu\text{m}$ particle sizes, and laser wavelength of 514.5 nm .

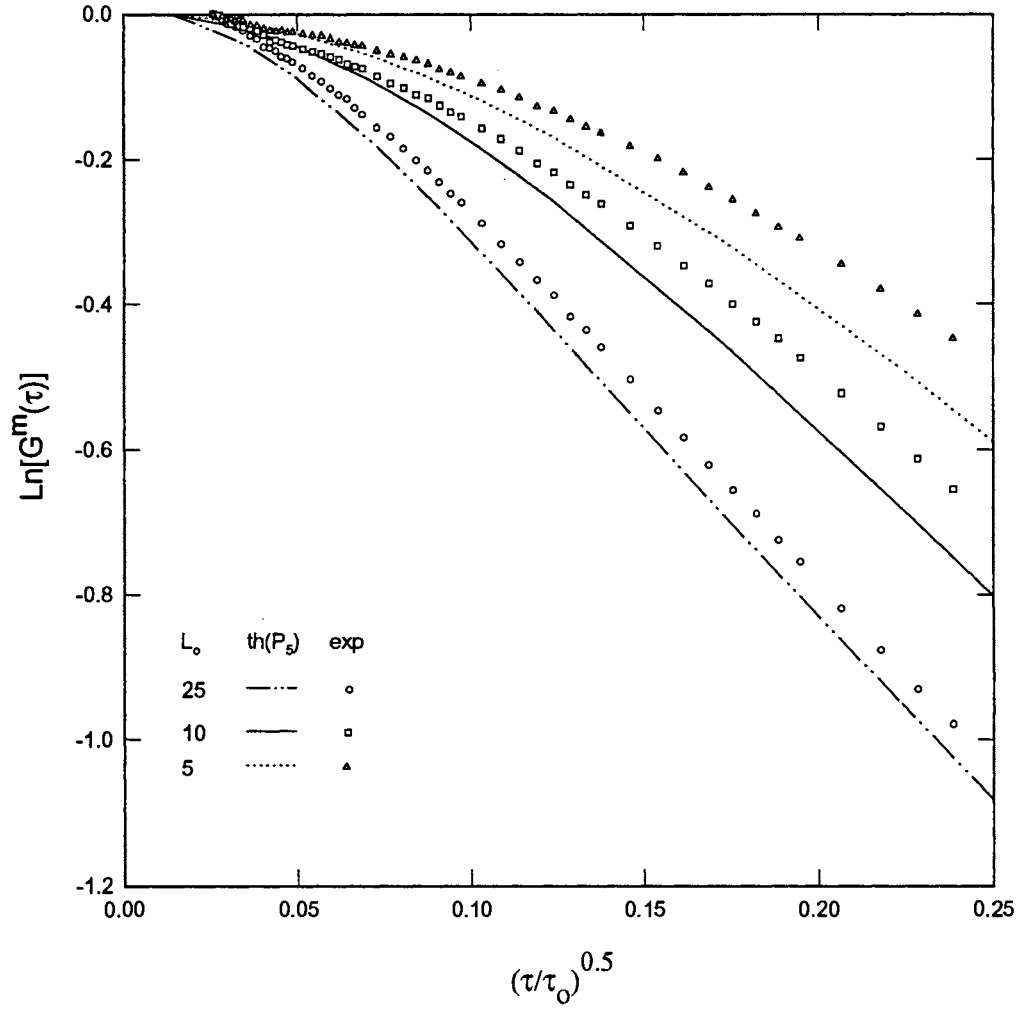


Fig. 97: Back-scattering: Comparison of improved P_5 approximation (with two index of refraction changes at the boundaries) with experimental data for different optical thicknesses (the same as Fig. 30), $0.3 \mu\text{m}$ particle sizes, and laser wavelength of 514.5 nm .

CHAPTER V

CONCLUSION AND RECOMMENDATIONS

Summary and Conclusions

This thesis report presents the overall experimental method and results for applying dynamic light scattering to one-dimensional test samples having various levels of multiple scattering, or various optical thicknesses. The basic experimental setup and procedures were discussed. Several important parameters and their effects on the correlation function were studied. It was shown that the glass cell back reflection affects the back-scattering correlation measurements for a detection angle of less than about 9° from the normal direction. The beam size plays an important role in one-dimensionality of the experimental measurements, and it can be varied according to the optical thickness of the sample. A beam size greater than 3.0 cm is recommended for the measurements even though a 2.0 cm beam size can be used for dense samples.

The slope or decay rate of the correlation function is directly related to optical thickness of the medium. As optical thickness increases, the correlation function decays faster for both back-scattering (at a short time) and transmission measurements. For back-scattering, the correlation functions for large optical thicknesses become very close to each other, approaching an asymptote. The correlation function decays faster for transmission as compared to back-scattering, and goes to zero as optical thickness approaches the semi-infinite limit.

Correlation function measurements for different optical thicknesses from 1 to 30 (effective optical thicknesses from about 0.7 to about 7) for different particle sizes of 0.3 μm , 0.091 μm , 0.497 μm , and 0.107 μm were compared to correlation transfer (CT) theory, considering one index of refraction effects and considering anisotropic scattering effects through the use of a single factor (f). The numerical results were obtained by using a preaveraged technique and 1 term Legendre polynomial g^1 expansion. These comparisons showed better agreement in transmission for bigger particle sizes and in back-scattering for smaller particle sizes. The use of the second index of refraction change, more realistic phase function, and more terms in the Legendre expansion for g^1 can improve numerical results to predict experimental data more accurately. The back-scattering correlation measurement compares well to the 3 term Legendre expansion for the single scattering g^1 for an infinite medium. The experimental data compares well to the single scattering g^1 equation at 30° and 45° (outside sample) off angle from transmission, and the data can be predicted by CT theory if more terms in the Legendre expansion for g^1 are used. It appears that CT theory, like radiative transfer (RT) theory, may be able to bridge the gap between single scattering correlation and highly multiple scattering correlation.

Other studies included the transition from single scattering to multiple scattering correlation and off angle (from direct transmission or back-scattering) effects on correlation. The results indicate that, at an optical thickness of 0.05, transition from single to multiple scattering begins. With regard to off angle measurements, dense media (optical thicknesses of 10 or greater) appear to be relatively insensitive to off angle detection for both transmission and back-scattering. However, thinner samples yield a correlation function that varies with detection angle. The experimental measurement for particle size of 0.3 μm shows that the detection angle does not significantly affect results at an optical

thickness of about more than 5 ($L_e=1.365$) in back-scattering and about more than 10 ($L_e=2.73$) in transmission.

The cross and parallel polarization correlation measurements decay differently for back-scattering for any optical thickness while they merge together at an optical thickness of about 18 for transmission when 0.3 μm particle sizes were used. In back-scattering, the unpolarized correlation function appears to be the average of the horizontal and vertical intensity correlation functions, while this is not necessarily true in transmission.

Since dynamic light scattering has been used to characterize particles in either very dilute or very dense suspensions, I have proposed a methodology for using CT theory and correlation measurements to determine particle size for media which cover the range from low to high multiple scattering. Reasonable results were found using this method for 0.3 and 0.497 μm particle diameters, but poor agreement was obtained for 0.107 μm particles. Even though the results do not show completely satisfactory agreement; this appears to be a promising methodology for determining particle size in different ranges of multiple scattering, if a more realistic phase function is used in the numerical solutions.

Since obtaining the exact results from the CT theory takes time, an improved P_N approximation was developed and compared to the 3 term Legendre expansion for single scattering g^1 from CT theory. The agreement is reasonable for an order of 5 (N of P_N) for back-scattering and an order of 3 for transmission. The sources of experimental errors in some areas were discussed and the reliability of the experimental data was demonstrated.

These results, which have not been reported or investigated in the past, present the effect of several important parameters on the correlation measurements.

Recommendations

Since this research was based on a new theory (CT) in the dynamic light scattering area, which should have the flexibility to study parameters such as detection angle, polarization, index of refraction, scattering/absorption, two- and three-dimensional geometries, etc., many areas can be recommended for study. But I recommend to investigate the following areas of dynamic light scattering in multiple scattering media in the near future in order to understand the capability of this theory to predict experimental research data.

In any experimental research, accuracy is the number one priority in order to have a reliable measurement even though there may be some parameters which are not sensitive in the measurement. In these experimental measurements, there were a few difficulties such as redirection of the laser beam by mirrors and lenses, alignment of the laser and optics, accuracy of placing the goniometer, higher than desired signal-to-noise ratio, instability of the laser pointing, etc., which can be improved by automating the system, using fiber optics, and using a more stable laser.

Even though there was good agreement between experimental data and numerical results in many cases, it was not satisfactory for all of the particle sizes and in all cases. It is suggested that the most probable source of error was due to the approximations which were made in the numerical results. Characterization of the particle sizes requires good prediction of the experimental data by numerical results for different particle sizes. So the approximation of a more realistic phase function in the numerical calculations is required so that the theoretical predictions can be more accurate for different sized particles and at low optical thicknesses.

Most particles not only scatter light but also absorb light. All of the results from this thesis were obtained using purely scattering particles. To apply CT theory in different areas of industrial applications, it is very important to study absorption in both areas of experiment and theory.

As presented earlier, using different detection angles or detecting the different conditions of polarization plays an important role in the correlation function measurements, specifically with regard to the reduction of noise and heterodyning. Most of the investigation in this research was focused on one particle diameter of 0.3 μm . Different polystyrene particle sizes have different characteristic phase functions which may change the detection angle and polarization results of this investigation. To better understand the effects of detection angle and polarization on the correlation function, different particle sizes must be thoroughly investigated in the experimental research when studying these two measurement areas. Since both experimental data and theoretical results are required to characterize the particle diameter, the theoretical polarization correlation function is needed in order to compare with the experimental data.

In practical situations, monodisperse particle distributions rarely exist, and there is always a mixture of different particle sizes and/or shapes. To apply the CT theory in these areas, research has to be conducted to study particle size distribution by using mixtures of two or three different particle sizes in the experimental research and also investigating the theoretical model to predict the experimental data.

REFERENCES

- Abramowitz, M. and Stegun, I.A. (1972), Handbook of Mathematical Functions, Dover, New York.
- Ackerson, B.J., Dougherty, R.L., Reguigui, N.M., and Nobbmann, U. (1992), "Correlation Transfer: Application of Radiative Transfer Solution Methods to Photon Correlation Problems," Journal of Thermophysics and Heat Transfer, Vol. 6, No. 4, pp. 577-588.
- Allen, T. (1981), Particle Size Measurement, 3rd ed., Chapman and Hall Ltd., London.
- Berne, B.J. and Pecora, R. (1976), Dynamic Light Scattering, Wiley, New York.
- Bunville, L.G. (1984), "Commercial Instrumentation for Particle Size Analysis", Modern Methods of Particle Size Analysis, ed. H.G. Barth, Willey, New York.
- Cao, J., Brown, D.J., and Rennie, A.G. (1991), "Laser-Diffraction Particle Sizing in Dense Suspensions and Sprays, with Correction for Multiple Scattering", J. of the Institute of Energy, Vol. 64, pp. 26-30.
- Carr, W. (1978), Particle Size Analysis, ed. M.J. Groves, Heyden, London, pp. 1-17.
- Charalampopoulos, T. T. and Felske, J.J. (1987), Combustion and Flames, Vol. 68, p. 283.
- Dorri-Nowkoorani, F., Nobbmann, U, Reguigui, N.M., Ackerson, B.J., and Dougherty, R.L. (1993), "Correlation Measurements of a Multiply Scattered Laser Beam by Fluid/Particle Suspensions", AIAA 93-2745, AIAA 28th Thermophysics Conference, Orlando, FL, July 6-9.

- Dorri-Nowkoorani, F., Tian, Y., Reguigui, N.M., Nobbmann, U., Ackerson, B.J., and Dougherty, R.L. (1994), "Improved P_N Approximation for One-Dimensional Scattering and Absorbing Media with Application to Correlation Transfer", AIAA 94-2096, 6th AIAA/ASME Joint Thermophysics and Heat Transfer Conference, Colorado Springs, CO, June 20-23.
- Fox, L. (1957), The Numerical Solution of Two-Point Boundary Problems, Oxford University Press, London.
- Harrison, W.D. (1988), "Measuring Particle Size Distribution at Full Process Concentration Using Both Laboratory and In-Line Instrument", Particle Science and Technology, Vol. 6, pp. 22-30.
- Hartley, P.A., Parfitt, G.D., and Pollack, L.B. (1985), Powder Technology, Vol 42, p. 35.
- Gougeon, P., Le Toulouzan, J.N., Gouesbet, G., and Thenard, C. (1987), "Optical Measurements of Particle Size and Concentration in Densely Laden Media Using a Visible/Infrared Double Extinction Technique", J. of Physics E., Vol. 20, No. 10, pp. 1235-1242.
- Gouesbet, G., Gougeon, P., Le Toulouzan, J.N., and Thioye, M. (1988), "Visible Infrared Double Extinction Measurements in Densely Laden Media, New Progress", Particle and Particle Systems Characterization, Vol. 5, No. 2, pp. 51-56.
- Jiang, X.Y. (1990), "Numerical Calculation Method for Solving for Source Functions at Reflective Boundaries of Semi-Infinite and Finite Media", Master of Science Report, Oklahoma State University.
- Kaplan, P.D., Kao, M. H., Yodh, A. G., and Pine, D. J. (1993), "Geometric Constraints for the Design of Diffusing-Wave Spectroscopy Experiments", Applied Optics, Vol. 32, No. 21, pp. 3828-3836.

- Liu, C.C. (1993), "Numerical Calculation of Radiation Transfer in One-Dimensional Media with a Reflective Top Boundary and Anisotropic Scattering", Masters Thesis, School of Mechanical and Aerospace Engineering, Oklahoma State University.
- Look, D.C., Jr. (1979), "Two-Dimensional Scattering from a Medium of Finite Thickness," Journal of Heat Transfer, Vol. 101, pp. 556-557.
- Maret, G. and Wolf, P.E. (1987), "Multiple Light Scattering from Disordered Media. The Effect of Brownian Motion of Scatterers", Z. Phys. B, Vol. 65, pp. 409-413.
- Modest, M.F. (1993), Radiative Heat Transfer, McGraw-Hill, Inc., New York.
- Orr, N.A., Hill, E.A., and Smith, J.F. (1980), Int. J. Pharm. Tech. and Prod. Mfr., Vol. 1, p. 4.
- Ozisik, M.N. (1973), Radiative Transfer, Wiley, New York.
- Pine, D.J., Weitz, D.A., Maret, G., Wolf, P.E., Herbolzheimer, E., and Chaikin, P.M. (1990a), "Dynamic Correlations of Multiply Scattered Light," from Scattering and Localization of Classical Waves in Random Media, ed. P. Sheng, World Scientific, Singapore, pp. 312-372.
- Pine, D.J., Weitz, D.A., Zhu, J.X., and Herbolzheimer, E. (1990b), "Diffusing-Wave Spectroscopy: Dynamic Light Scattering in the Multiple Scattering Limit", J. Phys. France, Vol. 51, pp. 2101-2127.
- Plantz, P.E. (1984), "Particle Size Measurements from 0.1 to 1000 μm , Based on Light Scattering and Diffraction", Modern Methods of Particle Size Analysis, ed. H.G. Barth, Wiley, New York.
- Reguigui, N.M., Dorri-Nowkoorani, F., Nobbmann, U., Ackerson, B.J., and Dougherty, R.L. (1993), "Particle Characterization Using Correlation Transfer Theory," AIAA 93-0141, 31st Aerospace Sciences Meeting, Reno, NV, January 11-14.

- Reguigui, N.M. and Dougherty, R.L. (1992), "Two-Dimensional Radiative Transfer in a Cylindrical Layered Medium with Reflecting Surfaces," Journal of Thermophysics and Heat Transfer, Vol. 6, No. 2, pp. 232-241.
- Sarofim, A.F. (1986), "Radiative Heat Transfer in Combustion: Friend or Foe", Twenty-First Symposium (Int) on Combustion, pp. 1-23.
- Scarlett, B. (1981), Particle Size Analysis, ed. N. Stanley-Wood and T. Allen, Willey, Chichester, pp. 219-231.
- Scarlett, B. (1992), "25 Years of Particle Size Conferences", Particle Size Analysis, ed. N.G. Stanley-Wood and R.W. Lines, Redwood Press Limited, England.
- Seigel, R. and J.R. Howell (1981), Thermal Radiation Heat Transfer, Hemisphere Publishing Corporation, N.Y.
- Tuzun, U. and Farhadpour, F.A. (1985), "Comparison of Light Scattering with Other Techniques for Particle Size Measurement", Particle Characterization, Vol. 2, No. 3, pp. 104-112.
- Viskanta, R., and Menguc, M.P. (1987), "Radiation Heat Transfer in Combustion Systems", Progress in Energy and Combustion Science, Vol. 31, pp. 97-160.
- Weiner, B.B. (1984), "Particle Sizing Using Photon Correlation Spectroscopy," from Modern Methods of Particle Size Analysis, ed. by H.G. Barth, Wiley, New York, pp. 93-116.
- Wolf, P.E., Maret, G., Akkermans, E., and Maynard, R. (1988), "Optical Coherent Backscattering by Random Media: An Experimental Study", J. Phys. France, Vol. 49, pp. 63-75.
- van de Hulst, H.C. (1957), Light Scattering by Small Particles, John Wiley and Sons, London.

van de Hulst, H.C. (1980), Multiple Light Scattering, Tables, Formulas, and Applications, Vol. 2, Academic Press, N.Y.

APPENDIXES

APPENDIX A

Error Analysis

Using more sensitive equipment or devices and automation of the experimental setup can significantly reduce the uncertainty of the data due to the inaccuracy of equipment and human error factors. There are a few factors in this experimental setup which may cause errors that affect the experimental measurements or conclusions made from the data. The investigation was focused on the following categories: temperature sensitivity, detector position, comparison of experiment to theory for single scattering, repeatability of the data, comparison of the experimental data to DWS, homodyning versus heterodyning, and laser stability.

Temperature Sensitivity

Temperature is used for characteristic delay time calculations [Eqs. (3-4) and (3-6)], and it can also cause natural convection in the sample. The room temperature was measured by a thermometer placed close to the experimental setup, and it was assumed that the sample solution was at the same temperature as the room. There was no natural convection observed for these submicron latex particles -- found by using an independent experimental setup. This independent experimental setup consisted of a regular powerful light bulb to illuminate the sample cell, a lens to magnify a small area of the cell, a camcorder to record or transfer the produced image by the lens to a monitor, and the monitor to see the picture. The room temperature was read to be 21°C in most experiments; and if the accuracy of the temperature measurement is $21^{\circ} \pm 1.0^{\circ}\text{C}$, τ_0 will be 2.58 ± 0.03 ms -- assuming a 0.300 μm particle diameter illuminated by the 514.5 nm

laser wavelength (used for almost all of the collected data). For back-scattering from an optical thickness of 5, Fig. A-1 shows this change for all of the channels and without shifting the experimental data. As this figure shows, there is not a significant change in the decay rate even for a long time.

Detector Position

In this experimental setup, the detector was moved manually to different angles which were marked on the experimental setup table. An accuracy of the detector position reading was less than ± 1.0 degree. Figure A-2 shows an example of decay rate change (about 5.88%) for theoretical single scattering g^1 by changing the angle by 1.0 degree. Even though this shows a small change for theoretical single scattering, as presented in the off angle measurement discussion, one degree does not affect correlation from a multiple scattering medium for high optical thicknesses; and it is not significant for dilute samples for short time. It is much more important for the single scattering correlation function.

Comparison of Experiment to Theory for Single Scattering

Figure A-3 presents the comparison of theoretical single scattering to the correlation measurements for very dilute samples at different angles. Reasonable agreement is observed, and the small deviation may be due to the sensitivity of correlation to the accuracy of the detector position readings. The differences between the theoretical and experimental slopes are 0.4%, 3.5%, and 5.2% for 29° , 34° , and 45° (outside sample), respectively. Since the effect of a very small angle change in the detector position is reduced as the solution becomes denser, the accuracy of the measurement increases for denser samples.

Repeatability of the Data

Figure A-4 shows back-scattering measurements at different times (dates) for an optical thickness of 10. This figure presents the data for all of the channels up to about 82, and they are not shifted. As illustrated in this figure, the data can be reasonably repeated on different days. Even though this repeatability is not perfect, it reveals the reliability of the points which have been used to draw conclusions in this thesis.

Comparison of the Experimental Data to DWS

Diffusive Wave Spectroscopy (DWS) which has been developed recently [Pine et al. (1990a)], has been compared satisfactorily to the transmitted experimental data from thick media [Kaplan et al. (1993)]. They show a maximum difference of about 5% between effective optical thicknesses from the experimental measurements determined from fitting DWS to the experimental data and effective optical thicknesses which were determined from Mie theory [they used the same equation as Eq. (3-20)].

Figure A-5 shows the comparison of transmitted experimental correlation for an optical thickness of 50 (corresponding to an effective optical thickness of 13.65 using Eq. (3-20)) to DWS and to the improved P_5 approximation. Using an effective optical thickness (Z/l^* in DWS) of 13.65 shows that DWS underestimates the experimental data while a Z/l^* of 14.5 (about 6% higher than 13.65) satisfactorily predicts the experimental correlation. These results are consistent with the results of Kaplan et al. (1993) and show the accuracy of these experimental measurements. This figure also presents the numerical results of the improved P_5 approximation for an optical thickness of 13.65 (the same as predicted from Mie theory) with and without index of refraction effects. It shows that this approximation predicts the experimental data well when a more realistic

theoretical model having a two index of refraction change at both boundaries was used. It should be mentioned that there was no refractive index change at the boundaries assumed in the DWS results presented on Fig. A-5.

Homodyning Versus Heterodyning

The signals which are detected by a PMT are a combination of scattered and/or unscattered light. The CT equation is based on the scattering and/or absorption of light passing through the medium, and it is concerned with a homodyne correlation function. But the heterodyne (unscattered) correlation function, which is based on local oscillation (usually with a small portion of the unscattered laser beam), can mix with the scattered light (homodyne signals) in the measurements and affect the correlation function (Figs. 9 and A-6). These heterodyne signals are caused by cell glass reflection in back-scattering (Fig. 9) or passing through the medium without scattering in dilute samples in the case of transmission (Fig. A-6) in this experimental setup. Its effects depend on the magnitude of the unscattered light as compared to scattered light.

Figure A-6 shows the effect of heterodyne signals through upward curvature on the plots (changing to smaller decay rates). The magnitude of the heterodyne signals are smaller (Fig. A-6) for a higher optical thickness of 3 as compared to an optical thickness of 1 when mixed with homodyne signals. This is due to the presence of more particles (thus greater scattered signal) and less chance of the laser beam being transmitted as unscattered. The decay rate of the homodyne correlation function is the square of the heterodyne correlation function decay rate [Berne and Pecora (1976)] or it is double the rate when plotted in the form of natural logarithm functions. All graphs were plotted in this form in this thesis.

Since the purity of the homodyne correlation measurement is important in these experiments, careful checking has been done by slowly moving a thin shiny needle in front of the detector pinhole to eliminate the homodyning and force the correlation function to become pure heterodyning. Figure A-7 presents a few results of this testing for an optical thickness of 5 in back-scattering. As shown in this figure, the decay rate becomes slower when going from pure homodyning to heterodyning. This decay rate is double for pure homodyne correlation as compared to the pure heterodyne correlation measurements (Fig. A-7). This pure homodyne correlation measurement which is shown in Fig. A-7, was used as a guideline (by repeating this correlation measurement) to check (if necessary) whether the glass back reflection was affecting the experimental measurements.

Laser Stability

An Argon-Ion Laser was used as a source of light providing known boundary conditions and known wavelength. Unfortunately, there were a few problems with the laser. One of the major problems was the instability of the laser beam positioning (changing its pointing direction with the time). This "walking" of the laser beam caused periodic (usually after two or three days) misalignment of the experimental setup and consequently, changes in the intensity of the incident laser light to the cell sample. Figure A-8 shows the change of detector count rates over a three hour period of time, starting from complete realignment of the experimental setup. These intensity data were recorded as the average of successive three minute periods of time during experimental correlation measurements for an optical thickness of 5 from 10° off angle back-scattering. The intensity was starting to drop after one and one-half hours from complete realignment (Fig. A-8), and there was about a 10% decrease after 3 hours.

Figure A-9 shows the correlation measurements corresponding to the intensity data of Fig. A-8 for the first measurement (3 minutes), thirtieth measurement (90 minutes), sixtieth measurement (3 hours), and the measurement after about 15 hours (the corresponding intensity is not in the Fig. A-8). There was no significant change in correlation function measurements, even though there was a change in the average intensity. This intensity change may have been responsible for some of the errors in the particle sizing. It should be mentioned that this experimental setup was frequently checked for alignment and then realigned when it was necessary (typically after two or three days).

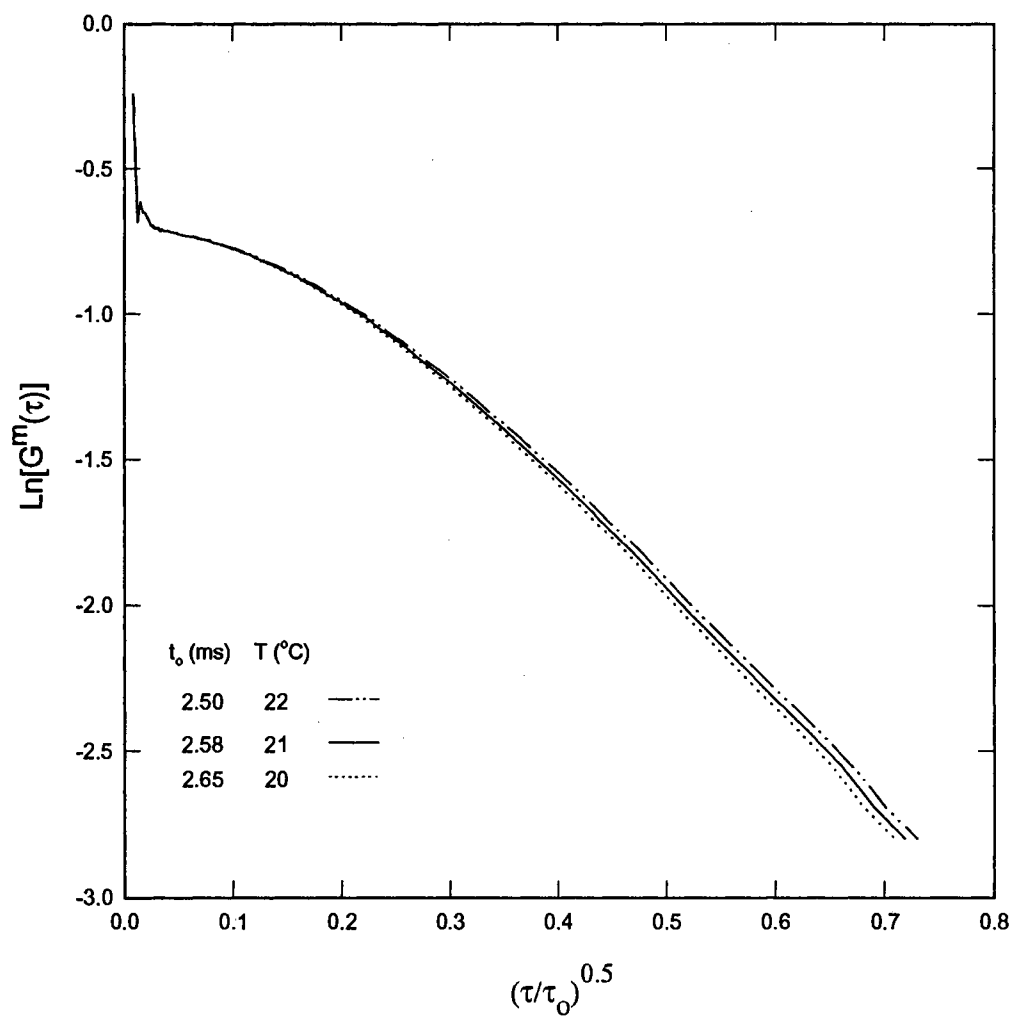


Fig. A-1: Back-scattering: Effect of τ_0 (which depends on temperature) on correlation measurements for optical thickness of 5, particle diameter of 0.3 μm , and wavelength of 514.5 nm.

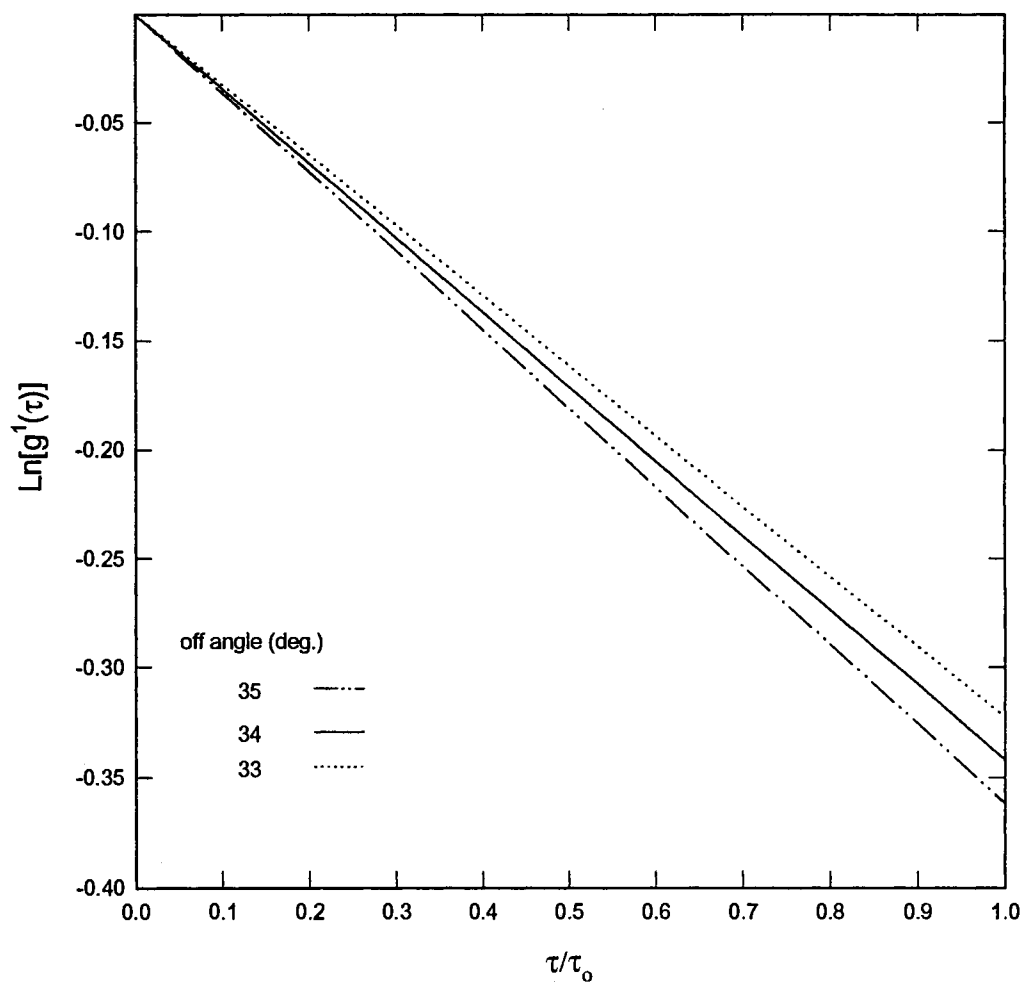


Fig. A-2: Transmission: Effect of detection angle change on theoretical single scattering g^1 .

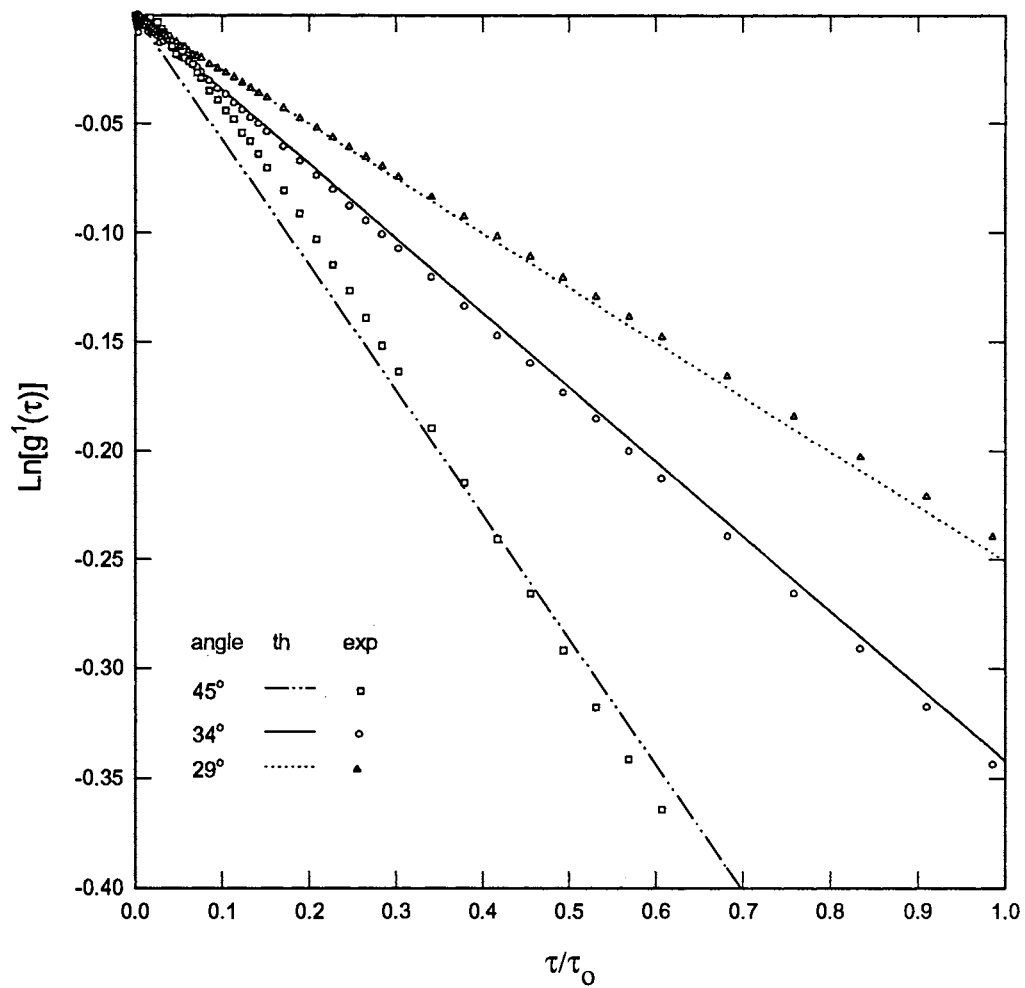


Fig. A-3: Transmission: Comparison of correlation measurements with theoretical single scattering g^1 for optical thickness of 0.05, particle diameter of $0.3 \mu\text{m}$, and wavelength of 514.5 nm , at different detection angles.

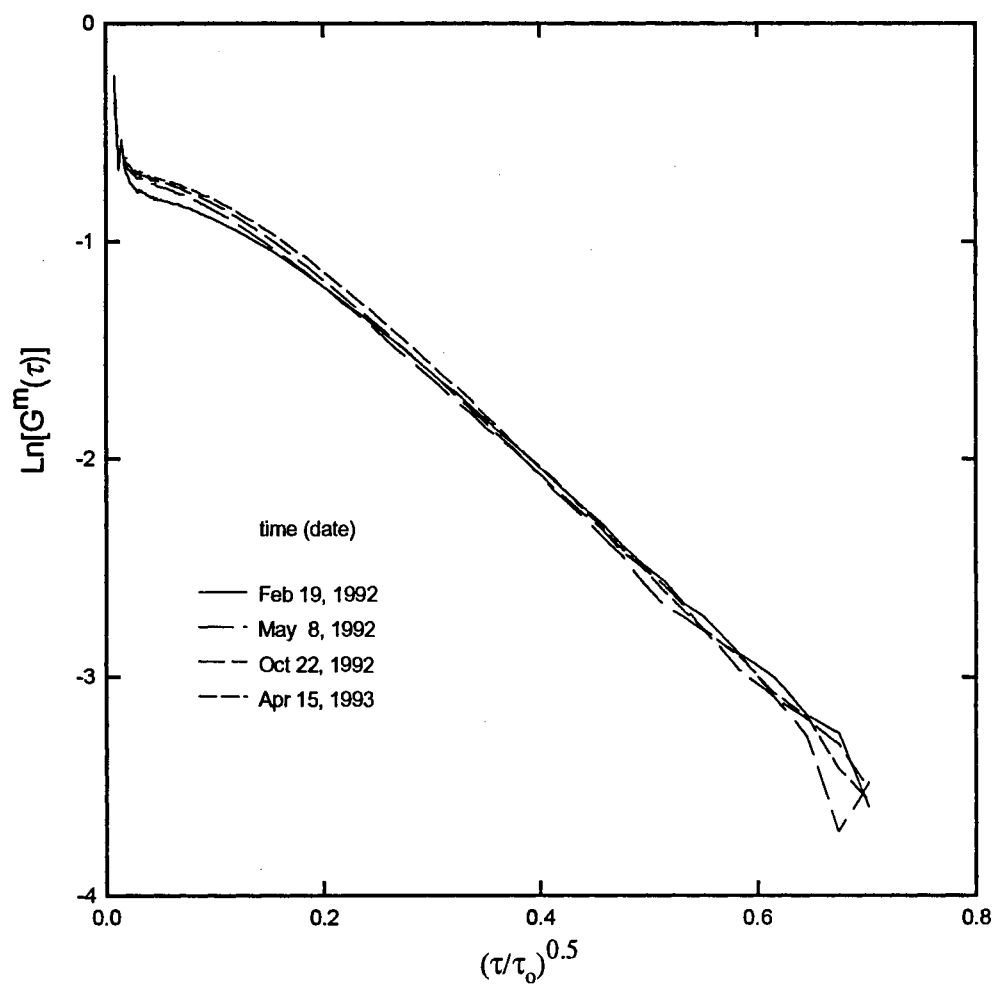


Fig. A-4: Back-scattering: Repeatability of the data at different times for optical thickness of 10, particle diameter of $0.3 \mu\text{m}$, and laser wavelength of 514.5 nm .

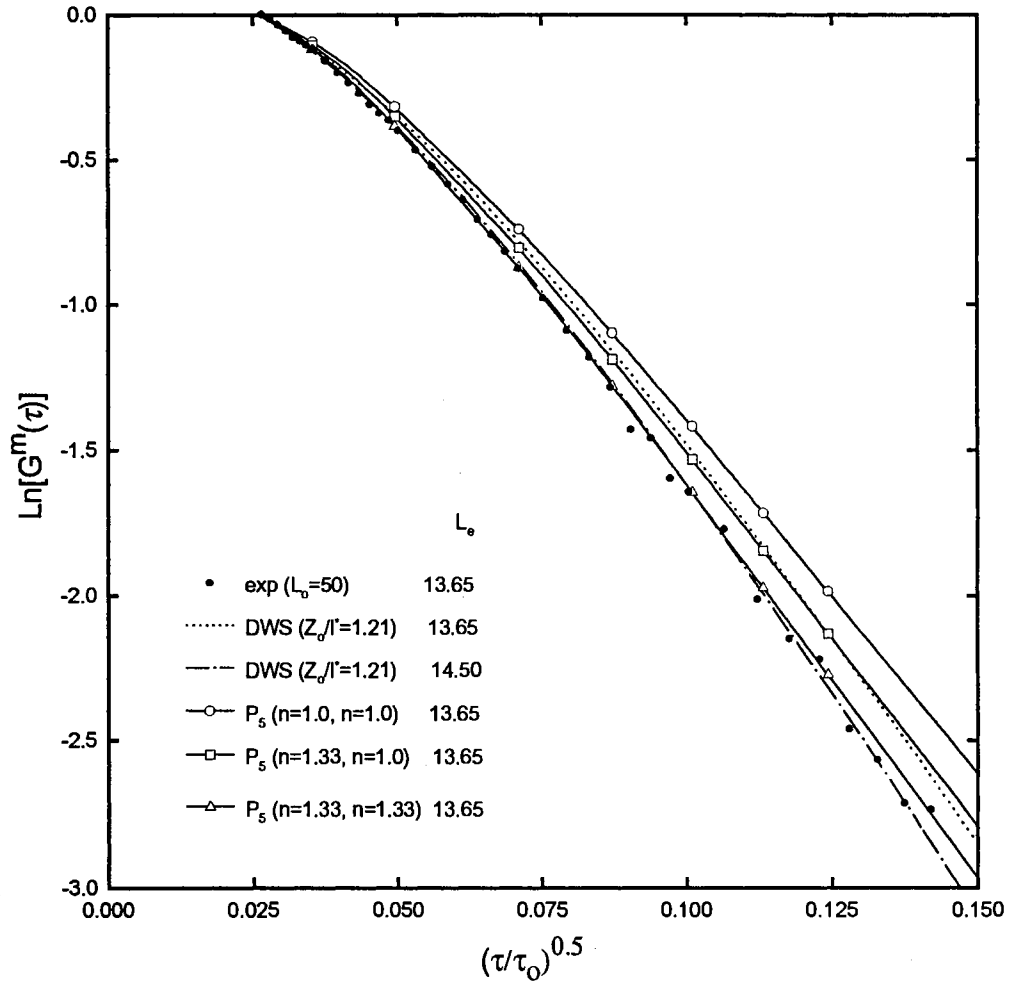


Fig. A-5: Transmission: Comparison of experimental correlation to the DWS ($z_0 / l^* = 1.21$) theory without considering internal reflection and improved P_5 approximation with and without index of refraction effects at the boundaries, for effective optical thickness of 13.65, particle diameter of 0.3 μm , and laser wavelength of 514.5 nm.

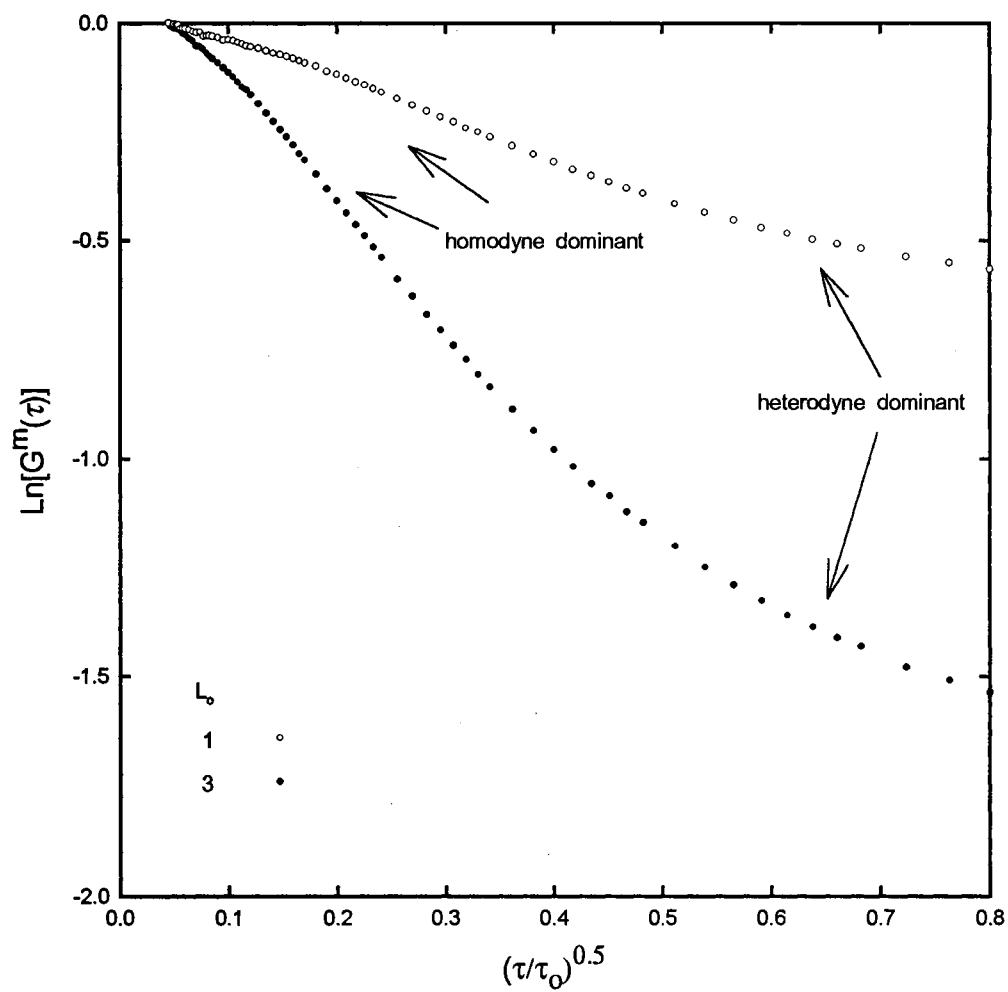


Fig. A-6. Transmission: Effect of heterodyning on homodyne correlation function measurements for low optical thicknesses of 1 and 3, particle diameter of $0.107 \mu\text{m}$, and laser wavelength of 514.5 nm .

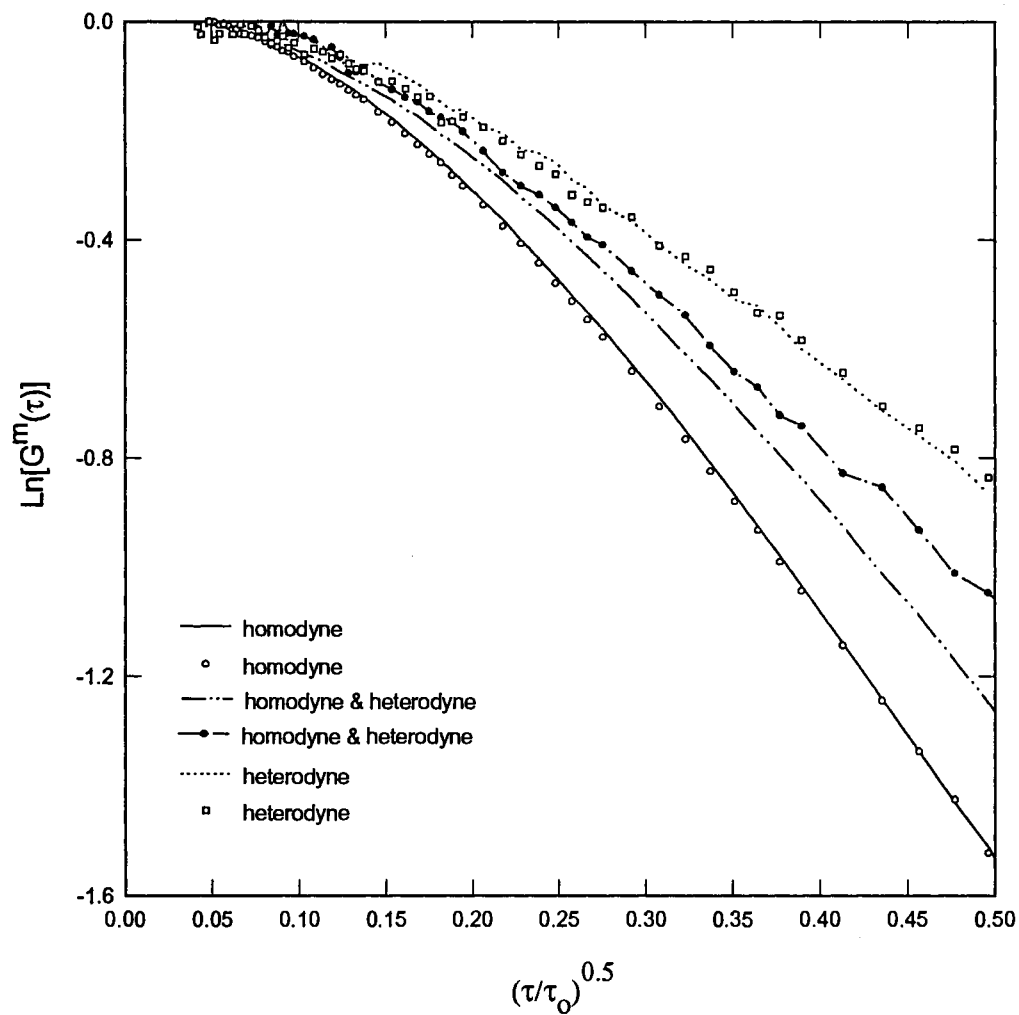


Fig. A-7: Back-scattering: Transition of correlation function measurements from pure homodyne signals to the pure heterodyne signals for optical thickness of 5, particle diameter of 0.3 μm , and laser wavelength of 514.5 nm.

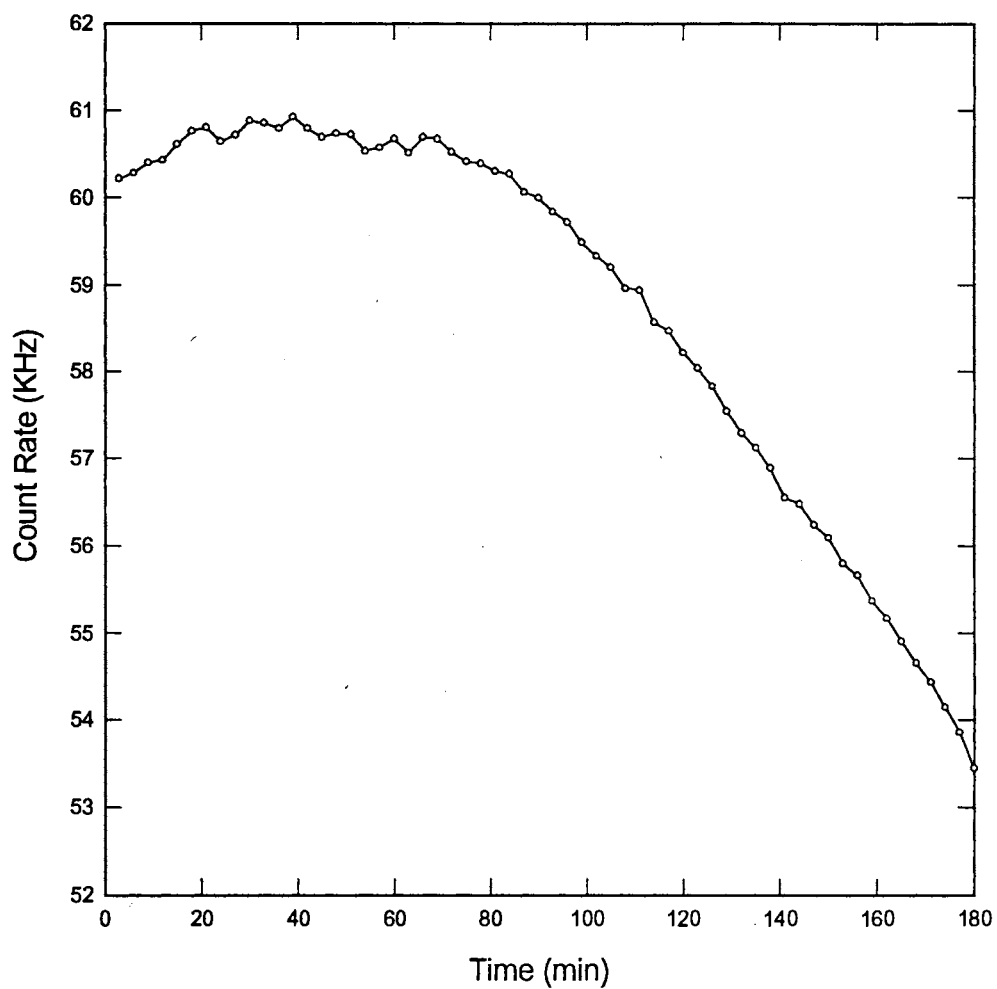


Fig. A-8: Back-scattering: Change of incident laser (Argon-Ion) intensity over the time due to misalignment of the experimental setup for optical thickness of 5, particle diameter of $0.3\ \mu\text{m}$, and laser wavelength of $514.5\ \text{nm}$.

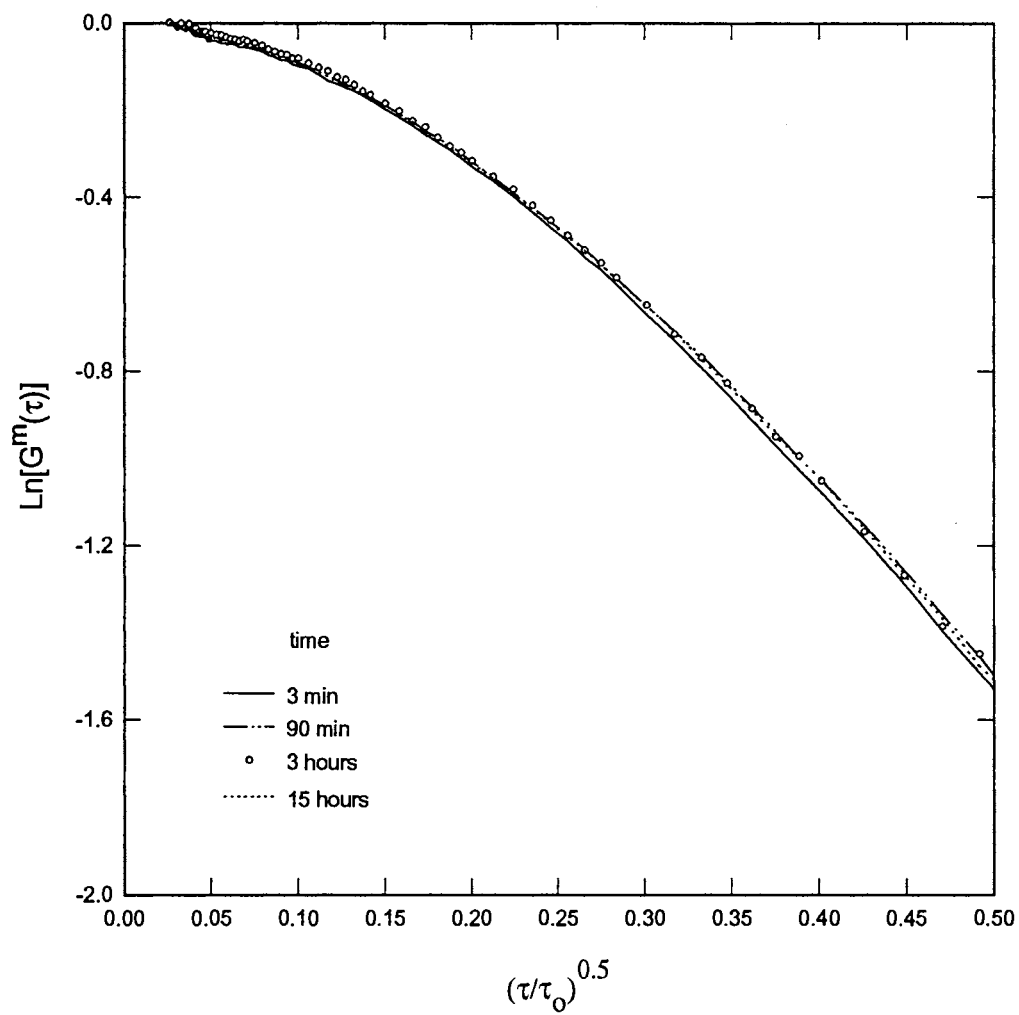


Fig. A-9: Back-scattering: Repeatability of the correlation measurements at different times corresponding to Fig. A-8 for optical thickness of 5, particle diameter of $0.3\ \mu\text{m}$, and laser wavelength of $514.5\ \text{nm}$.

APPENDIX B

1 Term g^1 Expansion Exact Program for Correlation Transfer (CT) Theory

This program was written by Jiang (1990) for absorbing and isotropic scattering media with index of refraction change at the top boundary using the RT equation. Since the CT equation is similar to the RT equation, the program has been simplified and modified for CT theory by changing the scattering albedo to correspond to the nondimensional delay time (τ/τ_0) which is input. The following is the source code and input data for 1 term Legendre g^1 expansion approximation for CT theory. The areas with lower case letters are modifications by F. Dorri-Nowkooorani and do not belong to the original program.

Program Source Code

```
PROGRAM jiang
C*****
C    THIS PROGRAM IS USED TO SOLVE correlation TRANSFER IN A
C    SCATTERING/ABSORBING FINITE MEDIUM WITH REFLECTIVE BOUNDARY
C    AT THE TOP OF THE MEDIUM.
C    IN THIS PROGRAM THE FUNDAMENTAL SOURCE FUNCTION, THE REFLE-
C    CTION FUNCTION AND THE TRANSMISSION FUNCTION WILL BE SOLVED
C    BY THE X AND Y FUNCTIONS.
C    OUTPUT FILES:
C    REFLECTED AND TRANSMITTED INTENSITIES AT BOTH BOUNDARIES.
C*****
C
c
c    modified by Farhad Dorri-Nowkooorani on July 1, 1993
c
    IMPLICIT REAL*8 (A-H,O-Z)
    DIMENSION T1(100),A1(100),T2(100),A2(100),T3(100),A3(100),
    &T4(100),A4(100)
    DIMENSION YN(6,400),T(400),A(400),BT1(400),BT2(400),AT1(400),
    +AT2(400),BL1(400),BL2(400),TL1(400),TL2(400),BS(400),TS(400),
    +RMU(10),ang(10)
    COMMON/BLK1/T,A,OME,AN,ang,rmu
    OPEN(UNIT=4,FILE='jgm.dat',STATUS='OLD')
    OPEN(UNIT=10,FILE='jgm.out')
    READ(4,*)N,AN,H,DELTA,k,tauo
    WRITE(10,60)N,AN,DELTA,tauo
    WRITE(10,85)
C
C    INPUT THE INITIAL VALUES
C
    eps=1.0d-10
    pi=3.141592653589779d0
```

```

      UCR=DSQRT(1.0D0-1.0D0/(AN*AN))
c
C      CALL DXA(N,AA,BB,T,A) TO GET T(I) AND A(I)
C
      IF(AN.EQ.1.0D0) THEN
        AA=0.0D0
        BB=1.0D0
        nn=n
        CALL DXA(nn,AA,BB,T,A)
      ELSE
        AA1=0.0D0
        BB1=UCR
        CALL DXA(N,AA1,BB1,T1,A1)
        AA2=BB1
        BB2=1.015D0*UCR
        CALL DXA(N,AA2,BB2,T2,A2)
        AA3=BB2
        BB3=1.085D0*UCR
        CALL DXA(N,AA3,BB3,T3,A3)
        AA4=BB3
        BB4=1.0D0
        CALL DXA(N,AA4,BB4,T4,A4)
        DO 3 I=1,N
          A(I)=A1(I)
          A(I+N)=A2(I)
          A(I+2*N)=A3(I)
          A(I+3*N)=A4(I)
          T(I)=T1(I)
          T(I+N)=T2(I)
          T(I+2*N)=T3(I)
          T(I+3*N)=T4(I)
3      CONTINUE
        nn=4*n
      ENDIF
      teta=pi/2.
      do 1 i=1,10
        ang(i)=dcos(teta)
        teta=teta-10.*pi/180.
1      continue
5      X=0.0D0
      XN=0.0D0
      DO 10 I=1,10
        RMU(I)=DSQRT(1.D0-(1.D0-ang(i)**2)/AN**2)
        YN(1,I)=1.0D0
        YN(3,I)=1.0D0
        YN(4,I)=1.0D0
10     YN(2,I)=1.0D0
      DO 20 I=1,NN
        YN(5,I)=1.0D0
20     YN(6,I)=1.0D0
      read(4,*,end=100)time
      ome=sinh(2*time)/(2*time*exp(2*time))
30     CALL RK5(10,NN,4,5,6,H,XN,YN)
      if(xn .ge. (tauo-eps)) go to 40
      GO TO 30

```

```

C
C      OUTPUT
C
40 DO 110 I=1,NN
    BT1(I)=YN(5,I)
    AT1(I)=YN(6,I)
110 CONTINUE
C
2  JU=0
    DO 130 I=1,NN
        BT2(I)=YN(5,I)
        AT2(I)=YN(6,I)
        DO 120 J=1,NN
            BT2(I)=BT2(I)+.5D0*OME*BT1(J)*RU(AN,T(J))*(YN(5,I)*YN(5,J)-
            +YN(6,I)*YN(6,J))/(T(I)+T(J))*T(I)*A(J)
            AT2(I)=AT2(I)+.5D0*OME*AT1(J)*RU(AN,T(J))*(YN(5,I)*YN(5,J)-
            +YN(6,I)*YN(6,J))/(T(I)+T(J))*T(I)*A(J)
        120 CONTINUE
        IF (DABS((BT2(I)-BT1(I))/BT2(I)).GT.DELTA) JU=JU+1
    130 CONTINUE
    IF (JU.EQ.0) GO TO 150
    DO 140 I=1,NN
        BT1(I)=BT2(I)
140  AT1(I)=AT2(I)
    GO TO 2
C
150 DO 170 L=1,10
    BO=YN(1,L)
    BT=YN(2,L)
    DO 160 I=1,NN
        BO=BO+0.5D0*OME*RU(AN,T(I))*BT2(I)*(YN(1,L)*YN(5,I)-YN(2,L)
        +*YN(6,I))/(T(I)+ang(L))*ang(L)*A(I)
        BT=BT+0.5D0*OME*AT2(I)*RU(AN,T(I))*(YN(1,L)*YN(5,I)-YN(2,L)
        +*YN(6,I))/(T(I)+ang(L))*ang(L)*A(I)
    160 CONTINUE
170 CONTINUE
C
    WRITE(10,50)XN,ome
    write(10,55)
55  format(4x,'t/to',4x,'teta',10x,'gm-',10x,'gm+')
    DO 3171 I=1,NN
        BL1(I)=(YN(5,I)*YN(3,K)-YN(6,I)*YN(4,K))/(T(I)+RMU(K))*T(I)
        +*RMU(K)
        TL1(I)=(YN(6,I)*YN(3,K)-YN(5,I)*YN(4,K))/(T(I)-RMU(K))*T(I)
        +*RMU(K)
        BS(I)=BL1(I)
        TS(I)=TL1(I)
3171 CONTINUE
C
35  JU=0
    DO 3131 I=1,NN
        BL2(I)=BS(I)
        TL2(I)=TS(I)
        DO 3121 J=1,NN
            BL2(I)=BL2(I)+.5D0*OME*BL1(J)*RU(AN,T(J))*(YN(5,I)*YN(5,J)-

```

```

+YN(6,I)*YN(6,J))/(T(I)+T(J))*T(I)*A(J)
IF (I.EQ.J) THEN
IF (I.EQ.1) THEN
TL2(I)=TL2(I)+.5D0*OME*BL1(J)*RU(AN,T(J))*(YN(5,I)*(YN(6,J)-
&YN(6,J+1))-YN(6,I)*(YN(5,J)-YN(5,J+1)))/(T(J)-T(J+1))*T(I)*A(J)
ELSE
TL2(I)=TL2(I)+.5D0*OME*BL1(J)*RU(AN,T(J))*(YN(5,I)*(YN(6,J)-
+YN(6,J+1))-YN(6,I)*(YN(5,J)-YN(5,J+1)))/(T(J)-T(J+1))*T(I)*A(J)
ENDIF
ELSE
TL2(I)=TL2(I)+.5D0*OME*BL1(J)*RU(AN,T(J))*(YN(5,I)*YN(6,J)-
+YN(6,I)*YN(5,J))/(T(J)-T(I))*T(I)*A(J)
ENDIF
3121 CONTINUE
IF (DABS((BL2(I)-BL1(I))/BL2(I)).GT.DELTA) JU=JU+1
3131 CONTINUE
IF (JU.EQ.0) GO TO 3155
DO 3141 I=1,NN
BL1(I)=BL2(I)
3141 TL1(I)=TL2(I)
GO TO 35
3155 DO 3157 I=1,10
BLRMU=(YN(3,I)*YN(3,K)-YN(4,I)*YN(4,K))/(RMU(I)+RMU(K))*
+RMU(I)*RMU(K)
BLMU=(YN(1,I)*YN(3,K)-YN(2,I)*YN(4,K))/(ang(I)+RMU(K))*
+RMU(K)*ang(I)
IF(I.EQ.K) GO TO 3256
TLMU=(YN(3,K)*YN(2,I)-YN(4,K)*YN(1,I))/(ang(I)-RMU(K))*
+ang(I)*RMU(K)
3256 DO 3156 J=1,NN
BLRMU=BLRMU+.5D0*OME*RU(AN,T(J))*BL2(J)*(YN(3,I)*YN(5,J)-YN(4,I)*
+YN(6,J))/(RMU(I)+T(J))*A(J)*RMU(I)
BLMU=BLMU+.5D0*OME*RU(AN,T(J))*BL2(J)*(YN(1,I)*YN(5,J)-YN(2,I)*
+YN(6,J))/(ang(I)+T(J))*A(J)*ang(I)
IF(I.NE.K) TLMU=TLMU+.5D0*OME*RU(AN,T(J))*BL2(J)*(YN(1,I)*
+YN(6,J)-YN(2,I)*YN(5,J))/(T(J)-ang(I))*A(J)*ang(I)
3156 CONTINUE
IF(I.EQ.K) TLMU=FLAGR(T,TL2,1.0D0,6,NN-6,400)
AIE1=(1.D0-RU(1/AN,ang(k)))*(1.0D0-RU(AN,RMU(i)))*BLRMU/
+(AN**2*RMU(I)*RMU(K)*4.*pi)*OME*ang(k)
AIE2=(EXP(-XN/(ang(i)))*RU(AN,ang(i))*BLMU+TLMU)*OME/(RMU(K)
+*ang(I)*4.*pi)*ang(k)*(1.d0-ru(1/an,ang(k)))
teta=dacos(ang(i))*180./pi
WRITE(10,1220) time,teta,AIE1,AIE2
3157 CONTINUE
1220 FORMAT(F8.5,3x,f5.2,3x,f11.7,3x,f11.7)
GO TO 5
50 FORMAT(/10X,'TAO= ',F8.5,3x,'omega= ',f8.5/
& 9X,'=====','/)
60 FORMAT(5X,'N= ',I3,5X,'AN= ',F6.3,5X,'error= ',f11.9,' tauo= ',f7.4)
70 FORMAT(1X,'-----')
85 FORMAT(1X,/)
100 close(5)
STOP
END

```

```

C
C SUBROUTINE
C
C
SUBROUTINE RK5(NPIC,NZMU,NFUN,NFUNP1,INFUN,H,XN,YN)
IMPLICIT REAL*8(A-H,O-Z)
EXTERNAL SUBROUTINE FCT
DIMENSION C(6),Z(6),A(6,5),YN(6,400),Y(6,400)
COMMON/BLK4/IDERV2,IDERV1,IDERV,IDER,IDER1,IDER2
COMMON/BLK6/AK(6,6,400)
COMMON/BLK9/DER(6,400)
DATA C(2),C(3),C(4),C(5),C(6) /.25D0,.25D0,.5D0,.75D0,1.0D0/
DATA Z(1),Z(2),Z(3),Z(4),Z(5),Z(6) /7.0D0,0.0D0,32.0D0,12.0D0,
132.0D0,7.0D0/
DATA A(2,1),A(3,1),A(3,2),A(4,1),A(4,2),A(4,3) /.25D0,.125D0,
1.125D0,0.0D0,-.50D0,1.0D0/
DATA A(5,1),A(5,2),A(5,3),A(5,4) /.1875D0,0.0D0,0.0D0,.5625D0/
DATA A(6,1),A(6,2),A(6,3),A(6,4),A(6,5) /-.428571428571429D0,
1.285714285714285D0,1.71428571428571D0,-1.71428571428571D0,
21.14285714285714D0/
CALL FCT(XN,YN,nzmu)
DO 10 L=1,NFUN
DO 10 I=1,NPIC
10 AK(L,1,I)=DER(L,I)*H
DO 15 L=NFUNP1,INFUN
DO 15 I=1,NZMU
15 AK(L,1,I)=DER(L,I)*H
DO 90 K=2,6
DO 30 L=1,NFUN
DO 30 I=1,NPIC
K1=K-1
SUM=0.D0
DO 20 J=1,K1
20 SUM=A(K,J)*AK(L,J,I)+SUM
30 Y(L,I)=YN(L,I)+SUM
DO 40 L=NFUNP1,INFUN
DO 40 I=1,NZMU
K1=K-1
SUM=0.D0
DO 35 J=1,K1
35 SUM=A(K,J)*AK(L,J,I)+SUM
40 Y(L,I)=YN(L,I)+SUM
X=XN+C(K)*H
CALL FCT(X,Y,nzmu)
DO 80 L=1,NFUN
DO 80 I=1,NPIC
80 AK(L,K,I)=DER(L,I)*H
DO 90 L=NFUNP1,INFUN
DO 90 I=1,NZMU
90 AK(L,K,I)=DER(L,I)*H
DO 101 L=1,NFUN
DO 101 I=1,NPIC
PHI=0.D0
DO 100 K7=1,6
100 PHI=PHI+Z(K7)*AK(L,K7,I)

```

```

101 YN(L,I)=YN(L,I)+PHI/90.D0
    DO 110 L=NFUNP1,INFUN
    DO 110 I=1,NZMU
    PHI=0.D0
    DO 108 K7=1,6
108 PHI=PHI+Z(K7)*AK(L,K7,I)
110 YN(L,I)=YN(L,I)+PHI/90.D0
    XN=XN+H
    RETURN
    END
C
SUBROUTINE FCT(XN,Y,nzmu)
IMPLICIT REAL*8(A-H,O-Z)
DIMENSION Y(6,400),T(400),A(400),RMU(10),ang(10)
COMMON/BLK1/T,A,OME,AN,ang,rmu
COMMON/BLK9/DER(6,400)
C
    YSUM=0.0D0
    DO 10 I=1,NZMU
10 YSUM=YSUM+Y(6,I)*A(I)/(T(I)+.1D-30)
C
    DO 20 I=1,NZMU
    DER(5,I)=0.5D0*OME*Y(6,I)*YSUM
20 DER(6,I)=-Y(6,I)/(T(I)+.1D-30)+.5D0*OME*Y(5,I)*YSUM
C
    DO 30 I=1,10
    DER(1,I)=0.5D0*OME*Y(2,I)*YSUM
    DER(2,I)=-Y(2,I)/(ang(I))+.5D0*OME*Y(1,I)*YSUM
    DER(3,I)=0.5D0*OME*Y(4,I)*YSUM
30 DER(4,I)=-Y(4,I)/RMU(I) + .5D0*OME*Y(3,I)*YSUM
    RETURN
    END
C
C
C    FUNCTIONS
C
C
FUNCTION RU(AN,U)
IMPLICIT REAL*8(A-H,O-Z)
IF((1.D0-1.D0/(AN*AN)).LT.0.D0) THEN
    UCR=0.D0
ELSE
    UCR=DSQRT(1.D0-1.D0/(AN*AN))
ENDIF
IF (U.LT.OCR) THEN
    RU=1.0D0
ELSE
    A=DSQRT(1.D0/(AN*AN)-(1.D0-U*U))
    RU=.5D0*(((A-U)/(A+U))**2+((A-U/AN**2)/(A+U/AN**2))**2)
ENDIF
RETURN
END
C
C
DOUBLE PRECISION FUNCTION FLAGR(X,Y,XARG,IDEQ,MIN,N)

```

```

      IMPLICIT REAL*8(A-H,O-Z)
      DIMENSION X(N),Y(N)
C   THIS SUBROUTINE CALCULATES INTERPOLATES BY LAGRANGE'S (IDEG-TH)
C   POLYNOMIAL APPROXIMATION METHOD--OUTLINED IN DETAIL IN "APPLIED
C   NUMERICAL METHODS",CARNAHAN,LUTHER,WILKES,PP.27-33.
      FACTOR=1.D0
      MAX=MIN+IDEG
      DO 2 J=MIN,MAX
      IF(XARG.NE.X(J)) GO TO 2
      FLAGR=Y(J)
      RETURN
2 FACTOR=FACTOR*(XARG-X(J))
      YEST=0.D0
      DO 5 I=MIN,MAX
      TERM=Y(I)*FACTOR/(XARG-X(I))
      DO 4 J=MIN,MAX
4 IF(I.NE.J) TERM=TERM/(X(I)-X(J))
5 YEST=YEST+TERM
      FLAGR=YEST
      RETURN
      END
C
C   SUBROUTINE DXA(N,AA,BB,X,A)
C

```

An Example of Data File (input data)

```

48 1.331 0.0001 1.0e-7 10 5.0
0.0
0.00020
0.00125
0.00246
0.00505
0.00761
0.01020
0.01282
0.01546
0.03000
0.04999
0.06760
0.09004
0.11797
0.14935
0.17568
0.21429
0.26923
0.33333

```

APPENDIX C

Finite Difference Method with Variable Grid Sizes

Most books on numerical techniques describe finite difference methods for equally spaced grid. The general procedure for developing the finite difference method with variable grid spacing follows the same procedure as for equally spaced grid. Let $f(x)$ be a function that can be expanded in a Taylor series. Then a Taylor series expansion of the functions $f(x_i+h_i)$ and $f(x_i+h_i+h_{i+1})$ about x_i are given as

$$\begin{cases} f(x_i + h_i) = f(x_i) + h_i f'(x_i) + \frac{h_i^2}{2} f''(x_i) + \dots \\ f(x_i + h_i + h_{i+1}) = f(x_i) + (h_i + h_{i+1}) f'(x_i) + \frac{(h_i + h_{i+1})^2}{2} f''(x_i) + \dots \end{cases} \quad (C-1)$$

where prime denote derivatives with respect to x . Eliminating $f''(x_i)$ between Eqs. (C-1) and reducing the result, the following formula for the first derivative by forward difference will be obtained:

$$f'(x_i) = -\frac{2h_i + h_{i+1}}{h_i(h_i + h_{i+1})} f(x_i) + \frac{h_i + h_{i+1}}{(h_i)(h_{i+1})} f(x_i + h_i) - \frac{h_i}{h_{i+1}(h_i + h_{i+1})} f(x_i + h_i + h_{i+1}) \quad (C-2)$$

Eliminating $f'(x_i)$ between Eqs. (C-1) and reducing the result, the formula for the second derivative by forward difference will be obtained:

$$f''(x_i) = 2 \left[\frac{1}{h_i(h_i + h_{i+1})} f(x_i) - \frac{1}{(h_i)(h_{i+1})} f(x_i + h_i) + \frac{1}{h_{i+1}(h_i + h_{i+1})} f(x_i + h_i + h_{i+1}) \right] \quad (C-3)$$

The first derivative by backward difference can be obtained by the same method as the forward difference. In this case, equations similar to Eqs. (C-1) are

$$\begin{cases} f(x_i - h_{i-1}) = f(x_i) - h_{i-1}f'(x_i) + \frac{h_{i-1}^2}{2}f''(x_i) + \dots \\ f(x_i - h_{i-1} - h_{i-2}) = f(x_i) - (h_{i-1} + h_{i-2})f'(x_i) + \frac{(h_{i-1} + h_{i-2})^2}{2}f''(x_i) + \dots \end{cases} \quad (C-4)$$

and the equation similar to Eq. (C-2) is

$$f'(x_i) = \frac{2h_{i-1} + h_{i-2}}{h_{i-1}(h_{i-1} + h_{i-2})}f(x_i) - \frac{h_{i-1} + h_{i-2}}{(h_{i-1})(h_{i-2})}f(x_i - h_{i-1}) + \frac{h_{i-1}}{h_{i-2}(h_{i-1} + h_{i-2})}f(x_i - h_{i-1} - h_{i-2}) \quad (C-5)$$

Equations (C-2), (C-3), and (C-5) are applied to Eqs. (3-42a), (3-43), and (3-42b), respectively, in the text, to make the appropriate matrix for the improved P_N approximation. The grid sizes are maintained as the Gaussian quadrature points which are used to solve the integrals numerically.

APPENDIX D

Modified P_N Approximation Program

Program Source Code

```
PROGRAM PN APPROXIMATION for correlation
implicit real*8 (a-h,o-z)
CHARACTER*12 OUTPUT
dimension aq(100),xq(100),backp(100),transp(100),amiuq(100)
DIMENSION A(400,400),C(50),P(400),TBC(40),dt(400),wq(100),bbc(40)
c
c      open datafile and read information from it
c
c      mpn.dat = name of datafile
c      OUTPUT = name of output file
c      npic = number of quadreture points
c      n = order of Pn approximation (must be odd numbers)
c      tau0 = optical thickness
c      amiuo = cosine of exiting angle
c      m1 = refractive index at incident beam boundary
c      m2 = refractive index at the other boundary
c
      open(2,file='mpn.dat',status='old')
      READ(2,*)OUTPUT,npic,n,tau0,amiuo,m1,m2
      OPEN(1,FILE=OUTPUT)
      PI=3.1415927d0
      NN=(N+1)/2.0d0
c
c      cosine of incident beam angle
c
      amiui=1.0d0
C
C      PRODUCE HEADING
C
      WRITE(1,30)N,tau0,amiuo
30 FORMAT(1X,'Order of P approximation=',I2/1X,'tau0=',F6.2/
& 1X,'Miu=',F4.2//1X,'omega',T11,'t/to',t18,'Backscattering',
& T42,'Transmission'/60('-')/)
      ASA=0.d0
      CALL DXA(NPIC,ASA,tau0,XQ,AQ)
      call dxa(npic,asa,1.d0,amiuq,wq)
      do 2 i=1,npic+1
      if (i .eq. 1) then
          DT(i)=xq(i)
```

```

        go to 2
    end if
    if (i .eq. npic+1) then
        dt(i)=tau0-xq(i-1)
        go to 2
    end if
    dt(i)=xq(i)-xq(i-1)
2    continue
c
c    read t/to from datafile
c
10  READ(2,*,end=999)time
    y=2*time
    w=dexp(-y)*dsinh(y)/y
    call coef(y,c,n+1)
    iter=0
    do 50 i=1,npic
        transp(i)=1.
        backp(i)=1.
50  continue
20  DO 120 I=1,NN
    sum=0.
    add=0.
    do 40 j=1,npic
        add=add+transp(j)*rou(amiuq(j),rn2)*amiuq(j)**(2*i-1)*wq(j)
        sum=sum+backp(j)*rou(amiuq(j),rn1)*amiuq(j)**(2*i-1)*wq(j)
40  continue
    TBC(I)=1.-rou(amiui,1./rn1)+sum
    bbc(i)=add
120 CONTINUE
    iter=iter+1
    write(*,*)'iter= ',iter
    if (iter .eq. 50) go to 999
    do 15 i=1,400
        do 25 j=1,400
            a(i,j)=0.
25  continue
15  continue
C
C    INPUT THE COEFFICIENTS FOR A'S TOP BC.
C
    t1=(2*dt(1)+dt(2))/(dt(1)*(dt(1)+dt(2)))
    t2=(dt(1)+dt(2))/(dt(1)*dt(2))
    t3=dt(1)/(dt(2)*(dt(1)+dt(2)))
    DO 160 I=1,NN
        DO 150 K=0,(N-1)/2
            AK=0.0
            AKP=0.0
            DO 140 L=0,K
                AK=AK+(-1.0)**L*FACT(4*K-2*L)/((2.*K-2.*L+2.*I)*

```

```

&      FACT(2*K-L)*FACT(L)*FACT(2*K-2*L))
      AKP=AKP+(-1.0)**L*FACT(4*K-2*L+2)/((2*K-2*L+2*I+1)
&      *FACT(2*K-L+1)*FACT(L)*FACT(2*K-2*L+1))
140    CONTINUE
      X=4.**K*(1.-W*C(2*K+1))
      A(I,K+1)=A(I,K+1)+t1*(2*K+1)*AK/X+(4.*K+3)*AKP/
&      2.**(2*K+1)
      A(I,K+1+NN)=A(I,K+1+NN)-t2*(2*K+1)*AK/X
      A(I,K+1+2*NN)=A(I,K+1+2*NN)+t3*(2*K+1)*AK/X
      IF (K .LT. 1) GO TO 150
      A(I,K)=A(I,K)+2.*t1*K*AK/X
      A(I,K+NN)=A(I,K+NN)-2.*t2*K*AK/X
      A(I,K+2*NN)=A(I,K+2*NN)+2.*t3*K*AK/X
150    CONTINUE
      A(I,NN*(npic+2)+1)=4.*PI*TBC(I)
160    CONTINUE
C
C      INPUT THE COEFFICIENTS FOR A'S AT INTERVALS
C
      J=0
      DO 180 I=NN,NN*npic,NN
        J=J+1
        DO 170 K=1,N,2
          II=I+(K+1)/2
          M=K+1
          IF (K .EQ. N) M=0
          T1=-2*M*(K+2)*(1.-W*C(K))/(2.*K+3.)
          T2=-2*(M**2*(1.-W*C(K))/(2.*K+3.)+K**2*(1.-W*C(K+2)))/
&          (2.*K-1.)
          T3=-2*K*(K-1.)*(1.-W*C(K+2))/(2.*K-1.)
          T4=(2.*K+1.)*(1.-W*C(K))*(1.-W*C(K+1))*(1.-W*C(K+2))
          A(II,(K+3)/2+(J-1)*NN)=T1/(dt(j)*(dt(j)+dt(j+1)))
          A(II,(K+3)/2+J*NN)=-T1/(dt(j)*dt(j+1))
          A(II,(K+3)/2+(J+1)*NN)=T1/(dt(j+1)*(dt(j)+dt(j+1)))
          A(II,(K+1)/2+(J-1)*NN)=T2/(dt(j)*(dt(j)+dt(j+1)))
          A(II,(K+1)/2+J*NN)=T4-T2/(dt(j)*dt(j+1))
          A(II,(K+1)/2+(J+1)*NN)=T2/(dt(j+1)*(dt(j)+dt(j+1)))
          IF (K .LT. 2) GO TO 170
          A(II,(K-1)/2+(J-1)*NN)=T3/(dt(j)*(dt(j)+dt(j+1)))
          A(II,(K-1)/2+J*NN)=-T3/(dt(j)*dt(j+1))
          A(II,(K-1)/2+(J+1)*NN)=T3/(dt(j+1)*(dt(j)+dt(j+1)))
170      CONTINUE
      A(I+1,NN*(npic+2)+1)=0.0
180    CONTINUE
C
C      INPUT THE COEFFICIENTS FOR A'S AT BOTTOM BC.
C
      t1=(2*dt(npic+1)+dt(npic))/(dt(npic+1)*(dt(npic+1)+dt(npic)))
      t2=(dt(npic+1)+dt(npic))/(dt(npic+1)*dt(npic))
      t3=dt(npic+1)/(dt(npic)*(dt(npic+1)+dt(npic)))

```

```

J=0
DO 200 I=ii+1,NN*(npic+2)
  ll=i-nn*(npic+1)
  DO 190 K=0,(N-1)/2
    AK=0.0
    AKP=0.0
    DO 130 L=0,K
      AK=AK+(-1)**L*FACT(4*K-2*L)/((2*K-2*L+2*(j+1))*
&      FACT(2*K-L)*FACT(L)*FACT(2*K-2*L))
      AKP=AKP+(-1)**L*FACT(4*K-2*L+2)/((2*K-2*L+2*(j+1)+1)
&      *FACT(2*K-L+1)*FACT(L)*FACT(2*K-2*L+1))
130    CONTINUE
      X=-4.**K*(1.-W*C(2*K+1))
      A(I,K+i-j)=A(I,K+i-j)+t1*(2*K+1)*AK/X-
&      (4.*K+3)*AKP/2**(2*K+1)
      A(I,K+i-j-NN)=A(I,K+i-j-NN)-t2*(2*K+1)*AK/X
      A(I,K+i-j-2*NN)=A(I,K+i-j-2*NN)+t3*(2*K+1)*AK/X
      IF (K .LT. 1) GO TO 190
      A(I,K+i-j-1)=A(I,K+i-j-1)+2.*t1*K*AK/X
      A(I,K+i-j-NN-1)=A(I,K+i-j-NN-1)-2.*t2*K*AK/X
      A(I,K+i-j-2*NN-1)=A(I,K+i-j-2*NN-1)+2.*t3*K*AK/X
190    CONTINUE
      A(I,NN*(npic+2)+1)=4.*pi*bbc(ll)
      J=J+1
200  CONTINUE
C
C    SOLVING SIMULTANEOUS EQUATIONS BY GAUSS ELIMINATION
C
      CALL GAUSS(A,P,NN*(npic+2))
c
c    store the value of "p" in more clear manner
c    "A" is "A(tau)" in intensity calculation in this manner
c
      do 210 k=0,(n-1)/2
        do 230 j=1,npic+2
          a(2*k+2,j)=p((j-1)*nn+k+1)
230      continue
210    continue
c
c    calculate even number of "A(tau)"
c
      do 250 k=0,n,2
        id=0
        isign=1
        temp1=-(k+1)/((2*k+1)*(1.-w*c(k+1)))
        temp2=-k/((2*k+1)*(1.-w*c(k+1)))
        do 240 j=1,npic+2
          if (j .eq. npic) then
            id=1
            isign=-1

```

```

        end if
        tt1=(2*dt(j-id)+dt(j+1-3*id))/
&      (dt(j-id)*(dt(j-id)+dt(j+1-3*id)))
        tt2=(dt(j-id)+dt(j+1-3*id))/(dt(j-id)*dt(j+1-3*id))
        tt3=dt(j-id)/(dt(j+1-3*id)*(dt(j-id)+dt(j+1-3*id)))
        t1=-tt1*a(k+2,j)
        t2=tt2*a(k+2,j+1-2*id)
        t3=-tt3*a(k+2,j+2-4*id)
        if (k .eq. 0) go to 260
        t4=-tt1*a(k,j)
        t5=tt2*a(k,j+1-2*id)
        t6=-tt3*a(k,j+2-4*id)
260      a(k+1,j)=isign*temp1*(t1+t2+t3)+isign*temp2*(t4+t5+t6)
240      continue
250  continue
C
C      calculate transmission and backscattering intensity at quadreture pts.
C
      iflag=1
      do 90 j=1,npic
        isign=1
300      ants=0.
        DO 280 k=1,n+1
          SUM=0.
          DO 270 i=2,npic+1
            sum=sum+a(k,i)*exp(-isign*(tau0-xq(i-1))/amiuq(j))*aq(i-1)
270      continue
          AL=0.
          DO 290 L=0,(K-1)/2
            AL=al+(-1)**L*FACT(2*K-2*L-2)*(isign*amiuq(j))**
&      (k-2*L-1)/(FACT(K-L-1)*FACT(L)*FACT(K-2*L-1))
290      CONTINUE
          al=al/2**(k-1)
          ants=ants+(2*k-1)*AL*c(k)*sum
280      CONTINUE
          if (isign .eq. 1) then
            trans=ants*w/(amiuq(j)*4*pi)
            tau=tau0
            tau0=0.
            isign=-1
            go to 300
          end if
          back=ants*w/(4*pi*amiuq(j))
          tau0=tau
          if ((abs(back-backp(j)) .gt. 1.e-4) .or.
&      (abs(trans-transp(j)) .gt. 1.e-4)) iflag=0
          backp(j)=back
          transp(j)=trans
90      continue
      if (iflag .eq. 0) go to 20

```

```

      do 91 i=1,npic
91    continue
C
C      calculate transmission and backscattering intensity
C
      isign=1
      an=rn2
301  ants=0.
      amiu=dsqrt(1.-(1.-amiuo**2)/an**2)
      DO 281 k=1,n+1
      SUM=0.
      DO 271 i=2,npic+1
        sum=sum+a(k,i)*exp(-isign*(tau0-xq(i-1))/amiu)*aq(i-1)
271    continue
      AL=0.
      DO 291 L=0,(K-1)/2
        AL=al+(-1)**L*FACT(2*K-2*L-2)*(isign*amiu)**(k-2*L-1)/
&      (FACT(K-L-1)*FACT(L)*FACT(K-2*L-1))
291    CONTINUE
      al=al/2**(k-1)
      ants=ants+(2*k-1)*AL*c(k)*sum
281  CONTINUE
      if (isign .eq. 1) then
        trans=ants*(1.-rou(amiu,an))*w/(amiu*4*pi*an**2)
        tau=tau0
        tau0=0.
        isign=-1
        an=rn1
        go to 301
      end if
      back=ants*(1.-rou(amiu,an))*w/(4*pi*amiu*an**2)
C
C      PRODUCE OUTPUT
C
      WRITE(1,220)w,time,back,trans
220  FORMAT(1X,F6.4,T10,f7.6,t16,F13.6,T40,F13.6)
      tau0=tau
      go to 10
999  STOP
      END

c
c  subroutine for calculating Legendre expansion coefficients (from Nafaa Reguigui)
c
      SUBROUTINE coef(Z,XK,IORDER)
C
C      RETURNS THE VALUES OF THE MODIFIED BESSEL FUNCTION OF
C      ALL ORDERS
C      UP TO IORDER AND AT THE REAL VALUE Z, i.e.,
C       $BM(i+1) = \sqrt{\pi/2Z} I(i+1/2)(Z)$ ,  $i=0,1,\dots,IORDER$ 
C      RETURNS THE VALUES AT THE VECTOR BM

```



```

100    CONTINUE
      TEMP=S(I)
      S(I)=S(MAX)
      S(MAX)=TEMP
    END IF
    DO 40 J=I+1,N
      IF (A(J,I) .EQ. 0.0) GO TO 40
      FACTOR=A(J,I)/A(I,I)
      DO 50 K=I,N+1
        A(J,K)=A(J,K)-A(I,K)*FACTOR
50      CONTINUE
40    CONTINUE
20    CONTINUE
    IF (A(N,N) .EQ. 0.0) THEN
      WRITE(*,*)' NO UNIQUE SOLUTION EXISTS'
      STOP
    END IF
    DO 60 I=N,1,-1
      SUM=0.0
      DO 70 J=I+1,N
        SUM=SUM+A(I,J)*X(J)
70    CONTINUE
      X(I)=(A(I,N+1)-SUM)/A(I,I)
60    CONTINUE
    RETURN
    END

c
c   Function to calculate reflectivity "rou"
c
function rou(amiu,m)
implicit real*8 (a-h,o-z)
if ((1.-1./m**2) .lt. 0.) then
  ucr=0.
else
  ucr=dsqrt(1.-1./m**2)
end if
if (amiu .lt. ucr) then
  rou=1.0
else
  s=dsqrt(1./m**2-(1.-amiu**2))
  temp1=((s-1./m**2*amiu)/(s+1./m**2*amiu))**2
  temp2=((s-amiu)/(s+amiu))**2
  rou=0.5*(temp1+temp2)
end if
return
end

c
C
C   FUNCTION TO CALCULATE FACTORIAL OF N
C

```

C

```
FUNCTION FACT(N)
implicit real*8 (a-h,o-z)
IF (N .EQ. 0) THEN
  FACT=1.0
  RETURN
END IF
FACT=1.0
DO 10 I=1,N
  FACT=FACT*I
10 CONTINUE
RETURN
END
```

c

c subroutine for numerical integration

c

```
SUBROUTINE DXA(N,AA,BB,X,A)
```

An Example of Data File (input data)

```
'mpn.out',48,5,13.65d0,0.9848,1.331,1.331
0.00020
0.00125
0.00246
0.00505
0.00761
0.01020
0.01282
0.01546
0.03000
0.04999
0.06760
0.09004
```

VITA

Farhad Dorri-Nowkoorani

Candidate for the Degree of

Doctor of Philosophy

**Thesis: MULTIPLE SCATTERING CORRELATION MEASUREMENTS
IN FLUID/PARTICLE SUSPENSIONS: APPLICATION TO
PARTICLE CHARACTERIZATION**

Major Field: Mechanical Engineering

Biographical:

Personal Data: Born in Abadan, Iran, On November 11, 1959, the son of Kamaledin and Fakhrosadat Dorri-Nowkoorani.

Education: Graduated from Hashroodi High School, Tehran, Iran in May 1978; received Bachelor of Science degree in Mechanical Power Technology from Oklahoma State University, Stillwater, Oklahoma in May 1984; recieved Master of Science in Engineering Technology from Murray State University, Murray, Kentucky in December 1985; recieved Master of Science in Mechanical Engineering from Oklahoma State University, Stillwater, Oklahoma in May 1989. Completed the requirements for the Doctor of Philosophy with the major in Mechanical Engineering at Oklahoma State University in May 1995.